Beam-, Target- and Double-Spin Asymmetry Measurements in Deeply Virtual π^0, π^+ and π^- Meson Production

Gavin William Murdoch

Submitted in fulfilment of the requirements for the
Degree of Doctor of Philosophy

School of Physics and Astronomy
College of Science and Engineering

March 2019

Beam-, Target- and Double-Spin Asymmetry Measurements in Deeply Virtual π^0, π^+ and π^- Meson Production

Gavin William Murdoch

Submitted in fulfilment of the requirements for the
Degree of Doctor of Philosophy

March 2019

Abstract

This thesis presents measurements of spin asymmetries in single pion electroproduction from the EG1-DVCS experiment carried out at the Thomas Jefferson National Accelerator Facility in 2009 with use of the CEBAF Large Acceptance Spectrometer. The experiment made use of a 6 GeV longitudinally polarised electron beam and (dynamically) longitudinally polarised targets of $^{14}NH_3$ and $^{14}ND_3$ (giving access to protons and deuterons), providing the means to measure three spin asymmetries: beam-, target-, and double-spin. Deeply Virtual Meson Production for the π^0, π^+ and π^- channels were studied for the kinematic range of $Q^2 > 1$ GeV^2 and $W > 2$ GeV. The collection of measurements includes the analysis of numerous reconstruction topologies, as well as making use of different target materials. These are the world's first charged pion spin asymmetry measurements in this kinematic regime. The sPlot maximum likelihood fit-based background subtraction technique was implemented in the data analysis, showing strong agreement with a traditional and commonly used cuts-based approach. This novel technique was thoroughly tested to develop implementation and execution. The results obtained will provide a reference point for future analyses at the upgraded experimental facility and motivate the use of the sPlot technique. These measurements will provide insight into the structure of nucleons through their interpretation in relation to Generalised Parton Distributions which describe sub-structure correlations between longitudinal momentum and transverse position of partons. In particular, here the spin asymmetries dependence on t, the squared four-momentum transfer to the target nucleon, carries information on the spatial parton distributions in the transverse plane.

Contents

List of Tables

List of Figures

Declaration

The work in this thesis is based on research carried out at the Nuclear Physics Group, School of Physics and Astronomy, University of Glasgow, UK. No part of this thesis has been submitted elsewhere for any other degree or qualification and it is all my own work unless referenced to the contrary in the text.

Chapter 1

Introduction, Motivation and Past Measurements

This introduction of theory will discuss the substructure of nucleons, electron scattering and a theoretical link to the imaging of nucleons. The formalism which connects these will be described in appropriate detail for the analysis performed in this thesis - the production of single pions. The relation of the theoretical description to the quantities measured experimentally will be presented.

Specific to the work of this thesis, spin asymmetry measurements were made for the process of Deeply Virtual Meson Production for electroproduction of single π^0 and π^+ from a proton target, and π^- from the neutron target. These reactions were studied at the Thomas Jefferson National Accelerator Facility, and the data analysis made use of a unique fit-based weighting technique. The results are presented with a focus on interpretation using the theoretical framework of Generalised Parton Distributions.

1.1 Introduction to the Substructure of Nucleons

The study of the internal structure of matter is of great interest in the field of nuclear physics, in which the experimental measurement reach is continuing to extend to new limits. Since the first discovery of a subatomic particle, the electron in 1897, an abundance of particles have been observed with there being a desire to explain them in terms of fundamental particles - ones with no substructure. The idea of an elementary particle description was found to be valid for *leptons* (such as the electron) which interact via three of the four fundamental forces of nature - the electromagnetic, gravitational and weak force. This was not the case for particles contained within nuclei (such as the proton) which also interact via the strong force, appearing to have a complex structure and therefore requiring adequate theoretical tools to describe this. Each of the fundamental forces have different effective strengths over varying ranges, with the strong force being dominant at the subatomic level (short length). Since the 1970s the theory of

quantum chromodynamics (QCD) has developed to describe interactions of the strong force, and forms a significant part of the Standard Model theory of particles with the electromagnetic and weak interactions. QCD explains the strong interaction in terms of gluon force carriers and the confinement of the fundamental *quark* particles within subatomic hadrons. It is these massless gluons which mediate the strong force and are responsible for binding quarks together.

A brief overview will be given on the theoretical ideas relevant to the work in this thesis, and will assume the reader has prior knowledge of hadron physics.

1.2 Hadrons

1.2.1 Classification and Properties

There are two classifications of hadrons - *baryons* consisting of three quarks, and *mesons* consisting of a quark-antiquark pair. This classification makes use of the specific reference to *valence quarks*, with these being the main internal composite particles used in the quark model description of hadrons. A simplistic description is that the gluon force carriers bind hadrons together in accordance with the content of their valence quark *flavour* and *colour*. There are six varieties of quark flavours: *up*, *down*, *charm*, *strange*, *top* and *bottom*. Each quark has a corresponding antiparticle being its antiquark. Their uniqueness is characterised by properties such as electric charge, intrinsic angular momentum (*spin*), baryon number, and the flavour quantum numbers: charm, strangeness, topness, bottomness and the third component of isospin (which is a property of observed symmetry). A *colour* charge value is also incorporated into their description as a conserved quantity in the creation and annihilation of particles-antiparticles and in any strong interaction process. The description of gluons also makes use of some of these parameters, such as electric charge, spin and colour charge.

Common baryons are protons and neutrons, which are stable in many configurations of atomic nuclei, but when unbound it is only the proton which is stable. The most abundant chemical element in the universe is hydrogen, mainly the first isotope (protium, ^1H) in which the nucleus is comprised of one proton. The properties of *nucleons* (protons and neutrons) are of great interest since they are constituents of almost all visible matter, exhibiting somewhat similar yet unique properties both externally and internally. Mesons are short-lived unstable hadrons, and can be categorised by the likes of their valence quark composition, spin configuration and orbital angular momentum, with a pion (π) being a *pseudoscalar meson* and a rho (ρ) being a *vector meson*. Pseudoscalar mesons and vector mesons are categorised as 0^- and 1^- respectively using the J^P classification, where J is total angular momentum and P is parity (symmetry of spatial transformations). Although gluons are massless, it is the energy of their interactions that contributes to the vast majority of the invariant mass of hadrons [1]. The strong force disallows any hadron's constituent quarks to be directly observed (as free quarks), with it

being more energetically favourable for another hadron to be created. This somewhat basic description allows for a rather deep understanding of nuclear matter composition and interactions, although it is clear upon closer examination (both theoretically and experimentally) that a full understanding of hadron structure requires a description which is significantly more complex.

1.2.2 Hadron Substructure

Experimental study of the internal composition of hadrons revealed a very rich structure, further to the valence quarks there is also a "sea" containing gluons and quark-antiquark pairs. Aspects of the quark-antiquark distributions can be thought of as diffuse pion clouds within the hadron. The total spin of a hadron has been theoretically proposed as a combination of the orbital angular momentum of the quarks and gluons, the intrinsic spin of quarks, and the gluon helicities. There is currently a "spin puzzle" due to the incomplete understanding of each contribution to the total observed spin of a hadron. These different constituents of hadronic matter (quarks and gluons) can be classed as "partons", allowing for a somewhat general description of their interactions when probed experimentally.

Hadrons examined using probes of different energy reveal structure information at different scales - the higher the energy, the finer the structure. This can be thought of as *imaging* hadrons, with access to not only spatial distributions of their constituents, but momentum as well. It is through the fundamental duality property that performing the mathematical Fourier transform of a function of position space yields the function in momentum space, with the converse being true. With these expressed as wave functions in a quantum mechanical system description, a statement can be made regarding the Heisenberg uncertainty principle:

$$\Delta x \Delta p_x \geq \frac{\hbar}{2} \tag{1.1}$$

where this is the relation describing the uncertainty of position and momentum in the x dimension, with the use of the reduced Planck's constant ($\hbar$). Importantly, there is a limit set on the precision to which these complementary variables can both be simultaneously known.

1.3 Electron Scattering

Since leptons are fundamental (and point-like), they are beneficial in experimentally probing hadrons as the interaction is rather well understood from a theoretical point of view. There will now be a focus on describing an electron probe on a proton in this body of work, in reference to the fact that the discovery of quarks was made with use of this scattering reaction. Note, it is through the electromagnetic force that the lepton and hadron interact in the scattering reaction. A virtual photon (γ^*) exists for a very short time and mediates the interaction, as it is the electromagnetic force carrier to be considered in the scattering calculations. This is implicit in

the scattering process descriptions. The four-momentum of the virtual photon is $q = (\nu/c,\ \mathbf{q})$, where ν is the virtual photon's energy, $\mathbf{q}$ its three-momentum, and c is the speed of light. It is the energy of the incident electron which sets the possible energy of the virtual photon in the scattering process, and can be calculated rather precisely.

The dominant scattering process for an incident low energy electron is *elastic*, in which both the momenta and total kinetic energy of the system are conserved before and after the scattering reaction. An example reaction is:

$$e(e) + p(p) \rightarrow e'(e') + p'(p') \tag{1.2}$$

where the corresponding four-momenta are given in parentheses for each particle. This reaction can be thought of as the electron and proton "bouncing" off one another.

Incident electrons of higher energies means that *inelastic* scattering is more likely to occur, and is a process in which the total kinetic energy is not conserved in the reaction i.e. it goes into other processes. The hadronic system changes due to the energy transferred and new particles are created, with an example being:

$$e(e) + p(p) \rightarrow e'(e') + X \tag{1.3}$$

where "X" represents new particles created according to cross-section probabilities of the scattering interaction. This reaction can be thought of as the proton being "shattered apart", i.e. there is fragmentation of the initial proton. *Electroproduction* is the term describing the production of particles in this type of scattering reaction induced by an electron.

Deep inelastic scattering (DIS) is an extension of the above, in which *deep* refers to the virtual photon probing very small distances in comparison to the size of the target hadron. Specifically, this is the case when $Q^2 \gg 0$ GeV^2 where $Q^2 = -q^2$ and quantifies the negative squared four-momentum transfer from the incident electron to the target particle. Note, use of a real photon probe (in a *photoproduction* experiment) would have $Q^2 \sim 0$ GeV^2. The probe resolution is set by the fact that virtual photon's wavelength is inversely proportional to Q^2, e.g. high Q^2 corresponds to short wavelengths. This allows for the fine structure of hadrons to be examined with the use of a high energy electron probe. It is in DIS experiments that the virtual photon scatters from individual partons within the target particle.

1.4 Nucleon Imaging

The imaging of nucleons benefits from information obtained via DIS such as longitudinal momentum and helicity distributions of partons. A "picture" of the nucleon is built up from considering the partons in transverse and longitudinal planes defined with respect to the momentum transfer axis in the reaction.

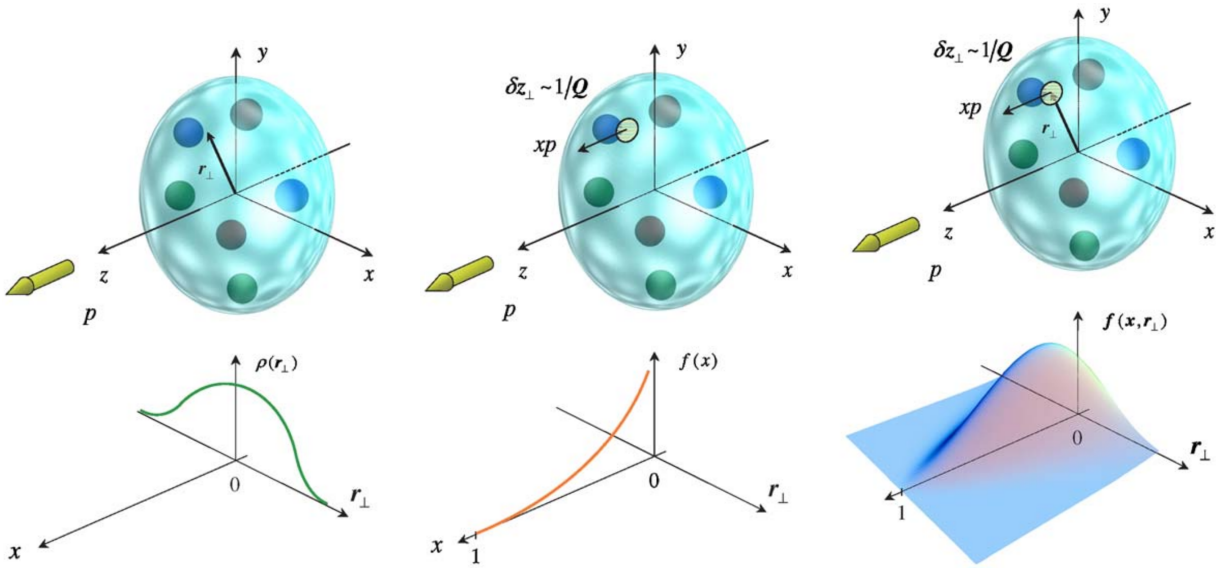

(a) Transverse position

(b) Longitudinal momenta

(c) Fully correlated distributions in coordinate and momentum space

Figure 1.1: Pictorial representations of the distributions accessible with (a) FFs, (b) PDFs and (c) GPDs in the infinite momentum frame in z. Note, the notation of $r_\perp$ in place of $b_\perp$ that is described in this work. [2].

Over recent years, the information and imaging was built up over stages from the use of Form Factors (FFs) and Parton Distribution Functions (PDFs). FFs make use of the transverse position of partons ($b_\perp$), with PDFs extending this approach to include the longitudinal momenta. Elastic scattering experiments give access to FFs via cross-section measurements, and DIS experiments give access to PDFs via structure functions which parameterise the DIS cross-section.

A recent development in the theoretical view of imaging was the introduction of Generalised Parton Distributions (GPDs). In the infinite momentum frame (in which the nucleon is travelling with infinite momentum in the z-axis, for example), GPDs can be interpreted as effectively relating the transverse position of partons ($b_\perp$) to their longitudinal momentum as a fraction of the nucleon's momentum (x). They are mathematical objects describing the correlation of these parameters for partons. GPDs can describe the nucleon's quark and gluon angular momentum components and essentially create a three-dimensional picture of the nucleon. GPDs are universal functions which can be investigated over a range of x to give a thorough description of the nucleon's substructure, furthering the understanding of QCD in the bound state regime.

Figure 1.1 shows pictorial representations of nucleon structure, in the infinite momentum frame in z, with respect to FFs, PDFs and GPDs respectively. This figure is one of the most intuitive ways of illustrating the nucleon "imaging" possible with GPDs, formed via fully correlated distributions in coordinate and momentum space.

1.5 GPDs

1.5.1 Introduction to GPDs and DVMP

There are few experimental options that give access to GPDs, with the most thoroughly studied process being Deeply Virtual Compton Scattering (DVCS), followed by Deeply Virtual Meson Production (DVMP). It is important to highlight that information obtained via GPDs should be independent of the experimental channel, and therefore testing the universality of descriptions is crucial.

In the GPD framework, a QCD factorisation (valid in the DIS region) separates the reactions into a *hard* and a *soft* part, where the former deals with the electron scattering from the quark (perturbative calculation), and the latter deals with the interaction within the nucleon (non-perturbative calculation). The *hard* part of the process is described in perturbative quantum electrodynamics (QED) due to the exchange of virtual photon with a charged object. Twist is defined in relation to the dimension and spin of an operator such that twist = dimension − spin [3] [4]. With respect to GPDs, it classifies the factors of $1/Q$ in the scattering amplitude and therefore twist-two refers to the $1/Q^2$ description. In this body of work, the *soft* part is parameterised by twist-two GPDs, and is not as easily calculable.

DVCS and DVMP are hard exclusive processes as they make use of the factorisation valid at high Q^2, and are reactions with a known final state particle configuration following the scattering.
In DVCS a real photon (on shell) is produced in the reaction

$$e(e) + p(p) \rightarrow e'(e') + p(p') + \gamma(q') \tag{1.4}$$

In DVMP a single meson is produced in the reaction

$$e(e) + p(p) \rightarrow e'(e') + N(p') + M(m) \tag{1.5}$$

where N represents a nucleon and M represents a meson. The corresponding four-momenta are given in parentheses for each particle.

To ensure one is truly considering the DVMP channel, it is common to impose kinematic restrictions ("DVMP cuts") which correspond to $Q^2 > 1$ GeV^2 and $W > 2$ GeV. W represents the invariant mass of the virtual photon and target nucleon system, and is equivalent to the final state hadronic system. This relation can be expressed as

$$W = \sqrt{(q+p)^2} = \sqrt{(p'+m)^2} \tag{1.6}$$

The criteria of $W > 2$ GeV is sufficiently high to avoid the "resonance region" which corresponds to scattering reactions in which the target nucleon is excited to an intermediate state before

decaying to its final state. In DVMP there is no intermediate state in the scattering reaction.

Exclusive processes are a significantly important area in the study of GPDs. "Handbag" diagrams representing DVCS and DVMP with use of a proton target are given in figures 1.2a and 1.2b respectively, specifically in which a virtual photon interacts with a quark. Figure 1.2a also indicates an important quantity related to the quark's longitudinal momentum as a fraction if the nucleon's momentum, x; the skewness, ξ, which is defined as the negative of half the longitudinal momentum fraction change for the struck quark. It is DVCS that is considered the cleanest way to access GPDs, as DVMP also includes a Distribution Amplitude (DA) which is related to the wave function of the meson [6] [7]. This gives sensitivity to the structure of the produced meson in the reaction which is also of key interest. The formation of the meson is described by the corresponding leading twist-two meson distribution amplitude (DA) while the transition from the initial nucleon to the final hadronic state is encoded in twist-two GPDs [8].

GPDs are functions of x, ξ, and the Mandelstam variable t (defined as the squared four-momenta transfer to the nucleon). ξ and t can be expressed as

$$\xi \approx \frac{x_B}{2-x_B} \qquad \text{and} \qquad t = (p'-p)^2 = (q-m)^2 \tag{1.7}$$

where ξ makes use of the dimensionless "Bjorken x" variable (x_B). Bjorken x is a way to quantify the *scaling* in the scattering interaction and is defined as

$$x_B = \frac{Q^2}{2p\cdot q} \tag{1.8}$$

Each of the fundamental quark flavours (q) have eight independent GPDs:

- Quark helicity conserving (*chiral-even*) GPDs: H^q, E^q, $\widetilde{H}^q$, $\widetilde{E}^q$
- Quark helicity-flip (*chiral-odd*) GPDs: H^q_T, E^q_T, $\widetilde{H}^q_T$, $\widetilde{E}^q_T$

The chiral-odd processes are ones in which there is a flip of the helicity of the quark from which the scattering takes place. These are also referred to as *transversity* GPDs, and are indicated by their subscript of "T", which is due to the scattering of a virtual photon with transverse polarisation. These are not directly accessible via DVCS at leading-twist (twist-two), but it is possible to access them through the pseudoscalar DVMP channel for example [6]. There is great motivation to study processes sensitive to the parton helicity-flip GPDs as there is little known about them at this point in time, so it will greatly benefit the understanding of little known aspects of the GPD framework. Note, H^q and E^q do not depend on the helicity of the quark so are referred to as *unpolarised* GPDs, but $\widetilde{H}^q$ and $\widetilde{E}^q$ do, so are referred to as *polarised* GPDs. This is analogous for the chiral-odd GPDs. The relation to GPDs is unique to different electroproduction processes, and it is therefore important to investigate each of these experimentally. Full imaging is only possible with the knowledge of all GPDs, for all flavours of quarks (and gluons).

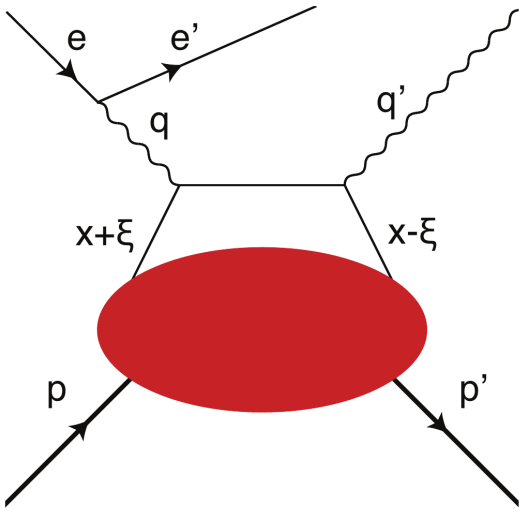

(a) DVCS: a real photon is produced in the reaction

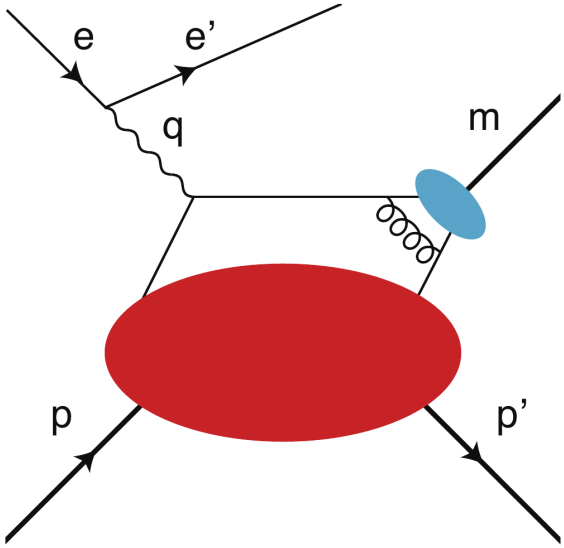

(b) DVMP: a meson is produced in the reaction. A gluon with two vertices is explicitly shown, as well as the Distribution Amplitude (**blue** ellipse)

Figure 1.2: Handbag diagrams representing (a) DVCS and (b) DVMP processes from a virtual photon interacting with a quark. The GPD parameterisation is represented by the **red** ellipse. [5].

DVMP of pseudoscalar mesons is the focus of this thesis work, particularly the production of a single neutral or charged pion from a nucleon. These are particularly sensitive to the helicity dependent GPDs $\widetilde{H}$ and $\widetilde{E}$ (unlike H and E for vector mesons), and therefore can provide complementary information to DVCS which is sensitive to all chiral-even GPDs [9] [10]. Pseudoscalar meson production from a neutron target is uniquely sensitive to $\widetilde{E}$, so is of great interest and therefore motivation to study the production of π^-. Flavour decomposition can also be achieved through combining measurements of different mesons in DVMP, such as that of the pseudoscalar meson η with π^0 [11].

GPDs can be indirectly accessed via functions parameterising the spin dependent variables of scattering cross sections and angular asymmetries such as: beam-spin asymmetries, longitudinal and transverse single target-spin asymmetries, double-spin (both beam-target-spin) asymmetries. These quantities are physically measurable and are therefore referred to as *observables*, with their connection to GPDs described in particular reference to *helicity amplitudes* - the first step in working towards accessing the GPDs [12]. The ultimate goal is to determine the functional dependence of GPDs, informed by experimental measurements, modelling any experimentally inaccessible aspects.

Particle	Quark Makeup	Spin	Charge
p	uud	$\frac{1}{2}$	$+1$
n	udd	$\frac{1}{2}$	0
π^0	$\frac{u\bar{u}-d\bar{d}}{\sqrt{2}}$	0	0
π^+	$u\bar{d}$	0	$+1$
π^-	$d\bar{u}$	0	-1

Table 1.1: Overview of the hadrons of interest in this thesis.

1.5.2 Generalised Quark Distributions

An introductory mathematical description will now be made with regards to the eight independent GPDs, highlighting some important aspects.

Important properties of the relevant hadrons for this body of work are shown in table 1.1. This work will only consider the GPDs relating to spin $1/2$ targets, due to a focus on use of a nucleon target in pion electroproduction processes. A focus will also be on GPDs relating to quarks as opposed to gluons, as they are the simpler of the parton species with regards to the formalism and scattering from quarks dominates the DVMP cross-section in the measurements presented in this work.

As defined and described in [7], it is useful to firstly consider the relation between GPDs and *generalised quark distributions*, making use of matrix elements of quark operators at a light-like separation. Firstly, consider a nucleon target which remains in the same isospin state after the scattering process. Making use of the chiral-even tensor operator $\bar{q}\gamma^+ q$ (light-cone Dirac matrix γ^+ for the infinite momentum frame, and quark and antiquark field operators q and $\bar{q}$), the quark helicity conserving GPDs H^q and E^q are introduced in the following generalised quark distribution:

$$\begin{aligned} F^q(x,\xi,t) &= \frac{1}{2}\int \frac{dz^-}{2\pi} e^{ixP^+z^-} \langle p'|\bar{q}(-\tfrac{1}{2}z)\gamma^+ q(\tfrac{1}{2}z)|p\rangle\Big|_{z^+=0,\mathbf{z}=0} \\ &= \frac{1}{2P^+}\left[H^q(x,\xi,t)\bar{u}(p')\gamma^+ u(p) + E^q(x,\xi,t)\bar{u}(p')\frac{i\sigma^{+\alpha}\Delta_\alpha}{2m}u(p)\right] \end{aligned} \tag{1.9}$$

where the subscript of +/- refers to the light-cone coordinate description, z is position and the average nucleon four-momentum is $P = (p+p')/2$. The final expression uses Dirac four-spinors (u and $\bar{u}$), Pauli matrix σ, momentum transfer $\Delta = p' - p$ and nucleon mass m, with a full and thorough description in reference [13].

The quark helicity conserving GPDs $\widetilde{H}^q$ and $\widetilde{E}^q$ are obtained with use of the operator $\bar{q}\gamma^+\gamma_5 q$ (again, evaluated at $z^+ = 0,\ \mathbf{z} = 0$):

$$\widetilde{F}^q(x,\xi,t) = \frac{1}{2P^+}\left[\widetilde{H}^q(x,\xi,t)\bar{u}(p')\gamma^+\gamma_5 u(p) + \widetilde{E}^q(x,\xi,t)\bar{u}(p')\frac{\gamma_5\Delta^+}{2m}u(p)\right]$$

The case of a non-zero helicity transfer is described by the use of the chiral-odd tensor operator $\bar{q}i\sigma^{+i}q$ with the superscript $i = 1,2$ (again, evaluated at $z^+ = 0,\ \mathbf{z} = 0$), resulting in the description of the quark helicity-flip GPDs H_T^q, E_T^q, $\widetilde{H}_T^q$ and $\widetilde{E}_T^q$ as

$$F_T^q(x,\xi,t) = \frac{1}{2P^+}\bar{u}(p')\left[H_T^q(x,\xi,t)i\sigma^{+i} + \widetilde{H}_T^q(x,\xi,t)\frac{P^+\Delta^i - \Delta^+P^i}{m^2} + E_T^q(x,\xi,t)\frac{\gamma^+\Delta^i - \Delta^+\gamma^i}{2m} + \widetilde{E}_T^q(x,\xi,t)\frac{\gamma^+P^i - P^+\gamma^i}{m}\right]u(p)$$

A frame independent description can be formed due to Lorentz invariance in which the GPDs only depend on the kinematic variables x, ξ and t, and is carried out in the relevant literature, [7].

Another important element of the framework is that there are *transition GPDs* which are the result of quasielastic transitions of the nucleon in the reaction, e.g. initial state proton (neutron) becomes a final state neutron (proton). Information on the hadron transition is contained in the GPDs for such processes. This must be considered for the π^+ and π^- electroproduction channels analysed in this thesis. The generalised quark distribution is simply an extension of equation 1.9, consider the specific case of $\gamma^* + p \to n + \pi^+$:

$$\begin{aligned} F_{p\to n}^{du}(x,\xi,t) &= \frac{1}{2}\int\frac{dz^-}{2\pi}e^{ixP^+z^-}\langle n(p')|\bar{d}(-\tfrac{1}{2}z)\gamma^+u(\tfrac{1}{2}z)|p(p)\rangle\Big|_{z^+=0,\mathbf{z}=0} \\ &= \frac{1}{2P^+}\left[H_{p\to n}^{du}(x,\xi,t)\bar{u}(p')\gamma^+u(p) + E_{p\to n}^{du}(x,\xi,t)\bar{u}(p')\frac{i\sigma^{+\alpha}\Delta_\alpha}{2m}u(p)\right] \end{aligned}$$

with chosen nomenclature referring to the fact that an up-quark is removed from the target nucleon and a down-quark returned.

As the analysis performed in this thesis covers both π^+ and π^- electroproduction, it is important to highlight the relation of transition GPDs to the flavour diagonal GPDs

$$H_{p\to n}^{du} = H_{n\to p}^{ud} = H_p^u - H_p^d \tag{1.10}$$

valid at constant values of x, ξ, t [14]. The following also apply: $H_p^u = H_n^d$, $H_p^d = H_n^u$, and $H_p^s = H_n^s$, with analogous relations for GPDs E, $\widetilde{H}$, $\widetilde{E}$.

This section has introduced the mathematical description covering the scattering processes of interest in this thesis.

1.5.3 Useful Properties of GPDs

For spin $\frac{1}{2}$ targets, there is also access to quark and antiquark (parton density) helicity distributions, $\Delta q(x)$ and $\Delta\bar{q}(x)$ [15]. It is through the *forward limit* property in which both ξ and t are zero, i.e. GPDs become functions of $(x,0,0)$, that one can obtain reduced quark GPDs

corresponding to ordinary spin dependent densities [6], e.g.

$$\begin{aligned} H^q &= q(x), & \widetilde{H}^q &= \Delta q(x), & \text{and} \quad & & \widetilde{H}^q_T &= \Delta_T q(x) & \text{for } x > 0, \\ H^q &= -\bar{q}(-x), & \widetilde{H}^q &= \Delta \bar{q}(-x), & \text{and} \quad & & \widetilde{H}^q_T &= -\Delta_T \bar{q}(-x) & \text{for } x < 0 \end{aligned}$$

It is important to highlight that for the case of $\xi = 0$, GPDs are equal to PDFs and in the forward limit the only surviving quark GPDs are H, $\widetilde{H}$ and $\widetilde{H}_T$.

Relations to Form Factors

Integrating the chiral-even GPDs over x can be used in relating them to the quark contributions of FFs via

$$\begin{aligned} \int_{-1}^{1} \mathrm{d}x\, H^q(x,\xi,t) &= F_1^q(t), \\ \int_{-1}^{1} \mathrm{d}x\, E^q(x,\xi,t) &= F_2^q(t), \\ \int_{-1}^{1} \mathrm{d}x\, \widetilde{H}^q(x,\xi,t) &= G_A^q(t), \\ \int_{-1}^{1} \mathrm{d}x\, \widetilde{E}^q(x,\xi,t) &= G_P^q(t), \end{aligned}$$

where $F_1^q(t)$, $F_2^q(t)$, $G_A^q(t)$, and $G_P^q(t)$ represent the quark contributions to the Dirac, Pauli, axial and pseudoscalar form factors respectively, which are elastic form factors of the nucleon. The integration over x removes the ξ dependence as a consequence of Lorentz invariance. The nucleon's anomalous magnetic moment is related to $F_1^q(t)$, with its charge radius related to both $F_1^q(t)$ and $F_2^q(t)$ [16]. $G_A^q(t)$ relates to the nucleon spin fraction carried by quarks. It is $G_P^q(t)$ that represents the pseudoscalar quark density distributions with regards to the nucleon's substructure [17]. Both $G_A^q(t)$ and $G_P^q(t)$ are still rather poorly known.

1.5.4 Ji's Spin Decomposition

It was Ji and collaborators who realised the means to access the orbital angular momentum of partons within the nucleon through GPDs, providing expressions that separated the orbital angular momentum from the spin component for quarks, although the terms remain unseparated for gluons [18]. This is a key motivation for today's focus on GPDs, with it being the most straightforward way to determine such information. It is therefore useful to very briefly highlight the main results relating to this with respect to both parton species.

Following the steps in [18], the QCD angular momentum operator can be explicitly formed in reference to that of the quark and gluon components as $\vec{J}^{QCD} = \vec{J}^q + \vec{J}^g$. The Ji decomposition of nucleon spin $(1/2)$ into its quark and gluon spin contributions, as well as orbital degrees of

freedom, is formulated as

$$J^N = \frac{1}{2} = \frac{1}{2}\sum_q \Delta q + \sum_q L_z^q + J_z^g \tag{1.11}$$

where the quark total angular momenta is given by $J^q \equiv \frac{1}{2}\Delta q + L_z^q$ [19]. In the forward limit of $t = 0$ when integrating over three-space, the angular momentum carried by quarks and gluons with respect to their expectation values is found to be

$$\langle J_3^q \rangle = \tfrac{1}{2}[A^q(0) + B^q(0)] \qquad \text{and} \qquad \langle J_3^g \rangle = \tfrac{1}{2}[A^g(0) + B^g(0)] \tag{1.12}$$

with $\sum_q \langle J_3^q \rangle + \langle J_3^g \rangle = 1/2$ for a nucleon. The A and B form factors are related to the moments of GPDs as follows:

$$\begin{aligned} A^q(t) + B^q(t) &= \int_{-1}^{1} \mathrm{d}x\, x\, [H^q(x,\xi,t) + E^q(x,\xi,t)], \\ A^g(t) + B^g(t) &= \int_{0}^{1} \mathrm{d}x\, [H^g(x,\xi,t) + E^g(x,\xi,t)], \end{aligned} \tag{1.13}$$

The expressions 1.12 and 1.13 are commonly referred to as *Ji's sum rules* [20] [21].

1.5.5 Helicity Amplitudes

GPD formalisms make use of factorisation theorems which allow for a helicity *amplitude* description of the meson production reaction, which is a convolution containing a mathematical description of the interaction of the virtual photon, the meson wave function and GPD functions. With specific reference to π^0 electroproduction from a proton as detailed in [22], the quark and gluon helicity amplitudes, M, relate to corresponding GPDs, F, via

$$M^{q,g}_{0\pm,\mu\pm} = \sum [\langle F^{q,g} \rangle + O(\langle \widetilde{F}^{q,g} \rangle)] \tag{1.14}$$

where the subscripts of M refer to the helicities of the produced pion and final proton, and the helicities of the virtual photon and initial proton, respectively. The convolution of the subprocess amplitude (hard scattering kernel), $\mathscr{H}$, and GPD is contained in the following relation:

$$\langle F^{q,g} \rangle = \sum_{\lambda} \int_{-1}^{1} \mathrm{d}\vec{x}\, \mathscr{H}^{q,g}_{0\lambda',\mu\lambda}(x,\xi,Q^2,t)\, F^{q,g}(x,\xi,t) \tag{1.15}$$

which also holds for the "$\widetilde{F}$" (polarised) GPDs [23]. The convolution cannot be resolved and therefore a GPD analysis is based upon these fundamental amplitudes, as they can be experimentally measured.

These helicity amplitudes are analogous to Compton Form Factors which are the experimentally accessible functions related to GPDs that can be measured in DVCS.

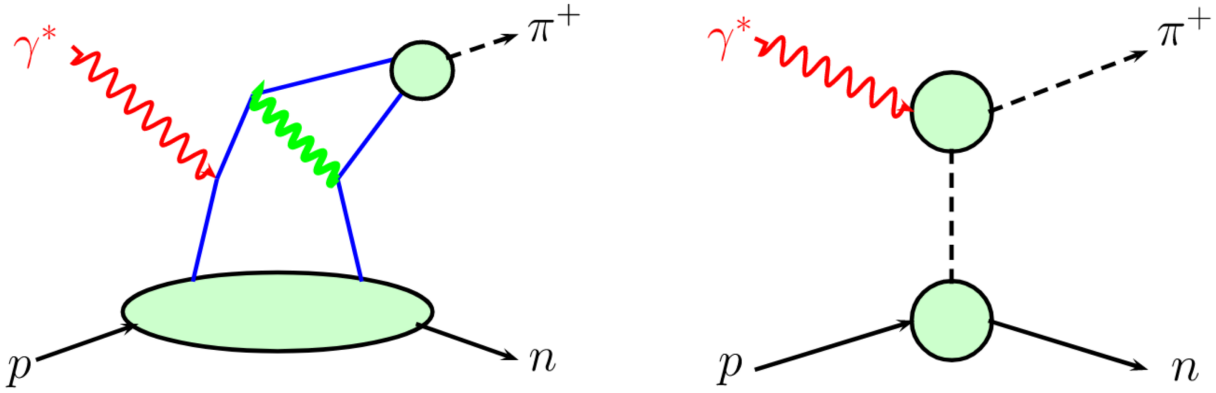

(a) DVMP GPD diagram

(b) π^+ electroproduction pion pole diagram

Figure 1.3: Diagrams representing the reaction of $\gamma^* + p \rightarrow n + \pi^+$: (a) GPD handbag diagram and (b) pion pole description. [23].

1.5.6 Pion Pole Contribution

Unlike the neutral pion, the electroproduction of charged pions contains a *pion pole* term which shows dominance in the GPD interpretation. It is estimated to be particularly dominant for large x_B and small t, and was found to dominate the longitudinal cross section for $-t < 0.3$ GeV^2 in [24]. Note, units of t are expressed as GeV due to c being expressed as a natural unit with value of 1, as will be the convention in this thesis. With regards to GPDs, the pion pole term is incorporated into $\widetilde{E}$.

For π^+ electroproduction, instead of the virtual photon interacting with a quark (figure 1.3a), it interacts with a virtual pion emitted by the initial nucleon (figure 1.3b). A description of the pole must take into account the coupling of the pion to the nucleon, and both of their structures. This term is non-negligible and means that there is additional information contained within these reactions, and of course the electroproduction of charged pions carries sensitivity to transition GPDs. With regards to the pole contribution to the amplitude, the relation between charged pions is $\mathscr{A}^{pole}_{\pi^+} = -\mathscr{A}^{pole}_{\pi^-}$.

Despite this pion pole complication, the production cross section of charged pions is larger than that of neutral pions and their detection efficiency is much better too, with regards to the experimental setup used in the analysis [25]. This motivates the study of electroproduction of charged pions as well as the neutral pion.

It is also suggested that full consideration of the pion pole contribution requires taking into account twist-three effects [23] [26].

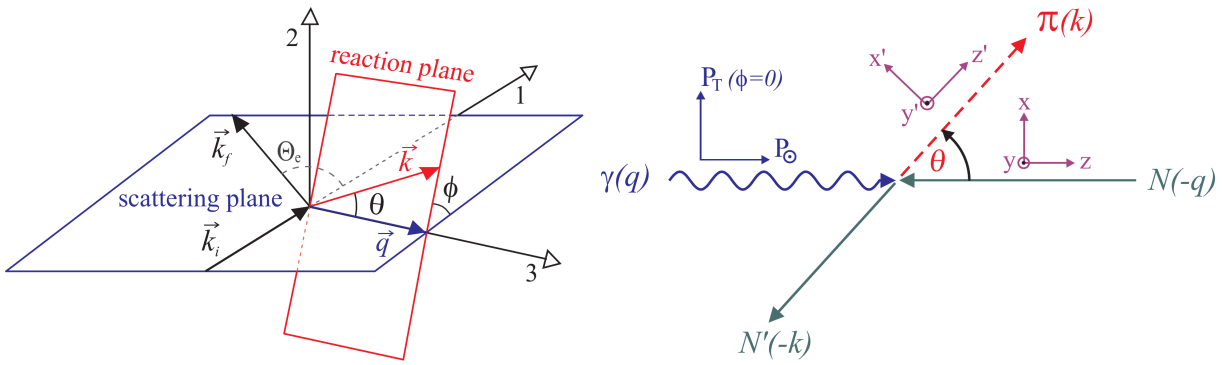

(a) Laboratory frame

(b) Centre of mass frame (virtual photon and nucleon target)

Figure 1.4: Diagrams showing the pion electroproduction reaction. [27].

1.5.7 Experimental Access to GPDs

Differential Cross Section and Asymmetries

Before explicitly stating the relation of helicity amplitudes to measurable observables in DVMP, it is best to describe the reaction and formation of the angular observable term ϕ. This angle ϕ is defined as being the opening angle between the scattering plane ($\vec{q} \times \vec{k}_i$) and reaction plane ($\vec{q} \times \vec{k}$) where $\vec{q}$, $\vec{k}_i$ and $\vec{k}$ represent the three-momenta of the virtual photon, incident electron, and the produced pion respectively. Diagrams of the reaction are shown in figure 1.4. These diagrams illustrate the following three important terms in the mathematical description of the reaction:

- Electron scattering angle θ_e calculated from $\vec{k}_i$ and $\vec{k}_f$
- Production of the pion at an angle θ to the virtual photon
- Opening angle ϕ between the scattering and reaction plane

Taking into account the virtual photon's energy ν and the negative squared four-momentum Q^2, the virtual photon's polarisation is

$$\varepsilon = \left(1 + 2\left(1 + \frac{\nu^2}{Q^2}\right) tan^2\left(\frac{\theta_e}{2}\right)\right)^{-1} \tag{1.16}$$

The previously defined Bjorken x variable can be expressed for the case of a stationary nucleon target of mass M such that

$$x_B = \frac{Q^2}{2p \cdot q} = \frac{Q^2}{2M\nu} \tag{1.17}$$

Considering a longitudinally polarised electron beam and target nucleon, the DVMP cross section is formed of components with respect to both the beam and target polarisations. There are

numerous structure functions ($\sigma_{...}$) which parameterise the DVMP cross section and are related to scattering amplitudes that describe the probabilities of specific scattering processes. The theoretical relation is then formulated between structure functions and the GPDs. With use of both longitudinally polarised beam (P_B) and target (P_T), the differential cross section for DVMP can be described as follows:

$$\begin{aligned}\frac{2\pi}{\Gamma(Q^2,x_B,E)}\frac{d^4\sigma}{dQ^2dx_Bdtd\phi} &= \sigma_T+\varepsilon\sigma_L+\sqrt{2\varepsilon(1+\varepsilon)}\sigma_{LT}^{cos(\phi)}cos(\phi)+\varepsilon\sigma_{TT}^{cos(2\phi)}cos(2\phi)\\ &+P_B\left(\sqrt{2\varepsilon(1-\varepsilon)}\sigma_{LU}^{sin(\phi)}sin(\phi)\right)\\ &+P_T\left(\sqrt{2\varepsilon(1+\varepsilon)}\sigma_{UL}^{sin(\phi)}sin(\phi)+\varepsilon\sigma_{UL}^{sin(2\phi)}sin(2\phi)\right)\\ &+P_BP_T\left(\sqrt{1-\varepsilon^2}\sigma_{LL}^{const}+\sqrt{\varepsilon(1-\varepsilon)}\sigma_{LL}^{cos(\phi)}cos(\phi)\right)\end{aligned} \tag{1.18}$$

where Γ is the virtual photon flux, and there are nine structure functions ($\sigma_{...}$) which parameterise the differential cross section, each with a dependence on Q^2, x_B, t. For visual purposes, the terms in equation 1.18 are colour coded on each line according to the type of electroproduction event which they relate to:

- Blue: Unpolarised beam and target
- Orange: Longitudinally polarised beam
- Purple: Longitudinally polarised target
- Green: Longitudinally polarised beam and target

The terms describing an unpolarised beam and target are often presented as the spin averaged cross section:

$$\sigma_0 = \sigma_T+\varepsilon\sigma_L+\sqrt{2\varepsilon(1+\varepsilon)}\sigma_{LT}^{cos(\phi)}cos(\phi)+\varepsilon\sigma_{TT}^{cos(2\phi)}cos(2\phi) \tag{1.19}$$

Note, the combined term of $\sigma_T+\varepsilon\sigma_L$ is sometimes referred to as the unseparated cross section, σ_U.

Asymmetries in ϕ can be formed according to equation 1.18 for single beam-, target-, and double-spin asymmetries. This makes use of an electron probe of different helicities, target particle with different polarisation orientations, and the combination of the polarised beam and target. The formation of these asymmetries will be described in more detail later, before asymmetry measurements are made as part of the analysis performed. These asymmetries hold direct relations with the structure functions described.

Relation to GPDs

Since the structure functions $\sigma_{...}$ parameterise the cross section of the reaction, it is these that give access to GPDs via helicity amplitudes.

With regards to the Goloskokov-Kroll model of GPDs, Kim explicitly expressed the asymmetries as functions of corresponding helicity amplitudes for pion electroproduction from a longitudinally polarised proton with use of a longitudinally polarised electron beam [22]:

$$
\begin{aligned}
A_{LU}^{sin(\phi)}\sigma_0 &= -\sqrt{\varepsilon(1-\varepsilon)}\ \text{Im}\ [2M^{U*}_{0+++}M_{0+0+} + (M^*_{0-++} - M^*_{0--+})M_{0-0+}] \\
A_{UL}^{sin(\phi)}\sigma_0 &= -\sqrt{\varepsilon(1+\varepsilon)}\ \text{Im}\ [2M^{N*}_{0+++}M_{0+0+} + (M^*_{0-++} + M^*_{0--+})M_{0-0+}] \\
A_{UL}^{sin(2\phi)}\sigma_0 &= -\varepsilon\ \text{Im}\ [2M^{U*}_{0+++}M^{N}_{0+++} + M^*_{0-++}M_{0--+}] \\
A_{LL}^{const}\sigma_0 &= \sqrt{1-\varepsilon^2}\frac{1}{2}[4\ \text{Re}\ (M^{N*}_{0+++}M^{U}_{0+++}) + |M_{0-++}|^2 - |M_{0--+}|^2] \\
A_{LL}^{cos(\phi)}\sigma_0 &= -\sqrt{\varepsilon(1-\varepsilon)}\ \text{Re}\ [2M^{N*}_{0+++}M_{0+0+} + (M^*_{0-++} + M^*_{0--+})M_{0-0+}]
\end{aligned}
$$

where the integrated cross section σ_0 is defined as

$$
\begin{aligned}
\sigma_0 = &\frac{1}{2}[|M^*_{0+++}|^2 + |M^*_{0--+}|^2 + |M^*_{0-++}|^2 + |M^*_{0+-+}|^2] \\
&+ \varepsilon[|M^*_{0+0+}|^2 + |M^*_{0-0+}|^2]
\end{aligned}
$$

The helicity amplitudes are related to the GPDs via equations 1.14 and 1.15.

Of particular importance is experimentally measuring the t dependence of the asymmetries, as this gives information on the transverse position of the struck parton, which is required for nucleon imaging. Measurements of the t dependence with regards to spin asymmetries will be carried out in this thesis for electroproduction of single π^0, π^+ and π^-.

Transverse Terms Correction to the Differential Cross Section

The theory discussed thus far has assumed a complete longitudinal polarisation of both the beam and target along the same axis - consider it being the z-axis. Although the electron beam is longitudinally polarised in the z-axis, the virtual photon can also have non-negligible x and y components of polarisation due to the nature of the electron scattering process with the target. The direction cosines of the polarisation of the virtual photon interacting with the target can therefore be formulated as

$$
\begin{aligned}
P_z &= cos(\theta_q) \\
P_y &= -sin(\theta_q)sin(\phi) \\
P_x &= sin(\theta_q)cos(\phi)
\end{aligned}
$$

making use of the angle θ_q which is defined as being between the beam direction and the momentum transfer (the virtual photon momentum), and ϕ which is the opening angle between the scattering plane and the reaction plane as previously defined. The x and y components give access to both longitudinal and transverse information related to the scattering process (structure functions, etc.). Now following the conventions of the MAID group [28], equation 1.18 can be be expressed as

$$\begin{aligned}\frac{2\pi}{\Gamma(Q^2,x_B,E)}\frac{d^4\sigma}{dQ^2dx_Bdtd\phi} = \sigma_T &+ \varepsilon\sigma_L + \sqrt{2\varepsilon(1+\varepsilon)}\sigma_{TL}cos(\phi) + \varepsilon\sigma_{TT}cos(2\phi) \\ &+ P_B\left(\sqrt{2\varepsilon(1-\varepsilon)}\left[\sigma_{TL'}sin(\phi)\right]\right) \\ &+ P_T\left(\left[P_y(\sigma_{T_y}+\varepsilon\sigma_{L_y})\right]\right. \\ &\quad +\sqrt{2\varepsilon(1+\varepsilon)}\left[P_x\sigma_{TL_x}sin(\phi) + P_y\sigma_{TL_y}cos(\phi) + P_z\sigma_{TL_z}sin(\phi)\right] \\ &\quad \left.+\varepsilon\left[P_x\sigma_{TT_x}sin(2\phi) + P_y\sigma_{TT_y}cos(2\phi) + P_z\sigma_{TT_z}sin(2\phi)\right]\right) \\ &+P_BP_T\left(\sqrt{1-\varepsilon^2}\left[P_x\sigma_{TT'_x} + P_z\sigma_{TT'_z}\right]\right. \\ &\quad \left.+\sqrt{2\varepsilon(1-\varepsilon)}\left[P_x\sigma_{TL'_x}cos(\phi) + P_y\sigma_{TL'_y}sin(\phi) + P_z\sigma_{TL'_z}cos(\phi)\right]\right)\end{aligned} \tag{1.20}$$

With reference to equation 1.20, the differential cross section can be expressed in terms of asymmetries as shown in equation 1.21, where only the dominant terms have been included.

$$\begin{aligned}\frac{2\pi}{\Gamma(Q^2,x_B,E)}\frac{d^4\sigma}{dQ^2dx_Bdtd\phi} = \sigma_0\Big[\,1 &\\ &+ P_B\left(A_{LU}^{sin\phi}sin(\phi)\right) \\ &+ P_T\left(A_{UL}^{const} + A_{UL}^{sin\phi}sin(\phi) + A_{UL}^{sin2\phi}sin(2\phi)\right) \\ &+ P_BP_T\left(A_{LL}^{const} + A_{LL}^{cos\phi}cos(\phi)\right)\Big]\end{aligned} \tag{1.21}$$

1.6 Past Measurements

This section discusses previous measurements, in particular many relevant studies performed at the Thomas Jefferson National Accelerator Facility. An overview will discuss significant results with regards to the GPD formalism, including both Deeply Virtual Compton Scattering and Deeply Virtual Meson Production measurements. The main focus will be on measurements most appropriate to the data analysis to follow, i.e. electroproduction of single pions in DVMP.

Since DVCS is considered the cleanest way to access and interpret GPDs, this channel was the initial focus of worldwide research efforts into the newly proposed formalism. The first publications showing success in realising the opportunities of GPDs originated from the HER-

MES Collaboration at DESY [29] and the CLAS Collaboration at the Thomas Jefferson National Accelerator Facility [30], both in 2001. Both presented the first measurements of the beam-spin asymmetry in hard exclusive electroproduction of photons. As anticipated, a clear non-zero asymmetry was observed for photons originating from DVCS and the main source of interference (the Bethe-Heitler process). The measurements were compared with GPD model calculations and highlighted the need for improved parameterisation as well as motivating expanding the measurements in this kinematic regime. The CLAS experiment operated at a much lower beam energy than HERMES and therefore suggested that GPDs could be accessed via the DVCS channel at relatively low energy and momentum transfers. Subsequently, significant time was devoted to researching DVCS in relation to GPDs and in 2007 the first measurements on DVCS off a neutron target were published [31]. This work provided a crucial experimental constraint on the parametrisation of E^q (the least constrained GPD) as it was particularly sensitive to DVCS off a neutron target. The measurements also provided a constraint on the nucleon's spin contribution from the up and down quarks. The success in DVCS research was motivation to study DVMP to gain further insight into utilising GPDs in understanding the partonic structure of nucleons. In 2008, scattering cross measurements were published for the π^+ DVMP channel across a range of Q^2 and were used to assess the QCD factorisation theorem [32]. It was found that the longitudinal cross sections agreed well with the scaling prediction, therefore suggesting GPDs can be accessed at relatively low Q^2.

For the first time, in a 2008 publication, significant beam-spin asymmetry measurements were presented for the exclusive DVMP process of $ep \rightarrow ep\pi^0$ [33]. The study measured a fit parameter (α) that is proportional to the structure function $\sigma_{TL'}^{sin\phi}$ which corresponds to the imaginary part of an interference of longitudinal and transverse helicity amplitudes. The results were non-zero over a wide kinematic region in Q^2, x_B and t as shown in figure 1.5, and therefore highlighted the importance of the interference term. This interference contribution to the meson production process crucially required the separation of L/T to gain better understanding of each contribution. This separation was successfully performed, with a 2012 publication presenting results showing that the contribution of the longitudinal cross section is small in comparison with that of the transverse cross section [25]. The study confirmed that the DVMP exclusive channel for π^0 offers direct experimental access to transversity GPDs, which was shown by the comparison of data to calculations including both longitudinal and transversity GPDs.

Asymmetry measurements were extended to those of target- and double-spin for the exclusive DVMP process of $ep \rightarrow ep\pi^0$ for the first time in 2017 [34]. Again, the experimental data had a wide kinematic coverage and the significant non-zero results were compared with leading order theoretical calculations as a function of t, as shown in figure 1.6. These results were found to highlight the importance of improving the parameterisation of the GPD H_T, and the possible need to take higher twist contributions into account.

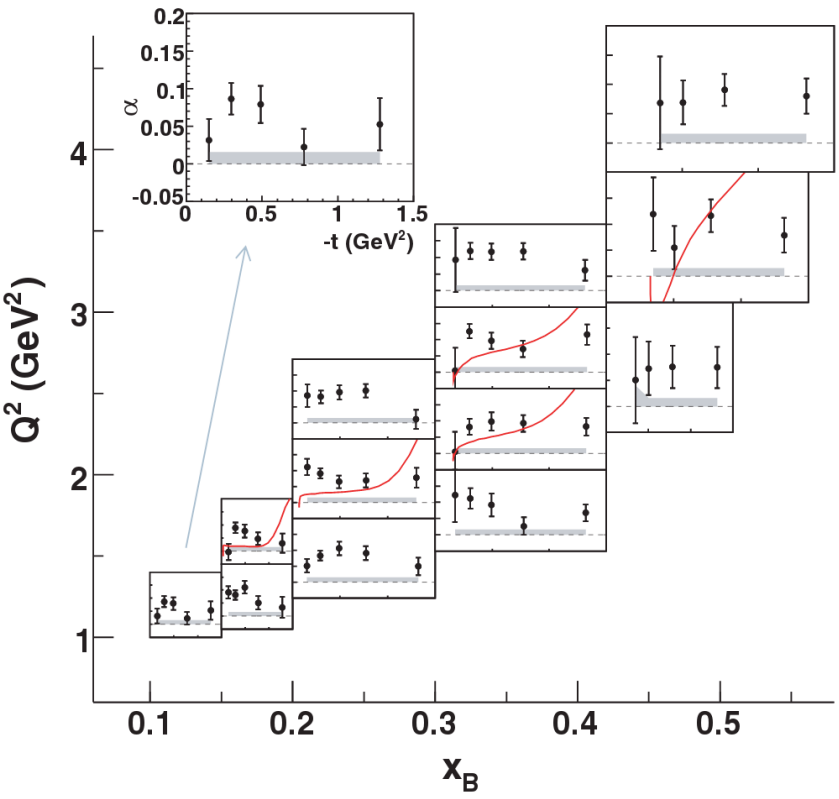

Figure 1.5: DVπ^0P extracted fit parameter α from the beam-spin asymmetry fit of $A_{LU} = \alpha sin\phi$, presented as a function of $-t$. The position and size of each individual plot approximately corresponds to the coverage of that data binned in Q^2 and x_B. The left plot was enlarged to show the x and y axis ranges that all plots use. The maximal size of systematic uncertainties are shown (**grey** shaded areas), and a JML model is included for selected bins (**red** lines). [33].

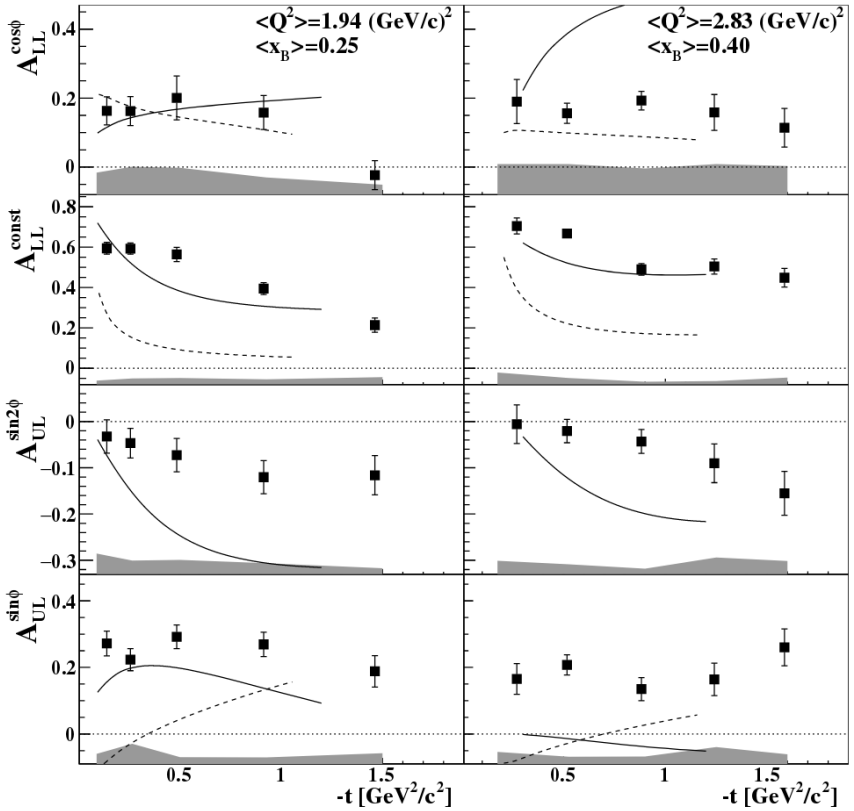

Figure 1.6: DVπ^0P target- and double-spin asymmetries moments ($A_{UL}^{sin\phi}$, $A_{UL}^{sin2\phi}$, A_{LL}^{const} and $A_{LL}^{cos\phi}$) measured for 2 bins in Q^2 and x_B, presented as a function of $-t$. The maximal size of systematic uncertainties are shown (**grey** shaded areas), and predictions from GPD formalisms are also included where appropriate: CGL (**black** solid line) and GK (**black** dashed line). [34].

Target- and double-spin asymmetries were published in 2017 for the exclusive reaction of $ep \rightarrow en\pi^+$, covering the kinematic range of $1 < Q^2 < 6$ GeV^2 and $1.1 < W < 3$ GeV [35]. The comprehensive study presented measurements across the resonance region and edged into the DVMP region. Comparisons made with different available models (including a GPD-inspired model) showed reasonable agreement for $W < 1.6$ GeV, but large differences were observed at higher W. These π^+ asymmetry results were beneficial in both providing powerful constraints on the nucleon resonance amplitudes and for fits used to extract GPD information. A previous publication by the same author in 2016 assessed both the target- and double-spin asymmetries for the slightly lower kinematic range of $0.05 < Q^2 < 5$ GeV^2 and $1.1 < W < 2.6$ GeV in exclusive π^+ and π^- electroproduction [36]. These measurements narrowly edged into the DVMP kinematic range of $Q^2 > 1$ GeV^2 with $W > 2.0$ GeV, but there were very few data-points for both channels. The comparison of π^- asymmetries to the available fit model were not in agreement across all values of W, which was not surprising due to limited data constraining the model for this channel - therefore highlighting the necessity for further measurements on π^- electroproduction.

GPDs will allow for a comprehensive description of the dynamical degrees of freedom inside the nucleon, and requires extensive measurements of both scattering cross sections and spin dependent angular asymmetries. The overview of DVMP measurements is particularly relevant, as the results presented in this thesis are crucial in further constraining GPD models which will continue to rely on a variety of experimental measurements over a wide kinematic range. In particular, spin asymmetry measurements will be presented for single pion DVMP, with the results for the charged pion channels being a first for this kinematic regime.

1.7 Summary

The theoretical aspects of the analysis performed have been discussed, from a basic description of electron scattering, to the experimental access to Generalised Parton Distributions via observables. An overview of the GPD formalism was presented, its relation to nucleon imaging being of significant importance. This chapter provided the relevant information for the experimental analysis performed, covering the electroproduction of single pions (π^0, π^+ and π^-) via the mechanism of Deeply Virtual Meson Production. Experimentally measuring the t dependence of spin asymmetries provides information on the transverse position of the struck parton via the GPD formalism, and is therefore crucial in the goal of creating a three-dimensional picture of nucleons. GPD relations to Form Factors develop the understanding of properties of the nucleon such as its charge radius and spin fraction carried by quarks.

Chapter 2

Experimental Facility

A leading experimental facility with a focus on nucleon internal structure studies is the continuous electron beam accelerator facility (CEBAF) at the Thomas Jefferson National Accelerator Facility (JLab) in Virginia, USA [37]. The experimental work presented in this thesis was carried out as part of JLab's "EG1-DVCS" experiment. This chapter will outline the relevant aspects of the CEBAF and the experimental apparatus.

2.1 The Facility

During the mid to late-1990s the CEBAF successfully operated according to design specifications in which an electron beam was simultaneously delivered to three end stations - experimental halls (A, B and C) at one end of the accelerator's "racetrack" configuration. This marked the beginning of an important era of experimental physics programmes. An overview diagram of the CEBAF can be seen in figure 2.1. Each experimental hall was somewhat unique in its physics motivations and goals and therefore individually comprised of specialised detector equipment, overall contributing to a broad physics programme at JLab. The CEBAF provided an electron beam with a 100% duty cycle (an always active beam signal) with each hall having the opportunity to induce reactions by either an electron or photon at energies up to 6 GeV, surpassing the initial design specification of 4 GeV [38].

2.2 The Accelerator

The pioneering design of the CEBAF complex is most apparent in being the first large scale facility utilising superconducting radiofrequency (SRF) technology and multipass beam recirculation, with motivation for these being to reduce capital and operating costs whilst allowing to easily upgrade the system (which is indeed the case during the time of writing).

Specific reference to figure 2.1 is useful in the upcoming description of the accelerator.

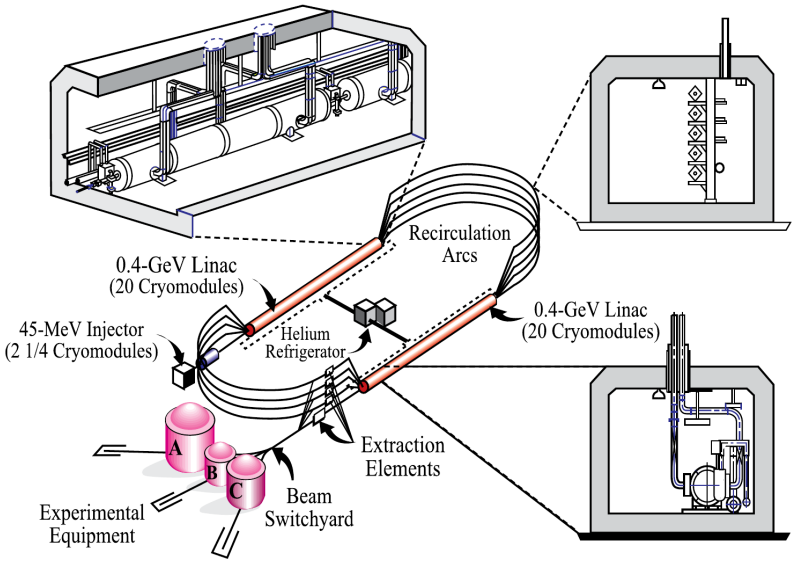

Figure 2.1: Overview of the general CEBAF configuration. [37].

In overview, a polarised electron beam was boosted in energy by a pair of antiparallel linear accelerators (linacs) in both north and south "straights" of the racetrack layout, linked by vertically separated recirculation lines, each finely tuned to transport electron beams of different energies.

2.2.1 Injector System

The three experimental halls were operated simultaneously with different beam settings, and therefore it was three independent laser beams (operating out of phase with one another) that induced electron beams which then advanced through the injector system [39] [40]. Circularly polarised laser light generated longitudinally polarised electrons (with energy of ~ 100 keV) via photo-emission from a Gallium Arsenide photoconductor cathode. The helicity of the polarised electron beam was periodically flipped between the positive (h^+) and negative (h^-) state at a rate up to 60 Hz. A Wien filter then oriented the beam polarisation relative to the beam direction according to the electric and magnetic fields applied by this device, crucially without altering the central beam orbit [41]. Further elements of the injector system "chopped" and "bunched" the electron beam into small longitudinal bunches (120° phase separation), with a nominal bunch frequency of 499 MHz - corresponding to delivery of beam to each experimental hall every 2.004 nanoseconds. Each of the three beam bunches could have an independent charge, therefore allowing for delivery of different beam currents to each hall in line with their unique experimental requirements. These electron beams were accelerated up to 45 MeV in the injector system before entry into the north linac of the main accelerator racetrack.

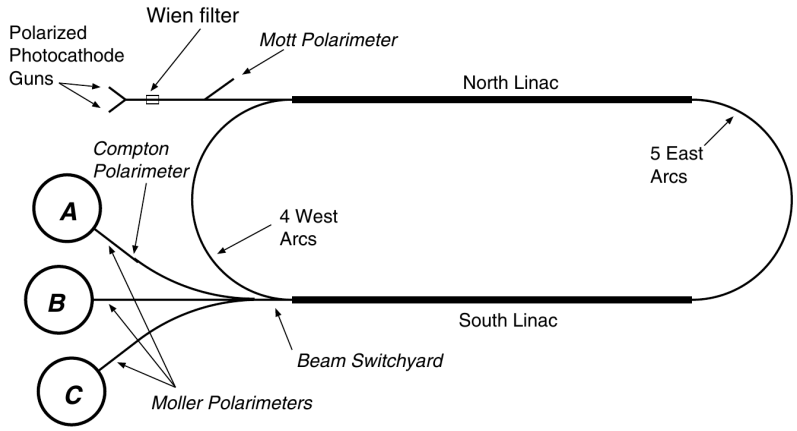

Figure 2.2: Overview of the accelerator, including polarimeter locations. [41].

2.2.2 Racetrack and Delivery

The main acceleration of electrons was performed in the linacs, each containing 20 high performance cryomodules operating at 2 K. Each cryomodule was an assembly of four vacuum insulated superconducting five-cell niobium cavity pairs, achieving the original acceleration gradient specification of 5 MV/m. Note, this SRF acceleration technology was also used in the injector system (2 1/4 cryomodules). The cavities accelerated the beam of electrons according to well defined resonant electromagnetic fields within the geometry of the chambers. It was the "C50" cryomodule refurbishment project that recovered the accelerator's full 6 GeV beam energy reach in 2009, having been damaged during Hurricane Isabel in 2003 [40].

The delivery of the 6 GeV maximum beam energy to all experimental halls was achieved with the full five-pass racetrack accelerator system, in which each pass increased the energy by 1.2 GeV. Of the vertically separated recirculation lines, five were in the east end and four in the west end. The CEBAF achieved a beam polarisation of $\sim 85\%$, with losses in the recirculation process being negligible.

Multiple polarimeters included in the CEBAF system and experimental halls ensured a highly precise measurement of the electron beam's spin polarisation. Figure 2.2 shows the locations of these, as well as other key features of the racetrack layout, including the injector system, beam switchyard, and east and west recirculation arcs. Monitoring and measurements of the beam polarisation were performed by the Mott polarimeter within the injector system, and with Møller polarimeters in each of the three experimental halls, with Hall A having an additional Compton polarimeter.

The high energy electron beam could be extracted from the racetrack for delivery after any number of passes, in accordance with the experimental energy requirement in each hall. Radiofrequency cavity "separator" technology at the beam switch-yard split the electron beam at 1497 MHz with bunches to each hall at 499 MHz.

2.3 Hall B and the CLAS Detector System

The novel Hall B detector system was the CEBAF large acceptance spectrometer (CLAS), with its purpose being to measure multi-particle final state reactions with a high detection efficiency. "Large acceptance" refers to the near 4π solid angle coverage which was essential for multi-particle final state reactions, however this unfortunately limited the maximum luminosity due to high occupancy rates in the detector systems. Solid state polarised target experiments (the focus of this thesis) required a low beam current, further reducing the total possible luminosity. Even with this taken into account, highly successful nuclear physics studies were performed with the somewhat limited event readout rate of CLAS.

The electron beam injected into Hall B travelled along the z direction ("beam axis"), and was centred at $(0,\ 0)$ with regards to the x and y axes. The CLAS detector system is best described using a spherical coordinate system in which r is the radial distance, θ is the polar angle and ϕ is the azimuthal angle with respect to the origin. The origin of the coordinate systems is the centre of CLAS, with positive z referred to as "downstream" and negative as "upstream".

2.3.1 Beamline Apparatus

The incoming CEBAF electron beam travelled along a straight beamline pipe to a fixed target at the centre of the CLAS detector. There were beam monitoring and diagnostic equipment at numerous locations along the pipe, both many meters before and after the target. Note, the analysis in this thesis focuses on an experiment using a polarised electron beam (as opposed to a photon beam), and there were specific crucial beam quantities measured using unique monitor systems:

- Polarisation - Møller Polarimeter
- Position and intensity - Beam Position Monitors (BPMs)
- Profile - Harp Wire Scanners
- Current - Faraday Cup

The CEBAF electron beam delivered to Hall B was typically polarised (longitudinally in the z direction) in the range of $40-85\%$ during its operation, and therefore a high precision measurement ($\delta P/P\ <\ 3\%$) was crucial for this key property throughout experimental running. Due to the stability of beam polarisation, measurements of this parameter were normally taken every second day using the Møller polarimeter. This monitoring system consisted of two 25 μm thick polarised Permendur foil targets tilted 20° to the beam axis, followed by two quadrupole magnets that bent the scattered Møller electron pairs for coincidence detection by lead/scintillating-fibre detectors at both sides of the beamline in the same horizontal plane [42]. The target chamber and paired detectors were located approximately -35 m and -28 m relative

to the centre of CLAS. The longitudinal beam polarisation was determined via an asymmetry calculation of the observed count rates of the scattered incident electrons and recoil electrons for positive and negative beam helicity states [41] [43].

A centralised beam position in the transverse (x-y) plane was ensured with use of three BPMs located -36.0 m, -24.6 m and -8.2 m relative to the centre of CLAS, with each comprised of three room temperature radiofrequency cavities [44]. The beam position could vary by a range of ± 3 mm from the target centre, and was achieved with an accuracy of 100 μm. The beam position at each BPM was continuously fedback and used in a rapid correction system, with the position measurement and current (intensity) information inserted into the data stream every 20 seconds. Calibrations of the BPMs were only carried out once per week (or less) due to the very high stability of the RF cavities.

The beam width was successfully kept within the range of $\sigma < 250$ μm with a precision of 10 μm and was monitored in dedicated Harp scan runs that were carried out after significant beam alterations (energy, current, etc.), or as part of diagnostic investigations. A "Harp" is an instrument that scans a pair of thin wires (tungsten or iron in Hall B) through the beam to measure the transverse (x-y plane) profile based on the detection of scattered electrons by photomultiplier tubes (PMTs) fixed around the beam pipe 6.8 m upstream. Similar to the BPMs, there were three Harps which made up this monitoring system, specifically at -36.7 m, -22.1 m and -15.5 m relative to the centre of CLAS. The transverse beam profile also allowed measurements of the beam halo (electrons outside the nominal longitudinal grouping), and therefore helped achieve quality beam conditions and ensured minimisation of beam losses [45].

The current of the electron beam delivered to Hall B was accurately measured with the Faraday Cup system, situated 29 m downstream, within the "beam dump tunnel" at the end of the beamline. A very large electrically isolated 4000 kg lead block effectively stopped the electron beam, and its deposited charge was drawn out and processed fast enough to provide real-time information on charge, as well as the integrated luminosity measurement for experimental runs [46]. The fast processing of this system was also suitable in providing measurements of charge variation between the two different beam helicity states in polarised electron experiments. Operational electron beam currents in Hall B were in the range of $1-30$ nA, and measured with a precision of less than 1% using the Faraday Cup.

Significant deviations from optimal beam parameters were reported to the Machine Control Centre (MCC) and corrected using upstream beam optics by the operations crew running the CEBAF accelerator.

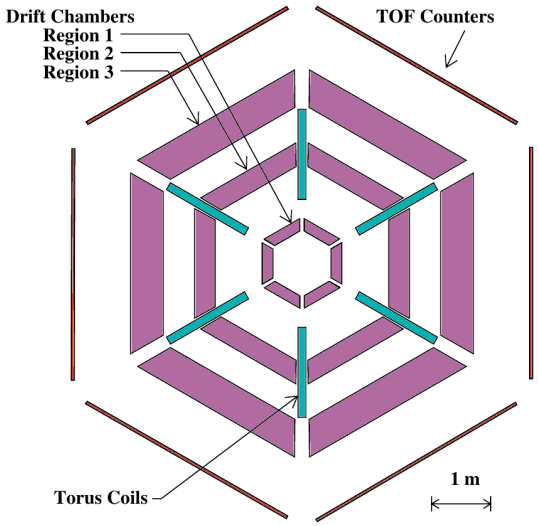

(a) Cut perpendicular to beam at CLAS' central target position (beam into-page)

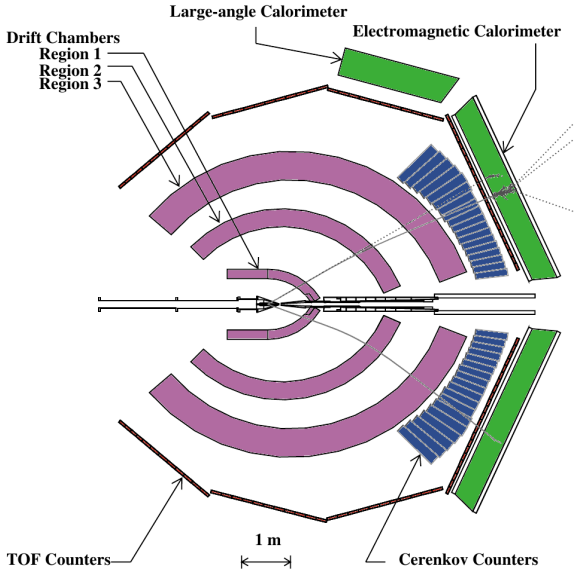

(b) Cut along the beamline (beam to the right). A typical interaction originating from a target in CLAS' centre is shown with associated photon, electron and proton tracks (from top to bottom)

Figure 2.3: Schematic cross-section views of CLAS, highlighting the **torus coils (cyan)**, **drift chambers (purple)**, **Cherenkov counters (blue)**, **TOF counters (red)** and **electromagnetic calorimeters (green)** (including **large-angle calorimeters (green)**). Both diagrams include a 1 m scale bar. Modified from [37].

2.3.2 The CLAS Detector System

CLAS was a segmented multilayer detector based around a toroidal magnetic field design optimised for tracking trajectories of charged particles over a large polar angle. There were six toroid shaped superconducting coils equally spaced in ϕ around the beamline which provided field azimuthal symmetry. This six "sector" segmentation of CLAS followed the geometry constraints of the torus coil, in which each sector could be considered as operating independently. Measurement and identification of particles was carried out in each sector with use of drift chambers (DC), Cherenkov counters (CC), time-of-flight scintillation counters (TOF) and electromagnetic calorimeters (EC). Schematic diagrams are shown in figure 2.3. In particular, figure 2.3a clearly shows the six sectors of CLAS and follows the clockwise numbering convention of one to six from the left (9 o'clock on a clock face) looking down the beamline (downstream). As a whole, CLAS was roughly spherical, measuring approximately 9 m across. Note, figure 2.3b shows the additional electromagnetic calorimeter detector known as the large-angle calorimeter (LAC), existing only in sectors one and two in which they extended the maximum polar angle coverage from 45° to 75°. However, the LAC will not be discussed in detail as it was not used in the work in this thesis. Additional information on the LAC is available in its response study paper [47].

To further help in understanding the CLAS detector system as a whole, it can be considered as three key parts:

- central detector sphere ($8^\circ < \theta < 142^\circ$), consisting of the torus and the drift chambers
- forward detectors ($8^\circ < \theta < 45^\circ$), consisting of the Cherenkov counters, forward TOF, and the (forward) electromagnetic calorimeters
- large-angle detectors ($\theta > 45^\circ$), consisting of the rest of the TOF and the large-angle electromagnetic calorimeters (LAC)

With regards to this description, please see figure 2.4 for further illustrations of the CLAS detector.

The CLAS detector system will now be described in greater detail; firstly the torus, then each of the subsystems at radially increasing distance from the centre of CLAS. Additional subsystems to the baseline CLAS design will then be discussed.

2.3.3 The Torus

The design of CLAS was formed around the novel superconducting torus magnet geometry of six individual kidney-shaped coils [48]. Each of the coils consisted of four layers of 54 turns of superconductor (aluminium-stabilised niobium-titanium/copper), and the torus operated at 4.5 K. The magnetic field produced was crucial for measuring not only the trajectories of charged particles, but also their momenta. Operating at the maximum design current of 3860 A produced an integral magnetic field of 2.5 Tm in the forward direction, reducing to 0.6 Tm at θ of 90°. However, for reasons of stable lifetime performance, the standard operating current was typically only 87% of the design maximum. Charged particles' trajectories were bent in the polar angle of θ with respect to the beam axis, but essentially unaffected in the azimuthal angle of ϕ. Fundamentally it was the torus geometry that successfully produced the magnetic field which was toroidal in the azimuthal direction. Positive torus current settings caused forward-going negatively charged particles to bend towards the beam axis and was referred to as the "in-bending" run condition. Conversely, negative torus current settings caused forward-going negatively charged particles to bend away from the beam axis and was referred to as the "out-bending" run condition. Therefore in-bending (out-bending) runs improved the detection of electrons that scattered at high (low) polar angles. The torus in Hall B can be seen in figure 2.5 which clearly shows the kidney-like shape of the superconducting coils, note, the length is 5 m and the diameter is approximately 5 m.

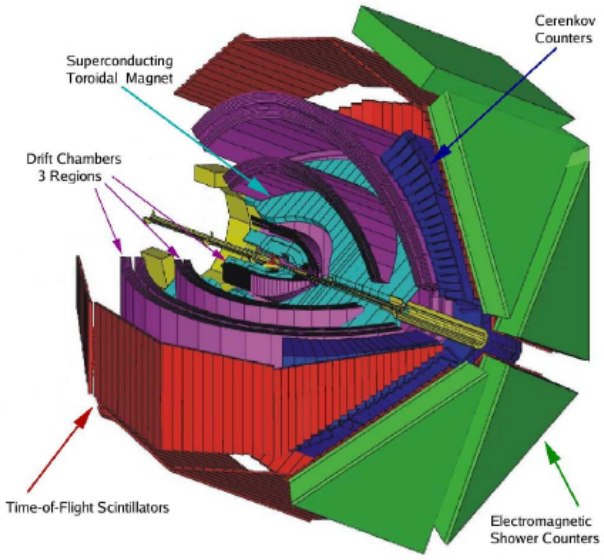

(a) Diagram of CLAS with all elements removed in sector three (including the **torus coils (cyan)** at either side), and the **EC (green)** removed in sector four for illustrative purposes. The **LAC (green)** can be seen on the top right in sectors one and two. Beam out-of-page at bottom right

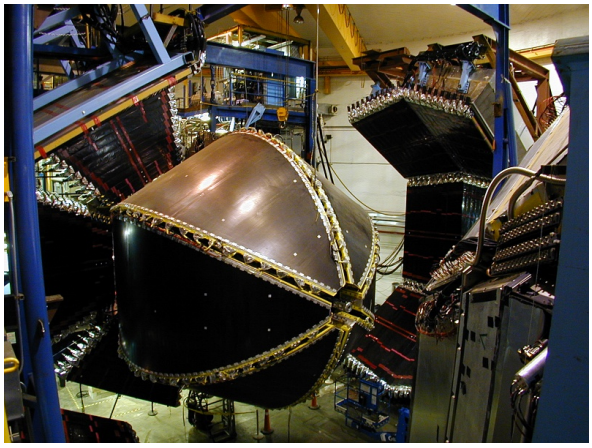

(b) Exploded view of CLAS in relation to the central detector sphere, with large-angle TOF pulled away (LAC visible on top on the right) and forward detectors extended downstream (bottom right). Beam out-of-page at bottom right

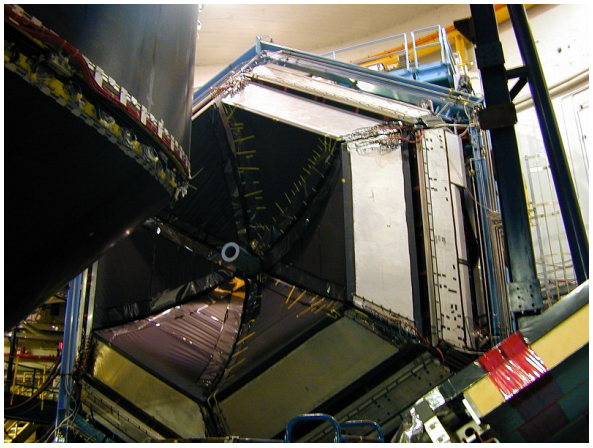

(c) The forward detector section has been extended downstream in relation to the central detector sphere (top left). Beam into-page at centre right

Figure 2.4: Diagram and photographs of CLAS for further clarification, from [50] and [51] respectively. As a whole, CLAS was roughly spherical, measuring approximately 9 m across.

Figure 2.5: Photograph showing the toroidal magnet in Hall B connected to its upstream beamline support structure on the left. The torus length is 5 m and the diameter is approximately 5 m. Modified from [51].

2.3.4 Drift Chambers

Tracking and momentum measurements of charged particles were carried out by the drift chambers [49]. Each of CLAS' six sectors contained three "regions" of drift chambers, each grouped into two "superlayers" of chamber bodies at different radii from the target:

- Region 1 - inside the torus, surrounding CLAS' central target position (low magnetic field)
- Region 2 - at approximately half the radius of the torus coils (high magnetic field)
- Region 3 - just outside the torus (low magnetic field)

The polar angle coverage of the drift chambers extended from 8° to 142°. Figure 2.3 is again very useful in illustrating the geometry of this subsystem within CLAS.

The chamber bodies consisted of a quasi-hexagonal cell pattern of wires, in which a sense-wire (positive voltage) was located at each centre surrounded by six field wires (negative voltages). Each superlayer was surrounded in its perimeter by guard wires maintained at a much lower voltage to minimise edge effects such as that of the grounded endplates of the chamber. A simplified representation of the wire cell layout can be seen in figure 2.6a.

The wires were strung parallel to the magnetic field (produced by the torus) in each region's inner superlayer, and titled at an angle of 6° with respect to this in the corresponding region's outer superlayer, which could then provide information in the ϕ direction.

Each chamber contained a gas mixture of 88% argon to 12% carbon dioxide, and was held at constant pressure, supporting fast drift velocities of electrons within the chamber volume. A charged particle traversing a chamber ionised the gas molecules and, due to the potential

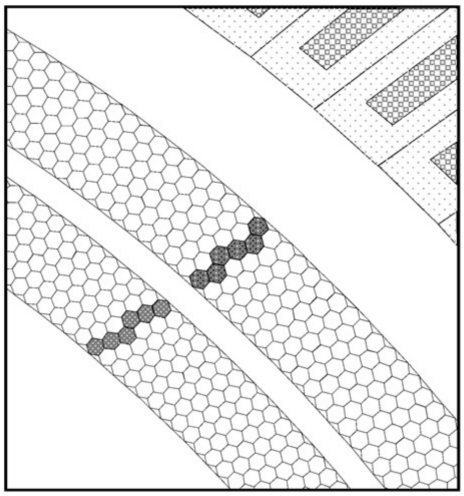

(a) The highlighted cells in both Region 3 superlayers show the detected trajectory of a charged particle. A portion of Cherenkov counters are visible at the top right. [49]

(b) Complete assembly of the Region 1 chambers on a test support fixture. Beam would be out-of-page. Modified from [51]

Figure 2.6: Images of the drift chambers, with (a) being a simplified representation of the wire cell design in a portion of Region 3, and (b) showing the Region 1 assembly on a test support fixture.

difference between the sense-wire and field wires, the electrons avalanched onto the positively charged sense-wire.

The time of signals from the sense-wire were used in measuring the "drift time" of the electrons, allowing for the charged particle's distance-of-closest-approach (DOCA) to be determined. This process was carried out for each sense-wire signal (above a threshold) to obtain tracking of the particle's trajectory through each of the drift chamber regions.

The high magnetic field provided by the torus produced sufficient curving of charged particles' trajectories in Region 2, and therefore helped obtain precise momentum measurements.

The magnetic field map of the torus was well known and therefore the charged particle tracks measured by the drift chambers could be extrapolated to determine their origin (which was expected to come from the target).

Figure 2.6b shows a photograph of the assembly testing of the Region 1 drift chambers.

2.3.5 Cherenkov Counters

One of the forward detector subsystems in CLAS was the Cherenkov counters which helped discriminate electrons from negatively charged pions and provide an event trigger on electrons [52].

The Cherenkov counters covered a polar angle from 8 to 45° with each sector in CLAS divided into 18 regions in θ. Each of these 18 regions contained a set of two light collection

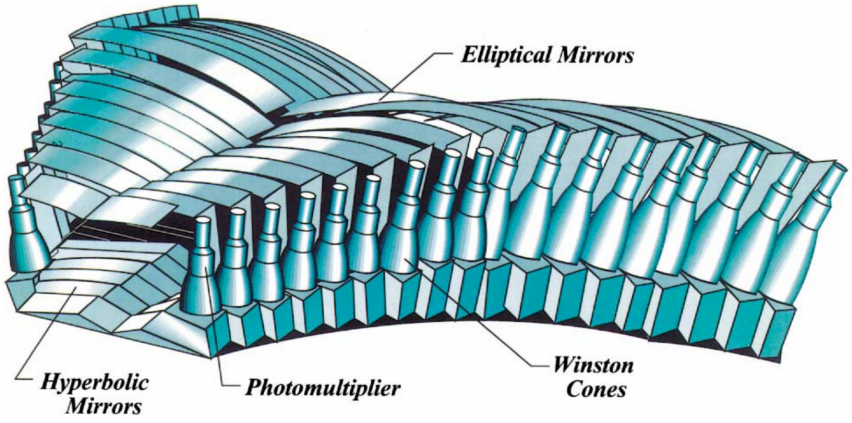

(a) Overview of the optical light collection system array in one sector, showing the division into 18 θ regions. [52]

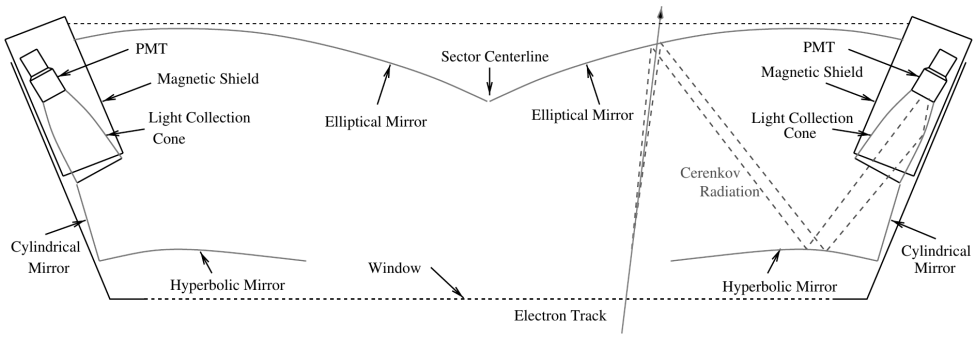

(b) Schematic diagram for one θ region of modules, highlighting the symmetry about the sector centreline. The production and collection of Cherenkov light can be seen in the region on the right. [37]

Figure 2.7: Diagrams of the layout and detection mechanism of the Cherenkov counters.

modules symmetric around the sector centreline in CLAS with the electronic hardware located in the projected space behind the torus coils, therefore ensuring the forward detector acceptance of particles was maximised. The operating mechanism of this detector subsystem was that *Cherenkov light* (radiation) was produced by charged particles travelling through a volume of gas radiator above the speed of light within that medium. This light was then reflected and focused by mirrors in the ϕ direction (θ angle information being preserved), collected by a "Winston" light cone, and finally detected by a magnetically shielded photomultiplier tube for electronic signal readout. The diagrams in figure 2.7 show an overview of the Cherenkov counters in one CLAS sector and one particular θ set of modules.

The radiator gas was perfluorobutane (C_4F_{10}) with a refractive index of 1.00153 which was held at constant pressure and had a pion momentum threshold of 2.5 GeV/c - being the momentum limit for successful discrimination from electrons. The Cherenkov counters acted as another CLAS subsystem which could be included in the electron event trigger.

2.3.6 Time-of-Flight Scintillation Counters

The time-of-flight scintillation counters (TOF) provided excellent particle timing information over a large polar angle: $8^\circ < \theta < 142^\circ$ [53]. This detector was imperative in event triggering and in particle identification (when paired with drift chamber information), using the precisely measured flight time of particles traversing the TOF relative to an event start time.

The design was based on long rectangular bars of plastic scintillator, Bicron BC-408 being known for its fast time response and high light output, with each counter having a uniform thickness of 5.08 cm. The counter arrangement is illustrated in figure 2.8 and will now be discussed. Lying parallel to the normal drift chamber wires, the scintillators were optimally oriented with a 2° lab frame angle subtended by each counter. The length of each counter varied across polar angles due to the torus coils' azimuthal constraints, ranging from 32.3 cm long (at the most forward-angle of $\sim 9^\circ$) to 445.1 cm (at a large angle of $\sim 78^\circ$). In the shadow region of the torus magnetic field, light guides were connected to each end of the counter and optically coupled to PMTs allowing for charge and timing measurements. The detector subsystem was grouped into four panels, with Panel 1 covering forward-angles ($8^\circ < \theta < 45^\circ$) and 2, 3 and 4 covering large angles ($\theta > 45^\circ$). A straight light guide configuration was used for the 15 cm wide scintillators covering forward-angles and the last four large-angle counters in Panel 4. All other counters were 22 cm wide and made use of bent light guides. Wider counters were used as the angular resolution requirement reduced at large angles due to the relation between angles subtended by particles scattering at high angles in the the centre-of-mass and the laboratory system. The time resolution requirement also reduced due to the longer flight time at large angles. This optimised design of the TOF ensured the time resolution was sufficient to meet the goals of this key detector within CLAS.

The time resolution achieved was well within the specification limits, with intrinsic resolutions for short counters measured as ~ 80 ps, and ~ 160 ps for longer counters. These values were obtained in initial cosmic tests utilising cosmic rays incident on the detector, but are largely in agreement with calibrations using a laser pulser and test interactions using different electron beam energies.

One important criteria of the TOF design specification was to separate pions and kaons up to a momentum of 2 GeV/c. Note, higher energy particles scatter at lower angles in θ and therefore required better time resolution. The TOF could also detect neutrons but its efficiency was limited to 5%.

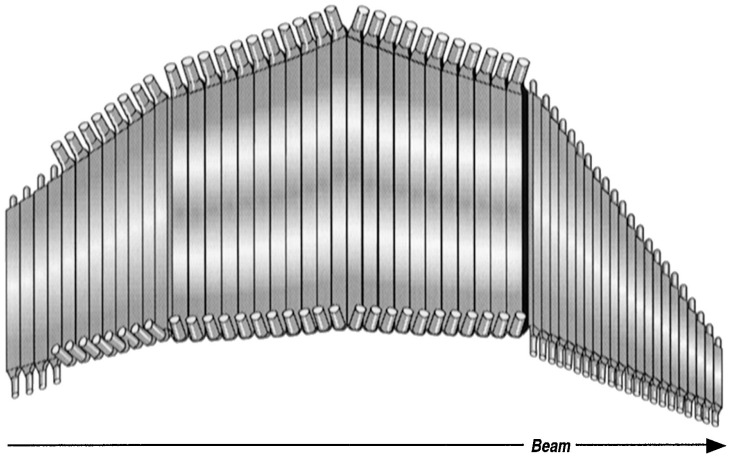

Figure 2.8: The four panel scintillator arrangement for one CLAS sector. In particular, the difference in counter length and width is clearly visible. [53].

2.3.7 Electromagnetic Calorimeters

The electromagnetic calorimeter (EC) was crucial in providing the event trigger on electrons with energies greater than 0.5 GeV [54]. The calorimeter had very good energy, position and timing resolution, therefore provided key measurements even in reactions involving both charged and neutral particles.

This *sampling calorimeter* covered forward-angles of $8^\circ < \theta < 45^\circ$ in all CLAS sectors, each based on a geometry of nearly equilateral triangles with area successively increasing with radial distance from the centre of CLAS. This design is shown in figure 2.9a and will now be discussed. A sampling calorimeter makes use of alternating layers of material, for the EC this was lead as the passive absorber (to initiate particle showers) and scintillator as the active detector (allowing for time and charge measurements). 39 layers of 10 mm thick scintillator bars were each followed by a 2.2 mm lead sheet. A novel design used three orientations of each layer's parallel arrangement of 36 scintillator paddles (10 cm wide) to each side of the triangle. A rotation of 120° recurred in the order for layers labelled as *planes U, V* and *W*, and provided stereo information on position of the deposited energy. Fibre-optic light guides were connected to each end of the scintillators and run along the triangles' sides to PMTs mounted on the back of the EC. Operation with a high energy electron beam motivated the EC design to have a thickness of 16 radiation lengths in total, therefore enabling it to contain electromagnetic showers. The *sampling fraction* of the EC is defined as the fraction of energy deposited in the scintillators to that of the particle's total energy, and therefore is used to reconstruct the total energy of incident particle. The total thickness ratio of lead to scintillator of 0.24 was related to the EC's sampling fraction for electrons - approximately $\frac{1}{3}$.

The EC was best suited in providing reliable measurements of particles interacting via the electromagnetic force, with the dominant initial mechanisms being electron-positron pair production for photons, and Bremsstrahlung for electrons (and positrons). A recurring cas-

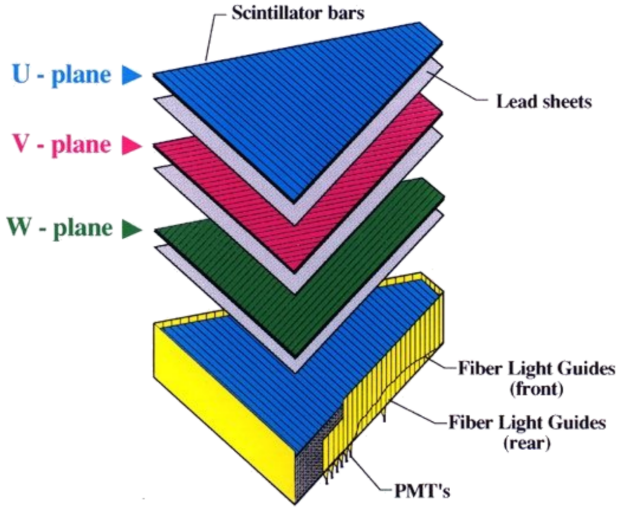

(a) Scintillation layer orientation within the triangular structure. [54]

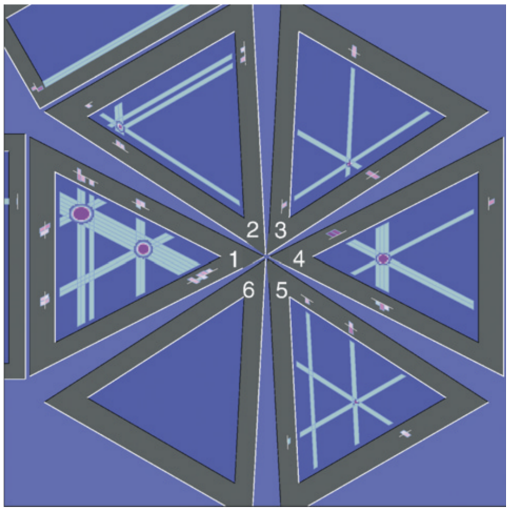

(b) Downstream view showing one hit reconstructed in sectors 2, 3, 4 and 5 each and two within sector 1. The large-angle calorimeter can be seen at the top left. [37]

Figure 2.9: Views of the electromagnetic calorimeter. (a) An exploded diagram of the sampling calorimeter design and readout system. (b) Successful event reconstruction of multiple hits, with the transverse energy spread highlighted as purple ovals for each hit.

cade of secondary particles were generated with progressively decreasing energy (a photon via Bremsstrahlung, and an electron-positron pair from a photon) until these were no longer the dominant interaction mechanisms, occurring when an electron/positron reached a critical energy. Interactions then occurred in the scintillator via ionisation and excitation, with this energy being read out to the PMTs. Note, hadrons (such as neutrons) interacting via the strong interaction deposited energy in a more complex process and the EC was not optimised for their detection and measurement.

Event reconstruction can be seen in figure 2.9b, highlighting the EC's segmentation allowing for the detection and measurement of multiple hits within one sector based on the clusters of energy deposited.

The EC helped in discriminating electrons from pions, further to the capabilities of the Cherenkov counters which were limited to pions of a momentum up to 2.5 GeV/c. This discrimination using the EC is described in detail later in the data analysis section of the thesis. For neutrons with an energy of at least 0.5 GeV, the detection efficiency was greater than 50%, where time-of-flight measurements allowed for discrimination from photons up to a momentum of 2.5 GeV/c. Neutrons above this momentum could still be identified using different criteria, however, this reduced the detection efficiency.

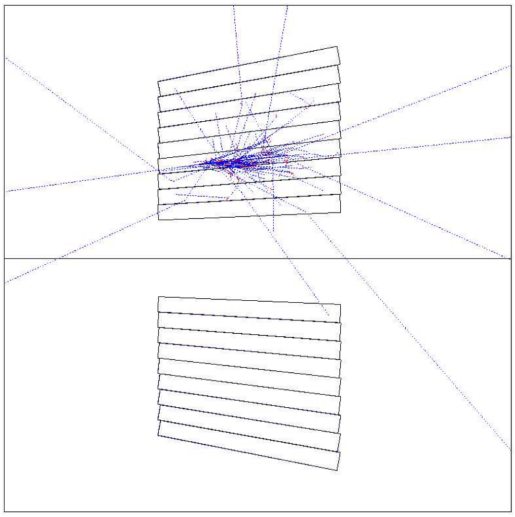

(a) Electromagnetic shower induced by a 1 GeV photon from a typical DVCS reaction. Cross-section view, cut along the beamline (beam to the right). [56]

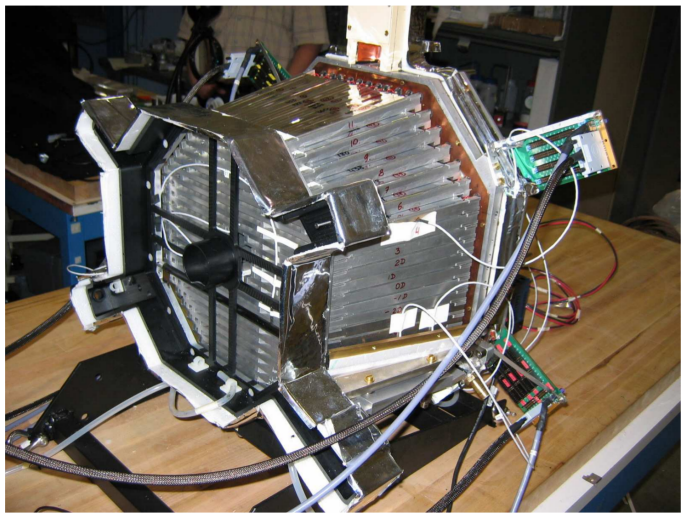

(b) Complete test bench assembly [57]

Figure 2.10: The IC crystal arrangement is clearly illustrated in the simulation geometry shown in (a), and in the photograph in (b).

2.3.8 Inner Calorimeter

An additional calorimeter was introduced in 2005 for experiments with a focus on Deeply Virtual Compton Scattering (DVCS) in which there was a need to increase the photon acceptance to include low forward-angles of $4^\circ < \theta < 16^\circ$ [55]. The inner calorimeter (IC) was a small detector located within the innermost region of the drift chambers and typically positioned centrally in CLAS. This device consisted of 424 lead tungstate trapezoidal crystals, each 16 cm long and increasing from 13x13 mm^2 (upstream end) to 16x16 mm^2 (downstream end). The front face of all crystals were aligned in the beam axis and angled towards optimal upstream focal points to enhance the detection of particles produced in upstream target experiments. This arrangement of dense scintillation material with high stopping power optimised the measurements of energy deposited by photons that induced electromagnetic showers along the crystal. Figure 2.10 illustrates the arrangement of crystals.

The IC provided good measurements of low forward-angle photons, however, it was also important to consider the effect on particles detected in CLAS which passed through the IC or its support structure.

The IC provided excellent low forward-angle coverage of photons that decayed from the neutral pion via $\pi^0 \rightarrow \gamma\gamma$.

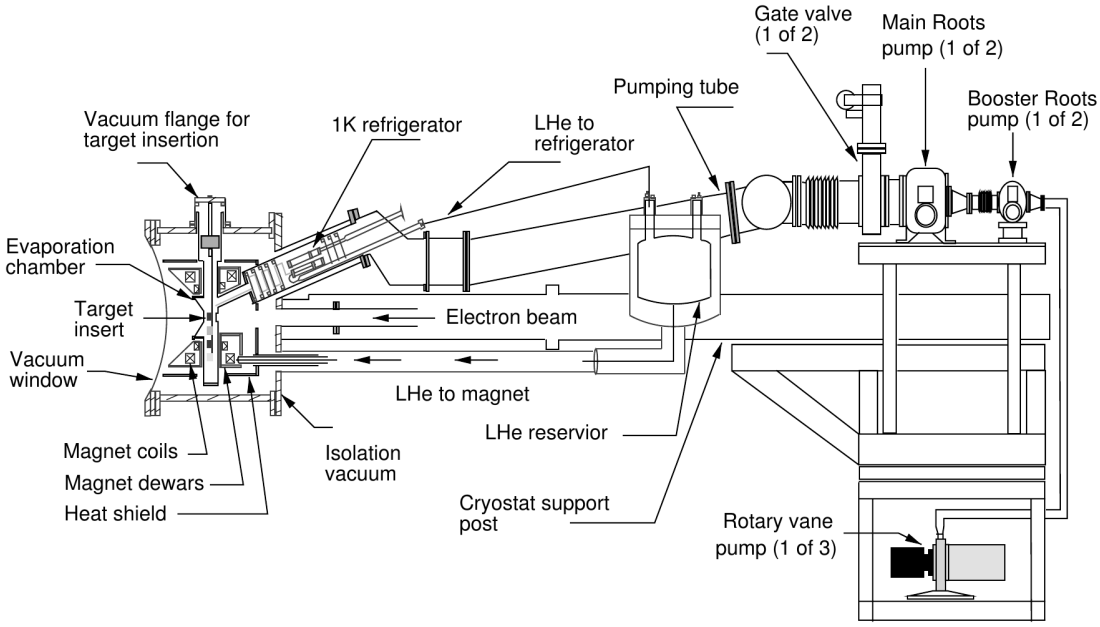

Figure 2.11: Design overview of the CLAS polarised target system. Note, beam to the left. [37].

2.3.9 Polarised Target System

The work in this thesis concentrates on an electron beam experiment with use of a polarised solid target in Hall B. Interestingly, photon beam experiments in the hall made use of polarised targets in two other unique systems: the Frozen Spin Target (FROST) [58], and the HDice Target [59].

The polarised target system developed for CLAS [60] provided a longitudinally polarised solid state target of protons and deuterons (allowing experimental access to loosely bound neutrons).

The technique of Dynamic Nuclear Polarisation (DNP) was utilised in which microwaves of frequency near the electron spin resonance were used to spin-flip an electron, resulting in a spin-flip of a nearby proton (or deuteron). This process was possible by using a compound containing hydrogen (or deuterium) doped with unpaired electrons (paramagnetic radicals) in a relatively low abundance. Spin relaxation times being very short for electrons ($\sim 10^{-3}$ s) but very long for nuclei ($\sim 10^{3}$ s) allowed electrons to easily induce spin-flips of other nearby nuclei. Net polarisation of the bulk material was achieved by the propagation of spin-flips of mutually interacting nuclei - known as “spin diffusion”.

Optimal operation of the DNP based target system developed required target material at a temperature of ~ 1 K to be held in a 5 T uniform magnetic field parallel to the beam axis. To meet this requirement, the target material and superconducting magnet were held in vacuum and both pumped with liquid helium (^4He).

The system required operation in an external field free region and was therefore rolled in from the upstream end on a rail-mounted cart. The nominal polarised target position was -0.57 m relative to the centre of CLAS, as opposed to other targets typically being more cen-

tral. An overview diagram can be seen in figure 2.11, and the main components of the assembly are as follows:

- **Superconducting Helmholtz Magnet:** two coils produced a 5 T magnetic field parallel to the beam axis. The field was uniform across the target volume and therefore did not affect the trajectory of the incoming beam. The geometry of this magnet constrained the opening angle for forward scattering particles to +/- 50°, this partly motivated the use of an upstream target position to the improve detection acceptance of CLAS.

- **1 Kelvin Refrigerator:** liquid helium (^4He) was pumped into a bath to cool and maintain target materials at $\sim$ 1 K upon insertion. This refrigerator system was angled at 25° to the horizontal to optimise the target system's operation with space constraints taken into account.

- **Target Sample Insert:** a remotely controlled motorised vertical aluminium rod insert system held four target materials within individual cells. Optimally designed to reduce scattered particles' energy loss, these individual "cups" were nominally 15 mm in diameter and 10 mm in length, with 0.2 mm plastic (polychlorotrifluoroethylene) walls, 25 μm aluminium entrance windows and 50 μm Kapton exit windows. The effective length of target material was measured as part of data calibrations. Figure 2.12a shows a diagram of this insert system.

- **Microwave System:** a constant microwave radiation polarised the target material on the beam axis into positive or negative spin states, according to the frequency used.

- **NMR System:** a resonant RLC circuit with a copper-nickel coil configuration around the top two target cells (polarisable material) provided the means to take online continuous wave Nuclear Magnetic Resonance (NMR) measurements. During radio frequency sweeping, the induced voltage in the circuit allowed the target's polarisation to be determined. This system also helped to quickly inform decisions on altering the polarising microwave frequency when needed.

The target system was very successful in achieving high polarisations, both positive and negative, with recorded maxima of 96% for protons and 46% for deuterons in the "EG1" experiment in its run period during 2000-2001. Figure 2.12b shows an example of polarisation history recorded with NMR measurements. An important element to consider is the target particle's magnetic moment, as this is related to the particle's total angular momentum and describes its behaviour in a magnetic field. Since the magnetic field and temperature are held at constant values in the solid state target system, it is the magnetic moment of the target particle that is the main factor in limiting the achievable polarisation. The ratio of the deuteron's magnetic moment to that of the proton is approximately 0.3, and therefore largely accounts for the difference in maximum polarisations achieved using the $^{15}NH_3$ and $^{15}ND_3$ targets.

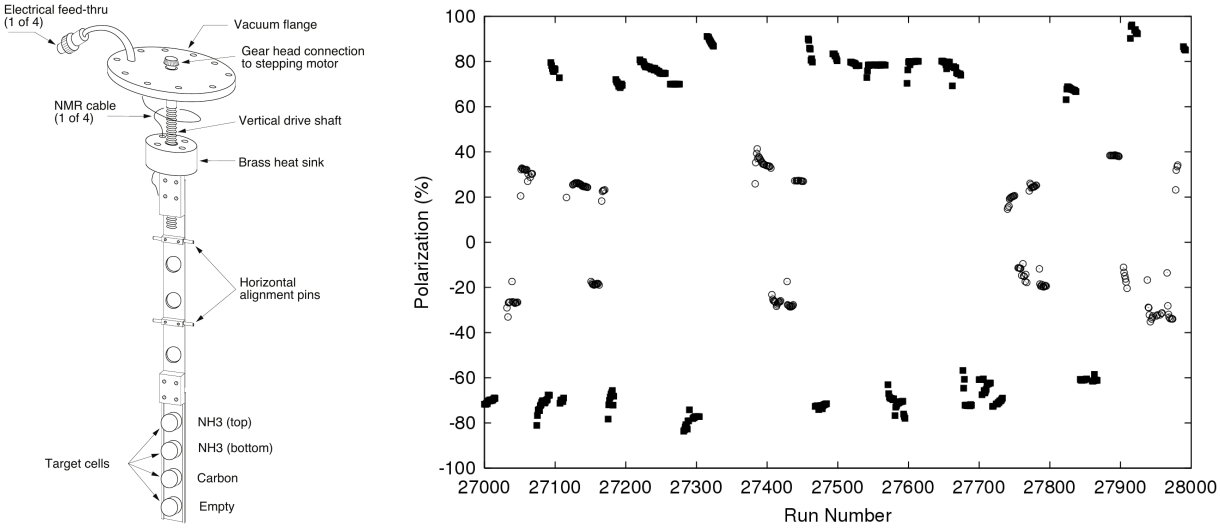

(a) Target sample insert diagram. [5]

(b) NMR polarisation measurements for $^{15}NH_3$ (■) and $^{15}ND_3$ (⊙) over 2000 consecutive hours of experimental running. [60]

Figure 2.12: The polarised target system for CLAS. Subfigure (a) shows a diagram of the target sample insert, excluding the NMR coils wrapped around the top two target cells. Subfigure (b) shows NMR measurements of target polarisation during the EG1 experiment.

Ensuring quality of target materials in this system was critical. Target material depolarisation was minimised by rastering the electron beam in a spiral over the sample cell using upstream *rastering* magnets. Radiation damage was treated with periodic annealing (heating of the material) and the target sample was eventually replaced when the maximum polarisation decreased significantly.

The polarised target system made it impossible to utilise the CLAS mini-torus - a small magnet surrounding the target, focusing Møller electron radiation produced in the target away from the drift chambers and towards a lead absorber around the beam pipe. However, the strong field of the Helmholtz magnet was found to be effective at dealing with much of this background and was also part of the motivation to use an upstream target position, ensuring low occupancy in the innermost drift chambers. Fortuitously the inner calorimeter also helped with the absorption of this radiation, although the IC's supplementary lead shielding (angled up from the beam pipe) was most successful for this. In 2005 [55] a purpose built 4.7 T superconducting solenoid was introduced (radially surrounding the target system when in use), this further suppressed the Møller background at high beam energies and therefore increased the luminosity for DVCS experiments [61] [62]. Figure 2.13 illustrates this setup and typical Møller electron background interacting with the IC and lead shielding in a polarised target DVCS experiment setup.

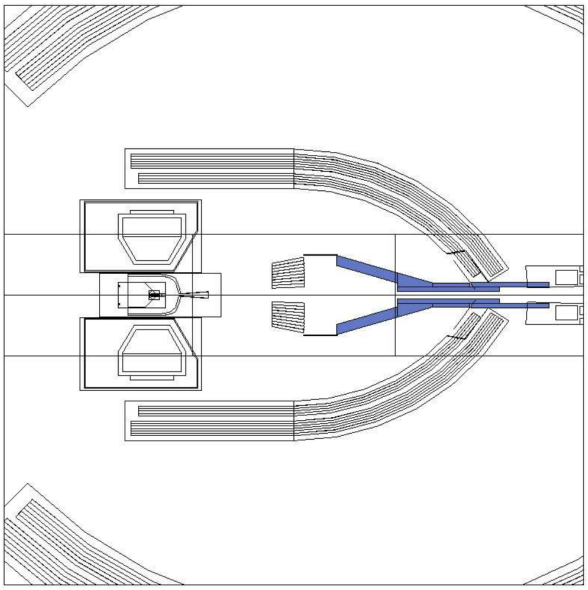

(a) Additional lead shielding introduced downstream of the IC is highlighted as **blue** and was used to absorb Møller electron background

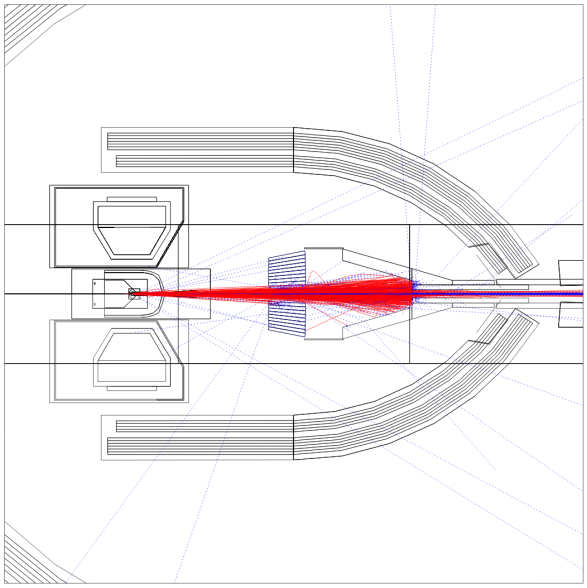

(b) Simulation example (with the superconducting solenoid on) showing photons as **blue** and Møller electrons as **red** tracks which, if not initially stopped by the IC, are typically absorbed by the lead shielding

Figure 2.13: The central section of CLAS, showing typical positions of the polarised target system within the 4.7 T superconducting solenoid (left in each image) and the IC (centre in each image). These are contained within the Region 1 drift chambers, with a portion of Region 2 visible at the top and bottom left in both images. Note, beam to the right. [56].

2.3.10 Trigger System

Data taking in CLAS utilised a unique trigger system design in which there were two "Levels" - **1** being deadtimeless, with the possibility to also use **2** as a second-level confirmation. The system was optimised for the CLAS setup ensuring reaction events of interest were recorded, with events due to accidental coincidences and detector noise being minimised. Speedy and efficient processing was achieved with the aid of grouping detector subsystems into coarse angle bins, and employing specialised and custom electronics. Analog PMT signals of detector subsystems were digitised to perform trigger logic operations, with the Trigger Supervisor custom electronics board handling the readout of all required information for the successful event.

Successful triggering on the scattered electron was crucial in CLAS during electron beam experiments, making use of signal information from the Cherenkov counters and electromagnetic calorimeter above electronic hardware thresholds. Hits in the EC above a total energy threshold helped isolate events with high momentum transfer in the reaction (as desired), and a further constraint was on the concentration of energy deposited in the inner layers which reduced contamination from minimum ionising pions.

Level 1 operated with multiple stages of *Memory Lookup*, comparing PMT channel information with preloaded patterns to ascertain the likelihood of the event containing particles of interest. This process was carried out for all six sectors independently, then combined allowing for geometrical constraints to be applied to event run periods with multiple particles of anticipated scattering properties. When only using Level 1 for the trigger system (CLASS 1), the converted event information was placed onto a readout queue with handling of this performed asynchronously, allowing for continual trigger system processing. The continuous electron beam from CEBAF into Hall B made the zero deadtime property of CLASS 1 crucial.

Accidental coincidences from cosmic rays and detector noise could satisfy the Level 1 trigger criteria, therefore the Level 2 trigger helped reduce these events by using drift chamber tracking information, although this introduced deadtime to the system.

The Level 2 trigger used *track templates* to determine if detected hits satisfied possible trajectories (using suitable granularity of drift cells), therefore allowing for a comparison to be made with the Level 1 hits. When using this additional trigger signal (CLASS 2), the Trigger Supervisor waited an optimal time to receive the confirmation signal and digitisation of tracks, unless the signal failed. During this deadtime no other Level 1 triggers could be accepted. Like CLASS 1, the processing of the readout queue was asynchronous to digitisation.

Minimising deadtime in CLAS experiments was critical, however not all events passing CLASS 2 were of interest, therefore offline analysis of the recorded data developed further conditions as part of initial event selection.

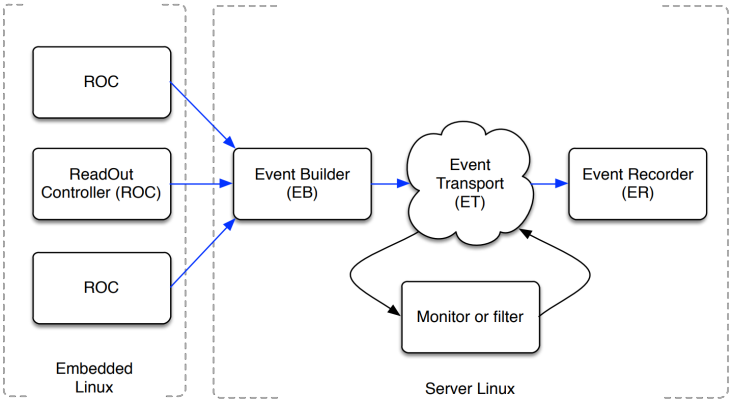

Figure 2.14: A simple small CODA system separated into the initial digitised data that ROCs bus to the control room online acquisition computer for further DAQ processing. [65].

2.3.11 Data Acquisition

The Trigger Supervisor successfully determining a "pass" trigger signal then prompted the Data Acquisition (DAQ) system to complete all further processes in the readout including digitisation, formatting, and storage of data.

The CEBAF Online Data Acquisition (CODA) software toolkit is unique to JLab, using a common framework in both software and hardware for consistency across the experimental halls at the laboratory [63] [64]. The DAQ architecture in Hall B was optimised according to the experimental scope of physics (trigger system, etc.), whilst making the best use of available technology from front end hardware to the UNIX file system. FASTBUS and Versa Module Europa (VME) crate electronic systems contained custom hardware modules such as analog-to-digital converters (ADCs) and time-to-digital converters (TDCs) which carried out the electrical signal digitisation.

Referring to the simplified CODA system in figure 2.14 is helpful in giving an overview of the DAQ. Readout Controllers (ROCs) - central processing units - in each electronics crate send digitised data via a network to the control room's online acquisition computer in which the Event Builder packs the event data into formatted *bank* data structures unique to the experimental setup. This completed event data is labelled and combined with trigger information to take its final form for offline analysis, and is therefore transferred to the Event Transport. This information can then be interfaced with experimental data monitoring processes, whilst being transferred in parallel to the Event Recorder for writing to disk (with this being backed up to a remote tape silo in the Computer Center).

Experiment configuration, control and monitoring is handled by the CODA Run Control system. Monitoring of the DAQ system as well as live data quality is crucial, including key detector and hardware parameters for offline calibrations such as power supply voltages, torus current, beam position, etc.

Group	Period	E_{beam} (GeV)	I_{torus} (A)	I_{target} (A)	*Target position* (cm)
1	A	5.892	2250	-121.4	-58.2
2	A	4.735	2250	-121.4	-58.2
3	B	5.967	2250	-121.4	-68.3
4	B	5.967	2250	-121.4	-68.3
5	B	5.967	-2250	-121.4	-68.3
6	B	5.967	2250	-121.4	-68.3
7	C	5.764	2270	121.4	-68.3
8	C	5.764	-2270	121.4	-68.3

Table 2.1: EG1-DVCS run information for 8 groups of data taking covering run periods A, B and C. The run settings are listed for beam energy (E_{beam}), torus current (I_{torus}), target magnet current (I_{target}) and target position. Note, the target position of 0 cm corresponds to the centre of CLAS. Adapted from [68].

2.4 EG1-DVCS Experiment

In 2005 JLab's Program Advisory Committee (PAC) approved two experiment proposals with common experimental apparatus and running requirements. It was the following two experiments that formed the EG1-DVCS run programme:

- Experiment E05-113: Semi-Inclusive Pion Production with a Longitudinally Polarized Target at 6 GeV [66]
- Experiment E05-114: Deeply Virtual Compton Scattering at 6 GeV with polarized target and polarized beam using the CLAS Detector [67]

Data analysed in this thesis was taken in the EG1-DVCS experiment which was obtained in three different run periods, spanning February to September 2009.

An overview of run information for the EG1-DVCS experiment is displayed in table 2.1. Note, only data from periods/parts B and C of the experiment were analysed in this thesis. Parts B and C share similarities in beam energy (E_{beam}), torus current (I_{torus}), magnitude of target magnet current ($|I_{target}|$), as well as the target position. The target position was altered to increase and optimise the acceptance of events from its original location in part A. The inclusion of data from part A would have required additional corrections to allow the results to be combined with those of parts B and C. The inner calorimeter was positioned at the centre of CLAS throughout the experiment, i.e. at $z = 0$ cm.

Each run period utilised all four target sample cells, with the use of different materials allowing appropriate background studies and systematic checks to be performed. It is only the top two cells of the target insert that used the microwave system to achieve polarisation of the material. The focus of part B was scattering reactions with polarised protons and therefore made use of $^{14}NH_3$ in both the "top" and "bottom" DNP cells, with the non-DNP cells containing ^{12}C and being empty. During part C of the experiment the $^{14}NH_3$ in the bottom DNP cell was switched

out for $^{14}ND_3$ to also give access to scattering reactions with polarised neutrons (loosely bound in polarised deuterons) [69]. The average length (L) between the aluminium target windows was found to be 2.01 cm and 2.05 cm for parts B and C, respectively. These window lengths correspond to the beamline entry and exit of the target system, i.e. the total length of the target cell and the liquid helium surrounding it in the helium bath. The Kapton target cells containing the target sample material were located in the centre of L, with an approximate length of 1.5 cm. However, the "packing fraction" (l_A) of the crumbled loose ammonia ($^{14}NH_3$) and deuterated ammonia ($^{14}ND_3$) beads in the cell was a more useful quantity which indicated the effective length as if it were a tightly packed material. This was found to be 0.860 cm and 0.910 cm for the top and bottom target cells for part B of the experiment, and 0.922 cm and 0.890 cm for the top ($^{14}NH_3$) and bottom ($^{14}ND_3$) target cells for part C of the experiment. It is important to highlight that the empty cell actually contained liquid ^4He from the helium bath, therefore allowing for a thorough study of the effect of this material surrounding cells that were filled. As the ^{12}C material was was not in the form of beads but was naturally tightly packed, its length was only of the order of 0.40 cm with the rest of the target cell being filled with liquid helium.

Note, contamination of $^{14}NH_3$ in the $^{14}ND_3$ target was found to be 10.5% (12.0%) for the positive (negative) torus current setting used in part C, and is detailed in [70].

To give a feel for the relative statistics obtained, it is useful to consider the accumulated charge for each part of the EG1-DVCS experiment [71]:

- Part A - 6.9 mC from 31 days of running
- Part B - 15.4 mC from 51 days of running
- Part C - 7.7 mC from 32 days of running

Integrated over the whole experiment, the approximate run times were:

- 70% on polarised protons in $^{14}NH_3$
- 20% on polarised deuterons in $^{14}ND_3$
- 10% on ^{12}C
- 1% on an empty target

High polarisations of both beam and target were achieved during the experiment:

- $\sim$ 80% - electron beam
- $\sim$ 80% - protons in $^{14}NH_3$
- $\sim$ 30% - deuterons in $^{14}ND_3$

The main difference between EG1-DVCS with previous CLAS experiments with the use of polarised ammonia targets was the addition of the inner calorimeter. Also, this was the only experiment where the ammonia used in the polarised solid target system was ^{14}N instead of ^{15}N, with the Kapton target cells being twice as long [72]. For simplicity and to improve readability, ^{14}N will now be be referred to as N in this thesis.

2.5 Summary

A thorough description of the experimental facility has been given, covering the accelerator and beam delivery system to Hall B. The relevant laboratory setup for the EG1-DVCS experiment was detailed, including the beamline apparatus, detector subsystems, polarised target system, trigger and data acquisition systems. An overview was given on the experimental data analysed in this thesis, highlighting key run parameters, accumulated statistics and unique aspects of the experiment.

Chapter 3

Pion Electroproduction Data Analysis - 1

The majority of PhD research was devoted to the data analysis work presented in this thesis, detailed in the following chapters. An overview of the analysis work will be presented with supporting motivations, as well as an outline of the total scope of the project which included studying many reaction channels to produce a meaningful contribution of new measurements in a distinct kinematic region. Important decisions were made independently in setting the ambitious range of analysis channels to therefore provide a thorough investigation with comprehensive measurements for the experimental dataset. The initial event selection stages described in sections 3.2.1 and 3.2.2 are important in detailing key information and corrections implemented in the analysis, although it should be highlighted that it was the EG1-DVCS run group that performed the calibrations and provided relevant code for the data corrections. All further event selection was investigated in rigorous detail as part of the independent research performed. Significant time was allocated to investigate and implement a relatively new innovative event selection technique, used to isolate the signal source for each analysis channel. The extensive research in using the new technique helped develop the implementation and execution. Spin asymmetry results presented for the charged pion channels are a first for this kinematic regime.

PhD research performed outside the scope of the main thesis work presented, involving the development of detector monitoring and calibration software, is detailed in appendix A.

3.1 Overview of Analysis

The data analysis covers Deeply Virtual Meson Production of the single π^0, π^+ and π^- electroproduction channels using the EG1-DVCS experimental dataset. Relevant previous analyses of Gary Smith [5] and Andrey Kim [22] carried out a common "cuts-based" analysis method, whereas this work implements a "fit-based" analysis - in particular, using the sPlot technique. A first attempt was made at extracting spin asymmetries for each pion electroproduction channel, making comparisons where possible, and drawing conclusions on improving a fit-based approach to data analysis.

The first DVMP channel analysed was π^0 from a proton target (using NH_3), which was also studied by Smith and Kim. Simulated data was only available for this channel, allowing for a thorough investigation of the sPlot technique before extending the analysis to the π^+ and π^- channels.

The initial event selection process is discussed in this chapter, the sPlot technique detailed in chapter 4, the spin asymmetry results presented and discussed in chapter 5, and final conclusions presented in chapter 6.

3.1.1 Pion Electroproduction with CLAS

CLAS provides efficient detection of neutral pions (π^0) and both positively and negatively charged pions (π^+, π^-). Studies of single pion electroproduction were performed in which there was only one pion produced in the electron scattering reaction.

Firstly note, the incoming electron interacts with nucleons electromagnetically via the exchange of a virtual photon (γ^*) and the electron is therefore scattered from the beamline, with this being implicit for all reactions. Since the electron beam properties are well known during the experimental run time, detection of the scattered electron with CLAS allowed for the energy-momentum four-vector of the virtual photon (exchange particle) to be determined.

For CLAS fixed target experiments using an electron beam:

- "initial state" describes the incoming electron and the target particle
- "final state" describes the scattered electron and the particles produced in the reaction (whether detected or not)

Pion electroproduction must obey charge conservation, and therefore the only possible single pion channels from nucleons are described with their initial and final states as follows:

$$ep \rightarrow e'p\pi^0$$

$$en \rightarrow e'n\pi^0$$

$$ep \rightarrow e'n\pi^+$$

$$en \rightarrow e'p\pi^-$$

Electron scattering on a neutron was possible with use of a deuteron target, and therefore should really be described as

$$ed \rightarrow e'n\pi^0(p)$$

$$ed \rightarrow e'p\pi^-(p)$$

During the reactions above, the initial state participant nucleon (active in the reaction) can be excited to a resonant (intermediate) state due to the exchange of the virtual photon. During de-excitation, the nucleon produces a pion with the final nucleon being found in the same or different isospin state (a proton or neutron) according to charge conservation. The possible resonant state of the active nucleon is implicit in the reaction descriptions, and includes all possible resonant states - as well as reactions which produce the final state particles with no intermediate state for the nucleon, e.g. Deeply Virtual Meson Production. DVMP cuts were imposed as part of the final event selection in this thesis, and therefore the distributions shown in this chapter contain reactions both with and without participant nucleon resonance states.

3.1.2 Pion Electroproduction Reaction Channels Studied

As a final state proton or neutron could be detected for the channels analysed, this particle was simply referred to as the nucleon, with the particular detected nucleon being obvious for each reaction examined.

Both exclusive and semi-inclusive topologies of reaction channels were examined, in which all active final state particles were detected and only some final state particles were detected, respectively.

The exclusive reaction topologies required the measurement of all final state particles, with the physical geometry of the CLAS detector system imposing an acceptance condition for this topology. These results are reliable due to the efficiency of CLAS, but the total number of measured events were limited in the EG1-DVCS experimental run period data.

The semi-inclusive reaction topologies considered only required the measurement of the final state scattered electron and produced pion, with no constraint on the detection of the nucleon in CLAS. This increased the total number of measured events to also include those with recoil nucleons otherwise poorly measured by the detector subsystems or not reconstructed in the CLAS offline software. It should be highlighted that these topologies also had a wider acceptance for the final state nucleons, as there was no longer a constraint from the detector subsystems of CLAS.

Considering the above, it was obviously beneficial to consider both the exclusive and semi-inclusive topologies for each of the pion electroproduction reaction channels, allowing to check for consistency and assess datasets with sufficient event numbers.

Table 3.1 gives an overview of the single pion electroproduction channels and topologies investigated, with an initial state deuteron giving access to reactions from either a proton or a neutron. Final state particles not detected are contained within parentheses in the reaction descriptions.

When using the deuterium target, the reaction channels were in fact not *fully* exclusive as the complete reaction description also contained a low-momentum recoil nucleon that was a *spectator* (inactive) in the reaction. The initial state spectator was also implicitly a final state spectator

Reaction ID	Reaction Topology	Final State Nucleon Detected
1a	$ep \rightarrow e'p\pi^0$	p
1b	$ep \rightarrow e'(p)\pi^0$	-
1c	$ed \rightarrow e'p\pi^0(n)$	p
2a	$ep \rightarrow e'n\pi^+$	n
2b	$ep \rightarrow e'(n)\pi^+$	-
2c	$ed \rightarrow e'n\pi^+(n)$	n
2d	$ed \rightarrow e'(n)\pi^+(n)$	-
3a	$ed \rightarrow e'p\pi^-(p)$	p
3b	$ed \rightarrow e'(p)\pi^-(p)$	-

Table 3.1: Overview of the topologies of the reaction channels studied.

too. Although it is was spectator, this nucleon did have some effect on the participant nucleon target particle due to their loose binding as a deuteron. Measurement of the low-momentum recoiling spectator nucleon would require a suitable detector system setup, which the EG1-DVCS experiment did not have. Literature is available on the Hall B experiment *Barely Off-Shell Nuclear Structure* which made use of a custom built detector located up-stream in CLAS for the measurement of recoil spectator protons [73]. When the participant target nucleon is detected in the final state in this thesis, it is referred to as the exclusive topology, however this could technically be considered as semi-inclusive due to the spectator target nucleon not being detected.

Further details are now given on the reaction channels and topologies analysed:

- π^0: both the exclusive (1a) and semi-inclusive (1b) topologies were studied with use of the NH_3 target. An analysis was also performed on the exclusive topology (1c) with use of the ND_3 target to check for consistency in the results.

- π^+: both the exclusive (2a) and semi-inclusive (2b) topologies were studied with use of the NH_3 target. An analysis was also performed on the exclusive (2c) and semi-inclusive (2d) topologies with use of the ND_3 target to check for consistency in the results.

- π^-: both the exclusive (3a) and semi-inclusive (3b) topologies were studied with use of the ND_3 target.

Preliminary results found that there was not sufficient statistics to successfully analyse π^0 electroproduction from a participant neutron in the deuterium target, corresponding to $ed \rightarrow e'n\pi^0(p)$.

Now that an overview has been given of the reaction channels and topologies analysed in this thesis, the event selection process will be described. For simplicity, the scattered electron e' will now be labelled as "e" and referred to as the electron, improving readability in histogram axis titles, etc. It will be clear from context whether the electron is the initial or final state electron, as will be the case for the nucleon in the reaction.

3.2 Event Selection

The event selection will be detailed, starting with an overview of calibrations and data corrections performed by the EG1-DVCS run group, then progressing sequentially through the particle identification criteria of the analyses and presenting key event distributions for each of the reaction channels.

3.2.1 Calibrations and Data Quality Control

The data recorded during the EG1-DVCS experiment had to be converted from the raw information measured into useful physics information to allow for any meaningful analysis to be performed. The ADC and TDC measurements were converted into hit time and position information, deposited energy and particle momenta, and is referred to as "cooking" (Hall B terminology). The data also had to be calibrated to account for any issues encountered and changes to the experimental configuration during the run time, therefore ensuring a complete set of reliable measurements. The EG1-DVCS run group was responsible for the cooking and calibration of the data, ensuring good stability for the detector subsystems before making the final data form available for analysis projects. Calibrations were carried out for each subsystem independently, then as a collective to ensure they were aligned appropriately in both space and time. Some of the key calibrations performed were

- DC: timing and alignment
- CC: pulse height correction and timing
- TOF: timing
- EC: energy and timing
- IC: energy and timing
- Polarised target system: polarisations from NMR signals

Several iterations of cooking and calibrations were performed to achieve the required high quality of optimised experimental data.

The run group also performed a loose cut to skim the large amounts of cooked data without losing events of interest in which

- the first particle was charged
- a neutral particle was also detected if the first particle was positively charged
- all detected neutral particles met additional criteria

as described in greater detail in [74].

Having successfully cooked and calibrated the data, the run group then investigated the quality of the data, flagging "bad" files to be excluded from analyses. This file selection ensured each event had associated Faraday Cup information (with correct content), a non-zero NMR target polarisation measurement, correct file structure and proper online database information. Stability in the inclusive electron count rate was studied [75], flagging bad files consistent with detector issues, and took into account experimental configuration changes such as target changes (such as material and polarisation), change of torus current and beam energy.

3.2.2 Data Corrections

Further investigations by the run group highlighted issues specific to the EG1-DVCS experimental setup, requiring corrections to the data before proceeding with final data analysis. An overview of findings from a few key investigations will be discussed.

Beam Raster

As described previously, the electron beam was spirally rastered over the face of the target material to minimise radiation damage to the polarised target, and therefore the beam coordinate in the x, y plane was continuously changing. The conversion of the raster ADC readings to beam position was required to determine the beam coordinate for each event, as required for all detailed physics analyses. The run group study used electron tracks to determine the relation between the measured current of the rastering magnets with the actual beam position in the x, y plane [76]. As part of the fitting method, the average (nominal) target position in z was determined for each run period of the experiment.

An investigation into the uniformity of beam coverage on the target cells achieved with the rastering found that there was "over-rastering" in which the beam scraped the edges of the target cells [77]. Runs with such irregularities were flagged as bad files.

Target Field

The use of the polarised target system with its 5 T superconducting magnet made it crucial to perform a detailed study on the tracking of charged particles for the experiment. With knowledge of the corrected beam position, and making use of the calibrated detector subsystems (DC, etc.), the calculation of charged particles' direction cosines from the event vertex were optimised [78]. An improvement of the tracking reconstruction was achieved, therefore the direction cosines calculations (and in turn the angular resolution of the experiment) improved. The target field rotation was also accurately determined, correcting the misalignment of the target solenoid axis orientation with that of the beamline. As a result of the investigation, the resolution of the vertex in the z-axis improved.

EC and IC

Both the EC and IC were studied in greater detail [79], as they were crucial subsystems to make good measurements of key particles.

The timing of the EC did not require corrections and a study was carried out to determine the optimal cut to differentiate between photons and neutrons based on optimising signal-to-noise ratios for this detector.

The energy of electrons in the EC was calculated well in the calibration stage using the total energy deposited. However, due to the different response of the EC to electrons and photons, run and sector dependent corrections were required for photons according to the formula

$$E_\gamma = 1.015 \, \frac{E_{tot}}{A(run,\ sector)} + 0.06 \tag{3.1}$$

making use of an optimised normalisation factor and offset value. This improved stability issues due to fluctuations of the EC's high voltage gains, as otherwise the basic conversion would have simply made use of the detector's sampling fraction such that $E_\gamma = E_{tot}/0.3$.

Using the event trigger time information measured by the TOF (a very well calibrated subsystem), the IC timing was corrected to be consistent for all run periods of the experiment. This was important as it allowed for the application of a systematic cut required to remove significant background of Møller electron radiation and accidental coincidences in the IC. The total reconstructed energy in the IC was then used in a pulse-height correction and improved the time resolution of the IC photons.

3.2.3 Fiducial Cuts

Before discussing the identification of particles, it is worthwhile describing a common procedure of excluding parts of detector subsystems in CLAS which show measurement inefficiencies. One example of this is in ignoring particles detected within a border of a few centimetres around each side of the triangular geometry of each sector of the electromagnetic calorimeter. This outer region is where some of the electromagnetic showering may spread outside of the active detector material, and therefore the energy and position measurements would be incorrect for the particle - of particular concern for electrons and photons. The "fiducial" regions exclude these areas, which are cut away in the selection of events. Fundamentally these cuts can only allow for *equal* or *fewer* signal events of interest being correctly reconstructed for use in the final spin asymmetry analysis performed. Although typically small regions, cuts of this sort have an effect on the acceptance.

Three fiducial cuts were investigated and developed by the EG1-DVCS run group, therefore allowing for consistency in use for all analyses. Two were for particles which would be detected in the CLAS baseline subsystems, with one for particles detected in the additional inner

calorimeter. The effectiveness of using these fiducial cuts was studied as part of this thesis work, and therefore will be discussed.

An IC "shadow fiducial cut" was available for charged and neutral particles which removed regions where these passed through part of the IC support structure before possible detection in the CLAS subsystems [80]. Very few particles could traverse the IC scintillators themselves due to their high stopping power, but the cut also removed these regions. Interactions with the support structure could knock out particles through multiple scattering, and further contributes to energy losses within the material. These regions correspond to low θ particles detected in CLAS. Figures 3.1a and 3.1b show the effect of this cut on proton candidates in the Region 1 drift chambers.

An EC fiducial cut removed poor detection efficiency regions at the edges of each triangular sector, ensuring the whole particle shower was contained within the EC. This allowed for a truly complete measurement to be made of a particle's total deposited energy and the nominal sampling fraction of the detector. This cut is of particular importance for electrons and photons where both energy and position are crucial values to confidently know. Figures 3.1c and 3.1d shows the effect of this cut on electron candidates in the EC.

An IC fiducial cut removed poor detection efficiency regions at the inner and outer edges of the inner calorimeter. The purpose of the IC was to detect low θ photons, however all particles interacting with the crystals and depositing clusters of energy were recorded by the DAQ. The main decay of the π^0 is to two photons, therefore a reliable measurement of photons in the IC was important in allowing the neutral pion to be reconstructed. Figures 3.1e and 3.1f show the effect of this cut on photon candidates in the IC. All particles detected in the IC are considered as candidate photons for the reaction. Note, the "hot spot" located at approximately $x = -5$ cm, $y = -8$ cm was found to be a bad electronic channel reading a false high value signal for each event so was also removed as part of this fiducial cut.

Despite the study of these cuts, it was decided to remove all fiducial cuts the final analyses to increase the total yield of signal events by approximately 10%. Consistent results were obtained, and this significant gain in signal statistics reduced the errors in the results. The inclusion of fiducial cuts did form the basis of the initial analysis work, but it was found that the unique fit-based analysis performed on this experimental dataset did not require the use of fiducial cuts in the end.

3.2.4 Particle Identification

Particle identification (PID) was the first step in each analysis in isolating the signal events for each reaction channel.

All analysis topologies required the measurement of the final state electron and pion, with the exclusive topology also requiring the additional detection of the final state nucleon which typically recoiled with high momentum.

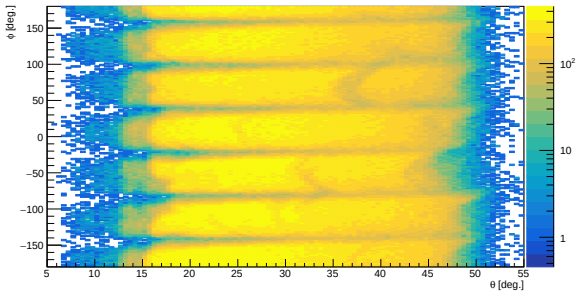

(a) Before the IC shadow fiducial cut

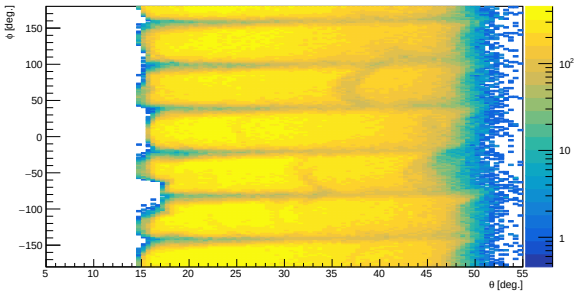

(b) After the IC shadow fiducial cut

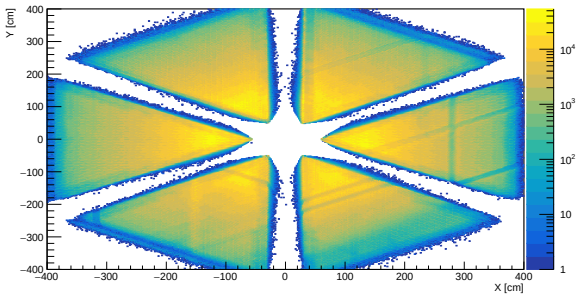

(c) Before the EC fiducial cut

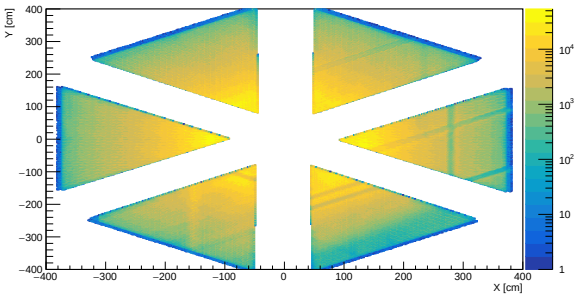

(d) After the EC fiducial cut

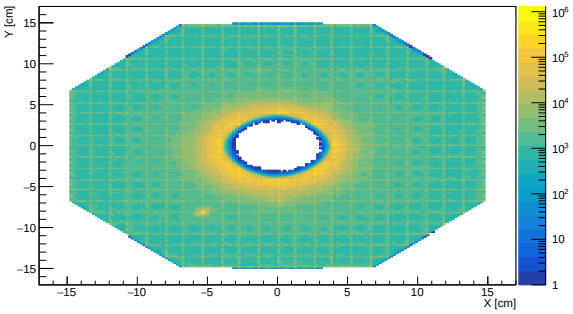

(e) Before the IC fiducial cut

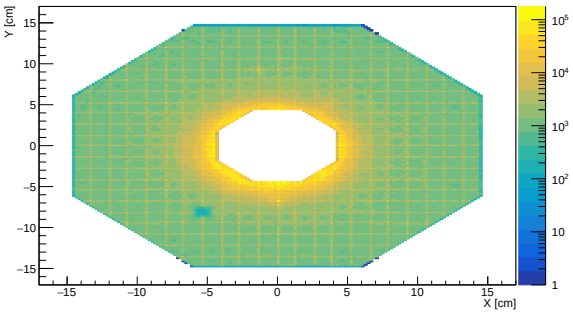

(f) After the IC fiducial cut

Figure 3.1: Plots (a) and (b) show candidate proton angular distribution of ϕ vs θ at the event vertex in the lab frame, before and after the IC shadow fiducial cut, respectively. Plots (c) and (d) show candidate electron hit positions in the electromagnetic calorimeter measured in the lab frame, before and after the EC fiducial cut, respectively. Plots (e) and (f) show candidate photon hit positions in the inner calorimeter measured in the lab frame, before and after the IC fiducial cut, respectively.

Reaction ID	Reaction Topology	Final State Negative Particles in CLAS	Final State Neutral Particles in CLAS	Final State Positive Particles in CLAS
1a	$ep \to ep\pi^0$	$= 1$	≥ 0	$= 1$
1b	$ep \to e(p)\pi^0$	$= 1$	≥ 0	≥ 0
1c	$ed \to ep\pi^0(n)$	$= 1$	≥ 0	$= 1$
2a	$ep \to en\pi^+$	$= 1$	≥ 1	$= 1$
2b	$ep \to e(n)\pi^+$	$= 1$	≥ 0	$= 1$
2c	$ed \to en\pi^+(n)$	$= 1$	≥ 1	$= 1$
2d	$ed \to e(n)\pi^+(n)$	$= 1$	≥ 0	$= 1$
3a	$ed \to ep\pi^-(p)$	$= 2$	$= 0$	$= 1$
3b	$ed \to e(p)\pi^-(p)$	$= 2$	$= 0$	≥ 0

Table 3.2: A summary of the initial skims on the reconstructed particles in CLAS in the data files.

Each event in the EG1-DVCS data files contained information on all reconstructed particles in CLAS, therefore a skim was implemented for each reaction topology, with a summary in table 3.2. The values used helped ensure that all the detected signal events were present, while minimising the file size significantly, and could be optimised under further investigation.

It is important to highlight that there was no such constraint placed on the particles detected in the inner calorimeter. As previously described, the IC covered a different polar angle than the main CLAS subsystems and therefore essentially acted as a supplementary detector increasing the overall detection acceptance. Particles detected in the IC were to be considered as candidate photons which were only of interest for the π^0 channel, and otherwise had no impact on the π^+ and π^- channels.

Following this skim for each channel, cuts were imposed on each reconstructed particle to identify it based on kinematic properties for the reaction of interest. These cuts were performed (if required) sequentially to select a candidate electron, π^-, proton, π^+, π^0, and finally the neutron. Cuts were used to sufficiently decrease contamination of incorrectly identified particles, so it should be highlighted that these cuts not only remove particles poorly measured but also some that are measured well - so it is a process which requires optimisation. The cut values for the identification of each particle were used without adapting them to each channel and topology analysed, therefore an optimisation could be further investigated but no significant issues were observed upon using this approach.

For each topology, exactly one of each final state particle was required to be identified, e.g. an event with two identified electrons was ignored. This requirement was imposed for each particle as part of the PID in the analysis.

Electron

A good quality measurement of the scattered electron was required for all channels, with a measurement of its energy deposited in the EC being crucial in calculating the energy transferred to the target in the reaction. All negative particles were considered as the candidate electron, and events with only one "good" electron successfully passing the following cuts were kept for further analysis. The negatively charged particle which did not pass at least one of the cuts could then be considered as the π^- for the relevant channel.

There are parameters which are commonly cut on as part of electron PID in CLAS analyses, so these were studied to improve confidence in what can be considered "tight" cuts. It is crucial to ensure that a negatively charged pion is not misidentified as being an electron in events. Examination of the final event sample later showed that cuts on the **EC minimum energy** and the **minimum number of photoelectrons in the CC** reduced the signal sample by approximately 10% but did not improve the accuracy of the final result, so these cuts were not included in the final data analyses. The number of good signal events gained was significantly larger than those in which the electron particle was actually a negatively charged pion (i.e. contamination of signal). These two cuts will still be discussed as to help highlight the issue of contamination in particle measurements.

Identification of the candidate electron required information on the negatively charged particle in the DC, CC, TOF and EC.

The following cuts on the electron candidate helped establish that the "electron" was identified correctly from sources of contamination:

1. **Vertex position window**

   Tracking information of the detected electron candidate was used to calculate the event vertex z-position for each event, and was compared to the known nominal target position for each run in the experiment. The Kapton target cell located centrally in the target system was approximately 1.5 cm in length in the z-axis of CLAS. A somewhat loose constraint on this event vertex position at the target of $|z| \leq 4$ cm allows for detector resolution effects and therefore mainly removed poorly reconstructed events. Figure 3.2 illustrates the motivation for this cut. Figure 3.2a highlights numerous events with the event vertex position being significantly outwith the physical limit of the target cell. Figure 3.2c shows a 2D representation in which the azimuthal information at the vertex was used for the detected electron candidate. The effect of the vertex position window cut is shown in figures 3.2b and 3.2d.

   This cut was purely used to remove events from the data sample based on prior knowledge of the target location, and did not actually identify a specific particle.

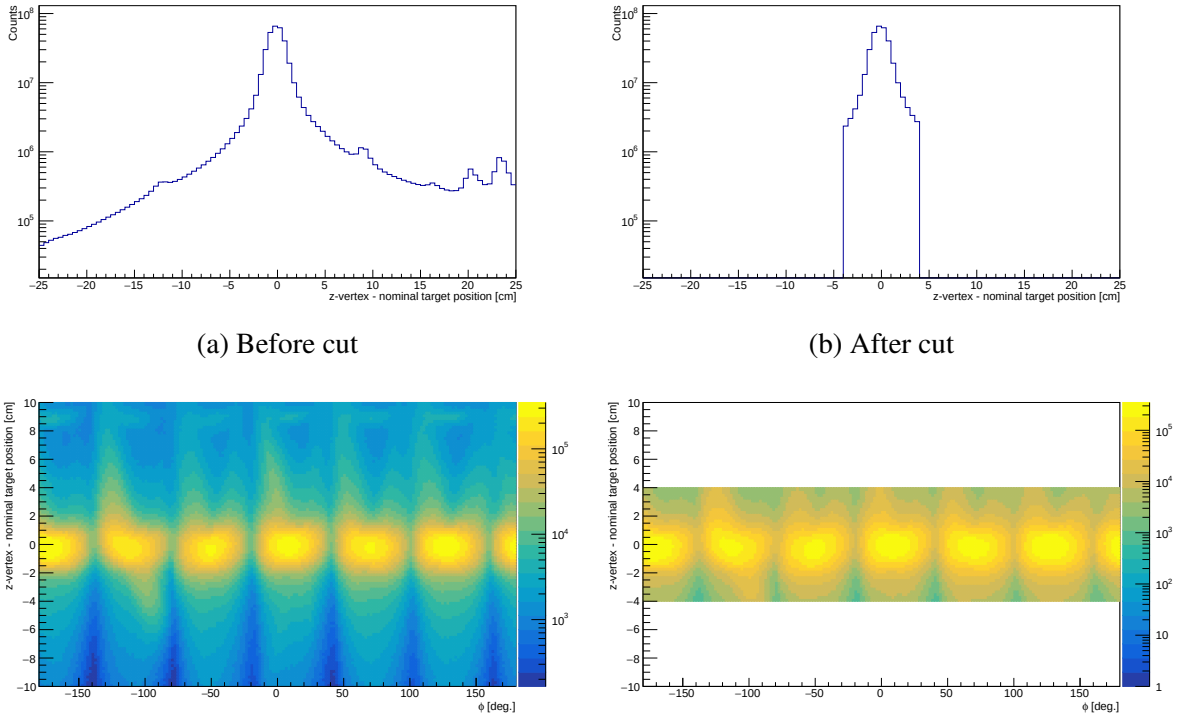

(a) Before cut

(b) After cut

(c) Before cut

(d) After cut

Figure 3.2: Calculated event z-vertex position using the detected electron candidate, before and after imposing the constraint of $|z| \leq 4$ cm. Top plots show 1D information, and bottom shows 2D plots using the ϕ angle at the vertex. Note, the top plots make use of a logarithmic scale in the y-axis.

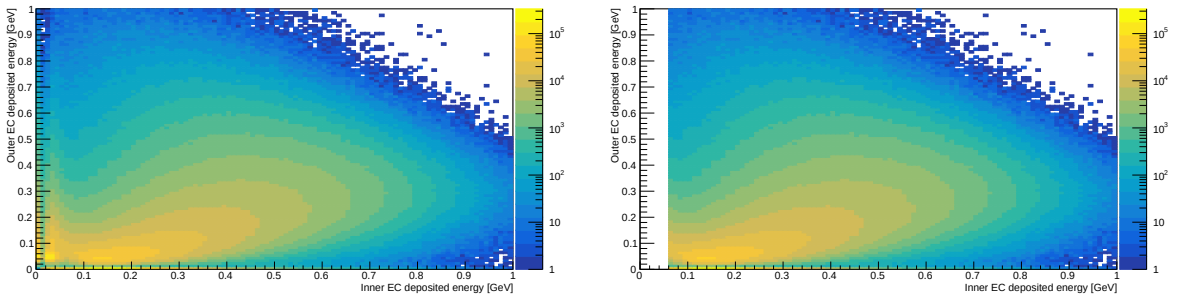

(a) Before cut

(b) After cut

Figure 3.3: 2D distribution of energy measured in the outer region of the EC against that in the inner region, before and after imposing a constraint of $EC_{inner} \geq 0.060$ GeV. The π^- contamination peak can be seen in (a) centred at $EC_{inner} = 0.030$ GeV and $EC_{outer} = 0.048$ GeV with smearing in the y-axis.

2. **EC minimum energy**

   π^- contamination could be removed by requiring a minimum deposited electron energy in the inner layers of the electromagnetic calorimeter. As previously described, the EC was a sampling calorimeter, with the first 15 cm of active scintillation material classed as the "inner" detector region, and the last 24 cm being the "outer". The minimum energy deposited in both the EC_{inner} and EC_{outer} active scintillation material was theoretically calculated based on the fact that charged pions are minimum ionising particles (MIPs) and therefore deposit a known energy of 2 MeV per cm of scintillation material in the EC. Based on the geometrical layer thickness properties of the EC, the MIP deposited energy values are $EC_{inner} = 0.030$ GeV and $EC_{outer} = 0.048$ GeV. Figure 3.3a clearly highlights the π^- contamination peak in the expected region (confirming successful prior detector energy calibrations), but of course smearing was observed due to the detector resolution. Taking the smearing into account, a cut of $EC_{inner} \geq 0.060$ GeV was deemed suitable and its inclusion is shown in figure 3.3b. No cut was placed on EC_{outer} due to the fact that there was a very large smearing of the π^- peak to values of $EC_{outer} > 0.048$ GeV (clearly observed for $EC_{inner} \approx 0.030$ GeV). This smearing was due to additional particles being knocked out from the EC's passive absorber lead sheets as the π^- traversed the detector subsystem. These additional particles were then detected in the EC's outer scintillation sheets *in addition* to the π^- total MIP deposited energy of 0.048 GeV. Therefore, it was more reliable to only cut on the EC_{inner} measurement.

3. **EC total energy**

   The next quantity considered was the ratio of the candidate electron's total energy measured in the EC to that of the momentum measured by the drift chambers. The most probable value was calibrated to be 0.3 for the EG1-DVCS dataset, when using the empirically-obtained negative offset of 0.12 to account for energy loss in the DC, CC, TOF, etc. Figure

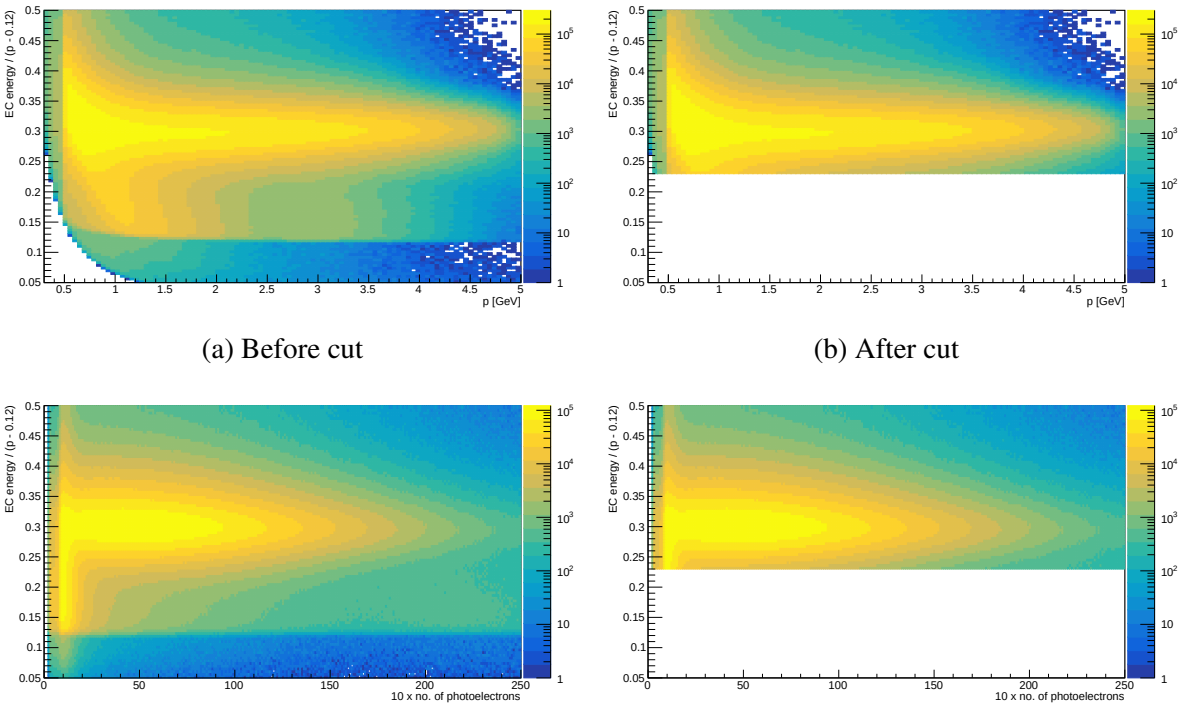

(a) Before cut

(b) After cut

(c) Before cut

(d) After cut

Figure 3.4: Candidate electron ratio of energy to momentum (with correction factor) was calibrated for the most probable value to be 0.3. This variable is plotted against momentum measured in the DC in the top plots, and the number of photoelectrons (multiplied by 10) measured in the CC in the bottom plots. These plots show the distributions before and after imposing the constraint of $E_{tot}/(p-0.12) \geq 0.23$.

3.4 shows this distribution in a intuitive way to highlight π^- contamination which does not sit well on the y-axis most probable value of 0.3. The contamination is most clear in figure 3.4c in which the x-axis shows the number of photoelectrons detected in the CC (multiplied by 10), with the clear peak at approximately 10 being π^- contamination. The contamination is also observed in figure 3.4a as the smeared signal that is most significant at low values of p with a y-axis value below 0.23. The CC distribution is discussed in the next electron PID cut. To improve the success of electron identification, a suitable cut was imposed as being $E_{tot}/(p-0.12) \geq 0.23$ and its effect can be seen in figures 3.4b and 3.4d.

4. **Minimum number of photoelectrons in the CC**

   The Cherenkov counters were quite a reliable subsystem for assisting in successful triggering and identification of electrons (and their separation from negatively charged pions).

   As indicated before, contamination of π^- could be seen in the candidate electron signal, and was particularly obvious when looking at measurements in the CC. An example of such a distribution of the number of photoelectrons measured in the CC is shown in figure

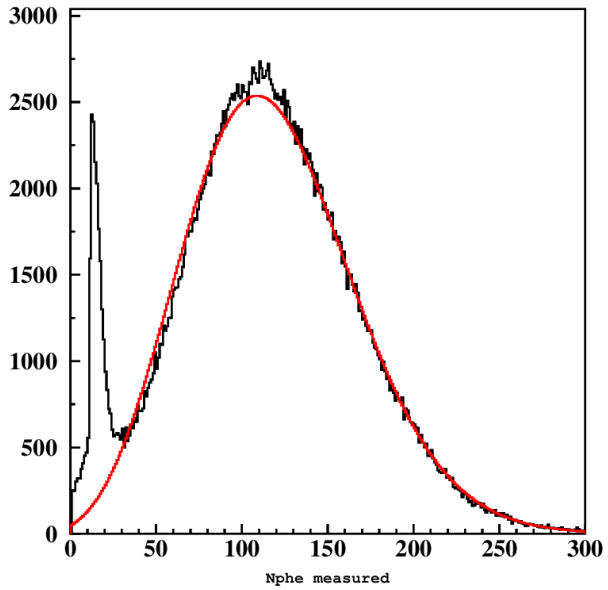

Figure 3.5: Example 1D histogram of the number of photoelectrons, "Nphe", measured in the CC (multiplied by 10), with number of counts in the y-axis. A parameterisation of the expected "true signal" is shown as a **red** curve overlaid on top of the distribution of data taken in the E6a experiment [81]. The "noise signal" at approximately 10 is a significant source of contamination in the good candidate electron events.

3.5. This figure was taken from a published CLAS report focusing on the contamination of the "noise signal" with a parameterisation of the expected electron's "true signal" shown as the **red** curve, therefore the distribution consists of two separate components. The fixed position of the noise signal peak at approximately 10 corresponds to internal noise above the set threshold for the CC. Events contributing to this peak were attributed to when a π^- track detected in the drift chambers was in coincidence with a CC internal noise signal. Both the noise signal and the expected true signal take the form of Poisson distributions. The momentum threshold for a pion to create its own true signal in the CC is 2.5 GeV. The vast majority of pions had a momentum less than this, but also contributed to contamination in the electron identification.

Figure 3.6 shows example distributions for channels analysed in this thesis. The 1D distribution in figure 3.6a highlights the level of contamination after imposing the cuts described thus far, and can be seen to be somewhat low. The 2D distribution in figure 3.6c is also useful in illustrating the contamination. An initial cut on this variable was imposed as $nphe\ (\times 10) \geq 20$, and appears to remove significant levels of signal as well as contamination with its effect seen in figures 3.6b and 3.6d. As previously stated, this cut was removed for the final analyses, but illustration of this contamination at this stage in the PID is important.

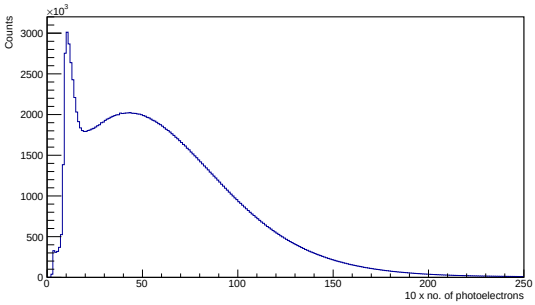

(a) Before cut

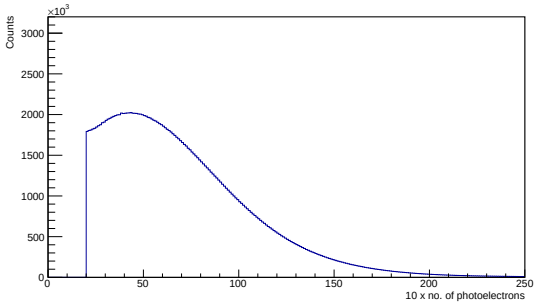

(b) After cut

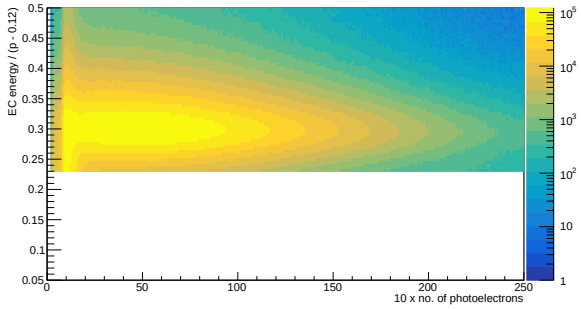

(c) Before cut

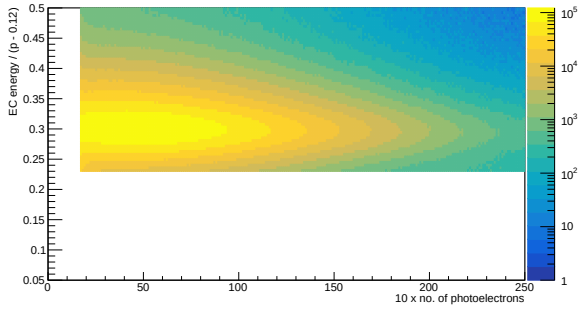

(d) After cut

Figure 3.6: Number of photoelectrons measured by the CC (multiplied by 10) for candidate electrons, with a "noise signal" peak observed at approximately 10. The bottoms plots show a 2D distribution which also includes total EC energy and momentum information. An initial cut was imposed as being $nphe\ (\times 10) \geq 20$, but later removed for final analyses.

5. **Measured time difference between CC and TOF**

   Timing information of candidate electrons was used to further remove pion contamination.

   The mass of an electron is negligible compared to that of a π^-, and therefore it was suitable to check that the velocity of the detected particle was sufficiently high when traversing the CLAS detector subsystems. Pions travelled slower than electrons of the same momentum due to their larger mass, and this was observed in timing measurements. The particle's timing measurement by the TOF subsystem was the most reliable measurement and therefore it was crucial to use this information in the calculation. It was most suitable to compare this time value with that made by the CC as opposed to the EC, since the CC was located at a larger radial distance from the TOF (approximately 1 m). This larger distance meant that pion contamination was more easily highlighted, even when detector resolutions were taken into account.

   The hit time in the TOF was subtracted from that in the CC such that

$$\Delta t = \left(t_{CC} - \frac{r_{CC}}{c}\right) - \left(t_{TOF} - \frac{r_{TOF}}{c}\right)$$

   where r is the distance from the target to the hit position in the detector subsystem, t is the measured time, and c is the speed of light. Figure 3.7 shows the effect of including a somewhat loose constraint on this timing measurement, specifically $|\Delta t| \leq 4$ ns. To highlight pion contamination, the data shown does not include the *minimum number of photoelectrons in the CC* cut.

   It is clear that this cut also removed events that were poorly reconstructed.

π^-

This section is only relevant for the π^- electroproduction reaction channel - both exclusive and semi-inclusive topologies.

After the successful PID of one good candidate electron, the other negative particle (which failed at least one of the electron PID cuts) could then be considered as the candidate π^-. The cuts imposed on these negatively charged particles were much less stringent than those of the electron. Identification of the candidate π^- required information of the negatively charged particle in the DC and TOF, as these provide adequate information to remove poorly reconstructed pions and minimise contamination. Due to the lower energy (and therefore momentum) of charged pions in the reactions of interest, the trajectories were bent much more than those of electrons and therefore the CC and EC were not used to identify pions to maximise the acceptance. Note, data has not been separated for the magnet settings producing inbending and outbending magnetic fields for charged particles. Unlike the electron in each event, a highly precise measurement of the pion's energy is not as crucial, and the pion's energy can be inferred from its momentum which is measured sufficiently well.

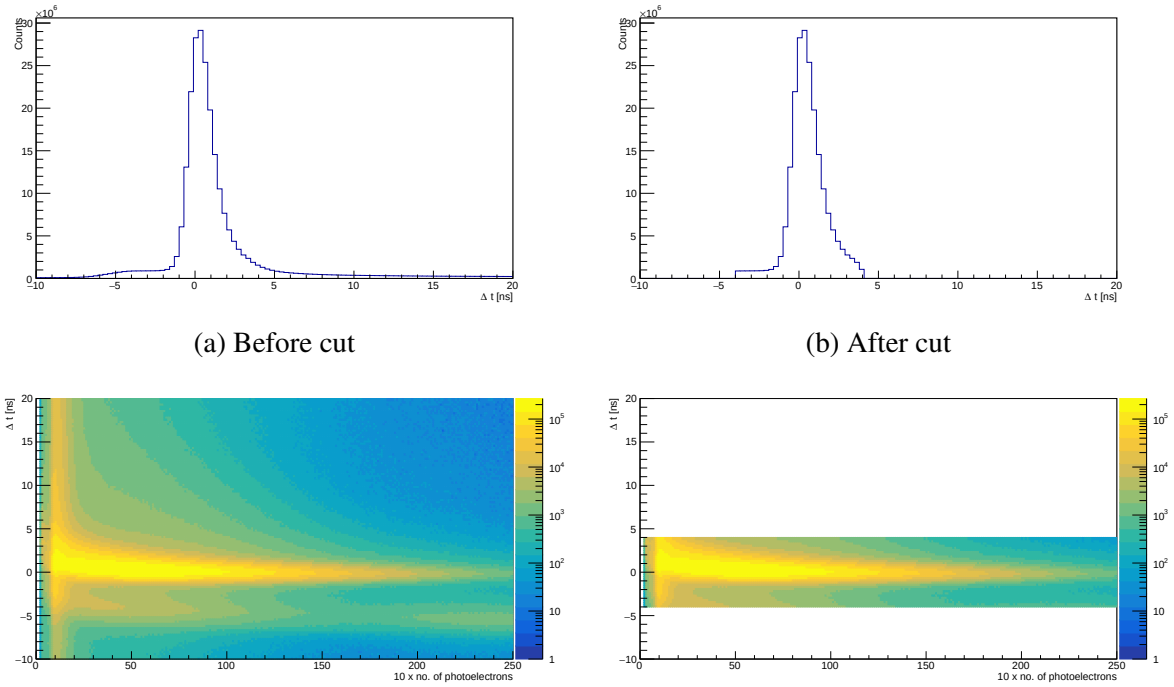

(a) Before cut

(b) After cut

(c) Before cut

(d) After cut

Figure 3.7: Measured time difference between CC and TOF for candidate electrons. The 2D plot also includes the number of photoelectrons (multiplied by 10) measured by the CC to highlight pion contamination. These plots show the distributions before and after imposing the constraint of $|\Delta t| \leq 4$ ns. The data in these plots does not include the *minimum number of photoelectrons in the CC* cut to highlight the contamination.

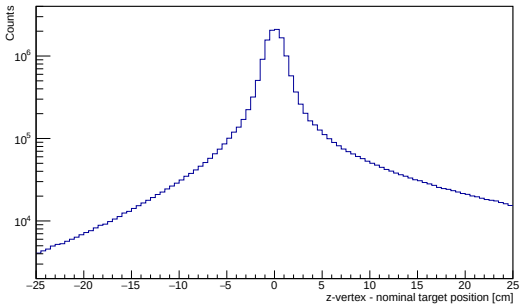

(a) Before cut

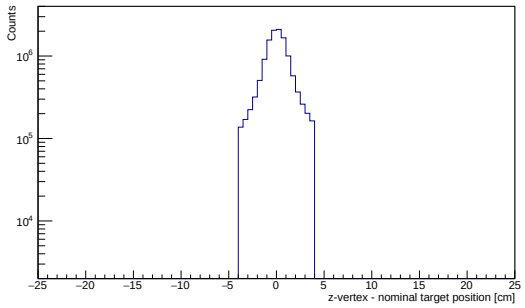

(b) After cut

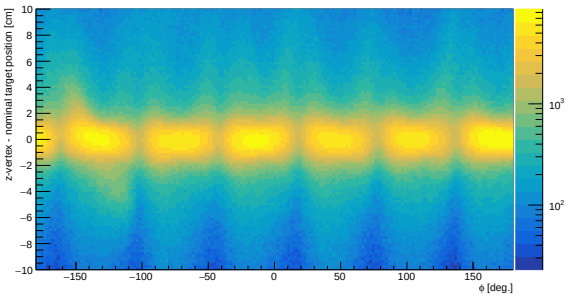

(c) Before cut

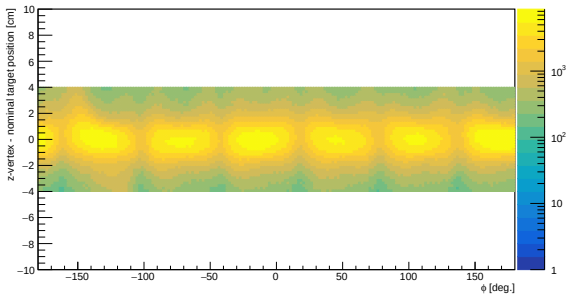

(d) After cut

Figure 3.8: Calculated event z-vertex position using the detected π^- candidate, before and after imposing the constraint of $|z| \leq 4$ cm. Top plots show 1D information, and bottom shows 2D plots using the ϕ angle at the vertex. Note, the top plots make use of a logarithmic scale in the y-axis.

The following two cuts on the π^- candidate helped establish that the pion was very likely to have been identified correctly:

1. **Vertex position window**

   Just like the electron PID cut, the same method was used for the π^- candidate using its tracking information. Similarly, the constraint on this event vertex position at the target was $|z| \leq 4$ cm.

   Figure 3.8 illustrates the use of this cut, with figure 3.8a showing the one clear peak observed, and 2D representation making use of the azimuthal angle in figure 3.8c.

2. **Momentum dependent β cut**

   A momentum dependent β cut was used to identify the particle as being a π^- in the event.

   The velocity relative to the speed of light is $\beta = v/c$, with c expressed as a natural unit with value of 1. Therefore, the TOF hit position (r_{TOF}) and time (t_{TOF}) measurements could be used such that $\beta = r_{TOF}/t_{TOF}$, where the distance travelled ("path length") is relative to the event vertex and the time relative to the event start time. The path length also takes into account the curved trajectory of the pion in the magnetic field. This measurement of β was then compared with the value obtained from the energy-momentum relation when

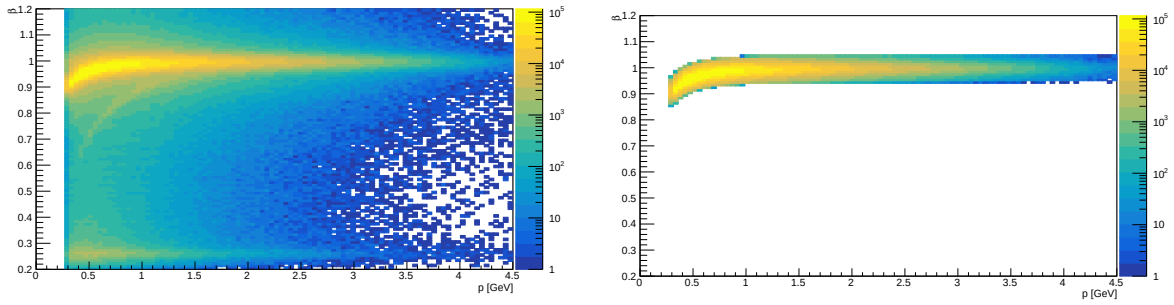

(a) Before cut

Figure 3.9: π^- momentum dependent β cut. One can see other negative particles which are excluded from this π^- identification.

making the assumption that the particle identified is the π^- with mass of 139.571 MeV as provided by the Particle Data Group (PDG) [82]. This makes use of the fact that $E = p/\beta$ in the energy-momentum relation of $E^2 = (pc)^2 + (m_0 c^2)^2$ where m_0 is the rest mass of the particle, and is therefore expressed as

$$\beta = \sqrt{\frac{p^2}{(m_{\pi^-})^2 + p^2}}$$

The difference in the β measurements described ($\Delta\beta$) was plotted as a function of momentum, then the distribution was binned (*sliced*) in momentum with a Gaussian fit around the most probable value expected at $\Delta\beta = 0.0$ defining an appropriate cut range for the data. Figure 3.9 shows the effect of this momentum dependent β cut on the β vs p distribution. Figure 3.9a highlights the main source of contamination of negatively charged kaons (underneath the pion signal curve) being successfully removed until approximately 1.5 GeV where there would be some misidentified pions in this PID.

Proton

This section is only relevant for the exclusive topology of the π^0 and π^- electroproduction reaction channels.

Like the π^- PID, cuts were applied to both the vertex position window and the momentum dependent β distribution to identify a good proton candidate for the event. The same vertex position window constraint of $|z| \leq 4cm$ was imposed, and again the momentum dependent β cut was determined for each bin in momentum with this cut using an assumed proton PDG mass of 938.272 MeV.

The effect of the momentum dependent β cut for the proton is shown in figure 3.10. Figure 3.10a highlights the main sources of contamination of positively charged kaons and pions (both above the proton signal curve) being successfully removed until approximately 2.0 GeV where

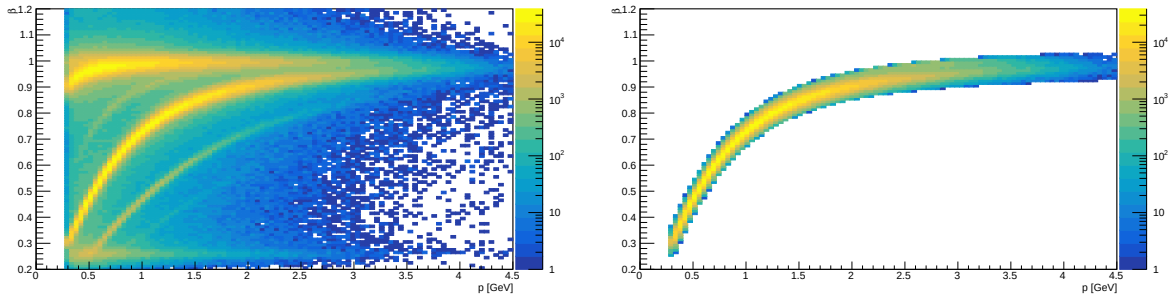

(a) Before cut (b) Before cut

Figure 3.10: Proton momentum dependent β cut. One can see other positive particles which are excluded from this proton identification.

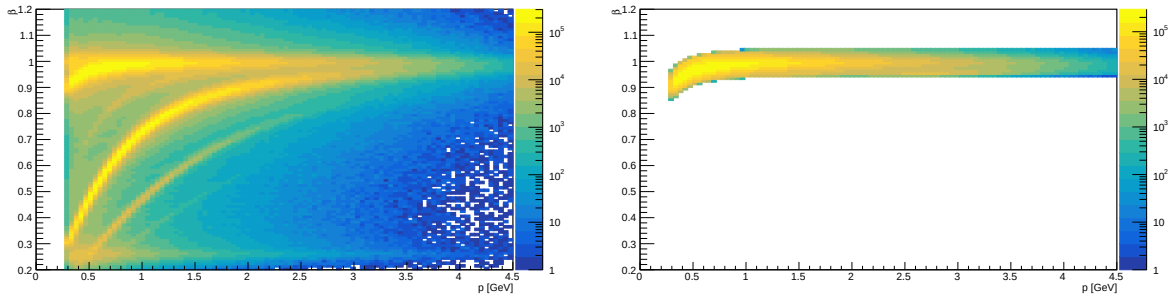

(a) Before cut (b) Before cut

Figure 3.11: π^+ momentum dependent β cut. One can see other positive particles which are excluded from this π^+ identification.

there would gradually be more misidentified protons in this stage of PID. Below the proton signal curve, the observed signal peaks correspond to deuterons and tritons.

π^+

This section is only relevant for the π^+ electroproduction reaction channel - both exclusive and semi-inclusive topologies.

Like the π^- and proton PID, the same vertex position window cut value was used, and the momentum dependent β cut instead assumed the positively charged pion PDG mass of 139.571 MeV. The effect of the momentum dependent β cut for the π^+ is shown in figure 3.11. Figure 3.11a highlights the main source of low momentum contamination being positively charged kaons which were successfully removed until approximately 1.0 GeV. As implied in the proton PID, the main source of high momentum contamination can be seen as being protons from approximately 2.0 GeV.

π^0

This section is only relevant for the π^0 electroproduction reaction channel - both exclusive and semi-inclusive topologies.

Neutral charged particles detected were tested as to whether they could successfully be identified as photons and reconstructed to form a neutral pion, as the main decay of $\pi^0 \rightarrow \gamma\gamma$ occurs very quickly after production in the reactions.

The EC was suitable in providing good measurements of neutrals, with the addition of the IC specifically to detect low θ photons. As previously described, the coverage of the IC was $4^\circ < \theta < 16^\circ$, with the EC extending this polar angle coverage up to 45°.

As they are not charged, neutral particles produce no tracks in the drift chambers and produce no Cherenkov radiation so are also undetected by the CC. Detection in the TOF is possible, but the efficiency is incredibly low so was not used in the PID.

In summary, detected photons could only be measured with confidence in the EC and IC, therefore there were 3 topologies in which the neutral pion's two decay photons could be detected in each event:

- Both photons in the EC ("EC-EC")
- One photon in the IC and one in the EC ("IC-EC")
- Both photons in the IC ("IC-IC")

Firstly, the PID of candidate photons detected in the EC was carried out using two cuts:

1. **β of neutrals**
   Photons travel at the speed of light, and therefore the measured velocity of neutral particles was a good indication of them being candidate photons in the event. This was calculated using $\beta = r_{EC}/t_{EC}$ taking into account the event vertex position (using information from the electron's measurements). Figure 3.12a shows the β distribution obtained, with a clear peak centred at 1 as expected with a Gaussian shape due to detector resolution effects. A Gaussian fit to this peak determines that the lower 3σ limit is at approximately 0.92. A rather low cut of $\beta > 0.8$ was imposed, shown in figure 3.12b, and corresponds to removing neutrons with momentum less than 1.25 GeV.

2. **Minimum energy**
   A cut was imposed on the minimum total energy measured in the EC which was used to improve the signal to background ratio of the neutral pions reconstructed from detected photons. The events with total measured EC energy less than 200 MeV were not particularly useful when investigating the reconstructed neutral pion, so a cut was set on the total energy as $E > 200$ MeV, with the total energy distribution shown before and after the cut in figure 3.13.

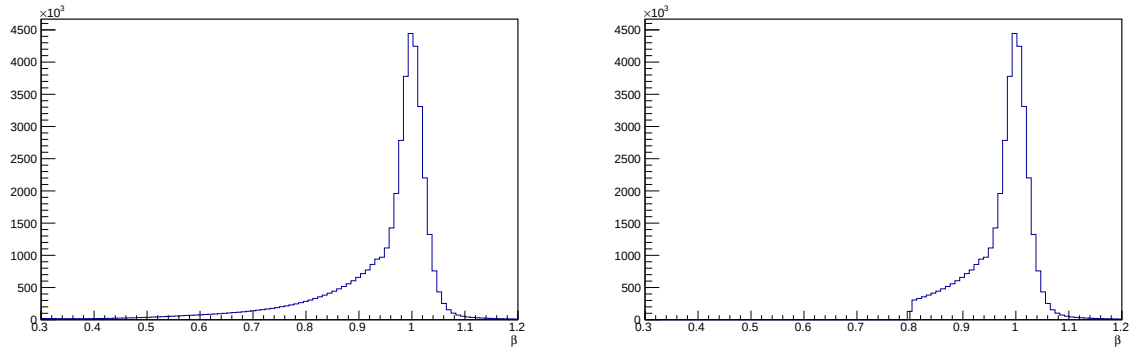

(a) Before cut (b) After cut

Figure 3.12: β for neutrals detected in the EC, with a low cut of $\beta > 0.8$ to remove neutrons from the candidate photons sample.

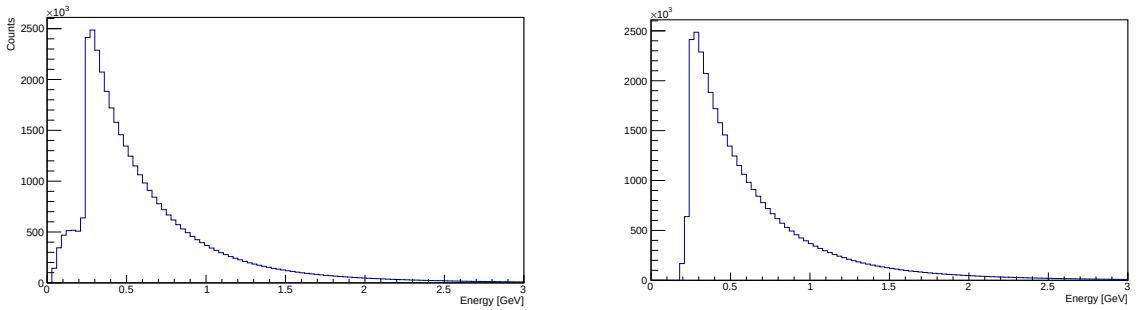

(a) Before cut (b) After cut

Figure 3.13: Total energy measured in the EC for neutrals, with a cut of $E > 200$ MeV.

The energy deposited by neutrons in the EC is not reliable so the contamination removed in this cut cannot easily be assessed.

Secondly, the PID of candidate photons detected in the IC was carried out using two cuts:

1. **Time of hit**

   A useful value to consider was the time of the particle "hit" in the IC for the photon candidate, with respect to the event start time (calculated using the electron). The short distance of 68.3 cm from the target to the IC was sufficient enough to assess this value for each particle detected in the IC, allowing to easily remove a lot of contamination. Photons (travelling at the speed of light) are shown with a time centred at zero in figure 3.14, and a suitable cut of $|t| < 2$ ns removes significant contamination and accidental photons that were not produced in the reaction being examined.

   The IC was a calorimeter therefore picked up any particles which interacted causing enough scintillation light to be read out for each crystal, and was of course particularly sensitive to charged particles, not just photons.

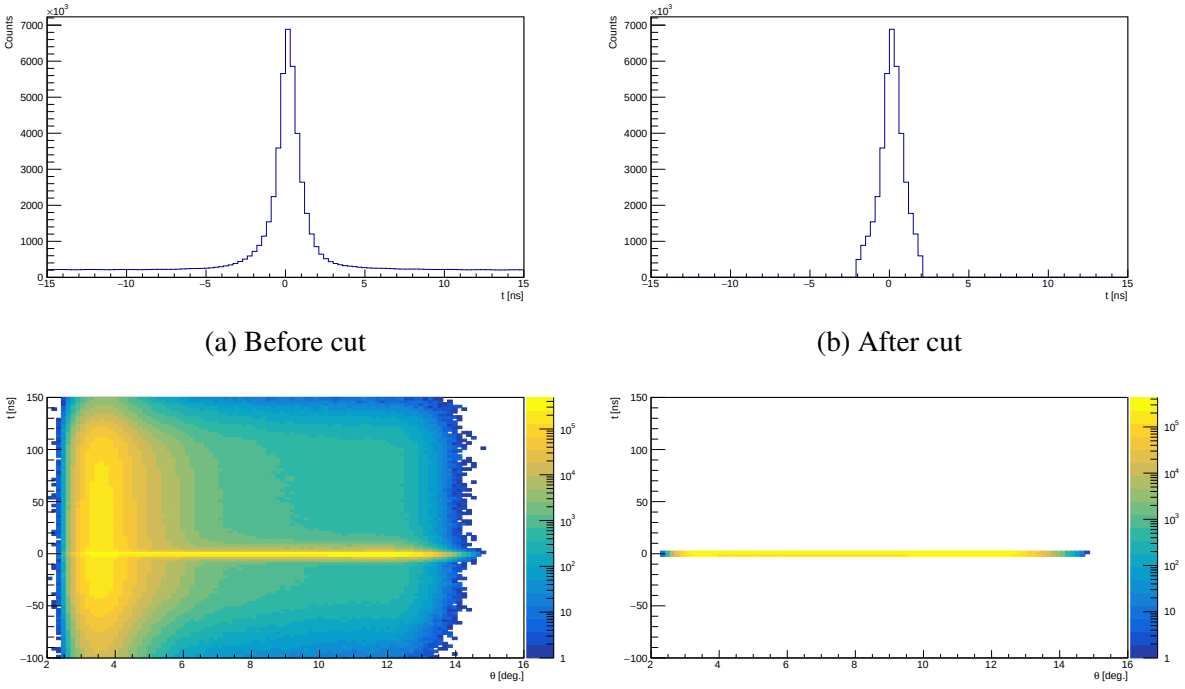

(a) Before cut

(b) After cut

(c) Before cut

(d) After cut

Figure 3.14: Calculated time of IC hit relative to the event start time for candidate photons, before and after imposing the constraint of $|t| < 2$ ns. Top plots show 1D information, and bottom shows 2D plots using the θ angle.

Figure 3.14c clearly shows low θ contamination corresponding to Møller electrons, with the majority removed in the time of hit cut.

2. **Energy of low θ particles**
   The previous cut removes the majority of the low θ Møller electron contamination, with energy and angular information allowing for a further reduction. Figure 3.15 clearly illustrates the contamination, and shows a suitable cut imposed on the distribution using information of energy deposited and the polar angle of the hit in the IC.

Finally, the energy-momentum four-vectors of all candidate photons passing the described cuts were then reconstructed to form the candidate π^0. Making use of the measured energy, and using the fact that $p_\gamma = E_\gamma$ for photons (since they are massless), each photon four-vector (P_γ) was constructed such that

$$P_\gamma = (c_x^\gamma.E_\gamma,\ c_y^\gamma.E_\gamma,\ c_z^\gamma.E_\gamma,\ E_\gamma)$$

where c_x^γ, c_y^γ and c_z^γ are the x, y and z direction cosines calculated from the hit position in the EC or IC in relation to the event vertex. The π^0 was formed by simply adding the four-vectors of two photons, i.e. $P_{\pi^0} = P_{\gamma_1} + P_{\gamma_2}$. The π^0 was reconstructed for all combinations of two candidate photons detected in the event, allowed by the fact that the only constraint on detected neutrals in CLAS was that there was a minimum number detected. It was found that there were events with

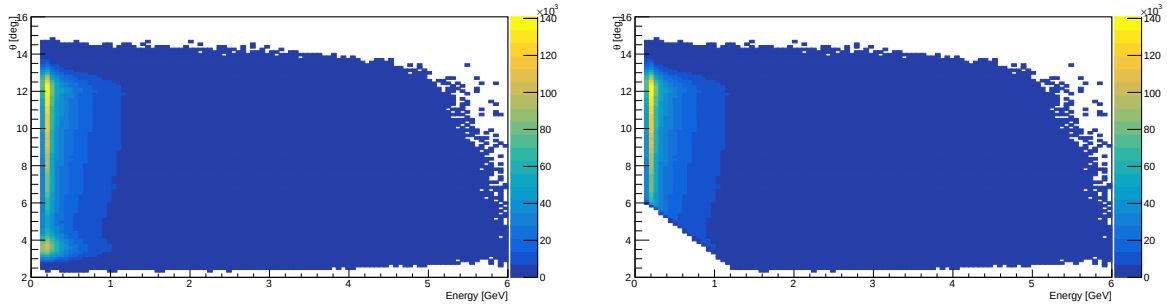

(a) Before cut

(b) After cut

Figure 3.15: θ vs energy for IC candidate photons, with contamination of low energy Møller electrons observed at low θ in the sample. A suitable cut on this distribution reduces this background. Note, these 2D plots do not use a logarithmic scale in the z-axis.

more than one candidate π^0 reconstructed.

Figure 3.16 shows the distributions of the invariant mass of the candidate π^0 particles in each event for all three reconstruction topologies of the decay candidate photons. Figures 3.16a, 3.16d and 3.16g show the level of background contamination for each topology before any cuts have been applied. It is also clear that the resolution of the IC detector was also significantly better than that of the EC, as indicated by the narrower width of the invariant mass signal peak. Firstly, a cut was performed to isolate a suitable sample of events where the invariant mass was close to that of the PDG mass of 134.977 MeV, with the effect of this cut shown in figures 3.16b, 3.16e and 3.16h. Secondly, events were only kept in the data sample in which there was one π^0 detected within the "good" invariant mass region for only one of the possible topologies, with the effect of this cut shown in figures 3.16c, 3.16f and 3.16i. As indicated by the counts for each topology in figures 3.16c, 3.16f and 3.16i, the number of events in which the pion was reconstructed for the IC-IC topology was significantly larger than that of the EC-EC or IC-EC topologies.

Neutron

This section is only relevant for the exclusive topology of the π^+ electroproduction reaction channel.

The most reliable information to use for the identification of candidate neutrons was the timing information recorded by the EC, and therefore the identification of neutrons relied on only one cut:

1. **β of neutrals**

   The velocity of neutrals was a good indication of them being neutrons (as opposed to photons).

   Similar to the β cut on neutrals detected in the EC being considered as photons, this velocity is a good indication of candidate neutrons when using a suitable cut value. Figure

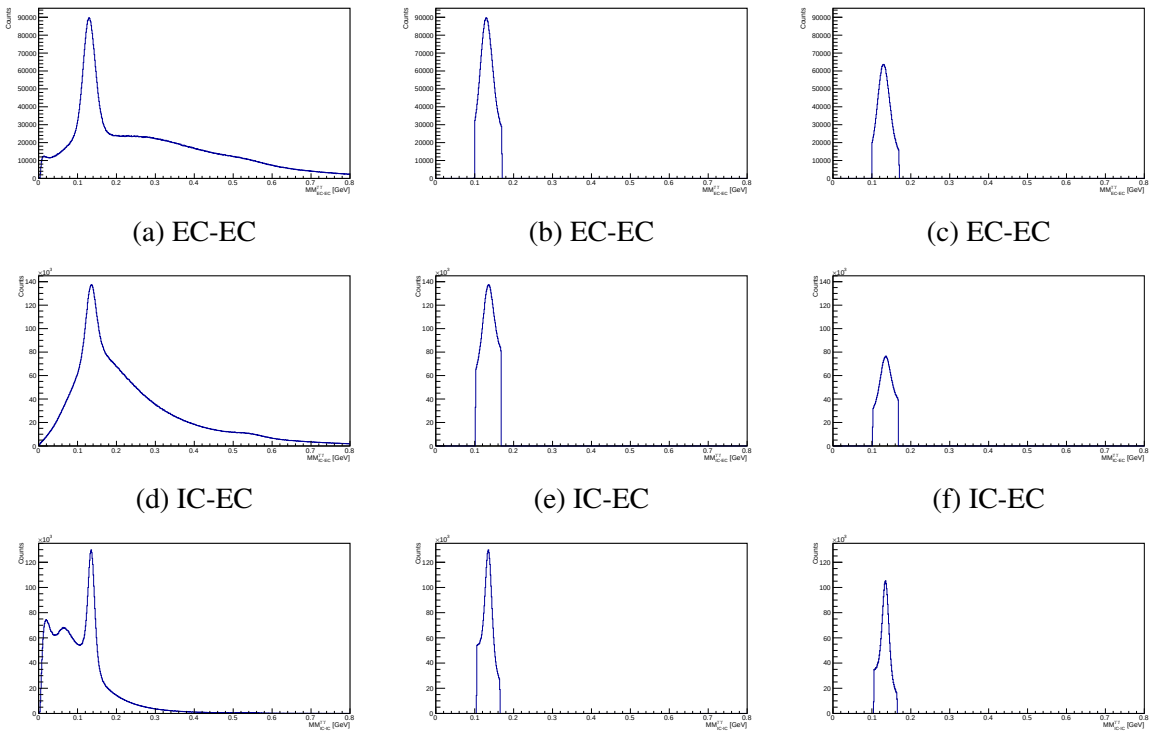

(a) EC-EC (b) EC-EC (c) EC-EC

(d) IC-EC (e) IC-EC (f) IC-EC

(g) IC-IC (h) IC-IC (i) IC-IC

Figure 3.16: Invariant mass distributions of the reconstructed π^0 from candidate photons for the three detected decay photon topologies of EC-EC (top), IC-EC (middle) and IC-IC (bottom). Left plots show all reconstructed candidate neutral pions using all combinations of candidate photons in the event, centre plots show the mass cut imposed on this distribution, and right plots show the events in which there is only one π^0 reconstructed and it falls within a specified mass range.

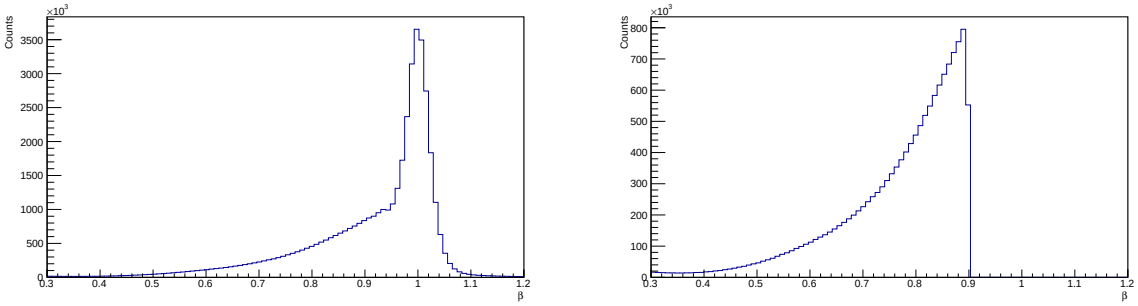

(a) Before cut (b) After cut

Figure 3.17: β for neutrals measured in the EC with a high cut of $\beta < 0.9$ to remove photons from the candidate neutron sample.

3.17 shows the distribution before and after a high cut of $\beta < 0.9$ was imposed, corresponding to the inclusion neutrons of momentum less than 1.94 GeV. The high cut was set to include as much neutron signal as possible, with a Gaussian fit to the photon peak having a lower 3σ limit at approximately 0.92.

Events in which only one candidate neutron met this cut were kept for analysis - this corresponded to a reduction in the statistics of figure 3.17b by 22% without a significant change in the shape of the β distribution.

3.2.5 Exclusivity Variables

Having successfully identified only one of each candidate particle required for each reaction channel analysed, it was then possible to reconstruct "exclusivity variables" for the event. This made use of each of the particle's energy-momentum four-vectors, and applied energy and momentum conservation to identify the reaction. These variables helped to exclusively identify the signal and background distributions in each data sample.

Firstly, the energy-momentum four-vectors were constructed, which made use of measured variables in the experimental setup. Momentum measurements of charged particles made with CLAS were of use for the scattered electron (e), charged pions (π^- and π^+) and proton (p). The neutral pion's four-vector was explicitly described in the π^0 PID section as the addition of two candidate decay photon four-vectors. For the case of the neutron (n), its momentum, p_n, was calculated using velocity and PDG mass as follows:

$$p_n = \frac{\beta_n M_n}{\sqrt{1-\beta_n^2}}$$

The energy-momentum four-vectors constructed to describe all reaction channels analysed were as follows:

$$
\begin{aligned}
P_{beam} &= (0,\ 0,\ E_{beam},\ E_{beam}), && \text{(electron beam)};\\
P_{p\ target} &= (0,\ 0,\ 0,\ M_p), && \text{(proton target)};\\
P_{n\ target} &= (0,\ 0,\ 0,\ M_n), && \text{(neutron target)};\\
P_{d\ target} &= (0,\ 0,\ 0,\ M_d), && \text{(deuteron target)};\\
P_e &= (c_x^e.p_e,\ c_y^e.p_e,\ c_z^e.p_e,\ p_e), && \text{(scattered electron)};\\
P_{\pi^-} &= \left((c_x^{\pi^-}.p_{\pi^-}),\ (c_y^{\pi^-}.p_{\pi^-}),\ (c_z^{\pi^-}.p_{\pi^-}),\ \sqrt{p_{\pi^-}^2+M_{\pi^-}^2}\ \right), && \text{(produced } \pi^-);\\
P_p &= \left(\ c_x^p.p_p,\ c_y^p.p_p,\ c_z^p.p_p,\ \sqrt{p_p^2+M_p^2}\ \right), && \text{(produced proton)};\\
P_{\pi^+} &= \left((c_x^{\pi^+}.p_{\pi^+}),\ (c_y^{\pi^+}.p_{\pi^+}),\ (c_z^{\pi^+}.p_{\pi^+}),\ \sqrt{p_{\pi^+}^2+M_{\pi^+}^2}\ \right), && \text{(produced } \pi^+);\\
P_{\pi^0} &= P_{\gamma_1}+P_{\gamma_2}\ , && \text{(produced } \pi^0);\\
P_n &= \left(\ c_x^n.p_n,\ c_y^n.p_n,\ c_z^n.p_n, \sqrt{p_n^2+M_n^2}\right), && \text{(produced neutron)};
\end{aligned}
\tag{3.2}
$$

where the energy (E_i), PDG mass (M_i) and momentum (p_i) related to the detected particle i. The direction cosines calculated for each event vertex are represented as c_j^i for the j direction (x, y and z-axis). The nominal electron beam position was always set as $(x, y) = (0, 0)$, however, the beam rastering was taken into account when calculating the direction cosines of all scattering particles. All target particles were assumed to be stationary (i.e. no momentum), and therefore the x, y and z momentum components were zero. For use in the π^- electroproduction analysis, the neutron target four-vector stated was a simplified model as there are no possible free neutron targets. The "neutron target" used in the EG1-DVCS experiment was the deuteron in ND_3, in which a neutron was bound with a proton and therefore both nucleons had some "Fermi motion" which should be taken into account. To do so, a four-vector was also included for the deuteron target definition which contained this information. Note, of course use of the deuteron allowed access to reactions with the bound protons - the results of which could be compared to the free proton measurements made using the NH_3 target.

Four-vectors could also then be used to provide a kinematic reconstructed description of the reactions. The virtual photon was described in the same way for all reactions:

$$
P_{\gamma^*} = P_{beam} - P_e \qquad \text{(virtual photon)}; \tag{3.3}
$$

For the analyses performed, the following four-vectors were utilised (when possible, and relevant to the exclusive or semi-inclusive topologies):

1. π^0

$$\begin{aligned} P_X^{e\pi^0} &= P_{beam} + P_{p\ target} - (P_e + P_{\pi^0}) && \text{(reconstructed proton)}; \\ P_X^{ep} &= P_{beam} + P_{p\ target} - (P_e + P_p) && \text{(reconstructed } \pi^0\text{)}; \\ P_X^{ep\pi^0} &= P_{beam} + P_{d\ target} - (P_e + P_p + P_{\pi^0}) && \text{(reconstructed spectator neutron)}; \end{aligned} \tag{3.4}$$

2. π^+

$$\begin{aligned} P_X^{e\pi^+} &= P_{beam} + P_{p\ target} - (P_e + P_{\pi^+}) && \text{(reconstructed neutron)}; \\ P_X^{en} &= P_{beam} + P_{p\ target} - (P_e + P_n) && \text{(reconstructed } \pi^+\text{)}; \\ P_X^{en\pi^+} &= P_{beam} + P_{d\ target} - (P_e + P_n + P_{\pi^+}) && \text{(reconstructed spectator neutron)}; \end{aligned} \tag{3.5}$$

3. π^-

$$\begin{aligned} P_X^{e\pi^-} &= P_{beam} + P_{n\ target} - (P_e + P_{\pi^-}) && \text{(reconstructed proton)}; \\ P_X^{ep} &= P_{beam} + P_{n\ target} - (P_e + P_p) && \text{(reconstructed } \pi^-\text{)}; \\ P_X^{ep\pi^-} &= P_{beam} + P_{d\ target} - (P_e + P_p + P_{\pi^-}) && \text{(reconstructed spectator proton)}; \end{aligned} \tag{3.6}$$

where the initial state information was implicit, and notation of P_X^{ABC} for the final state particles (ABC) used were explicitly stated in the superscript. For events later deemed as signal, the reconstructed particle is stated in the parentheses. For example, the "reconstructed proton" $\left(P_X^{e\pi^0}\right)$ shown in 3.4 makes use of the four-vectors of the final state scattered electron and produced π^0.

These four-vectors of reconstructed particles then allowed their properties to be examined and used, such as energy, momentum and direction cosines. For both the exclusive and semi-inclusive topologies, if not all final state particles produced in the reaction are used in the construction of the four-vector, then it essentially describes what can be considered as the "missing" particle for that reaction. For example, the "reconstructed neutron" $\left(P_X^{e\pi^+}\right)$ shown in 3.5 is "missing" in the reaction for the four-vector constructed for both exclusive and semi-inclusive topologies, as it only made use of the final state scattered electron and produced π^+. The invariant mass distribution of the missing particle was of particular interest in assessing the signal data, and was calculated as $MM = \sqrt{E^2 - |\vec{p}|^2}$ using the energy and momentum information. The missing mass labelling convention can be made clear when considering the reconstructed proton in 3.4 such that $MM_X^{e\pi^0}$ is referred to as the pion missing mass as it makes use of the final state pion, with the scattered electron's detection implicit due to its requirement for all channels. Similarly for the reconstructed pion for this channel, MM_X^{ep} is referred to as the proton missing

mass. It was best to deal with the nucleon (proton or neutron) missing mass in its squared form due to the peak of interest (at the pion's PDG mass) being so close to zero, and therefore is labelled as $(MM_X^{ep})^2$. For the exclusive topologies of the π^0 and π^- channels, a comparison was made on the proton and pion *cone angles*. The cone angle is defined as the angle between two three-vectors. Therefore, the proton cone angle is the angle between the momentum three-vector of the detected final state proton (p_d) and the momentum three-vector of the reconstructed final state proton (p_r) calculated with reference to the origin $\mathbf{0}$:

$$\angle\, \vec{p}_d\, \mathbf{0}\, \vec{p}_r = \arccos\left(\frac{\vec{p}_d \cdot \vec{p}_r}{|\vec{p}_d||\vec{p}_r|}\right)$$

Similarly, this relation also holds true for calculation of the pion cone angle.

Having described the exclusive variables for the analyses, their test on simulated data will be presented first.

3.2.6 Simulations

Due to issues with running EG1-DVCS simulations at the time of thesis writing, only data from previous simulations were available for analysis. Simulated data only existed for π^0 electroproduction, and in particular focussed on the Deeply Virtual Meson Production kinematical region.

These simulations were used in showing the expected kinematic distributions of the particles in the reaction with realistic detector acceptance and efficiencies taken into account, aiding the PID stages of event selection. The reliable simulations described the signal shape of missing mass distributions which were crucial for the final stages of signal event selection.

Generating Simulated Data

GSIM is the CLAS geometry and tracking simulation framework, effectively utilising the Geant simulation platform developed by the European Organisation for Nuclear Research (CERN) [83]. Monte Carlo methods are employed in Geant, providing the necessary random sampling techniques to successfully model the scattering reactions relevant to the interests of JLab.

The generation of simulated data required key parameters to be set according to the experimental run conditions, such as:

- Beam particle, and its energy-momentum four-vector
- Target material and cell type
- Position of the polarised target system's superconducting magnet
- Torus magnetic field map and current
- Inclusion of relevant detector subsystems, such as the inner calorimeter

In particular, the scattering reaction and kinematic region of interest were set as being $ep \rightarrow ep\pi^0$ in the deep inelastic scattering regime.

GSIM then generated millions of events based upon the set criteria, and the GSIM post-processor (gpp) was used to introduce realistic Gaussian smearing to the data based on the individual response of the detector subsystems. Unique issues and inefficiencies observed in the real data were also introduced into the simulated data with gpp to closely match the performance. Similar to real data, the Monte Carlo simulated data was cooked to obtain useful information (hit time and position, etc.) for physics analyses to be performed.

Simulated Data Signal

Simulated data was studied for part B of the EG1-DVCS experimental run. These simulations used an NH_3 target, so were greatly beneficial in understanding the anticipated signal distribution of the real experimental target data (NH_3 and ND_3). Preconfigured files were used for the generation of background electrons. This section focuses on the fully exclusive reaction of $ep \rightarrow ep\pi^0$.

The same particle identification event selection processing of real data (detailed in section 3.2.4) was also applied to simulated data. The simulated data clearly illustrates the signal with realistic experimental and detector effects taken into account, with no other sources of background contamination. Figures 3.18a and 3.18b show the missing mass distributions obtained after successful PID of the final state particles, with their correlation shown in figure 3.18c.

The pion missing mass and proton missing mass squared distributions take the form of a convolution of shapes. It was found that these can be approximately described by a Voigtian (convolution of Breit-Wigner and Gaussian). Due to the asymmetrical distributions, a more appropriate convolution would be of Breit-Wigner and bifurcated Gaussian (a Gaussian with different widths on left and right side), however, this shape was not available in the *RooFit* package [84] which would later be used in the final event selection process. Studies found that using a bifurcated Gaussian shape was the most suitable for the sPlot fit (defined later) when no simulated data was available, with a further discussion on this to follow. This conclusion was only reached by analysing this simulated data, and will be examined as part of the consideration of systematic uncertainties.

It was best to deal with the proton missing mass in its squared form due to the expected signal peak position at the pion PDG mass being so close to zero on the GeV scale, and therefore squaring this variable removed issues with the very large background in this region. It was important to consider both missing mass distributions to check for consistency in results and assess the efficiency of particles detected, as well as the PID cuts.

The distributions in figure 3.19 highlight that the proton cone angle is a wider distribution that extends much further than the pion cone angle for this channel. This is due to the resolution of neutral pion reconstruction being worse than that of the proton.

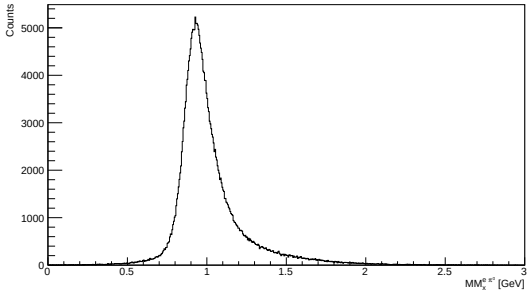

(a) Pion missing mass

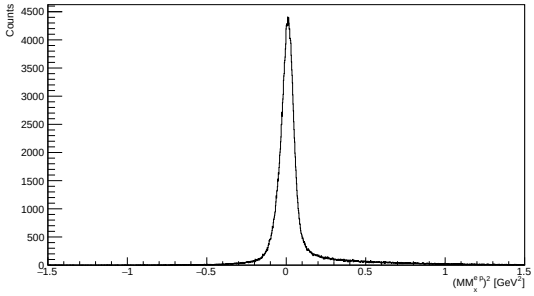

(b) Proton missing mass squared

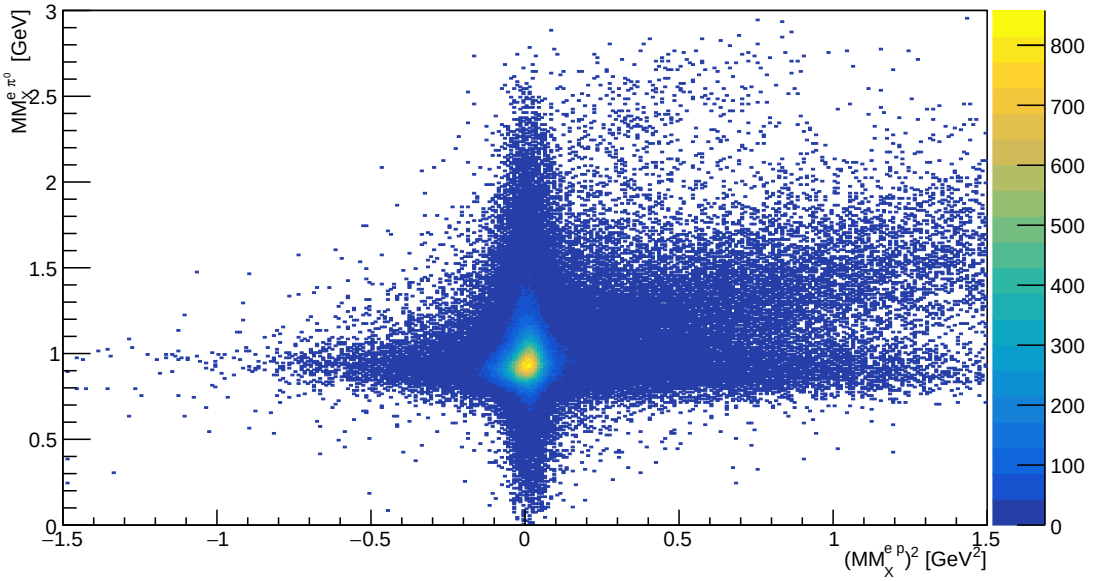

(c) 2D plot of pion missing mass vs proton missing mass squared

Figure 3.18: Simulated data for the exclusive topology: $ep \rightarrow ep\pi^0$

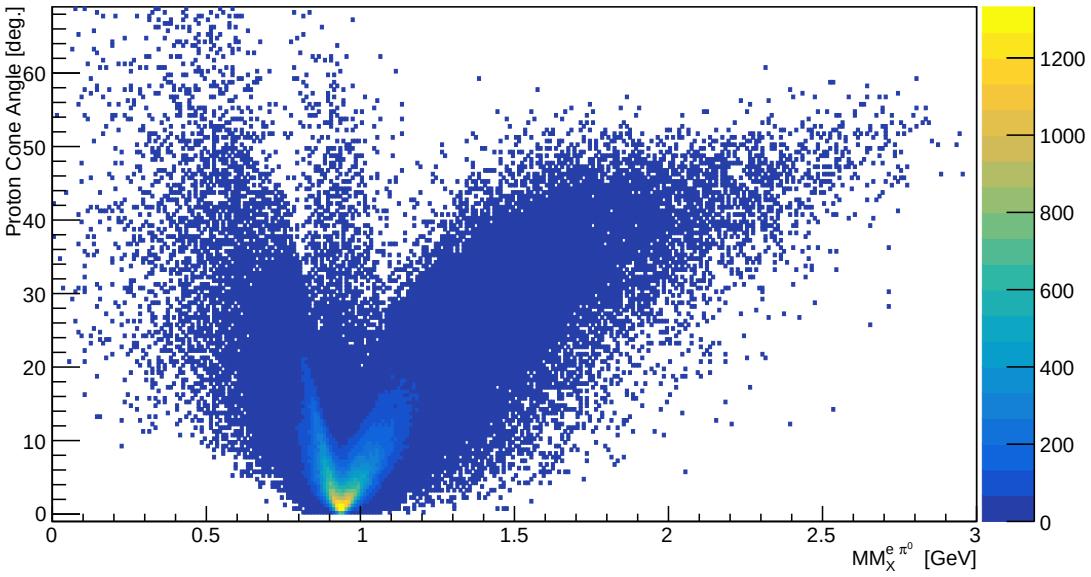

(a) Proton cone angle vs pion missing mass

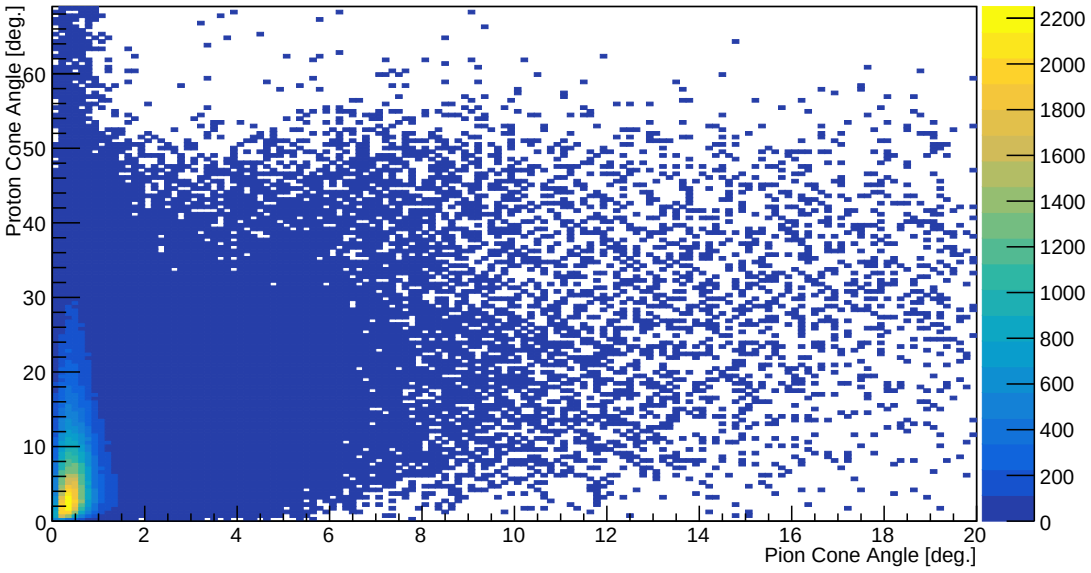

(b) Proton cone angle vs pion cone angle

Figure 3.19: Simulated data for the exclusive topology: $ep \rightarrow ep\pi^0$

3.2.7 Missing Mass Distributions - π^0 Channel

Making use of the missing mass distributions of the simulated data, a visual comparison was made to the real experimental data using NH_3 and ^{12}C targets for the exclusive topology of the π^0 channel, as shown in figure 3.20. Note, the data shown here is for the entire dataset which includes the regions of low Q^2 and W combined with that of the DVMP region. This gives an indication of total signal data for the W resonance region, which was not included in the final analyses of this thesis. The pion missing mass signal peak is expected to be peaked at the PDG mass of the proton (0.938 GeV), and the proton missing mass squared at the PDG mass of the neutral pion squared (0.0182 GeV^2), as made clear in the simulated data plots in figures 3.20a and 3.20b.

The nitrogen component of the targets contribute as background to the signal of interest in single π^0 electroproduction from the free polarised proton (NH_3 data), with other real experimental effects observed too. Signal was observed in the real NH_3 data, however, much of the missing mass distributions are "nuclear background" in which events are from interactions with nitrogen, as well as the target's helium bath, target cell's aluminium and Kapton windows, etc. Figures 3.20c and 3.20d show the distributions obtained for the NH_3 data and the effect of the large nuclear background spanning the signal region of interest, smearing the signal peak's Gaussian like shape due to the nuclear background increasing with missing mass. The simulated data did not describe this nuclear background particularly well, but did successfully show the expected signal distributions.

The nitrogen element of the target in both NH_3 and ND_3 was investigated using a ^{12}C solid state target for the same experimental run conditions, and was not polarised. This allowed to assess contributions from bound protons in a nuclear target of similar atomic number, and obviously also contained reactions from the the helium bath, etc. Figures 3.20e and 3.20f show the ^{12}C data (red) overlaid on the NH_3 data (blue). These background distributions were appropriately scaled in an attempt to describe the nuclear background element of the NH_3 and ND_3 data, but this was mainly for visual purposes at this stage in the analysis to highlight significant π^0 electroproduction events being detected. The nuclear background data was scaled to approximately match the leading edge of each of the distribution, as this region should be comparable. If time permitted, a more thorough investigation could be performed to determine an optimum scaling factor based on electron beam charge information measured with the Faraday Cup. The scaling of the ^{12}C background data profile was dealt with much more appropriately with use of the sPlot technique (defined later) in the later stages of analysis. Signal is well observed at the expected values in both missing mass distributions, with other prominent peaks observed in the proton missing mass squared plot. The other peaks correspond not only to events with particles incorrectly identified as the neutral pion (contamination passing all PID), but to events in which there were other final state particles in the final state, and therefore not the single π^0 reaction channel of interest.

Particle	Particle Symbol	PDG Mass [GeV]	Mass Squared [GeV^2]
Proton	p	0.938272	Not required
Neutron	n	0.939565	Not required
Neutral pion	π^0	0.134977	0.018219
Charged pion	$\pi^{+/-}$	0.139571	0.019480

Table 3.3: List of particles and their masses, noting that mass squared is only given for relevant particles.

The distributions in figure 3.21 are particularly useful in highlighting the signal and the huge nuclear background, with them being distinguishable from one another. To compare these distributions with those of the simulated data previously shown (figure 3.19), the Deeply Virtual Meson Production kinematic region must be selected (using the "DVMP cuts" specified in section 1.5.1) so that they are compatible, this is shown in figure 3.22. This comparison indicates the validity of the distributions obtained from simulations. It is obvious that there is a significant number of π^0 electroproduction signal events.

The next step was to ensure that the correct reaction channel was isolated and that nuclear background events were removed from the data sample before continuing to the final stages of analysis.

These missing mass variables are typically cut as part of "exclusivity cuts" in a common cuts-based analysis to help ensure the reaction channel signal of interest is isolated, but this is not required when using the sPlot technique. A description of the fit-based method will be described in chapter 4.

3.2.8 Missing Mass Distributions - All Channels

The missing mass distributions can be assessed for each of the exclusive topologies of the reaction channels investigated. The data shown is for the whole kinematic region, and is therefore a combination of both the resonance and DVMP regions. The plots in figure 3.23 highlight the differences in the distributions, and give a preliminary indication of the significance of signal events for each channel. The PDG masses of relevant particles are listed in table 3.3.

The pion missing mass should peak at the mass of the proton for the π^0 and π^- reaction channels, and at the mass of the neutron for the π^+ reaction channel. The signal peak of the pion missing mass should be centred at the mass of the relevant final state nucleon of the reaction, with a width determined by the detector resolution of CLAS. The signal-to-background ratio differs for each channel (and topology) and affects the shape of the signal peak. A signal peak was observed for all channels.

The nucleon missing mass squared should peak at the π^0 mass squared for the π^0 reaction channel, and at the $\pi^{+/-}$ mass squared for the $\pi^{+/-}$ reaction channels. This signal peak was most easily observed for the π^0, with much smaller significance in the $\pi^{+/-}$ reaction channels.

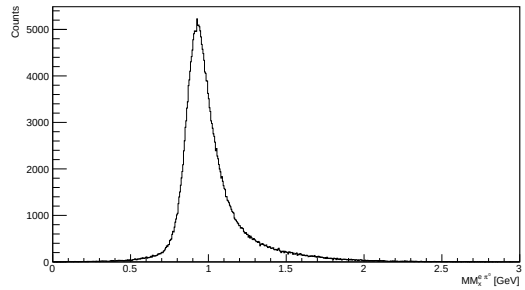

(a) Simulated data: pion missing mass

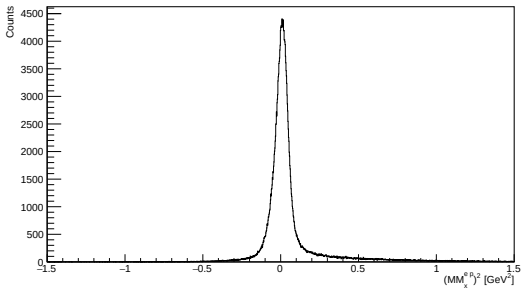

(b) Simulated data: proton missing mass squared

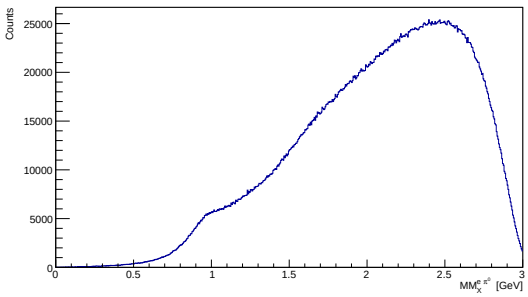

(c) NH_3 data: pion missing mass

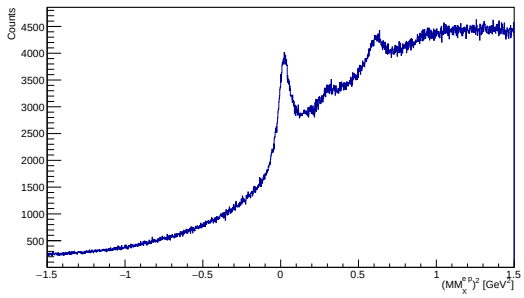

(d) NH_3 data: proton missing mass squared

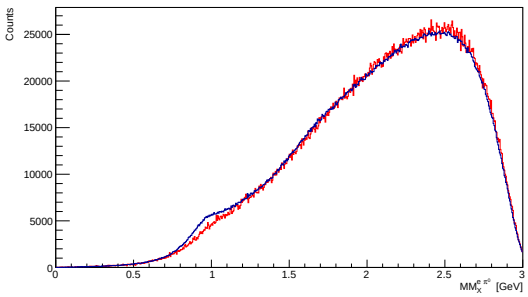

(e) NH_3 with ^{12}C data overlaid: pion missing mass

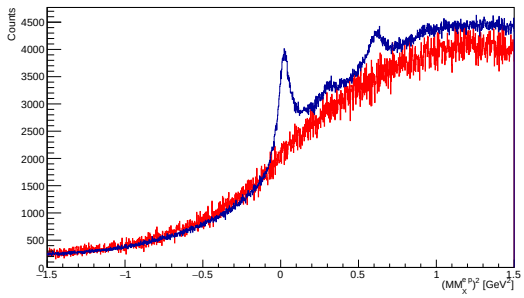

(f) NH_3 with ^{12}C data overlaid: proton missing mass squared

Figure 3.20: Distributions for the exclusive topology of the π^0 channel. Top plots correspond to simulated data, with the middle solely being NH_3 data (**blue**), and the bottom showing ^{12}C overlaid (**red**). Pion missing mass is shown on the left, and proton missing mass squared is shown on the right.

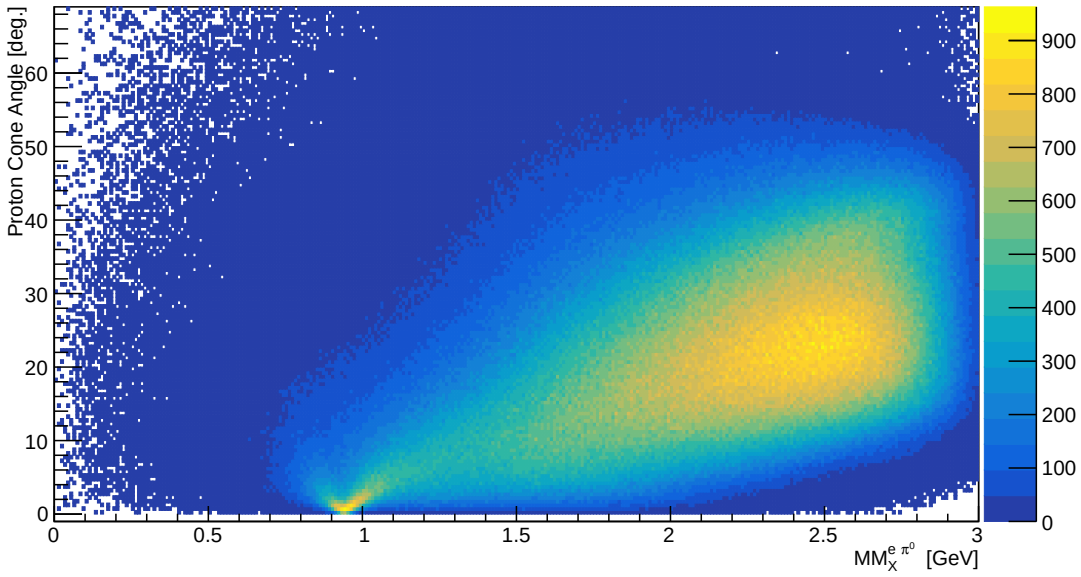

(a) Proton cone angle vs pion missing mass

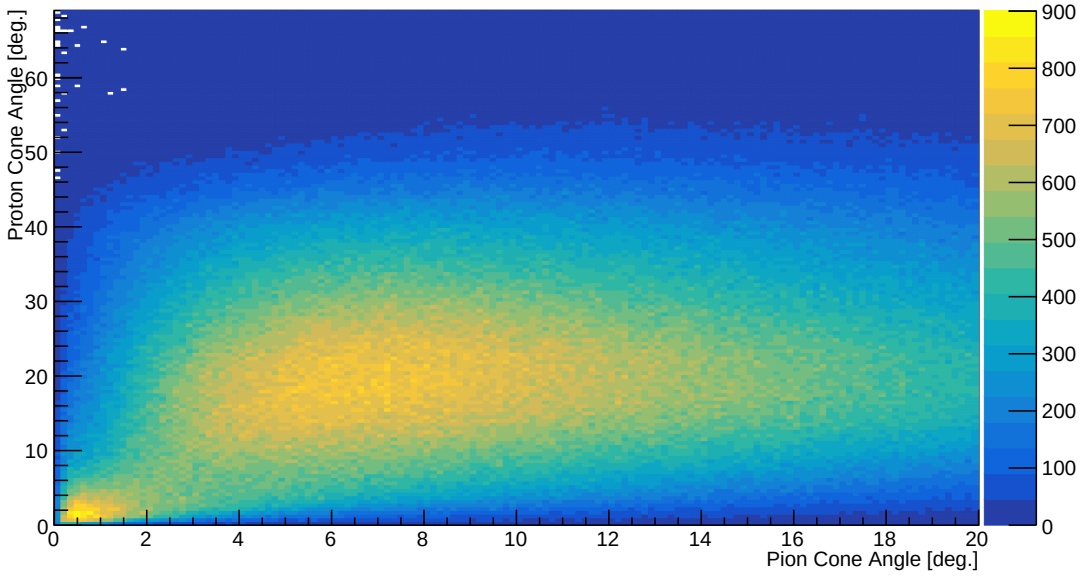

(b) Proton cone angle vs pion cone angle

Figure 3.21: NH_3 data for the exclusive topology: $ep \rightarrow ep\pi^0$

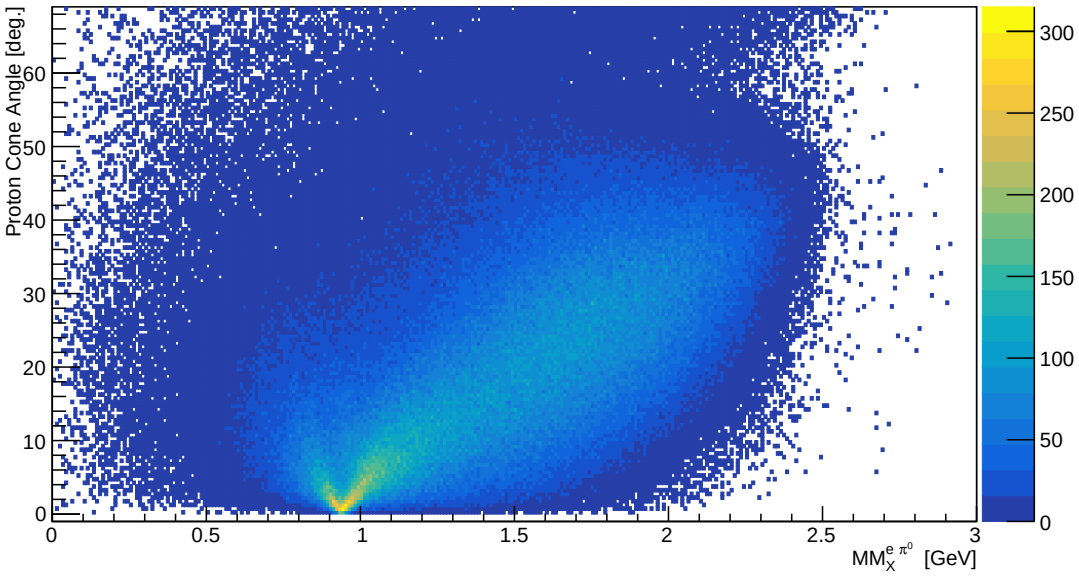

(a) Proton cone angle vs pion missing mass

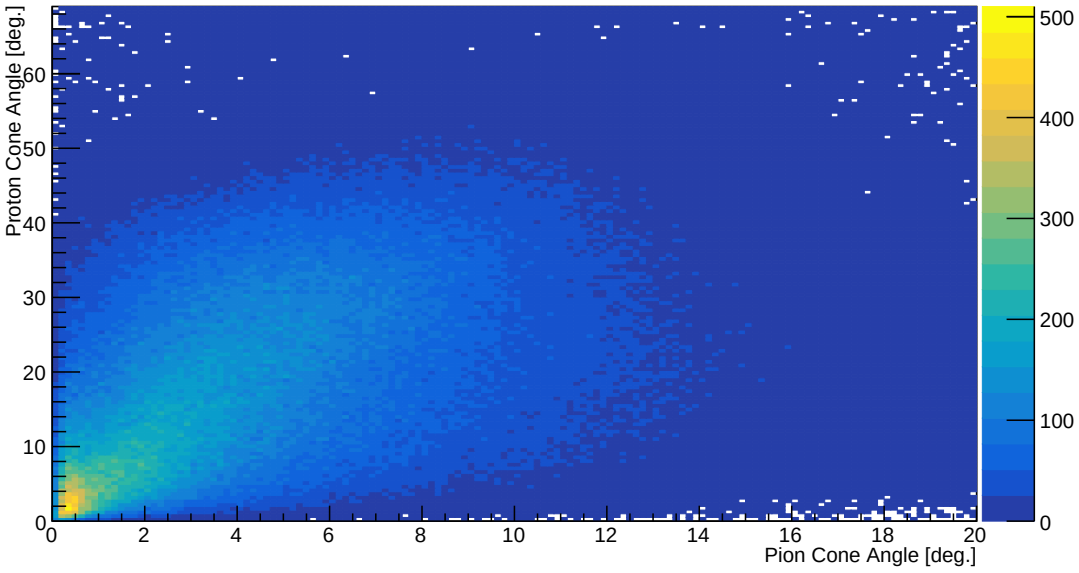

(b) Proton cone angle vs pion cone angle

Figure 3.22: NH_3 data (DVMP region) for the exclusive topology: $ep \rightarrow ep\pi^0$

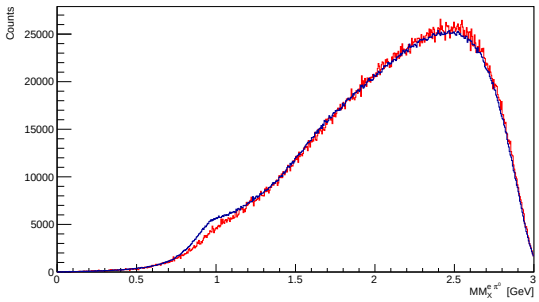

(a) $ep \rightarrow ep\pi^0$: π^0 missing mass

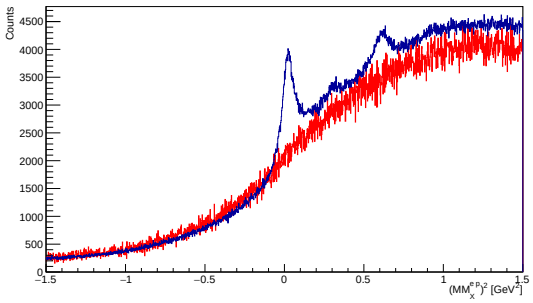

(b) $ep \rightarrow ep\pi^0$: proton missing mass squared

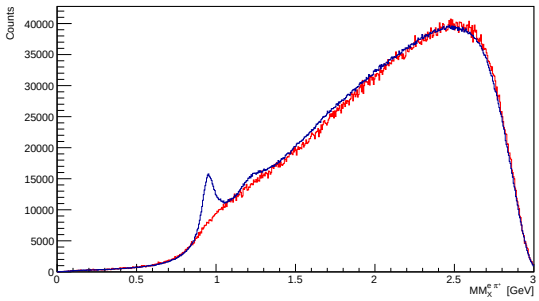

(c) $ep \rightarrow en\pi^+$: π^+ missing mass

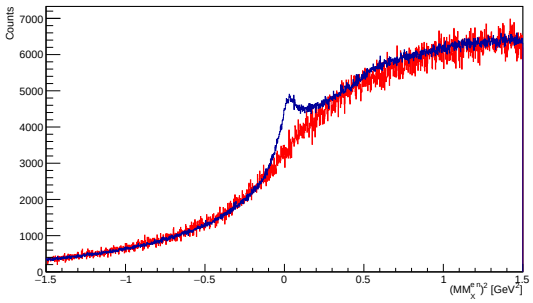

(d) $ep \rightarrow en\pi^+$: neutron missing mass squared

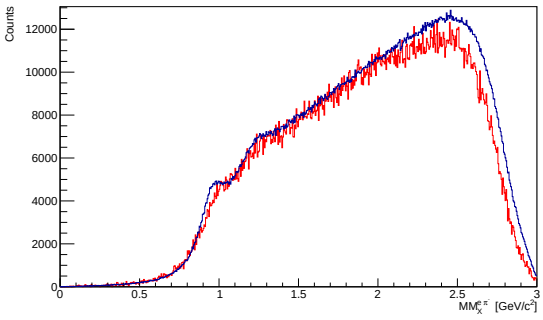

(e) $ed \rightarrow ep\pi^-(p)$: π^- missing mass

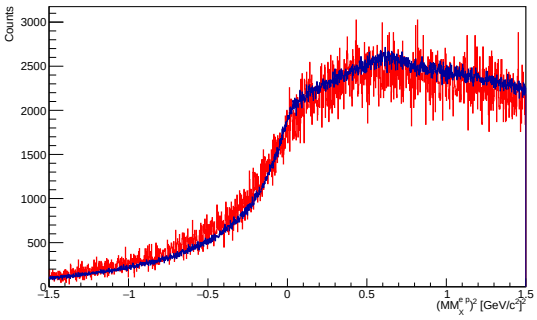

(f) $ed \rightarrow ep\pi^-(p)$: proton missing mass

Figure 3.23: Distributions for all three exclusive topologies of the pion reaction channels with nuclear background data approximations overlaid (**red**); left - pion missing mass; right - nucleon missing mass squared.

For run period C both the ND_3 and ^{12}C data were quite limited in statistics, with this being most obvious when scaling the background data. The background scaling of ^{12}C for run period C was problematic, with the counting error of each bin being very large and making it difficult to assess the significance of the single π^- electroproduction signal in both missing mass distributions. The use of different target material for the nuclear background profile for the π^- channel is discussed later.

One other key peak in the π^+ electroproduction data (figure 3.23c) and π^- electroproduction data (figure 3.23e) is the multi-meson electroproduction observed at approximately 1.2 GeV. These events are reactions in which there was an additional final state pion that was undetected in CLAS, i.e. $ep \rightarrow en\pi^+(\pi^0)$, which conserves charge.

Visually, it is clear from figure 3.23 that most signal events are observed for the π^+ channel, followed by the π^0 and π^- channels. This due to a combination of factors including the differential cross section for each channel, the detection efficiency of the final state particles in CLAS, and the length of experimental running with the NH_3 and ND_3 targets.

The two-dimensional plots in figure 3.24 are very informative in displaying the distribution of data and show the significance of the single pion electroproduction signal peaks.

Comments will be made for key elements of each of the the missing mass distributions for the exclusive topologies of the reaction channels.

π^0 Reaction Channel

The missing mass distributions for the π^0 channel is the combination of all three topologies of π^0 decay photon combinations; EC-EC, IC-EC, and IC-IC. Therefore these contain a combination of the different resolutions in measurements of the pion, based on the angular distributions of these decay photons. The energy resolution of the IC was much better than the EC, therefore the π^0 was measured best when both decay photons were detected in the IC. Most neutral pions were produced in very forward-angles, therefore typically both decay photons were detected in the IC.

The signal peaks are shown in figures 3.23a and 3.23b. Part of the reason the proton missing mass squared peak is more prominent is due to the proton measurements in CLAS being significantly more precise than that of the neutral pion, although both signals mainly correspond to the same signal events, as is clearly shown in the 2D plot in figure 3.24a. This two-dimensional plot also highlights the quality of measurement for both the π^0 and proton, and shows contamination for the exclusive topology of this channel was small for the signal region.

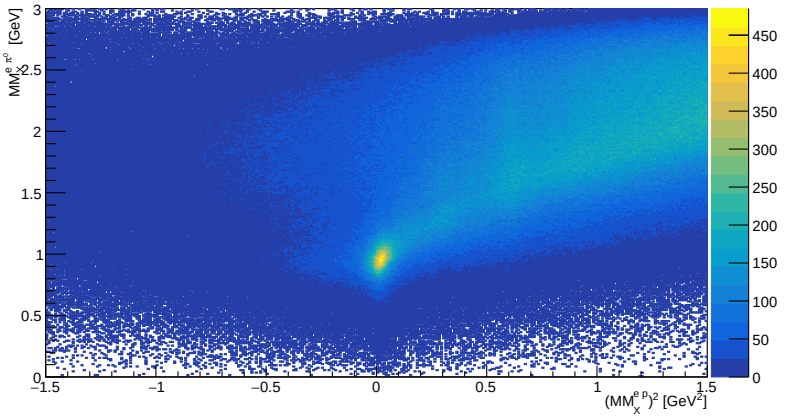

(a) $ep \rightarrow ep\pi^0$

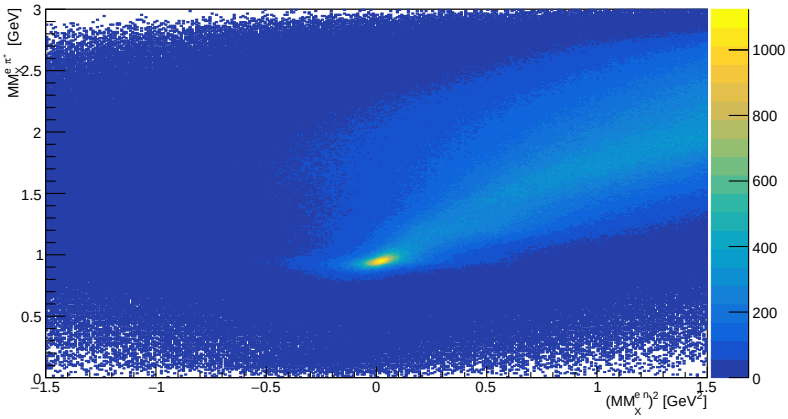

(b) $ep \rightarrow en\pi^+$

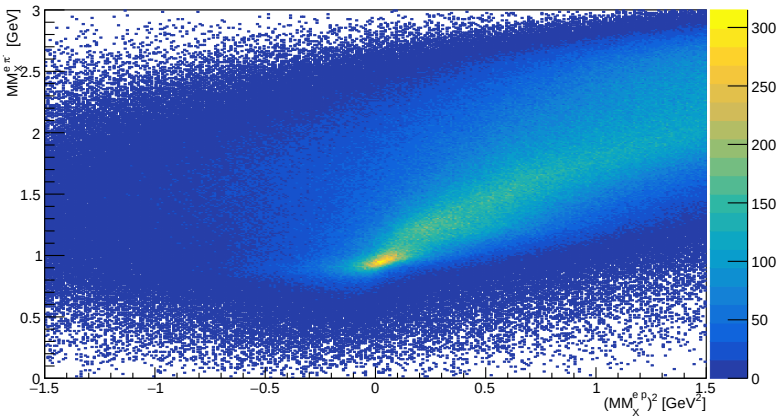

(c) $ed \rightarrow ep\pi^-(p)$

Figure 3.24: Distributions for all three exclusive pion reaction channels. 2D plots of pion missing mass vs nucleon missing mass squared.

π^+ Reaction Channel

As the detected π^+ was measured rather well in CLAS, the signal peak is very clear in the pion missing mass distribution, as shown in figure 3.23c.

The final state nucleon in this reaction is a neutron, but it is important to highlight that its measured four-vector is not particularly reliable. This is due to the the neutron's momentum being an approximation calculated from the neutron's time-of-flight measurement. Although a peak is observed in the neutron missing mass squared distribution in figure 3.23d, the signal peak must be rather wide with the signal-to-background ratio being lower when using this missing mass calculation.

The 2D plot in figure 3.24b shows that the measured four-vector of the neutron is only somewhat reliable (as described above), with this being the reason for the observed spread in the signal in the x-axis (corresponding to the neutron missing mass squared).

π^- Reaction Channel

This channel makes use of the deuterium target, and therefore there was Fermi smearing of the signal peaks in both of the missing mass distributions (as the event reconstructed assumed a stationary neutron target, which is not true). All final state particles (except the spectator proton from the deuteron) were detected in CLAS and had reliable measured four-vectors for this reaction channel but the Fermi smearing and low statistics specific to run period C are significant issues.

The signal peak is clearest in the pion missing mass distribution (figure 3.23e), as opposed to that in the proton missing mass distribution (figure 3.23f) which is due to the pion being better reconstructed for the reaction. The Fermi smearing of the signal peaks is very apparent in comparison to the π^0 and π^+ channels.

The 2D plot in figure 3.24c highlights the issue of Fermi smearing in that the signal is spread in both the x and y axes.

3.2.9 Missing Mass Distributions - Exclusive and Semi-Inclusive Topologies

A comparison was also made between the exclusive and semi-inclusive topologies of the reaction channels according to the definitions previously outlined in this work.

The pion missing mass distribution was compared for each channel as shown in figure 3.25. The signal-to-background ratio was lower for the semi-inclusive topologies due to the less strict event selection constraints, and therefore the ^{12}C data was not overlaid in these plots for the purpose of clarity.

There is significant signal in both of the semi-inclusive topologies of the π^+ and π^- channels, but not the for π^0 channel as the event selection was likely not strict enough and introduced

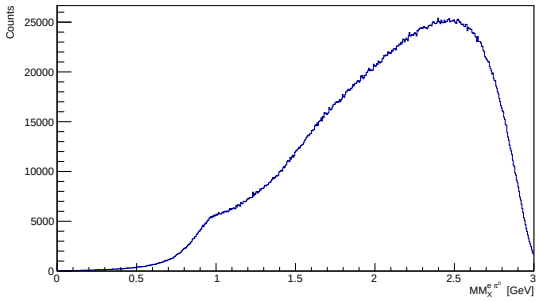

(a) Exclusive: $ep \rightarrow ep\pi^0$

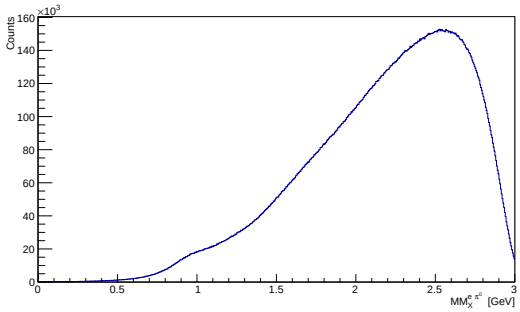

(b) Semi-Inclusive: $ep \rightarrow e(p)\pi^0$

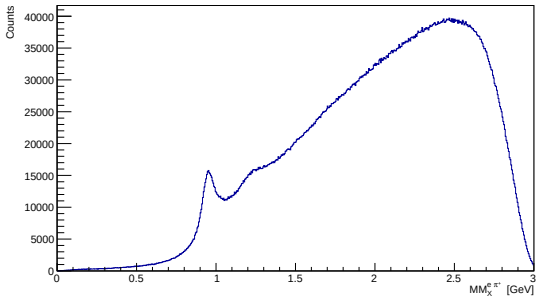

(c) Exclusive: $ep \rightarrow en\pi^+$

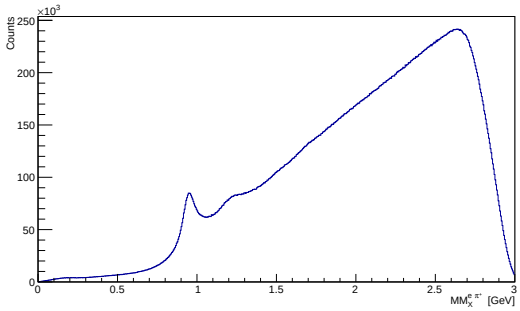

(d) Semi-Inclusive: $ep \rightarrow e(n)\pi^+$

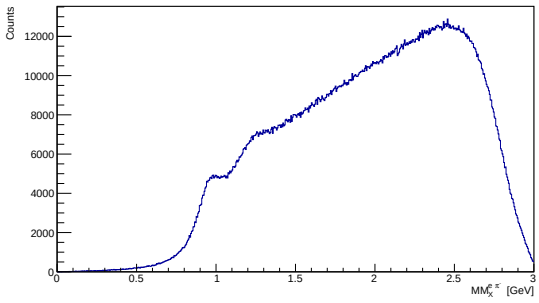

(e) Exclusive: $ed \rightarrow ep\pi^-(p)$

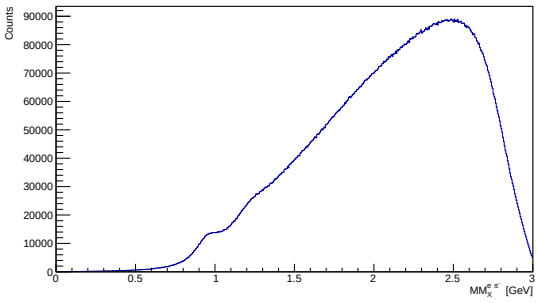

(f) Semi-Inclusive: $ed \rightarrow e(p)\pi^-(p)$

Figure 3.25: Comparison of pion missing mass distributions between exclusive topologies (left) and semi-inclusive topologies (right).

a huge amount of nuclear background events and those from other reactions. This essentially concluded the investigation on the semi-inclusive topology of the π^0 channel.

3.2.10 Cuts-Based Exclusive Event Selection

Further selection for exclusivity of the signal events from nuclear background was clearly still required after the PID stage, and this process tends to be in the form of kinematic cuts on the measured event in most analyses. The analyses performed in this thesis differ from the more standard cuts-based approach in exclusive event selection of the reaction channel of interest, instead a fit-based technique was utilised. It is useful to briefly discuss the cuts-based approach as this was initially investigated as a possible method. In cuts-based analyses it is important to

take into account what can be thought of as the "signal-to-background" ratio, in which as much background is removed with sufficient signal still being retained.

As mentioned, there are a considerable number of events which pass the PID stage but contain misidentified particles and reactions with additional undetected final state particles such as the π^0 in $ep \rightarrow en\pi^+\pi^0$, etc. The sample contains events from bound nucleons in nitrogen, as well as those in the helium bath, so these must also be removed from the signal to be analysed. There were observable kinematic differences in these events forming the background.

The work of Bosted et al. provides a useful overview of a cuts-based analysis on single charged pion ($\pi^{+/-}$) electroproduction for a similar CLAS experiment known as "EG1b" [36]. With reference to a data sample approximating nuclear background for each reaction channel (e.g. ^{12}C target), typical kinematic cuts are performed on the:

- Pion missing mass
- Nucleon missing mass squared
- Missing energy of the total reconstructed event for reactions with a deuterium target, with knowledge that the binding energy within the deuteron is ~ 2 MeV
- Angular distributions between reconstructed and detected particles

These types of kinematical cuts help isolate the reaction of interest, and improve the signal-to-background ratio. The event sample would contain reactions from polarised hydrogen (or polarised deuterium), but also those from unpolarised bound nucleons in the nitrogen element of the target material which were not of interest. A correction factor, known as the "dilution factor", would have to be introduced to account for this dilution in the final signal event sample.

3.3 Summary

This chapter outlined the three pion electroproduction channels of interest and described each topology studied as part of this thesis. The event selection process was detailed, including essential calibrations and data corrections. The particle identification procedure covering all analyses was described in great detail, with this being the first step of event selection for each channel. Exclusive variables were formed and used in assessing the significance of signal obtained in multiple topologies. Simulation data provided preliminary insight into the success of the particle identification stage of event selection and highlighted the large nuclear background in the experimental data obtained. The final stage of event selection to obtain the final data samples makes use of the fit-based sPlot method that will be described and shown in practice in the following chapter.

Chapter 4

Pion Electroproduction Data Analysis - 2

4.1 Overview of sPlot

sPlot is a technique in which event-by-event signal (and background) weights are determined from the fitting of a probability density function (PDF) to a "discriminating" variable in a data set [85]. The weights determined (*sWeights*) from the fit then allow for uncorrelated variables to be plotted resulting in the true separated distributions.

Simply put, a *signal* source can be disentangled from *background* sources when providing suitable model shapes in a fit performed on a suitable distribution.

Firstly, the data containing these sources (*species*) is fit with a log-Likelihood expression:

$$\mathscr{L} = \sum_{e=1}^{N} \ln\Big\{ \sum_{i=1}^{N_s} N_i \mathrm{f}_i(y_e) \Big\} - \sum_{i=1}^{N_s} N_i$$

where e is the event number, N the total number of events, i the species index, N_s the number of species in the data sample, N_i the yield of events in species i, f_i the PDF of the discriminating variable for species i, y the discriminating variable, and $\mathrm{f}_i(y_e)$ the PDF value for species i for discriminating variable y and event e. The only free parameters in the fit are the species yields, N_i, and therefore maximising $\mathscr{L}$ allows for these values to be determined for the data sample.

Secondly, the inverse of the covariance matrix is formed from the Likelihood fit as:

$$\mathbf{V}_{nj}^{-1} = \frac{\partial^2(-\mathscr{L})}{\partial N_n \partial N_j} = \sum_{e=1}^{N} \frac{\mathrm{f}_n(y_e)\mathrm{f}_j(y_e)}{(\sum_{k=1}^{N_s} N_k \mathrm{f}_k(y_e))^2}$$

The sWeights for each event e and species n, ${}_s\mathscr{P}_n(y_e)$, can then be determined for uncorrelated discriminating and control variables:

$${}_s\mathscr{P}_n(y_e) = \frac{\sum_{j=1}^{N_s} \mathbf{V}_{nj}\mathrm{f}_j(y_e)}{\sum_{k=1}^{N_s} N_k \mathrm{f}_k(y_e)}$$

Comprehensive proofs on this technique are provided in the relevant literature, [85]. These sWeights are then used in weighting events to reproduce the true distributions of the species in the control variables.

As previously highlighted, events with reactions from polarised protons and neutrons were the *signal* source of interest, analysed with the use of NH_3 and ND_3 targets, respectively. The *background* source was comprised of many components and was successfully separated.

In this work, a fit was performed to a missing mass distribution (pion missing mass, or nucleon missing mass squared) for each analysis, with there being only one signal and background probability distribution function. The use of sPlot was the final part of the event selection process.

Ideally, realistic simulated data provides an accurate description of the signal shape of the experimental data. As mentioned, the nuclear background shape was accurately described with the real data obtained with the ^{12}C target. As simulated data was not available for all reaction channels, it was important to study the suitability of different signal shape approximations using the RooFit package, in which it was found that a bifurcated Gaussian shape best described the signal shape.

Plotting uncorrelated "control" variables using signal weights was useful in illustrating the success of the sPlot technique.

The benefits of the sPlot technique are clear when considering some of the clear disadvantages of implementation of a cuts-based approach. A cuts-based method typically uses numerous kinematic variables to remove background from the signal source, but generally also removes signal events in the process. Due to the extensive range of reaction channels analysed in this thesis, a cuts-based approach would be somewhat impractical timewise, as it requires thorough investigations and meticulous optimisation of the signal-to-background ratio for each channel. The correlation of kinematic variables with regards to both signal and background sources must be carefully considered to ensure informed choices are made on the most appropriate cut criteria implemented. Considering a semi-inclusive topology, there would be significant limitations on the possible number of useful reconstructed kinematic variables to impose cuts on, whereas the sPlot technique would be successful with the use of only one appropriate kinematic variable. With reference to the target materials in the EG1-DVCS experiment, a cuts-based approach requires the final data sample to be corrected by a dilution factor (to remove events from unpolarised nitrogen nucleons), whereas the sPlot technique avoids this by successfully identifying and removing these events as part of the background source. Changes to the cut criteria would require that the dilution factor be recalculated, and would be a fairly lengthy process for the number of channels analysed.

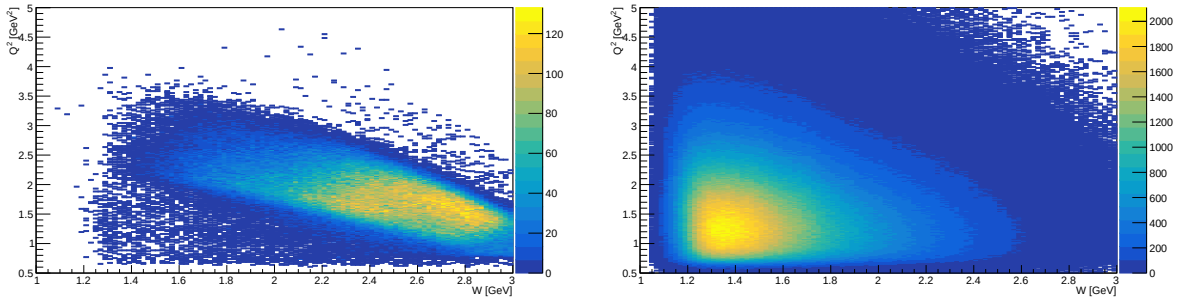

(a) Simulated data

(b) NH_3 data

Figure 4.1: 2D plots of Q^2 vs W for the simulated (left) and NH_3 (right) data. This is before imposing the DVMP cuts.

4.2 Final Event Selection Using sPlot

The final event selection is demonstrated for the exclusive topology of the electroproduction of the neutral pion, i.e. $ep \rightarrow ep\pi^0$. The results were validated by comparison to an analysis with exclusivity cuts, which in this particular case confirms a negligible background contribution.

4.2.1 Plotting Comparable Data Before Fitting

As simulated data was only available for the exclusive π^0 topology, it was important to first perform a fit making use of this information. The simulated data were generated with a focus on the Deeply Virtual Meson Production regime corresponding to $Q^2 > 1$ GeV^2 and $W > 2$ GeV (the "DVMP cuts"). Therefore the NH_3 data also had to be isolated for this region before performing the fit to ensure similar kinematics. Before these cuts were imposed to match the kinematics, 2D distributions are shown for both of these data sets in figure 4.1 and highlights the distribution of the large nuclear background.

The kinematics in this DVMP region differ from the integrated (combined) distributions shown up until this point, and it was important to check the missing mass distributions for the DVMP region with regards to the full NH_3 and ^{12}C data samples. This can be assessed by comparing figure 4.2a with 4.2c, and figure 4.2b with 4.2d. It is clear that the uncertainty in each bin is much larger due to the statistics being lower for the DVMP region, however, the trends in the NH_3 and ^{12}C data are consistent. The effect of the DVMP cuts on the signal in the simulated data was negligible.

A one dimensional fit performed using the sPlot technique (i.e. pion missing mass) allowed for signal and background weights to be used in plotting control variables (i.e. proton missing mass squared, etc.). This was used as a check for quality of the background subtraction technique. Consider initial sPlot fits performed over the following ranges for the pion missing mass and proton missing mass squared, respectively:

- Fit range 1: 0.40 GeV to 1.60 GeV
- Fit range 2: -0.40 GeV^2 to 0.40 GeV^2

Values outside of the fit range were completely excluded. Therefore it is important to view how the missing mass control variable is affected by these "cuts" including both the NH_3 and background ^{12}C data. Figure 4.2e (4.2f) shows data in the DVMP region when imposing fit/cut range 2 (1), as described above.

4.2.2 Performing and Assessing the sPlot Fit

The one dimensional sPlot fits were performed over the specified fit ranges for both of the discriminatory variables to demonstrate consistency between these two possible variables to obtain weights from.

For the exclusive π^0 topology, the technique made use of the simulated data to model the shape of the signal contained within the NH_3 data. The background shape was modelled using the ^{12}C dataset, therefore accurately included any physics contained within the fit region which a basic polynomial approximation would not necessarily describe.

Making use of simulated data for modelling the signal shape is the ideal case for implementing the sPlot fit method and therefore performed well in isolating the signal source from the background.

A one dimensional fit made to the pion missing mass is shown in figure 4.3a, and to the proton missing mass squared in figure 4.3b. The signal PDF shape shown in the figures is an important visual representation of the signal source (free protons) disentangled from the NH_3 data.

The fit parameters displayed in the legend in these figures are:

- Yld_BG - yield of background events
- Yld_Signal - yield of signal events
- alphaA - simulated data smoothing value
- alphaB - background data smoothing value
- offA - simulated data x-axis offset
- offB - background data x-axis offset
- scaleA - simulated data scaling factor
- scaleB - background data scaling factor

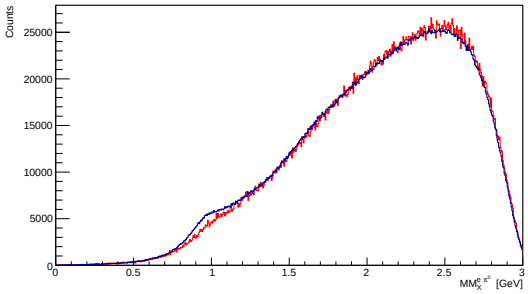

(a) Whole dataset - pion missing mass

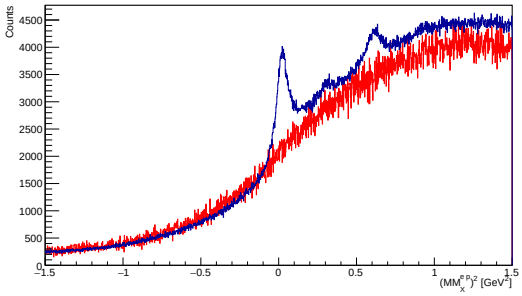

(b) Whole dataset - proton missing mass squared

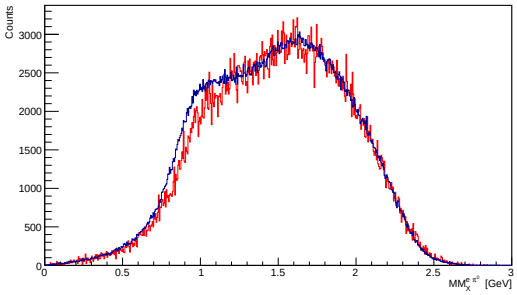

(c) DVMP region of dataset - pion missing mass

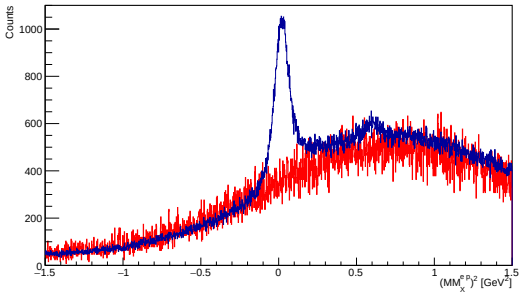

(d) DVMP region of dataset - proton missing mass squared

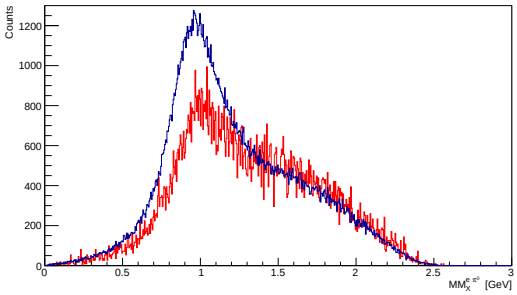

(e) DVMP region of dataset with sPlot fit range constraint - pion missing mass

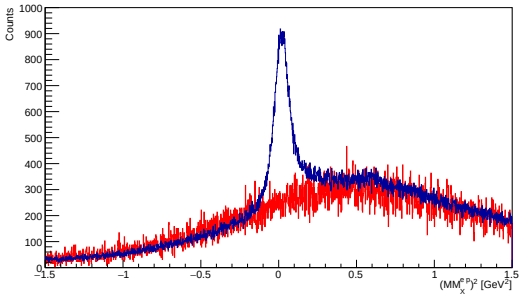

(f) DVMP region of dataset with sPlot fit range constraint - proton missing mass squared

Figure 4.2: Distributions for the exclusive topology of the π^0 channel. Top plots correspond to the data obtained for the whole dataset, middle plots include the DVMP cuts, and the bottom plots also include the sPlot fit range constraint. NH_3 data (**blue**) overlaid with ^{12}C data (**red**). Pion missing mass is shown on the left, and proton missing mass squared is shown on the right.

The yield of signal events for the fit is important and corresponds to the number of events which were contained in the final data sample once the signal weights were applied. Note, in the sPlot fits (such as those shown in figures 4.3a and 4.3b), the y-axis scale shows "Events" as a fraction of the fit range divided by the number of bins.

sPlot fits were later performed without the use of simulated data as the signal shape template. A bifurcated Gaussian shape was used to model the signal shape with the following parameters:

- SIMm - mean of signal shape PDF
- SIMwL - width on left of signal shape PDF
- SIMwR - width on right of signal shape PDF

A wide fit range was used to demonstrate that the signal shape was successfully modelled in the NH_3 data, as well as modelling the background well across the distribution. The fits do benefit from the simulated data, but one can see that the total fit PDF doesn't exactly match the NH_3 data points. The signal-to-background ratio is lower for the pion missing mass fit (figure 4.3a) than for that of the proton missing mass squared (figure 4.3b). This is believed to be a contributing factor to the discrepancy in the yield of signal obtained for each of the fits. The signal and background weights obtained in each of these preliminary fits could then be used to plot the missing mass control variable, with the background distribution in figure 4.3c being comparable to that in figure 4.2f, and the background distribution in figure 4.3d being comparable to that in figure 4.2e. There appears to be signal weighted counts with values less than zero - implying that the fit was not completely successful and this can imply some contamination, but this value of zero weighted counts is pretty much within error in figure 4.3d, which was plotted with weights obtained from what appears to be the most reliable distribution that was fit to. Therefore, the fit to the proton missing mass squared distribution was solely focussed on for the exclusive topology of the π^0 channel.

4.2.3 Plotting Extra Control Variables with sWeights

Again, it is useful to view the two dimensional plots shown in figure 4.4. These variables have been plotted using the signal weights and therefore show the isolated signal source within the NH_3 data. The fit range constraint means that this is not directly comparable to the previous data shown which imposed no cut, however, the results are clearly very compatible with the results obtained for the simulated data (figure 3.19).

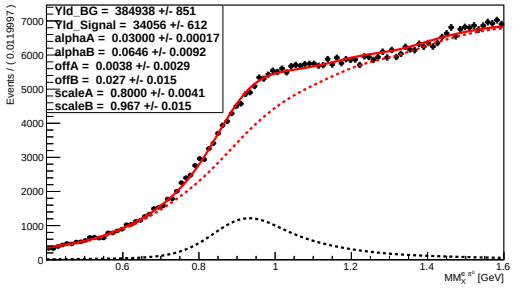

(a) Fit to pion missing mass

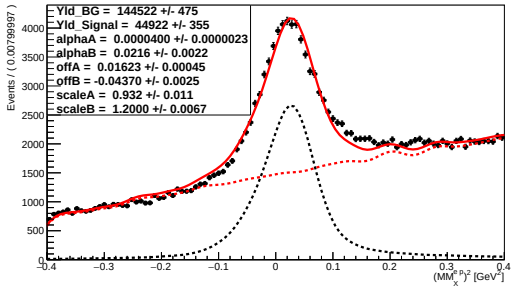

(b) Fit to proton missing mass squared

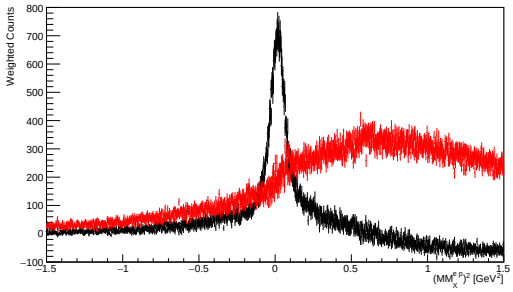

(c) Proton missing mass squared using weights obtained in fit shown in (a). Signal weighted (**black**), and background weighted (**red**)

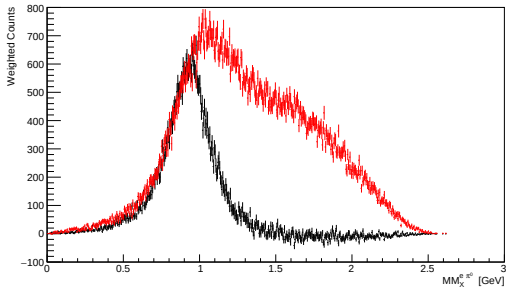

(d) Pion missing mass using weights obtained in fit shown in (b). Signal weighted (**black**), and background weighted (**red**)

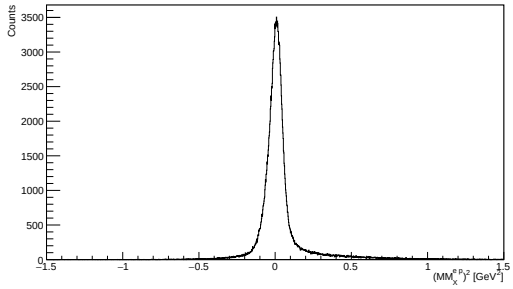

(e) Simulated proton missing mass squared distribution when including a pion missing mass cut of 0.4 GeV to 1.60 GeV

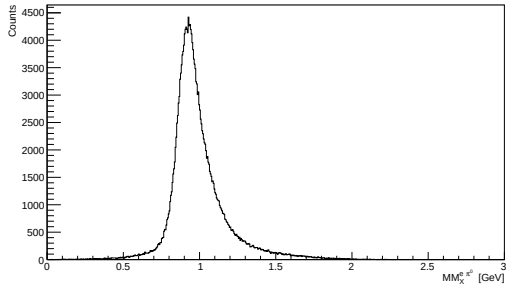

(f) Simulated pion missing mass distribution when including a proton missing mass squared cut of -0.40 GeV^2 to 0.40 GeV^2

Figure 4.3: Exclusive: $ep \rightarrow ep\pi^0$. Comparison of sPlot fit to the pion missing mass (a) and proton missing mass squared (b). These show the total fit Probability Density Function (PDF) (**red** solid line), background PDF based on the ^{12}C data template (**red** dashed line), and the signal PDF (**black** dashed line). Relevant control variable distributions plotted with the weights obtained from the fits are shown in (c) and (d), respectively. Simulated data missing mass distributions are shown in (e) and (f).

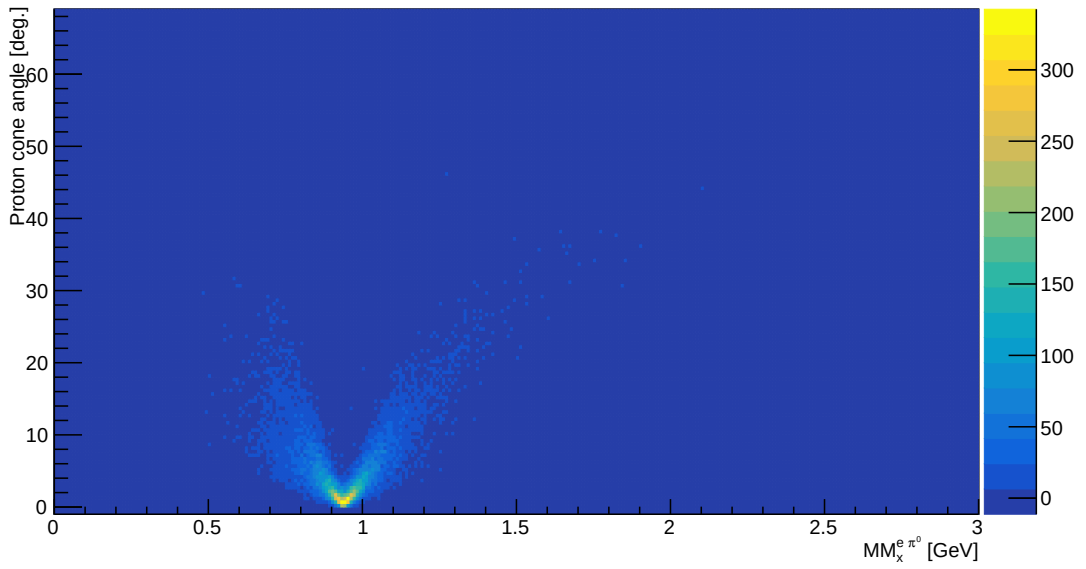

(a) Proton cone angle vs pion missing mass

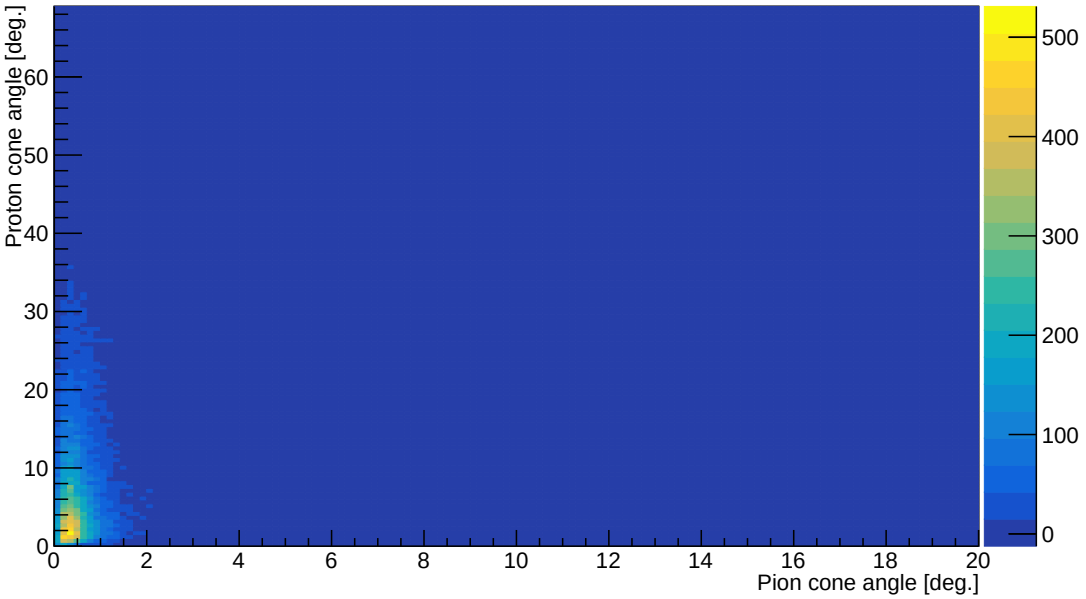

(b) Proton cone angle vs pion cone angle

Figure 4.4: Signal weighted distributions for the exclusive topology: $ep \rightarrow ep\pi^0$

4.2.4 Cross-Check of sPlot Technique

A cross-check of the signal weighted pion cone angle distribution was performed with a background subtraction technique without the use of the sWeights, but instead using the yield of background events determined with the sPlot fit. The sPlot fit modelled the background of the NH_3 data using ^{12}C data which had to be scaled appropriately. Therefore a scaling factor could be calculated from this sPlot fit but used without weights, according to the ^{12}C data within the fit range with the following calculation:

$$Scaling factor = \frac{Yld\_BG}{\sum {}^{12}C \text{ events in fit region}}$$

$$Scaling factor = \frac{144,522}{16,134}$$

$$Scaling factor = 8.96$$

The signal source was contained within the sPlot fit range, with all other events excluded. However, the scaling factor calculated was valid to be used in background subtractions that included the previously excluded events (outwith the fit range). Note, this was calculated for the DVMP region and therefore was only valid for the DVMP region, not the resonance region for example.

Figure 4.5 shows the one dimensional plot of pion cone angle, using both signal and background sWeights obtained from the sPlot fit.

The comparison using the scaling factor in the background subtraction method is shown in figure 4.6. The data within the sPlot fit range for the DVMP region is shown in figure 4.6a, with the background subtracted signal shown in figure 4.6c. Using the same scaling factor but including all NH_3 and ^{12}C data in the DVMP region, the same figures are shown in figures 4.6b and 4.6d. It is clear that the signal obtained from background subtraction using the ^{12}C scaled data is comparable in figures 4.6c and 4.6d. Not only this, but the cross-check with the sPlot weighting method is confirmed by directly comparing figure 4.6c with figure 4.5 which show very strong agreement. This highlights the success of the sPlot technique.

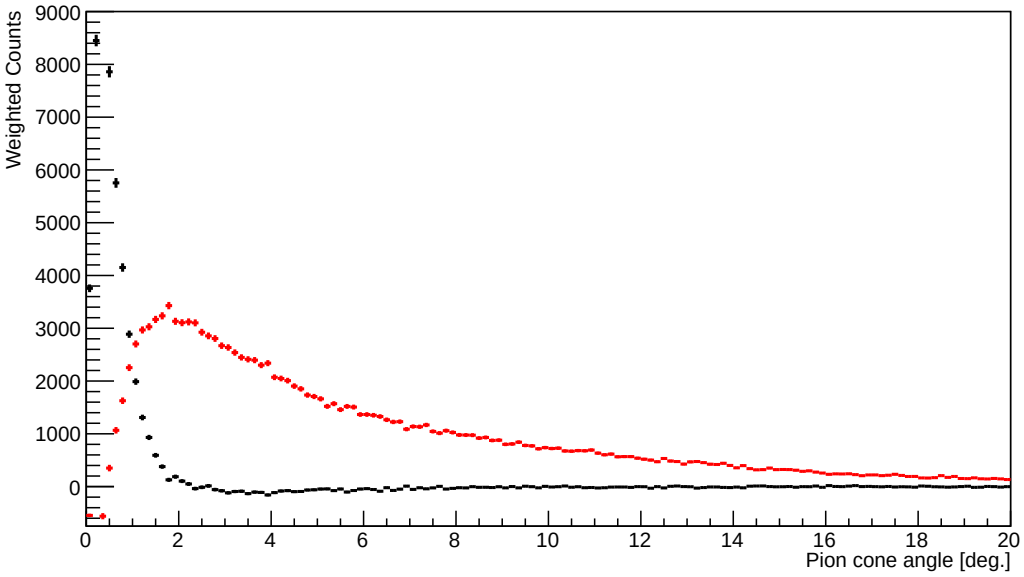

Figure 4.5: Pion cone angle distribution. Signal weighted (**black**) and background weighted (**red**).

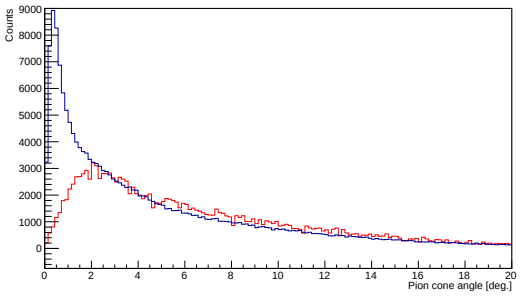

(a) NH_3 (**blue**) and ^{12}C (**red**)

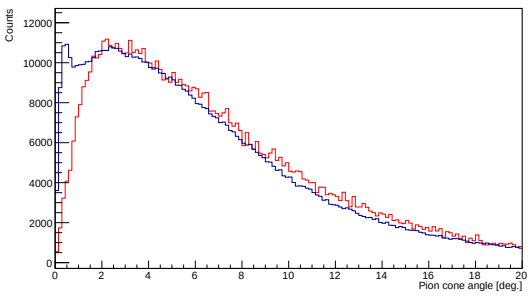

(b) NH_3 (**blue**) and ^{12}C (**red**)

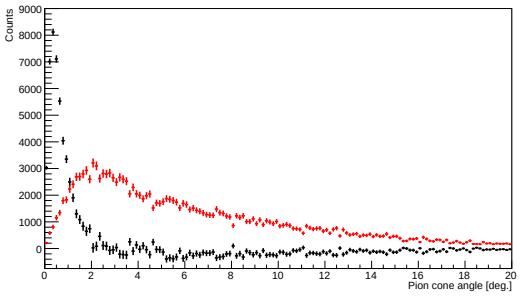

(c) Signal obtained from background subtraction of ^{12}C (**red**) from NH_3 (**blue**) in (a). **^{12}C** background is overlaid

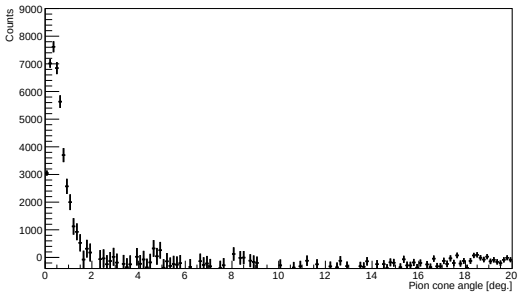

(d) Signal obtained from background subtraction of ^{12}C (**red**) from NH_3 (**blue**) in (b)

Figure 4.6: Pion cone angle distributions obtained from the scaling factor background subtraction method. Left plots only contain data within the fit range, and right plots contain the whole DVMP dataset.

4.3 Summary

This chapter outlined the sPlot technique and its use within the scope of this thesis in obtaining the final event data samples for each reaction topology analysed. The method of performing an sPlot fit with use of the simulated data was presented, with its result showing very strong agreement with a background subtraction technique. A thorough description of the extraction of spin asymmetries can now be given, following with the results presented for each DVMP channel that made use of the sPlot method in obtaining the final event data samples.

Chapter 5

Results and Discussion

The measured spin asymmetries will be described in greater detail, as well as the means to extract these experimentally with use of the sPlot method for the final event selection. The results for the three DVMP channels will be systematically presented with appropriate comparisons, comments and discussion.

5.1 Asymmetries

Due to the use of both polarised beam and target, three asymmetries could be extracted in the EG1-DVCS experiment:

- A_{LU} - beam-spin
- A_{UL} - target-spin
- A_{LL} - double-spin (beam and target)

The first (second) subscript represents the polarisation of the beam (target), either being unpolarised (U) or longitudinally polarised (L). With regards to these three asymmetries, the total cross section can be expressed as

$$\sigma = \sigma_0(1 + P_B A_{LU} + P_T A_{UL} + P_B P_T A_{LL}) \tag{5.1}$$

where P_B and P_T are the longitudinal beam and target polarisations.

This can be related to the differential cross section expression given in equation 1.20, which can be expressed in terms of asymmetries:

$$\begin{aligned}\frac{2\pi}{\Gamma(Q^2,x_B,E)}\frac{d^4\sigma}{dQ^2dx_Bdtd\phi} = \sigma_0\Big[\,1 \\ &+P_B\Big(A_{LU}^{sin\phi}sin(\phi)\Big) \\ &+P_T\Big(A_{UL}^{const}+A_{UL}^{sin\phi}sin(\phi)+A_{UL}^{sin2\phi}sin(2\phi)\Big) \\ &+P_BP_T\Big(A_{LL}^{const}+A_{LL}^{cos\phi}cos(\phi)\Big)\Big]\end{aligned} \tag{5.2}$$

Note, as previously defined, the relevant spin averaged cross section is

$$\sigma_0 = \sigma_T+\varepsilon\sigma_L+\sqrt{2\varepsilon(1+\varepsilon)}\sigma_{TL}cos(\phi)+\varepsilon\sigma_{TT}cos(2\phi) \tag{5.3}$$

The beam-, target-, and double-spin asymmetries expressed in equation 5.2 will be individually described in relation to the differential cross section (equation 1.20) which included x and y components of the virtual photon's polarisation.

Beam-Spin Asymmetry

The beam-spin asymmetry can be expressed as

$$A_{LU} = \sigma_e/\sigma_0 \tag{5.4}$$

where

$$\sigma_e = \sqrt{2\varepsilon(1-\varepsilon)}\sigma_{TL'}sin(\phi) \tag{5.5}$$

Target-Spin Asymmetry

The target-spin asymmetry can be expressed as

$$A_{UL} = \sigma_z/\sigma_0 \tag{5.6}$$

where

$$\begin{aligned}\sigma_z = &\big[P_y(\sigma_{T_y}+\varepsilon\sigma_{L_y})\big] \\ &+\sqrt{2\varepsilon(1+\varepsilon)}\big[P_x\sigma_{TL_x}sin(\phi)+P_y\sigma_{TL_y}cos(\phi)+P_z\sigma_{TL_z}sin(\phi)\big] \\ &+\varepsilon\big[P_x\sigma_{TT_x}sin(2\phi)+P_y\sigma_{TT_y}cos(2\phi)+P_z\sigma_{TT_z}sin(2\phi)\big]\end{aligned} \tag{5.7}$$

Double-Spin Asymmetry

The double-spin asymmetry can be expressed as

$$A_{LL} = \sigma_{ez}/\sigma_0 \tag{5.8}$$

where

$$\begin{aligned}\sigma_{ez} =& \sqrt{1-\varepsilon^2}\left[P_x\sigma_{TT'_x} + P_z\sigma_{TT'_z}\right] \\ &+\sqrt{2\varepsilon(1-\varepsilon)}\left[P_x\sigma_{TL'_x}cos(\phi) + P_y\sigma_{TL'_y}sin(\phi) + P_z\sigma_{TL'_z}cos(\phi)\right]\end{aligned} \tag{5.9}$$

5.1.1 Experimental Formulation of the Asymmetries

The spin asymmetries in ϕ for beam-, target- and double-spin (beam-target-spin) were formed as follows:

$$A_{LU}(\phi_i) = \frac{1}{P_B}\frac{N_i^{\rightarrow} - N_i^{\leftarrow}}{N_i^{\rightarrow} + N_i^{\leftarrow}} \tag{5.10}$$

$$A_{UL}(\phi_i) = \frac{1}{P_T}\frac{N_i^{\Rightarrow} - N_i^{\Leftarrow}}{N_i^{\Rightarrow} + N_i^{\Leftarrow}} \tag{5.11}$$

$$A_{LL}(\phi_i) = \frac{1}{P_B P_T}\frac{(N_i^{\rightarrow\Rightarrow} + N_i^{\leftarrow\Leftarrow}) - (N_i^{\rightarrow\Leftarrow} + N_i^{\leftarrow\Rightarrow})}{N_i^{\rightarrow\Rightarrow} + N_i^{\leftarrow\Leftarrow} + N_i^{\rightarrow\Leftarrow} + N_i^{\leftarrow\Rightarrow}} \tag{5.12}$$

where i represents the ϕ bin, with the choice being made to form the asymmetries with 12 equally spaced ϕ bins. Each ϕ distribution was created using the signal weights obtained from the sPlot fit. The electron beam and target were longitudinally polarised along the z-axis (beamline), with there being two possible orientations for each - positive and negative. The right (left) arrow superscripts refer to positive (negative) polarisation, with the single (double) arrow referring to the beam (target). These expressions are the final spin asymmetries that were formed, but as a preliminary step in assessment of results "raw" spin asymmetries were considered in which the expressions had yet to be divided out the factors of $1/P_B$, $1/P_T$ and $1/P_B P_T$ for the beam-, target-, and double-spin asymmetries respectively. These raw spin asymmetries will be shown alongside any sPlot fits made for the upcoming results for each of the reaction channels. The dividing out of raw spin asymmetries to obtain final spin asymmetries is implied for all results in which the data is shown binned in t.

5.1.2 The Fitting Method

The fits performed to the beam-, target- and double-spin asymmetries (all functions of ϕ) were:

$$\begin{aligned} A_{LU} &= [p_0] + [p_1]sin(\phi) \\ A_{UL} &= [p_0] + [p_1]sin(\phi) + [p_2]sin(2\phi) \\ A_{LL} &= [p_0] + [p_1]cos(\phi) + [p_2]cos(2\phi) \end{aligned} \tag{5.13}$$

which contain a maximum of three free fit parameters (p_0, p_1 and p_2).

To align with the asymmetry convention of equation 5.2, this can be expressed as

$$\begin{aligned} A_{LU} &= A^0_{LU} + A^{sin\phi}_{LU} sin(\phi) \\ A_{UL} &= A^0_{UL} + A^{sin\phi}_{UL} sin(\phi) + A^{sin2\phi}_{UL} sin(2\phi) \\ A_{LL} &= A^0_{LL} + A^{cos\phi}_{LL} cos(\phi) + A^{cos2\phi}_{LL} cos(2\phi) \end{aligned} \tag{5.14}$$

To improve readability, the terms A^0_{LU}, A^0_{UL} and A^0_{LL} correspond to A^{const}_{LU}, A^{const}_{UL} and A^{const}_{LL} respectively.

In the beam-spin asymmetries formed A^0_{LU} corresponds to the y-axis offsets, which could be corrected for by normalising the number of events in each polarisation state (contributing to the asymmetry) to the total beam luminosity for that polarisation state. This means that A^0_{LU} just quantifies the normalisation required for the beam-spin asymmetry, as the parameter takes no other physical meaning. This is not the case for A^0_{UL} where it is actually a combination of the normalisation required and the contribution from terms which arise due to the y component of virtual photon polarisation (albeit small). A^0_{LL} is of importance for the double-spin asymmetry, again being a combination of the normalisation required and the contribution from terms which arise due to the x component of virtual photon polarisation but mainly due to the z component. This z component is significant and although the value extracted should be corrected by normalisation, there is still useful information in the trend and progression of the parameter's dependence on t for the double-spin asymmetry. It is mainly due to the virtual photon's z component that the following terms are significant: $A^{sin\phi}_{UL}$, $A^{sin2\phi}_{UL}$ and $A^{cos\phi}_{LL}$. Kim found that there is a significant correlation between $A^{cos\phi}_{LL}$ and the $cos(2\phi)$ term of the unpolarised cross section of equation 5.3 which is part of the double-spin asymmetry that is formed [22]. To account for this a second order cosine term, $A^{cos2\phi}_{LL}$, was included in the double-spin asymmetry fit function of 5.14. This additional term is required to essentially "correct" the $A^{cos\phi}_{LL}$ term in the fit so that it matches the fit form Kim obtained with a "simultaneous fit" method. The fit functions detailed in 5.14 essentially align with those of Smith [5], and are therefore suitable for the comparison of π^0 asymmetry results presented in section 5.1.4.

The functions shown in 5.14 were used to fit the relevant asymmetry distributions using the *Least Squares* fitting method. This method obtains the best fit by performing a minimisation

of the sum of the squares of the offsets (*residuals*). These residuals are defined as being the difference between each data point (i) and the fitted value returned by the fit function. This is a commonly used mathematical procedure and was deemed suitable for the objective of this work in which there were sufficient data in each bin so the associated counting error followed Poisson statistics. The "counting error" in each bin could be treated as one standard deviation of a Gaussian distribution as required for error treatment with the Least Squared method. This allowed to confidently estimate the fit parameters.

Time permitting, a simultaneous fit would have been performed and compared (such as an Extended Maximum Likelihood fit), but would have required simulated data for each reaction channel.

5.1.3 Summary of Reaction Channels Studied

An outline of the results presented for each of the pion DVMP channels is as follows:

- $\underline{\pi^0}$:
  - Comparison of part B NH_3 target results obtained (with and without the use of simulated data) to those of Smith
  - Comparison of raw spin asymmetry results from part C ND_3 with part B NH_3
  - Relevant reactions:
    * $ep \rightarrow ep\pi^0$
    * $ed \rightarrow ep\pi^0(n)$
- $\underline{\pi^+}$:
  - Comparison of part B NH_3 target results obtained for the exclusive and semi-inclusive topologies
  - Comparison of part C ND_3 target results obtained for the exclusive and semi-inclusive topologies
  - Comparison of part B NH_3 and part C ND_3 target results obtained for the exclusive topology
  - Comparison of part B NH_3 and part C ND_3 target results obtained for the semi-inclusive topology
  - Comparison of results obtained for both target materials for both topologies
  - Relevant reactions:
    * $ep \rightarrow en\pi^+$
    * $ep \rightarrow e(n)\pi^+$
    * $ed \rightarrow en\pi^+(n)$
    * $ed \rightarrow e(n)\pi^+(n)$
- $\underline{\pi^-}$:
  - Comparison of part C ND_3 target results obtained for the exclusive topology (using sPlot fits to different variables) with that of the semi-inclusive topology
  - Relevant reactions:
    * $ed \rightarrow ep\pi^-(p)$
    * $ed \rightarrow e(p)\pi^-(p)$

Bin	1	2	3	4	5
$-t$ (GeV^2)	0.00→0.20	0.20→0.39	0.39→0.72	0.72→1.20	1.20→2.00

Table 5.1: Binning of the variable t used on all DVMP datasets.

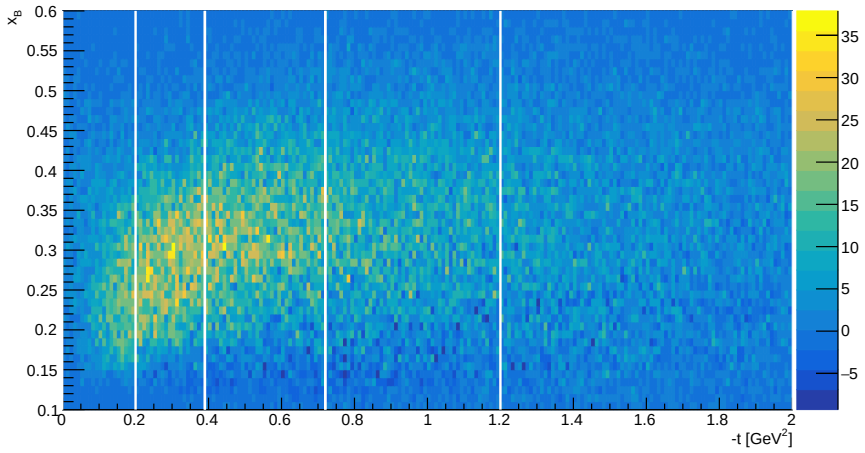

Figure 5.1: sPlot signal weighted plot of Bjorken x vs $-t$ for the channel $ep \rightarrow ep\pi^0$.

For each channel, raw spin asymmetries were compared for each topology (when possible) and then the data was binned in t to assess the dependence. The binning choice for t is detailed in table 5.1, and was determined by the kinematic coverage (statistics) of the dataset with regards to this variable, as shown in figure 5.1.

Each data point is plotted at the mean value of t in each bin, and no x-axis offset has been applied (unless explicitly stated, as for the π^0 channel). The sPlot fit was performed for each of the binned datasets ensuring the most appropriate use of the method in determining signal and background weights. The fit parameters extracted in each bin for each of the raw beam-, target- and double-spin asymmetry fits were divided out appropriately by the beam and target polarisations as previously described. The results in this analysis work use the mean of the signal weighted values of P_B and P_T for each t bin.

The motivation for studying semi-inclusive topologies was that the yield of signal significantly increased, therefore reducing statistical uncertainties in the results. Meaningful results could be obtained for the charged pion channels with regards to the semi-inclusive topologies, but now for the neutral pion channel. The signal-to-background ratio was too small in the pion missing mass distribution for the π^0 semi-inclusive topology, as previously shown in figure 3.25b, and therefore it could not be successfully fit to using the sPlot method. This is likely to be due to the loose event selection criteria and the fact that the resolution of the measurements of neutral pions was worse than that of charged pions, and therefore greatly affected the prominence of the signal peak in the pion missing mass distribution. It is worth highlighting that in the semi-inclusive topologies studied in this thesis it is the final state pion (not the nucleon) that is detected to ensure that it is the single pion electroproduction channel of interest. It is im-

portant to realise that although the same single pion electroproduction signal can be isolated in both exclusive and semi-inclusive topologies for each DVMP channel, the kinematic coverage is different between them due to detector acceptance imposing momentum constraints on the detected nucleon. This should be taken into account when comparing the results of any exclusive and semi-inclusive topologies presented.

DVMP of π^0 and π^+ was analysed with the use of the NH_3 (part B) and ND_3 (part C) targets as a means to check for any differences in the reaction on a free and a quasi-free target nucleon before the π^- analysis which was only possible with use of the ND_3 target. This was an important cross-check, and therefore a variety of related results were obtained for the EG1-DVCS experimental dataset.

All sPlot fits performed and results presented are for the Deeply Virtual Meson Production kinematic region of $Q^2 > 1$ GeV^2 and $W > 2$ GeV.

5.1.4 Results - π^0 Channel

Simulated data was only available for the part B run period (making use of the NH_3 target), and solely focused on the production of DVMP events for neutral pions, not charged pions. This was an important opportunity to test the sPlot method with and without the use of simulated data in modelling the signal shape distribution. A bifurcated Gaussian was used to model the signal source distributions without the use of simulated data, and would therefore be the model choice for the subsequent charged pion analyses. It was crucial to check that the results were in agreement for the π^0 channel with the use of simulated data, and with the use of a bifurcated Gaussian signal shape model.

Another important point in studying DVMP of the neutral pion was that a comparison could be made with the work of Smith [5], thereby testing the sPlot method on the more conventional cuts-based exclusive event selection as previously described. Some important points on Smith's work will now be discussed. The π^0 results were obtained from the part A and part B run periods and were combined, as they both made use of a NH_3 target. The PID was rather strict, with a signal yield of only approximately 29000 events for the final combined data set. In calculating the final binned asymmetries, Smith used a single overall value of P_B and P_T that was calculated as an average for the whole dataset (part A and part B) for both polarisation states, not in each t bin. Smith performed a beam-spin asymmetry fit including the term $A_{LU}^{sin2\phi} sin2\phi$ in addition to that expressed in equation 5.14, but was found to be insignificant. Smith also made use of a *dilution factor* to account for DVMP reactions from unpolarised nucleons in the nitrogen element of the target - this was not required for the sPlot method which successfully isolated the signal of interest with no contamination of this sort. The t bin limits in this analysis match those of Smith.

The comparison of results for the NH_3 target will be presented first, followed by a comparison of the raw spin asymmetries obtained with the NH_3 and ND_3 target.

Run Period B - NH_3 Target

With the proton missing mass squared distribution of the final DVMP event sample for the exclusive topology of neutral pion DVMP, an sPlot fit was made to this variable with and without a simulated data signal shape model as shown in figures 5.2a and 5.2b respectively. The fits indicate that the simulated data identifies almost 10% more signal events (43900 +/- 300 compared to 39600 +/- 300). It can be seen that the simulated shape helps identify events in the "tail" region, for example events with a proton missing mass squared value larger than 0.2 GeV^2. The associated raw spin asymmetries are plotted below each of the fits in figure 5.2 for all three cases: beam-, target- and double-spin. A comparison of the fit parameters for all three raw spin asymmetries produced for both fits shows that the difference in signal yield has no significant effect. All raw spin asymmetry fit parameters agree well within error for these two sPlot fits.

This comparison indicates that the signal shape choice of a bifurcated Gaussian model appears to be suitable and it was therefore used for the charged pion electroproduction reaction channels (π^+ and π^-) which could not benefit from the use of having simulated data. As previously stated, use of a Voigtian as the signal shape was also studied, but the use of a bifurcated Gaussian was found to be the best possible signal shape model at the time of analysis (based on shapes available in the RooFit package). The bifurcated Gaussian takes the asymmetrical signal shape into account by allowing for different widths at the left and right side.

Having studied the sPlot fits and raw spin asymmetries for the unbinned (integrated) DVMP dataset, the data were then binned into the 5 t bins. This allowed for a comparison to be made between the results for both signal shape models with reference to the results of Smith's π^0 analysis on the same EG1-DVCS experimental dataset. Note, Smith's results are a combination of the results with use of the NH_3 target from both part A and part B. Part A utilised a different target position which was not optimised for acceptance and required additional corrections to allow for the results to be combined with those of part B, therefore they were excluded from the work in this thesis.

The results of the beam-spin, target-spin and double-spin asymmetries are shown in figures 5.3, 5.4 and 5.5 respectively. The results from the fit using a bifurcated Gaussian as the signal shape (shown as **blue-grey squares** ■) were offset in $-t$ by $+0.05$ for clarity as they otherwise sat on top of the results obtained with use of the simulated data as the signal shape model (shown as **forest green multiplication signs** $\times$). The results from Smith's work made use of fitting with the Least Squares method, however, Smith extended his work to use the Extended Maximum Likelihood method and only observed a small improvement in the errors for each data point.

The results of the beam-spin A_{LU}^0 term shown in figure 5.3a appear to show a flat trend, although a slightly non-zero result for the first bin in t. The results of the beam-spin $A_{LU}^{sin\phi}$ term shown in figure 5.3b appear to be small at the lowest and highest t values, but there seems to be a rather flat trend for the middle data points. The results of the target-spin A_{UL}^0 term shown in figure 5.4a appear to show a flat trend, although slightly non-zero results are observed for the third and fourth bins in t. The results of the target-spin $A_{UL}^{sin\phi}$ term shown in figure 5.4b appear rather flat, but seems to be a noticeable increase in the second and third data points in t before a gradual decrease and plateau. The results of the target-spin $A_{UL}^{sin2\phi}$ term shown in figure 5.4c appear to slightly oscillate with increasing t, but this is a difficult observation to interpret due to the small magnitude and associated uncertainties. The results of the double-spin A_{LL}^0 term shown in figure 5.5a show a clear trend which initially increases to a peak value before significantly decreasing with increasing t, and is significant based on the magnitude and relatively small errors. The results of the double-spin $A_{LL}^{cos\phi}$ term shown in figure 5.5b appear to slightly oscillate with increasing t, but again is a difficult observation to interpret due to the small magnitude and associated uncertainties.

The results here show very good agreement with those of Smith for all fits with errors taken into account, and the data seem to follow the same trends in their t dependence. This shows that the binned data is also rather consistent whether using simulated data or not in the sPlot fit, and that the results match those of an independent analysis of this same channel and dataset.

As previously mentioned, beam and target luminosity corrections were not carried out for the work in this analysis, but their effect was assumed to be almost negligible for the part B dataset. This run period of the experiment had very well timed changes in data taking with regards to obtaining equal amounts of data with all polarisation orientations of the beam and target. This seems to be the case based on the A^0_{LU} term shown in figure 5.3a which is consistent with zero in all bins except the first (in which it is very small). Assuming the target luminosity corrections are indeed negligible, the theory indicates that the constant term for the target-spin asymmetry (A^0_{UL}) should be investigated to check whether there is an observable effect related to the y component of the virtual photon polarisation. It is likely that the statistics for this channel are far too low to see any effect on the constant term of the target-spin asymmetry in the current dataset. Note, there are no data points in Smith's work to compare for these constant terms.

The π^0 analysis on the NH_3 data has shown the success of the sPlot method in comparison to the commonly used "cut" based analysis method. It is highly important to point out that the sPlot fit was made to the proton missing mass squared distribution and made little use of the detected π^0 in the event. This means that the PID was strict enough (albeit looser than that of Smith's analysis), and ensured that the sPlot fit isolated the signal source relating to the DVMP channel - not the DVCS channel (production of one photon) which could be a source of background. This shows that less information can be used to obtain comparable final results.

It was found that the results obtained for this channel were most trusted (good quality of fit) when fitting to the proton missing mass squared, as opposed to the pion missing mass. This is suspected to be due to the fact that the pion missing mass peak is much more prominent (as the proton is measured more accurately than the neutral pion), and therefore easier to fit to. The results were somewhat in agreement, therefore meaning that the sPlot fit successfully isolated the same signal source dataset regardless of the discriminatory variable used. The test of this hypothesis will be presented in the π^- analysis results section.

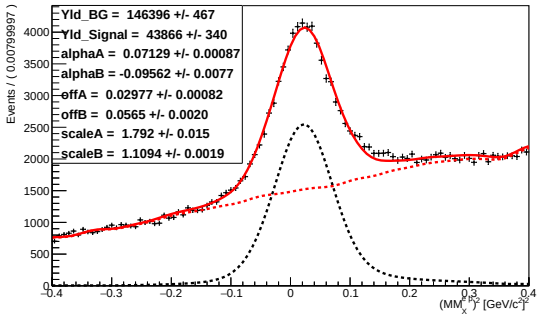

(a) Fit signal shape using simulated data

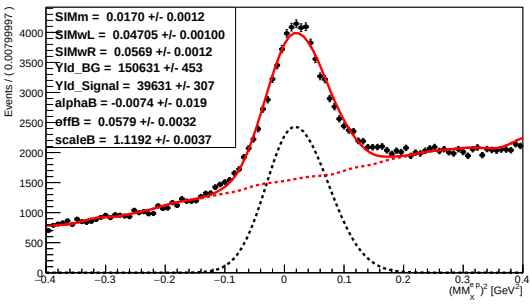

(b) Fit signal shape using bifurcated Gaussian

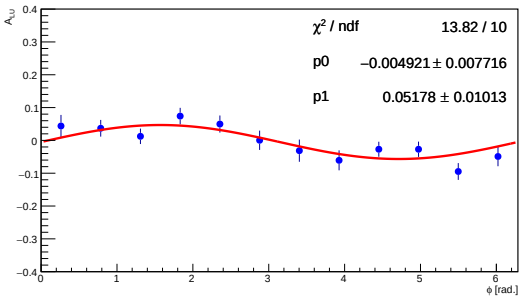

(c) Raw beam-spin asymmetry (A_{LU})

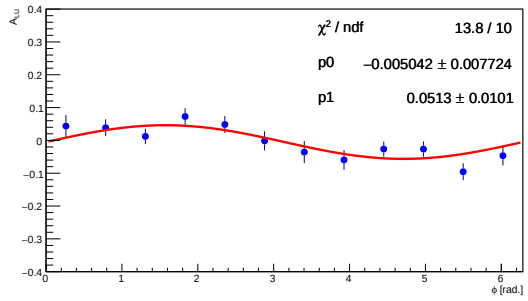

(d) Raw beam-spin asymmetry (A_{LU})

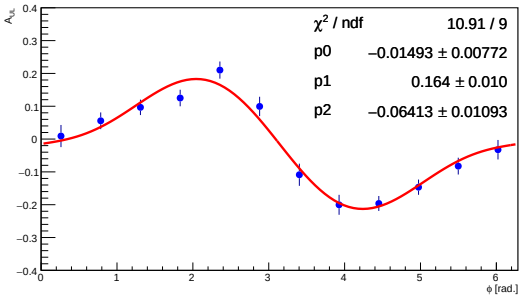

(e) Raw target-spin asymmetry (A_{UL})

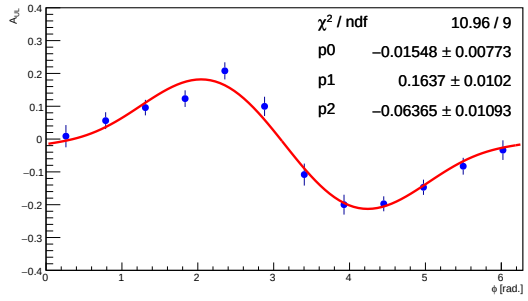

(f) Raw target-spin asymmetry (A_{UL})

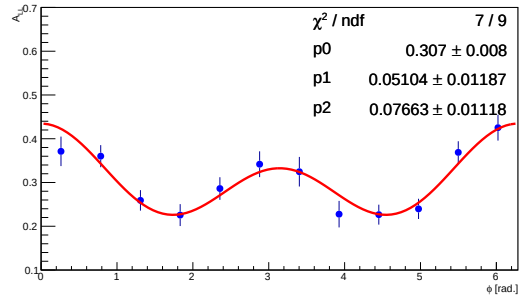

(g) Raw double-spin asymmetry (A_{LL})

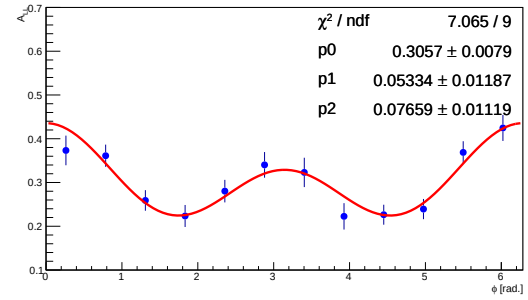

(h) Raw double-spin asymmetry (A_{LL})

Figure 5.2: π^0 channel: exclusive topology, NH_3 target. sPlot fits made to the proton missing mass squared using simulated data as the signal shape (a), and a bifurcated Gaussian (b). These show the total fit Probability Density Function (PDF) (**red** solid line), background PDF based on the ^{12}C data template (**red** dashed line), and the signal PDF (**black** dashed line). Corresponding "raw" spin asymmetries are shown below both fits (left and right) for the beam-, target- and double-spin asymmetries respectively, (c)-(h).

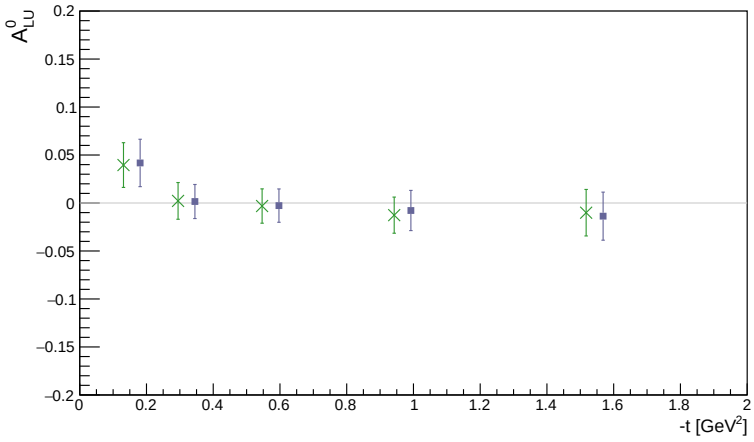

(a) A^0_{LU}

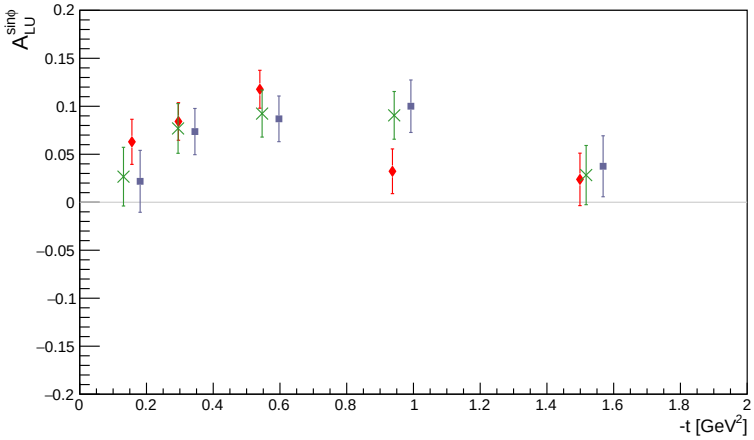

(b) $A^{sin\phi}_{LU}$

Figure 5.3: π^0 channel: exclusive topology, NH_3 target. Beam-spin asymmetries binned in t. Shown for the data selected using fits to the proton missing mass squared using simulated data as the signal shape (**forest green multiplication signs** $\times$), bifurcated Gaussian (**blue-grey squares** ■ offset in $-t$ by $+0.05$), and overlaid with the results of Gary Smith (**red diamonds** ♦) where appropriate [5].

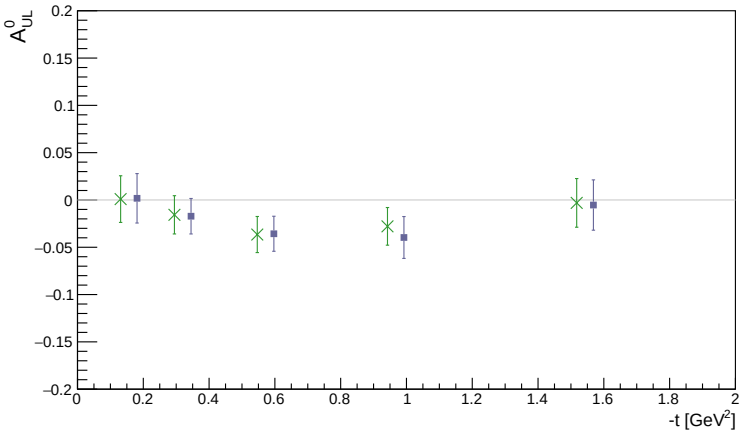

(a) A^0_{UL}

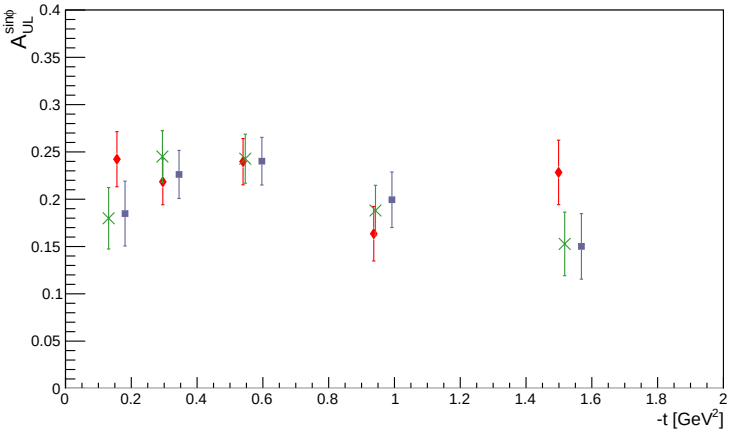

(b) $A^{sin\phi}_{UL}$

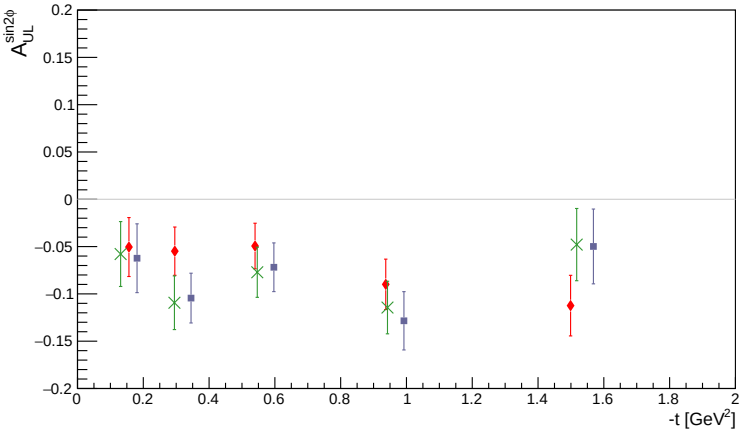

(c) $A^{sin2\phi}_{UL}$

Figure 5.4: $\underline{\pi^0 \text{ channel:}}$ exclusive topology, NH_3 target. Target-spin asymmetries binned in t. Shown for the data selected using fits to the proton missing mass squared using simulated data as the signal shape (**forest green multiplication signs** $\times$), bifurcated Gaussian (**blue-grey squares** ■ offset in $-t$ by $+0.05$), and overlaid with the results of Gary Smith (**red diamonds** ♦) where appropriate [5].

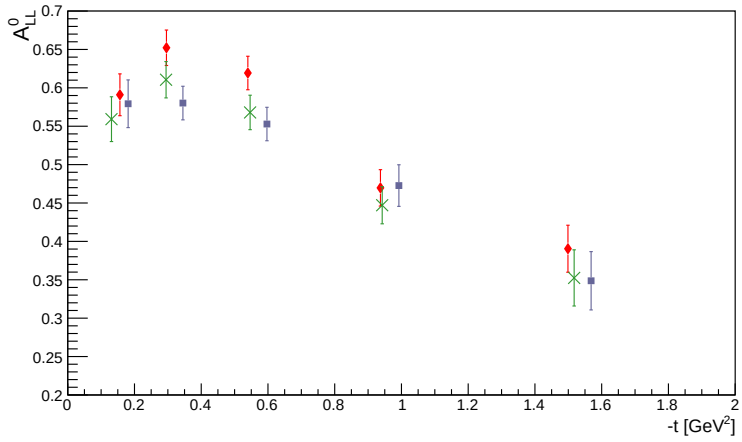

(a) A^0_{LL}

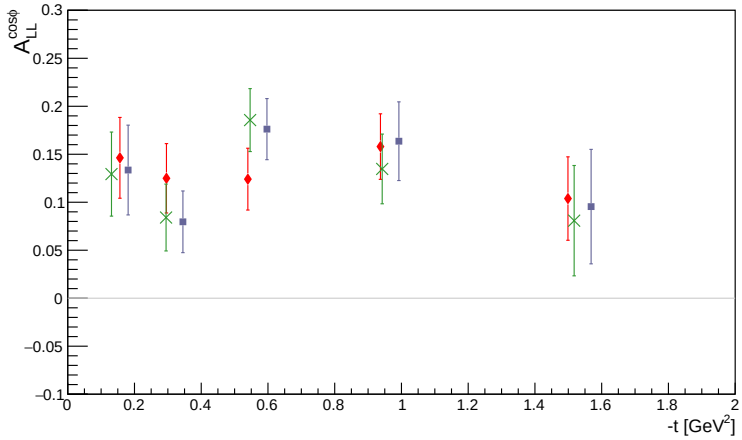

(b) $A^{cos\phi}_{LL}$

Figure 5.5: π^0 channel: exclusive topology, NH_3 target. Double-spin asymmetries binned in t. Shown for the data selected using fits to the proton missing mass squared using simulated data as the signal shape (**forest green multiplication signs** $\times$), bifurcated Gaussian (**blue-grey squares** ■ offset in $-t$ by $+0.05$), and overlaid with the results of Gary Smith (**red diamonds** ♦) [5].

Run Period C - ND_3 Target

The next goal was to compare results obtained for π^0 DVMP with use of the part C ND_3 target, which gives access to a polarised proton loosely bound in a deuteron. This was to check whether the measurement of the meson production on a free and a quasi-free nucleon give consistent results, as expected. The statistics were rather poor for this run period and therefore it was not possible to confidently fit and measure asymmetries with the data binned in t. However, the sPlot fit using a bifurcated Gaussian as the signal shape on the unbinned data could still be performed.

An sPlot fit was made to the proton missing mass squared distribution, and can be checked against the fit from the part B NH_3 target data in figure 5.6a with the part C ND_3 target data in figure 5.6b. For consistency both fits use a bifurcated Gaussian as the signal shape model. The sPlot method appears to be successful again, and the difference in statistics is clear from the decrease in yield of signal from 39600 +/- 300 to 4600 +/- 200. This resulted in much larger uncertainties for the associated raw spin asymmetries for part C, as shown below the plot of the fit in figure 5.6. Note, the same y-axis limits are used in both plots of the raw beam- and target-spin asymmetries in the plots to help highlight the issue with regards to the low statistics. The raw spin asymmetries appear to be generally similar but a more suitable representation of the fit parameters is shown in figure 5.7. This shows a comparison of the fit parameters p_1 (all raw spin asymmetries), and p_2 (raw target- and double-spin asymmetries) for the NH_3 target and ND_3 target data. This indicates there is consistency for the raw spin asymmetries.

It was found that the beam and target luminosity normalisation of the data was much more of an issue for the part C data, therefore it was not possible to make a comparison of the fit parameters which were affected by this - p_0 for all asymmetries. Specifically, there was a significant difference in the amount of data taken with a positive target polarisation with respect to a negative polarisation.

For completeness, p_2 has been included in the comparison of the double-spin asymmetries fit parameters, as it has an effect on the measured p_1 value.

Overall the measurements do show reasonable agreement in this investigation of the π^0 DVMP channel from a proton in both NH_3 and ND_3, but the statistics for the ND_3 are too low to allow binning in t.

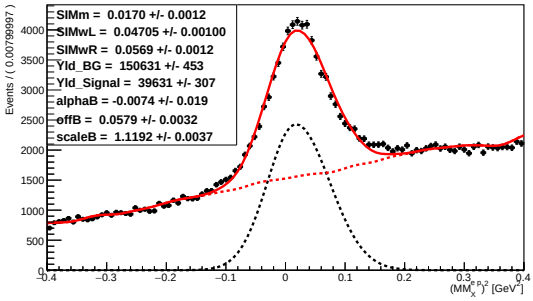

(a) Fit to the part B NH_3 data

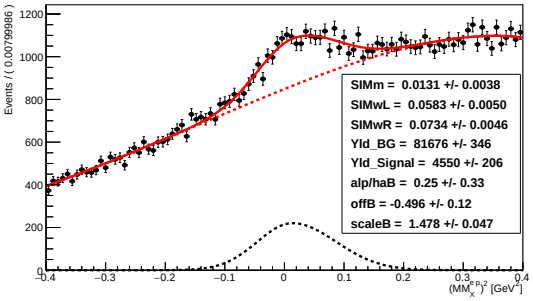

(b) Fit to the part C ND_3 data

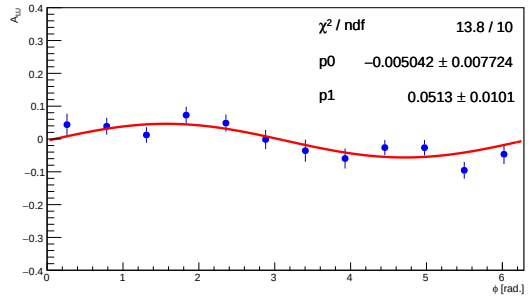

(c) Raw beam-spin asymmetry (A_{LU})

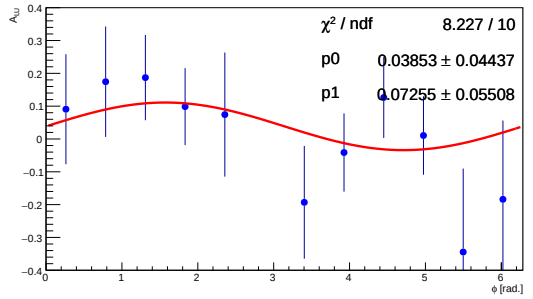

(d) Raw beam-spin asymmetry (A_{LU})

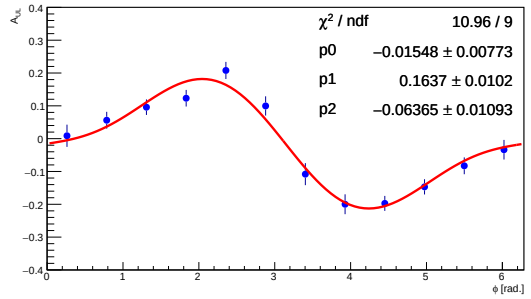

(e) Raw target-spin asymmetry (A_{UL})

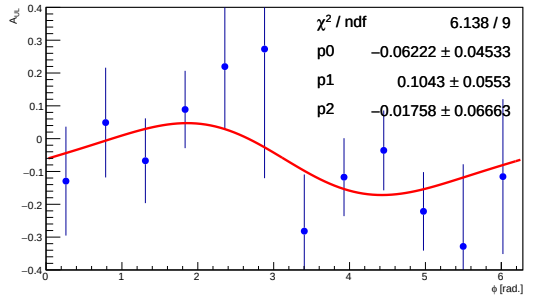

(f) Raw target-spin asymmetry (A_{UL})

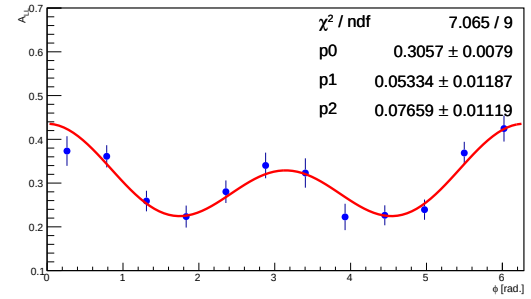

(g) Raw double-spin asymmetry (A_{LL})

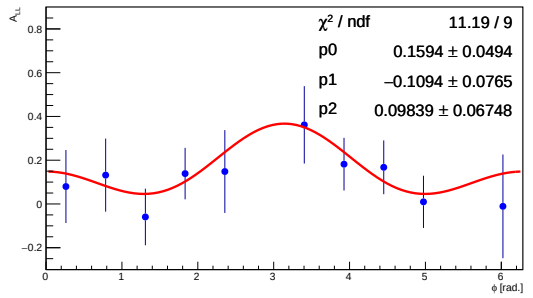

(h) Raw double-spin asymmetry (A_{LL})

Figure 5.6: π^0 channel: exclusive topology, part B NH_3 target (left) and part C ND_3 target (right). Both sPlot fits were made to the proton missing mass squared using a bifurcated Gaussian. Corresponding "raw" spin asymmetries are shown below both fits (left and right) in three rows for the beam-, target- and double-spin asymmetries respectively.

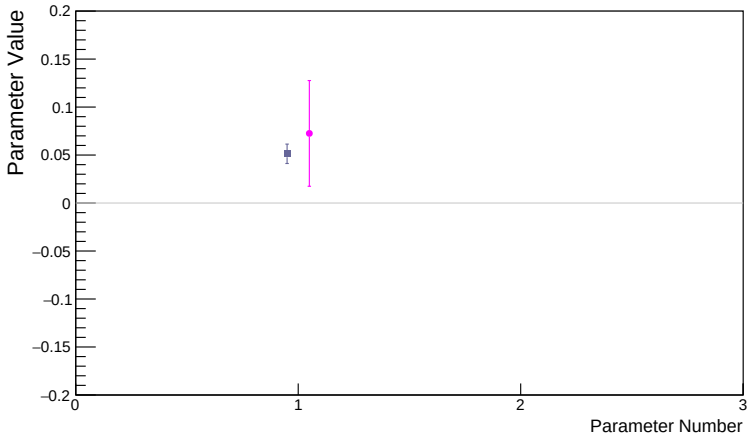

(a) Raw beam-spin asymmetries fit parameters

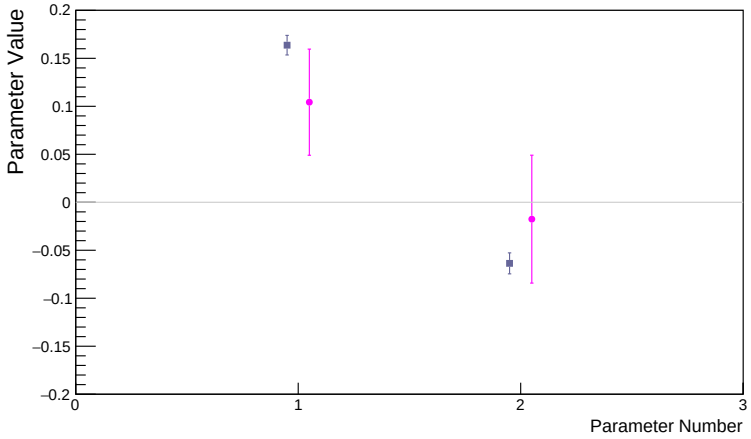

(b) Raw target-spin asymmetries fit parameters

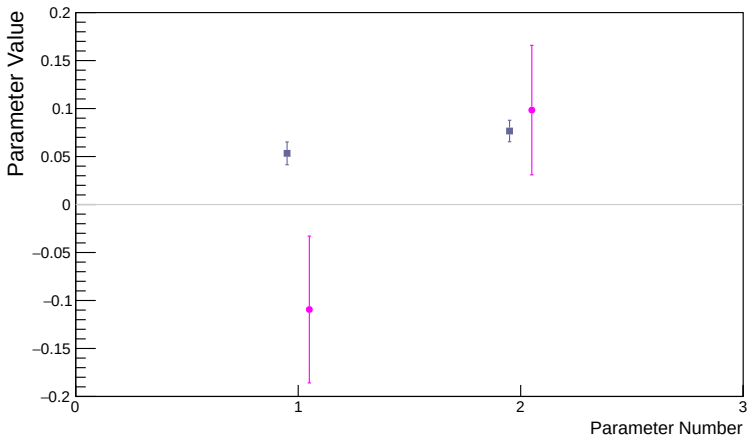

(c) Raw double-spin asymmetries fit parameters

Figure 5.7: π^0 channel: exclusive topology, part B NH_3 target and part C ND_3 target. Comparison of fit parameters obtained from the raw beam-, target- and double-spin asymmetries: part B NH_3 target (**blue-grey squares** ■) and part C ND_3 target (**magenta circles** ●). Only the appropriate fit parameters for each raw spin asymmetry are compared.

5.1.5 Results - π^+ Channel

The spin asymmetry measurements presented are a first for this charged pion channel in this kinematic regime. Insight on the charged pion channels for DVMP can be gained through the unique trends observed in these important first measurements.

As highlighted there was no simulated data for the DVMP π^+ channel and therefore the signal shape was modelled by a bifurcated Gaussian, as justified from being a suitable choice for the π^0 channel.

For this channel the sPlot fits were performed on the pion missing mass. This was to avoid using information from the measured neutron in the final state as its energy and momentum were not measured well with CLAS. Due to the rather good measurement of the π^+, it was easy to perform the sPlot fit to the distribution and this was suitable for the exclusive and semi-inclusive topologies for both the NH_3 and ND_3 target data.

As will be shown, this analysis channel has the highest statistics. The asymmetry results will be presented binned in t for exclusive and semi-inclusive topologies with use of both the NH_3 and ND_3 target. Note, the pion pole contribution should be considered in this channel as it is known to dominate the results in the region of $-t < 0.3$ GeV^2.

The comparison of results for the NH_3 target will be presented first for the exclusive and semi-inclusive topologies, followed by a comparison for the ND_3 target. The results will then be compared for both targets for the exclusive topology, then for both targets for the semi-inclusive topology. Finally, the results will be compared for both targets and both topologies.

Run Period B - NH_3 Target

The sPlot fit performed can be assessed for both the exclusive and semi-inclusive topology, as shown in figures 5.8a and 5.8b respectively. Most of the sPlot fit parameters appear to be consistent, with the yield of signal determined as being 38400 +/- 400 for the exclusive topology and 143000 +/- 900 for the semi-inclusive topology. The corresponding raw spin asymmetries are shown below the sPlot fits in figure 5.8 and appear to be similar. Note, the same y-axis limits are used in both the exclusive and semi-inclusive topology plots for each of the asymmetries. The beam and target raw spin asymmetry $sin\phi$ fit terms corresponding to p_1 are significantly larger for the π^+ channel than for the π^0 in the NH_3 target data.

A comparison of the fit parameters for the two topologies was then made for the binned beam-, target- and double-spin asymmetries as shown in figures 5.9, 5.10, and 5.11. As previously highlighted, there was no beam and target luminosity correction (which should be negligible for this part B run period). This should, however, be considered when viewing the constant term in the asymmetry plots.

With reference to the spin asymmetry measurements of the semi-inclusive topology, comments will be made on the results presented. The results of the beam-spin A^0_{LU} term shown in figure 5.9a appear to show a flat trend, although a slightly non-zero result for the first bin in t.

The results of the beam-spin $A_{LU}^{sin\phi}$ term shown in figure 5.9b appear to show a very flat trend across all data points, and clearly non-zero at the low and high t values which is uniquely different from the π^0 channel. The results of the target-spin A_{UL}^{0} term shown in figure 5.10a appear to show a non-zero trend that is rather flat, although the results for the first and second bins in t being significantly larger and non-zero is not observed for the π^0 channel. The results of the target-spin $A_{UL}^{sin\phi}$ term shown in figure 5.10b appear flat for the first three bins in t before the very significant increasing magnitudes observed for the fourth and fifth bins, unique to this channel. The results of the target-spin $A_{UL}^{sin2\phi}$ term shown in figure 5.10c gradually decrease with increasing t, which is a distinctive trait of this channel. The results of the double-spin A_{LL}^{0} term shown in figure 5.11a appear to be somewhat flat with slight oscillations, in particular a large deviation is observed for the fourth bin in t. The results of the double-spin $A_{LL}^{cos\phi}$ term shown in figure 5.11b are very unique with the first two bins in t being centred around zero before observing a significant jump to negative values which slowly decrease in magnitude with increasing values of t. The trends observed for the double-spin asymmetry results for the π^+ channel are distinct from those of the π^0 channel. Note, the pion pole contribution will dominate the results in the region of $-t < 0.3$ GeV^2.

It is very clear that the results are consistent between the two topologies, with the errors approximately halving when looking at the semi-inclusive data in comparison to the exclusive data. This confirms the success of the sPlot method even when reducing the constraints on PID and event selection criteria. It is important to keep in mind that the kinematic coverage of the data was different, with a wider range covered for the semi-inclusive case due to there being no constraint on measuring a neutron in the EC of CLAS which has a limited θ and ϕ acceptance. The effect of this kinematic coverage difference appears not to be significant, but indeed will be present. This may be the reason for a small systematic shift of the binned beam- and target-spin asymmetries between the two topologies, although is within the statistical uncertainty.

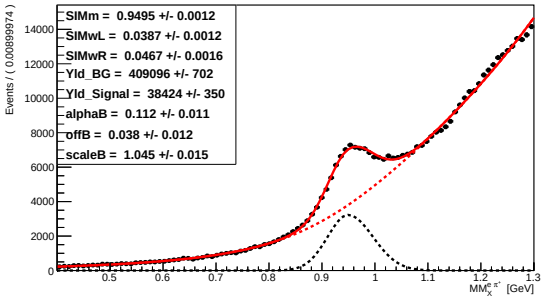

(a) Exclusive topology fit

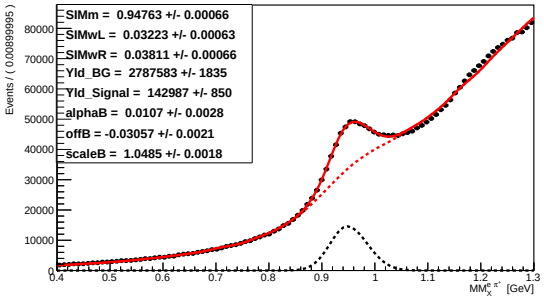

(b) Semi-Inclusive topology fit

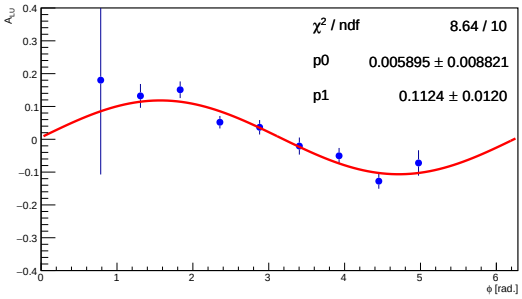

(c) Raw beam-spin asymmetry (A_{LU})

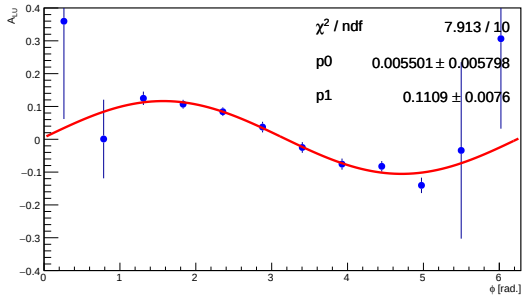

(d) Raw beam-spin asymmetry (A_{LU})

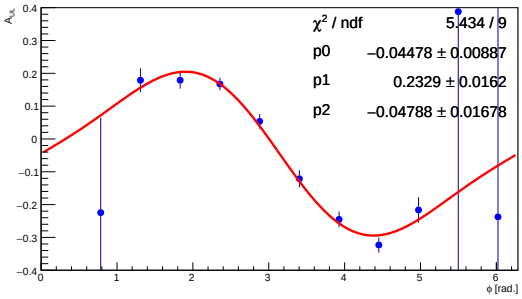

(e) Raw target-spin asymmetry (A_{UL})

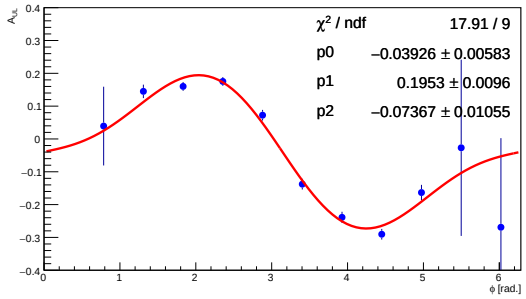

(f) Raw target-spin asymmetry (A_{UL})

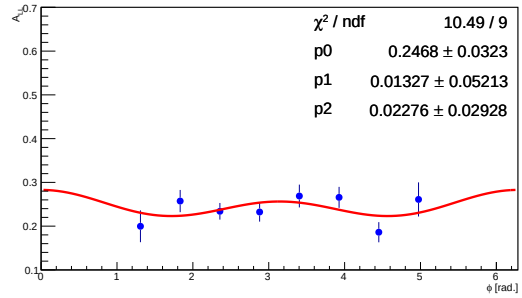

(g) Raw double-spin asymmetry (A_{LL})

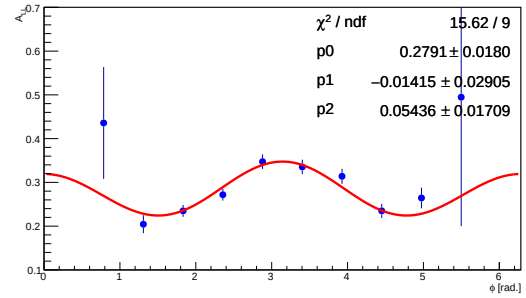

(h) Raw double-spin asymmetry (A_{LL})

Figure 5.8: π^+ channel: exclusive topology (left) and semi-inclusive topology (right), NH_3 target. sPlot fits made to the pion missing mass using a bifurcated Gaussian as the signal shape. Corresponding "raw" spin asymmetries are shown below both fits (left and right) in the three rows for the beam-, target- and double-spin asymmetries respectively.

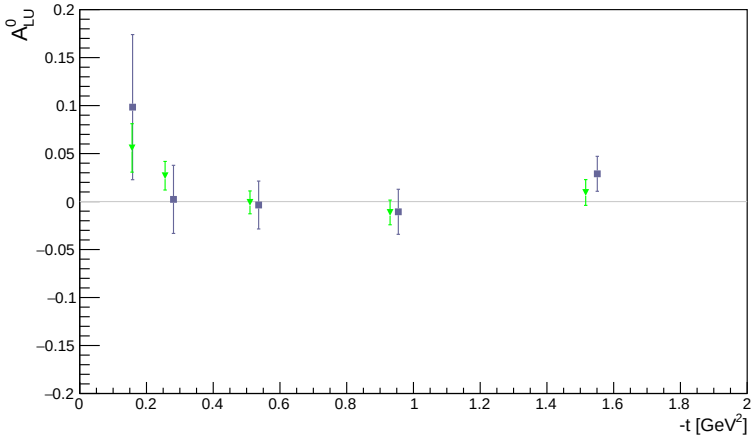

(a) A^0_{LU}

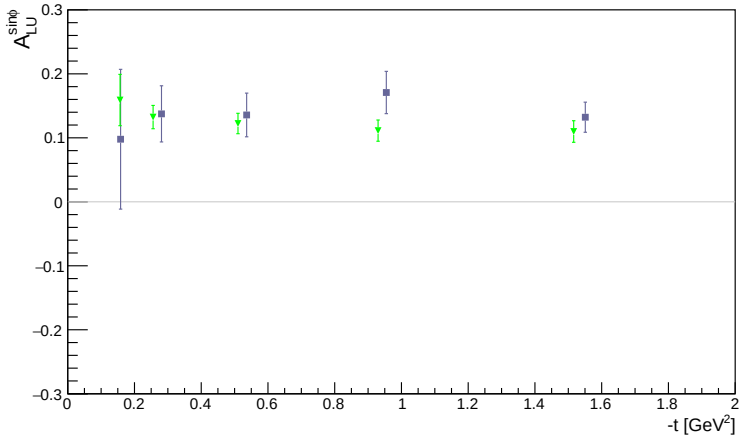

(b) $A^{sin\phi}_{LU}$

Figure 5.9: π^+ channel: NH_3 target. Beam-spin asymmetries binned in t. Shown for the data selected using the fits made to the pion missing mass using a bifurcated Gaussian as the signal shape for the exclusive topology (**blue-grey squares ■**) and semi-inclusive topology (**green down-pointing triangles ▼**).

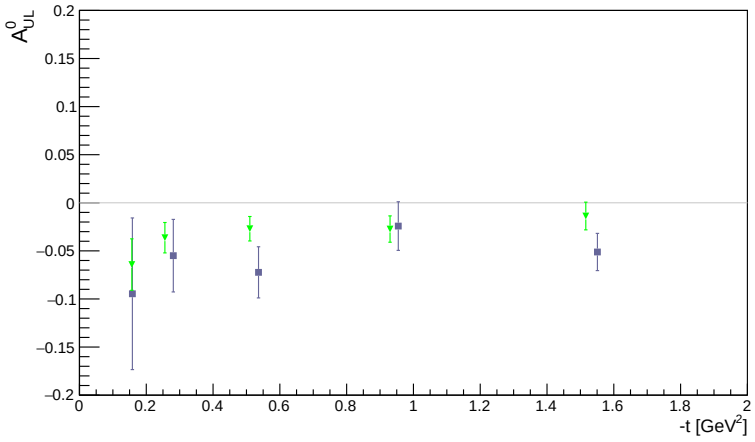

(a) A^0_{UL}

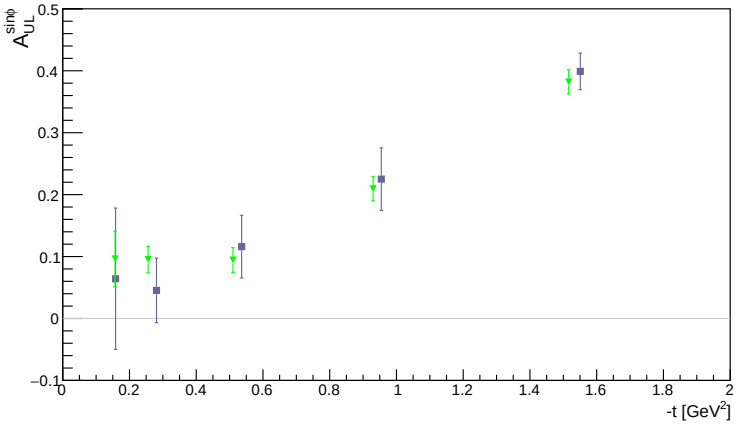

(b) $A^{sin\phi}_{UL}$

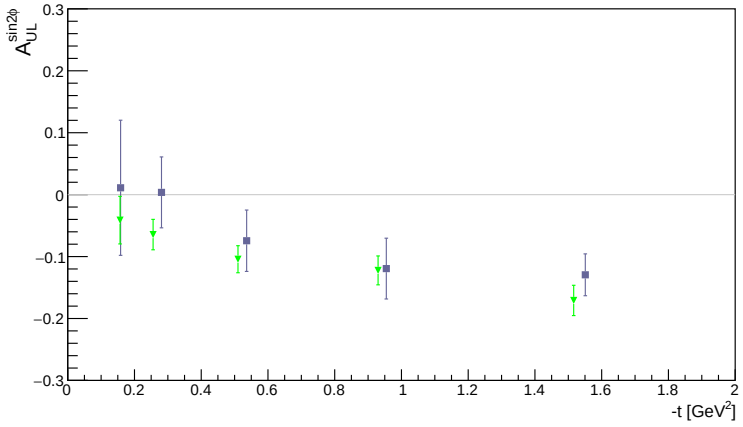

(c) $A^{sin2\phi}_{UL}$

Figure 5.10: π^+ channel: NH_3 target. Target-spin asymmetries binned in t. Shown for the data selected using the fits made to the pion missing mass using a bifurcated Gaussian as the signal shape for the exclusive topology (**blue-grey squares ■**) and semi-inclusive topology (**green down-pointing triangles ▼**).

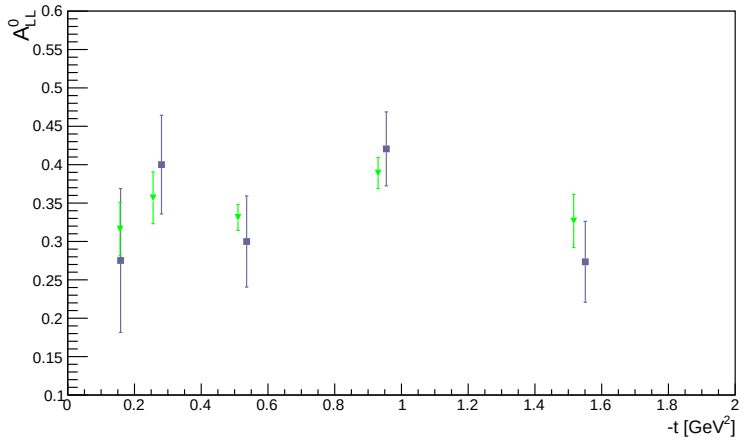

(a) A^0_{LL}

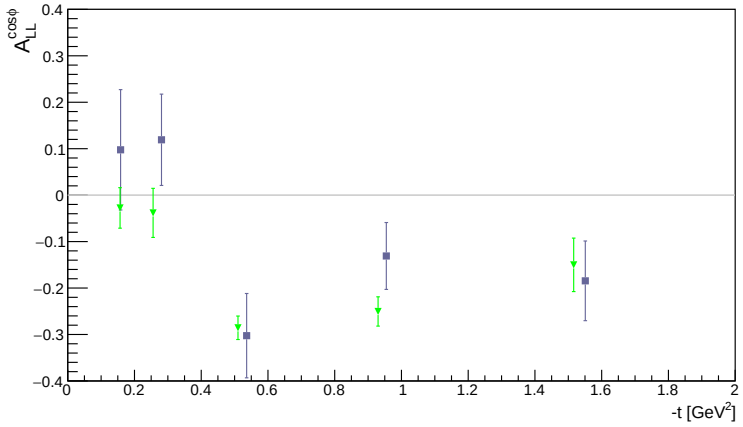

(b) $A^{cos\phi}_{LL}$

Figure 5.11: π^+ channel: NH_3 target. Double-spin asymmetries binned in t. Shown for the data selected using the fits made to the pion missing mass using a bifurcated Gaussian as the signal shape for the exclusive topology (**blue-grey squares ■**) and semi-inclusive topology (**green down-pointing triangles ▼**).

Run Period C - ND_3 Target

The high statistics for the π^+ channel with use of the NH_3 target was a clear indication of the possibility to cross-check this channel with use of the ND_3 target with data binned in t.

The sPlot fits and corresponding raw spin asymmetries for the measurement on the ND_3 target are shown in figure 5.12 and appear to be fairly consistent. The yield of signal is 18200 +/- 300 for the exclusive topology and 47700 +/- 800 for the semi-inclusive topology. It is clear that the signal-to-background ratio is less than in the NH_3 data. The signal peak is smeared for both topologies in comparison to the NH_3 data which is due to the fact that the proton target is loosely bound in a deuteron and therefore has some Fermi momentum in this nucleus. It is for this reason that both the left and right sides of the bifurcated Gaussian signal shape are wider for the ND_3 data.

The binned beam-, target- and double-spin asymmetries are shown in figures 5.13, 5.14, and 5.15. There is consistency between the two topologies. The errors are quite large for the sine and cosine ϕ terms of the target- and double-spin asymmetries.

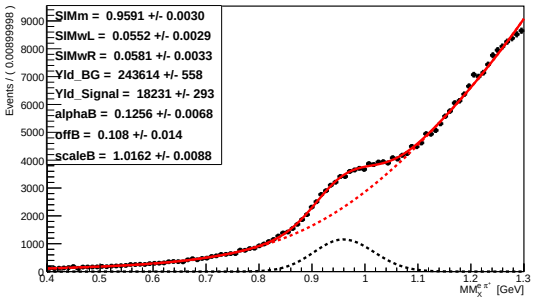

(a) Exclusive topology fit

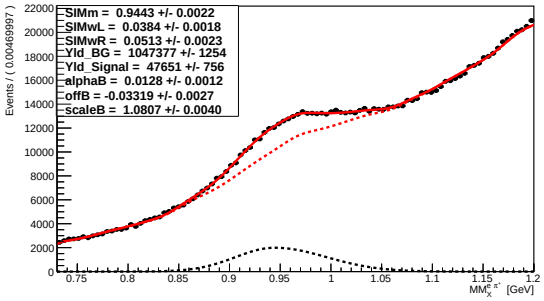

(b) Semi-Inclusive topology fit

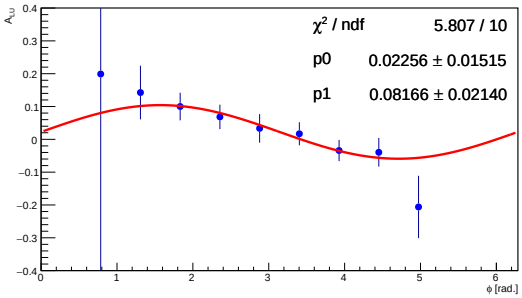

(c) Raw beam-spin asymmetry (A_{LU})

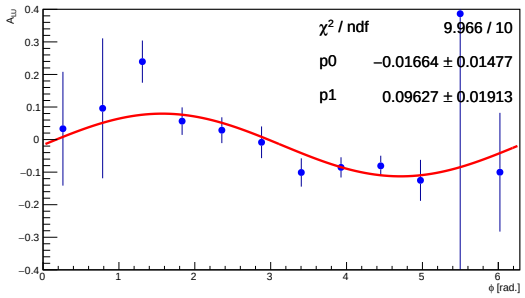

(d) Raw beam-spin asymmetry (A_{LU})

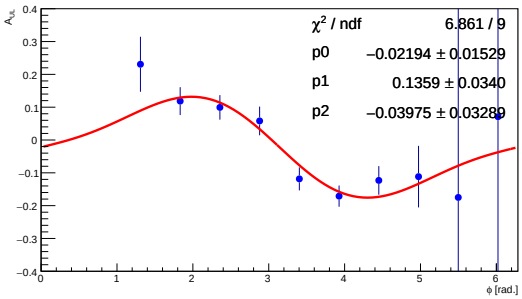

(e) Raw target-spin asymmetry (A_{UL})

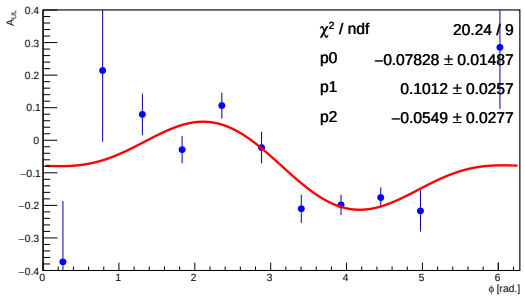

(f) Raw target-spin asymmetry (A_{UL})

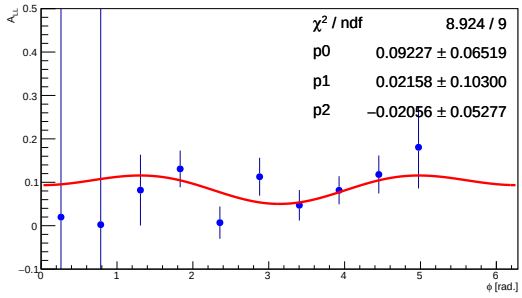

(g) Raw double-spin asymmetry (A_{LL})

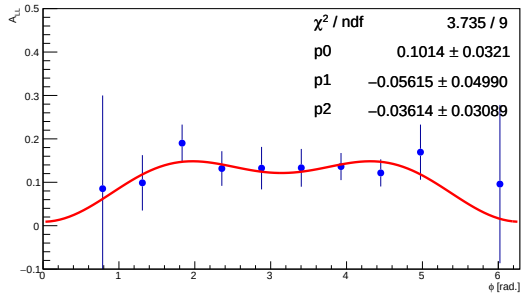

(h) Raw double-spin asymmetry (A_{LL})

Figure 5.12: π^+ channel: exclusive topology (left) and semi-inclusive topology (right), ND_3 target. sPlot fits made to the pion missing mass using a bifurcated Gaussian as the signal shape. Corresponding "raw" spin asymmetries are shown below both fits (left and right) in the three rows for the beam-, target- and double-spin asymmetries respectively.

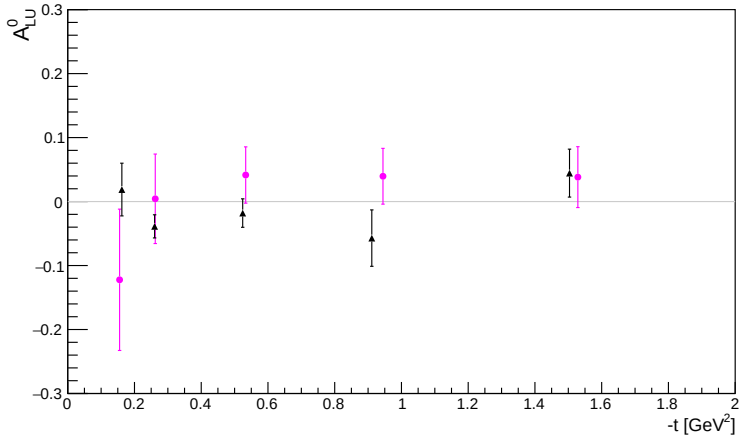

(a) A_{LU}^{0}

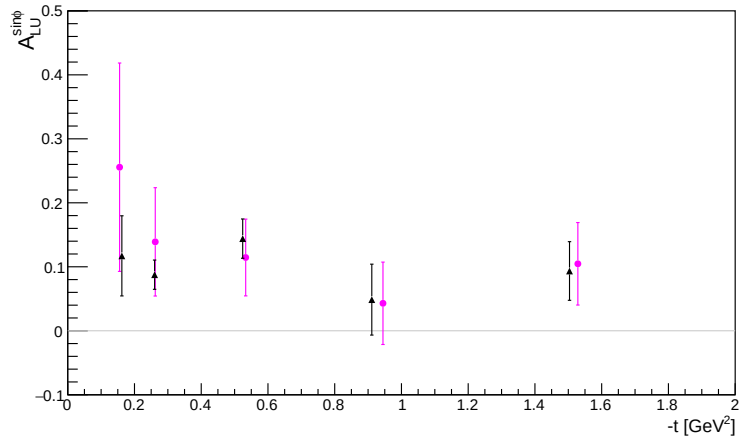

(b) $A_{LU}^{sin\phi}$

Figure 5.13: π^+ channel: ND_3 target. Beam-spin asymmetries binned in t. Shown for the data selected using the fits made to the pion missing mass using a bifurcated Gaussian as the signal shape for the exclusive topology (**magenta circles ●**) and semi-inclusive topology (**black up-pointing triangles ▲**).

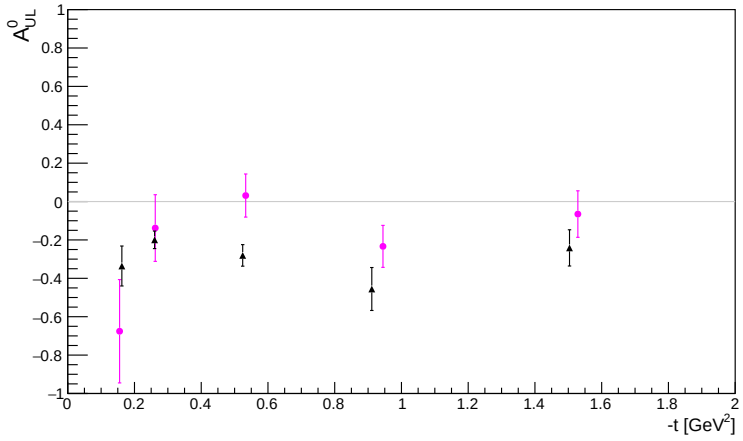

(a) A^0_{UL}

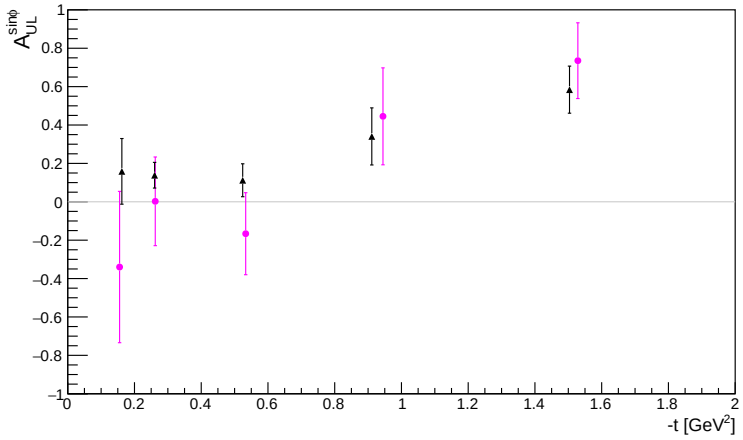

(b) $A^{sin\phi}_{UL}$

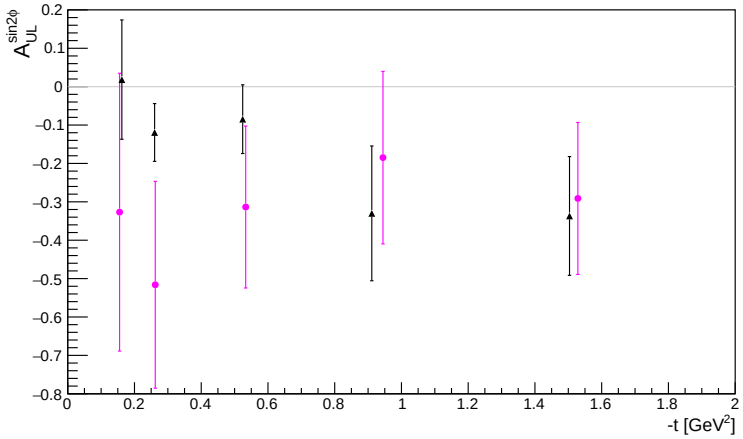

(c) $A^{sin2\phi}_{UL}$

Figure 5.14: π^+ channel: ND_3 target. Target-spin asymmetries binned in t. Shown for the data selected using the fits made to the pion missing mass using a bifurcated Gaussian as the signal shape for the exclusive topology (**magenta circles ●**) and semi-inclusive topology (**black up-pointing triangles ▲**).

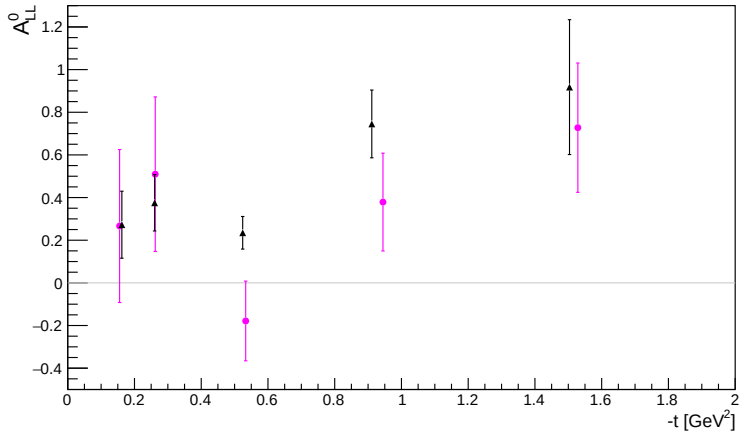

(a) A_{LL}^{0}

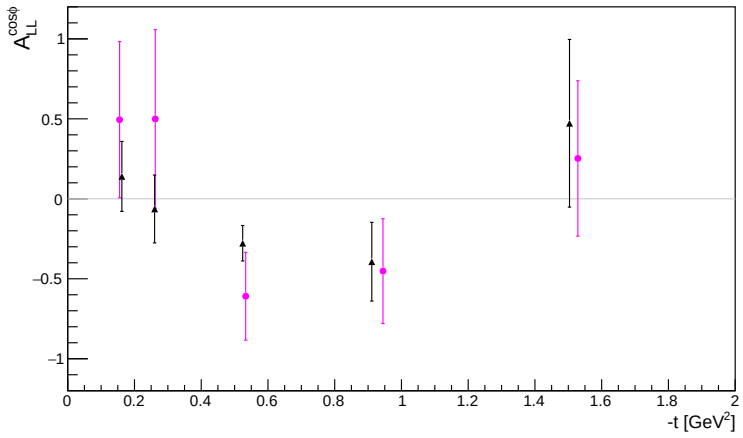

(b) $A_{LL}^{cos\phi}$

Figure 5.15: π^+ channel: ND_3 target. Double-spin asymmetries binned in t. Shown for the data selected using the fits made to the pion missing mass using a bifurcated Gaussian as the signal shape for the exclusive topology (**magenta circles ●**) and semi-inclusive topology (**black up-pointing triangles ▲**).

Comparison of Exclusive π^+ Results from the NH_3 and ND_3 Targets

Figure 5.16 is a reminder of the sPlot fits and raw spin asymmetries obtained for the exclusive topology for the NH_3 and ND_3 data.

For ease of comparison, the binned beam-, target- and double-spin asymmetries are shown in figures 5.17, 5.18, and 5.19. These figures really highlight the issue of low statistics for the ND_3 target data. The results do appear broadly consistent but it is difficult to make conclusive statements due to the extremely large error bars on the parameters from fits to the ND_3 data.

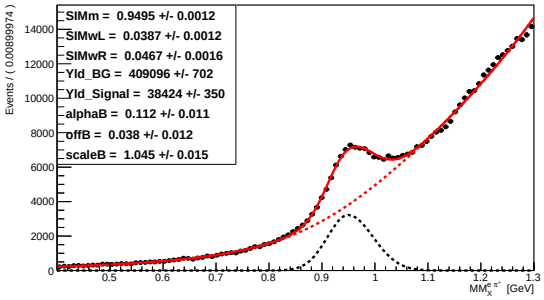

(a) Exclusive topology fit for NH_3 data

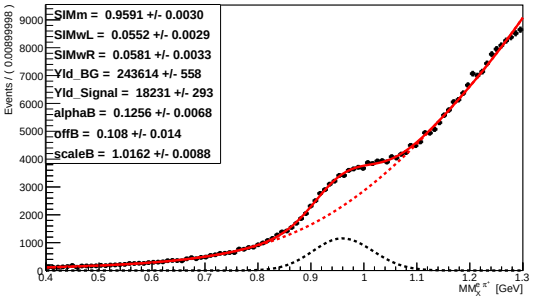

(b) Exclusive topology fit for ND_3 data

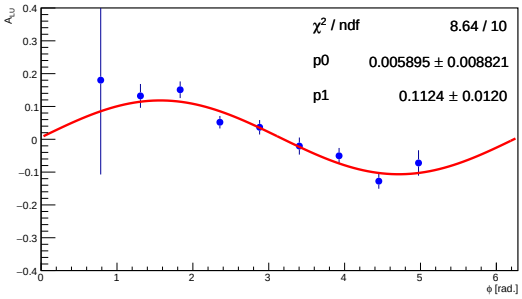

(c) Raw beam-spin asymmetry (A_{LU})

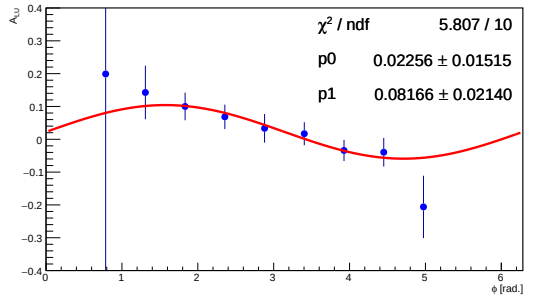

(d) Raw beam-spin asymmetry (A_{LU})

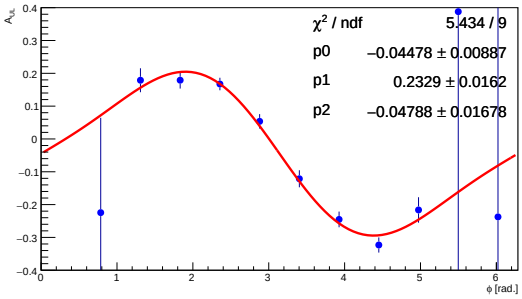

(e) Raw target-spin asymmetry (A_{UL})

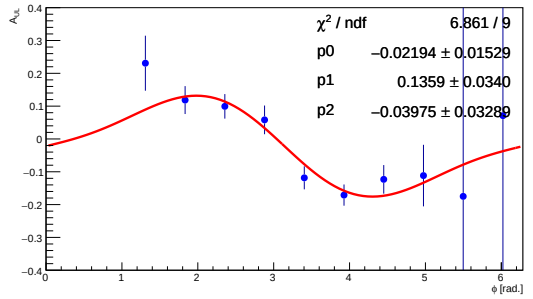

(f) Raw target-spin asymmetry (A_{UL})

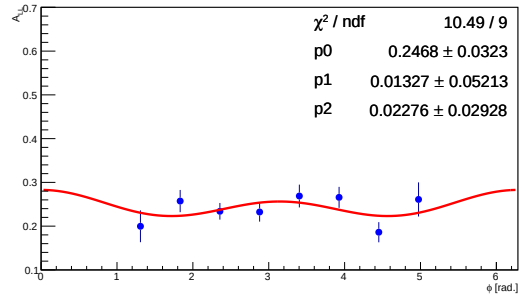

(g) Raw double-spin asymmetry (A_{LL})

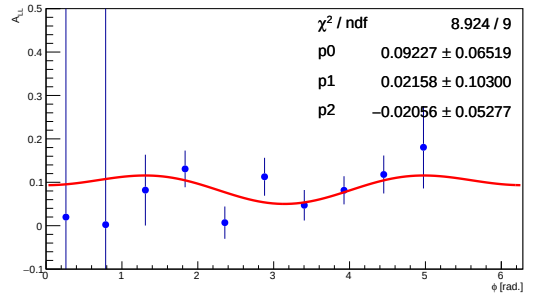

(h) Raw double-spin asymmetry (A_{LL})

Figure 5.16: π^+ channel: exclusive topology, part B NH_3 target (left) and part C ND_3 target (right). sPlot fits made to the pion missing mass using a bifurcated Gaussian as the signal shape. Corresponding "raw" spin asymmetries are shown below both fits (left and right) in the three rows for the beam-, target- and double-spin asymmetries respectively.

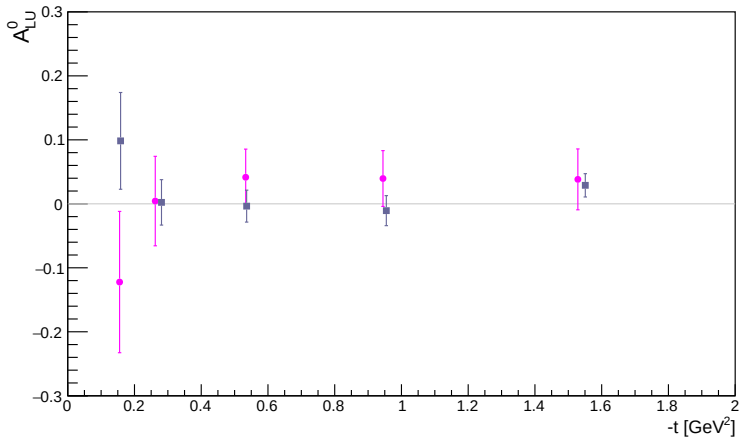

(a) A^0_{LU}

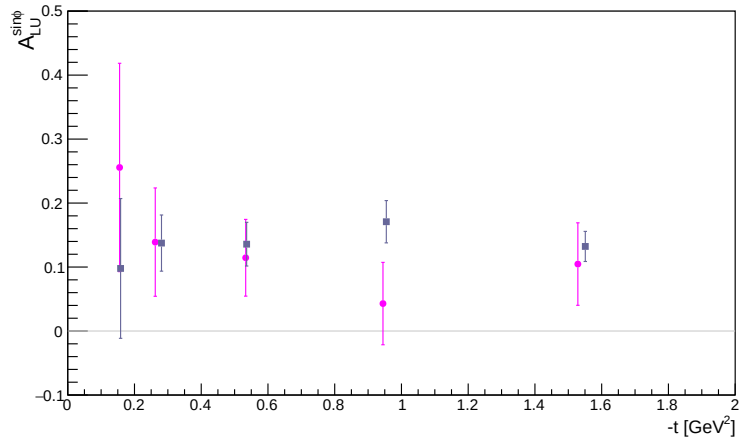

(b) $A^{sin\phi}_{LU}$

Figure 5.17: π^+ channel: exclusive topology. Beam-spin asymmetries binned in t. Shown for the data selected using the fits made to the pion missing mass using a bifurcated Gaussian as the signal shape for the NH_3 target (**blue-grey squares** ■) and ND_3 target (**magenta circles** ●).

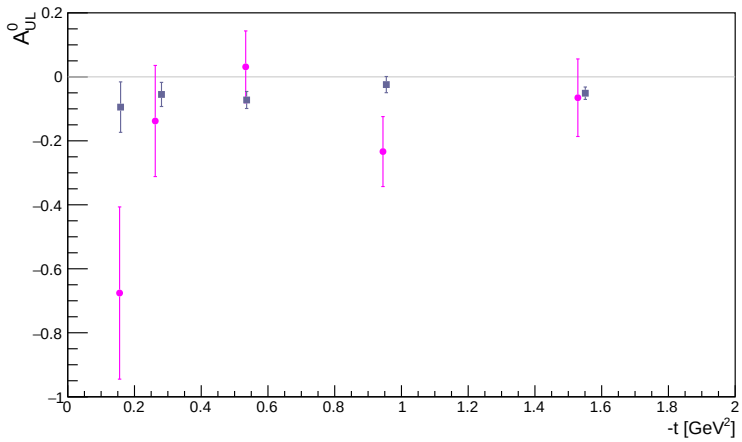

(a) A^0_{UL}

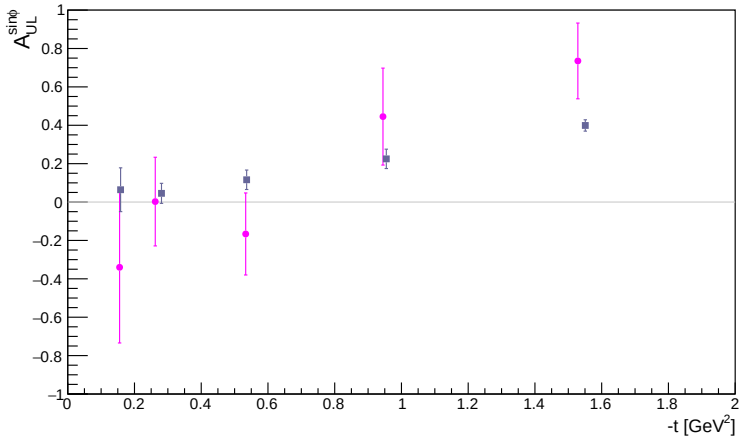

(b) $A^{sin\phi}_{UL}$

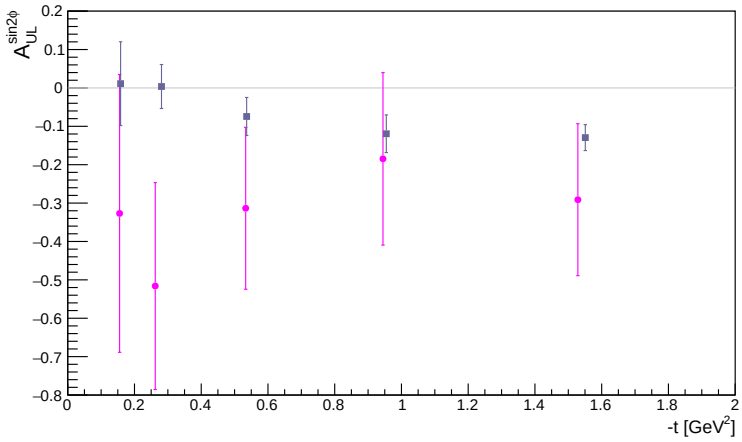

(c) $A^{sin2\phi}_{UL}$

Figure 5.18: π^+ channel: exclusive topology. Target-spin asymmetries binned in t. Shown for the data selected using the fits made to the pion missing mass using a bifurcated Gaussian as the signal shape for the NH_3 target (**blue-grey squares** ■) and ND_3 target (**magenta circles** ●).

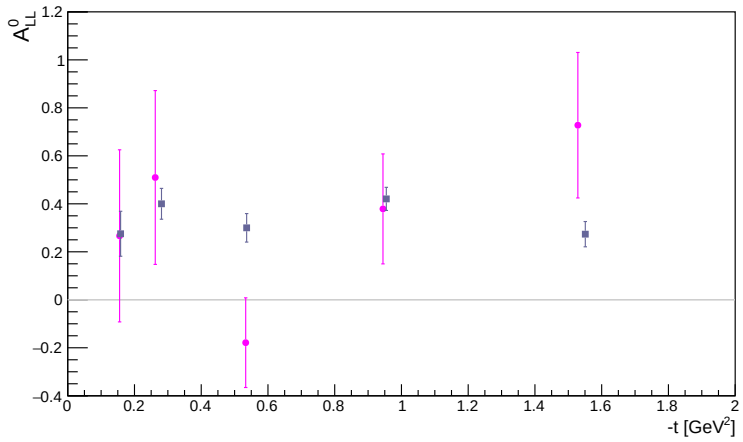

(a) A_{LL}^{0}

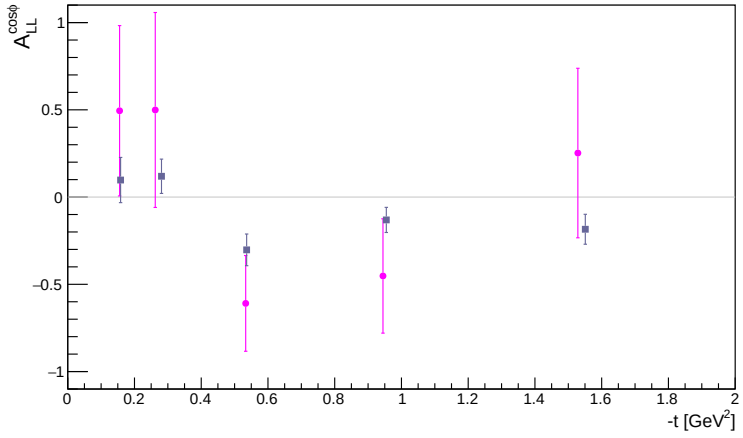

(b) $A_{LL}^{cos\phi}$

Figure 5.19: π^+ channel: exclusive topology. Double-spin asymmetries binned in t. Shown for the data selected using the fits made to the pion missing mass using a bifurcated Gaussian as the signal shape for the NH_3 target (**blue-grey squares** ■) and ND_3 target (**magenta circles** ●).

Comparison of Semi-Inclusive π^+ Results from the NH_3 and ND_3 Targets

Similarly, the sPlot fits and raw spin asymmetries obtained for the semi-inclusive topology for the NH_3 and ND_3 data are shown in figure 5.20. Since the statistics are highest for the semi-inclusive topology for the NH_3 data, these results will be particularly useful as a cross-check. It can be seen that the raw double-spin asymmetry shape appears to be quite different for the ND_3 data, with the errors being almost as large as the p_1 and p_2 fit parameters.

The binned beam-, target- and double-spin asymmetries are shown in figures 5.21, 5.22, and 5.23. The large difference in the constant term of the target-spin asymmetry implies that the target luminosity correction is quite significant for the ND_3 data, and will also have an effect on the constant term of the double-spin asymmetry. Most of the sine and cosine term results seem compatible when taking the uncertainties into account.

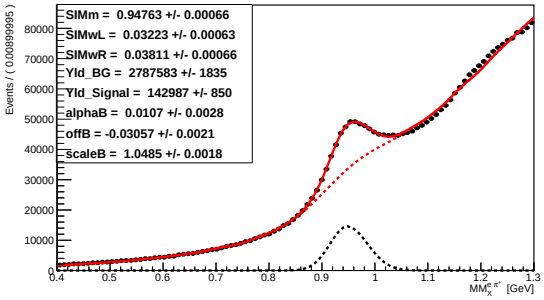

(a) Semi-Inclusive topology fit

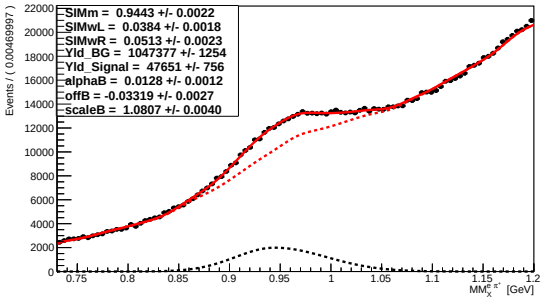

(b) Semi-Inclusive topology fit

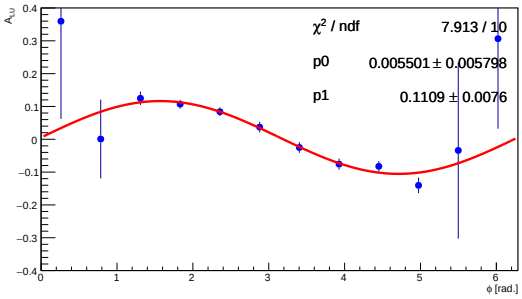

(c) Raw beam-spin asymmetry (A_{LU})

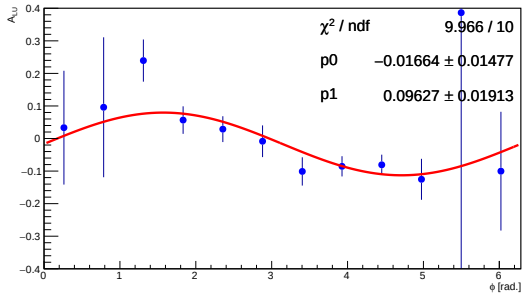

(d) Raw beam-spin asymmetry (A_{LU})

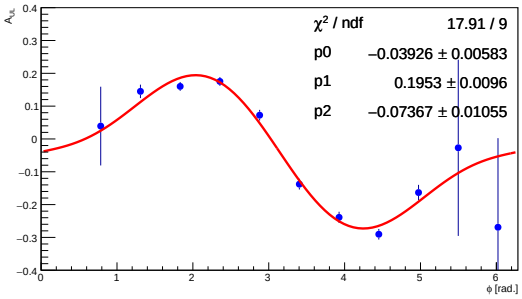

(e) Raw target-spin asymmetry (A_{UL})

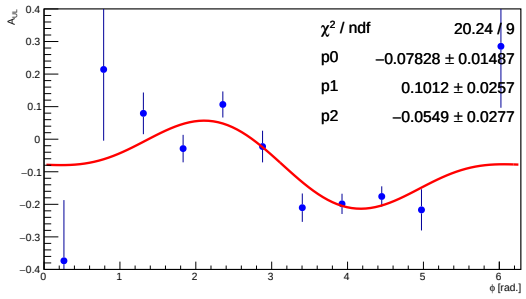

(f) Raw target-spin asymmetry (A_{UL})

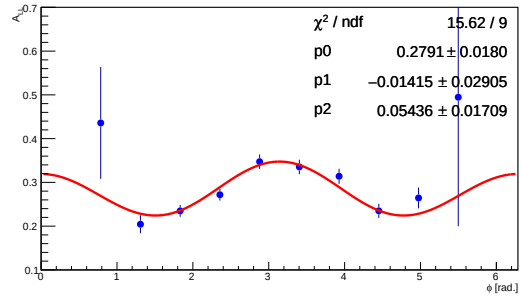

(g) Raw double-spin asymmetry (A_{LL})

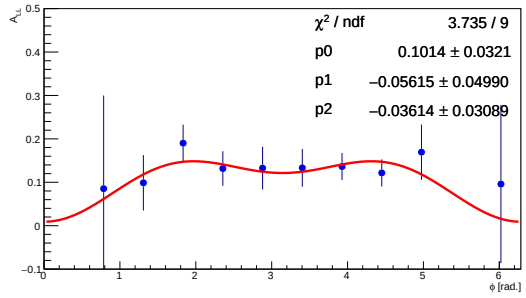

(h) Raw double-spin asymmetry (A_{LL})

Figure 5.20: π^+ channel: semi-inclusive topology, part B NH_3 target (left) and part C ND_3 target (right). sPlot fits made to the pion missing mass using a bifurcated Gaussian as the signal shape. Corresponding "raw" spin asymmetries are shown below both fits (left and right) in the three rows for the beam-, target- and double-spin asymmetries respectively.

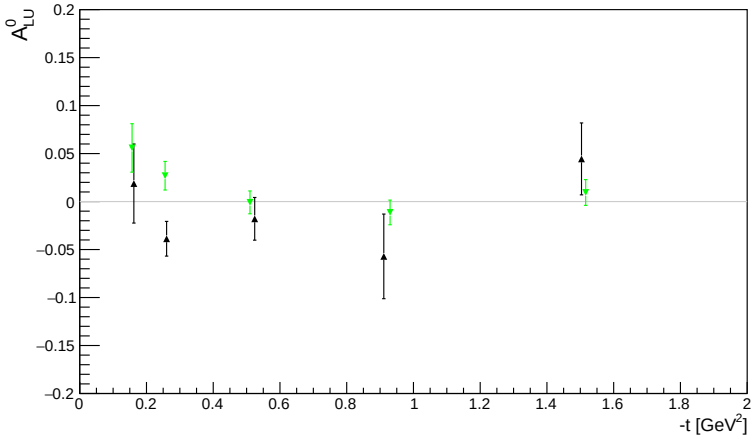

(a) A^0_{LU}

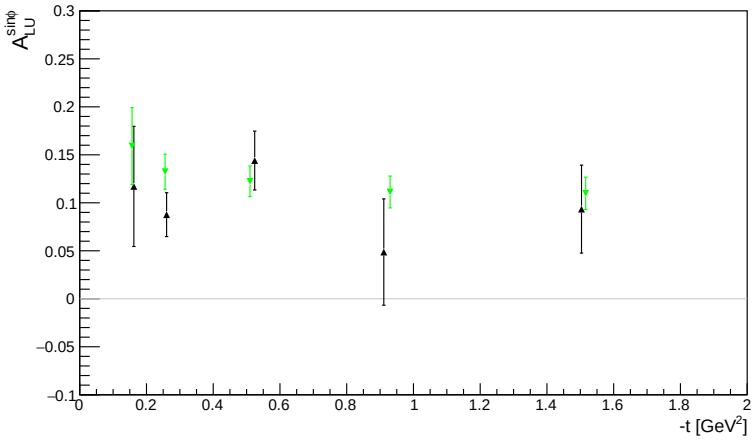

(b) $A^{sin\phi}_{LU}$

Figure 5.21: π^+ channel: semi-inclusive topology. Beam-spin asymmetries binned in t. Shown for the data selected using the fits made to the pion missing mass using a bifurcated Gaussian as the signal shape for the NH_3 target (**green down-pointing triangles ▼**) and ND_3 target (**black up-pointing triangles ▲**).

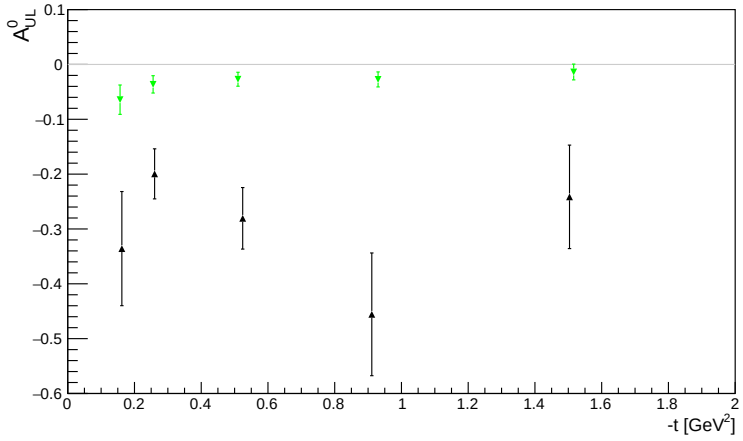

(a) A^0_{UL}

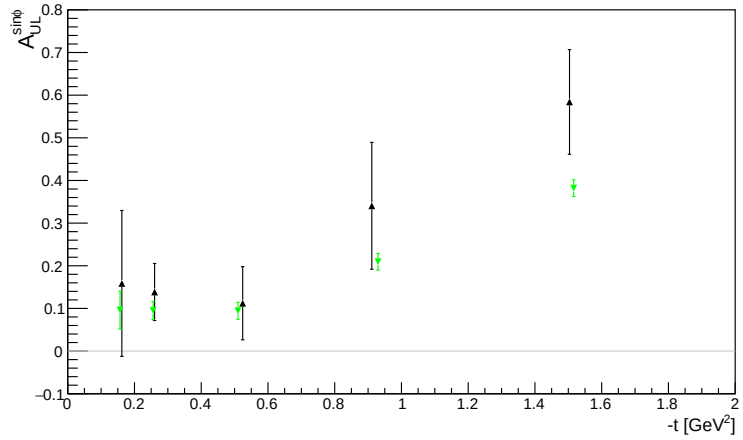

(b) $A^{sin\phi}_{UL}$

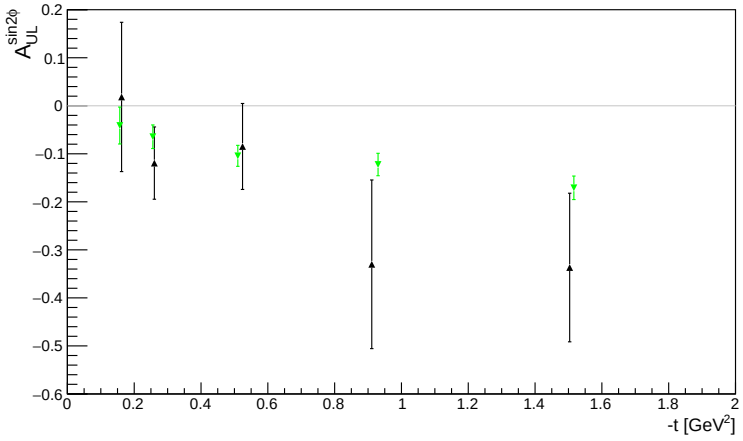

(c) $A^{sin2\phi}_{UL}$

Figure 5.22: π^+ channel: semi-inclusive topology. Target-spin asymmetries binned in t. Shown for the data selected using the fits made to the pion missing mass using a bifurcated Gaussian as the signal shape for the NH_3 target (**green down-pointing triangles ▼**) and ND_3 target (**black up-pointing triangles ▲**).

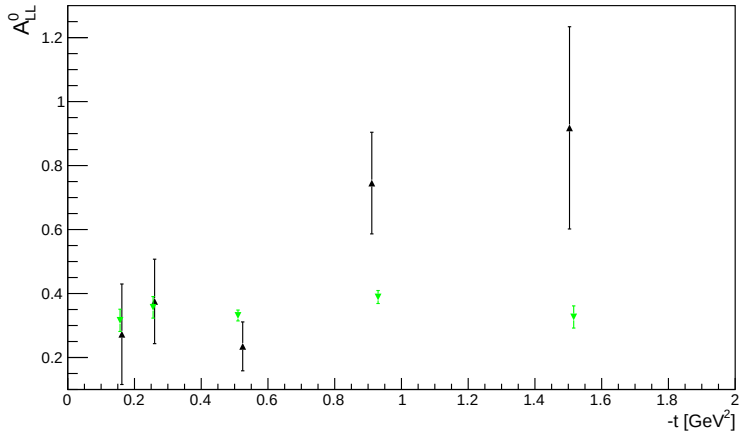

(a) A_{LL}^{0}

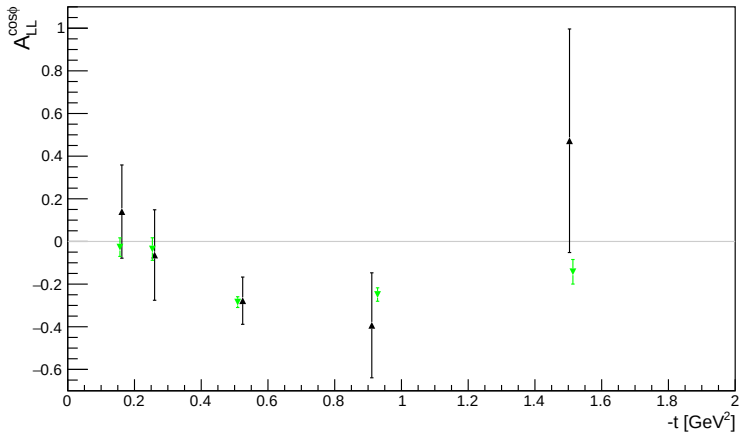

(b) $A_{LL}^{cos\phi}$

Figure 5.23: π^+ channel: semi-inclusive topology. Double-spin asymmetries binned in t. Shown for the data selected using the fits made to the pion missing mass using a bifurcated Gaussian as the signal shape for the NH_3 target (**green down-pointing triangles ▼**) and ND_3 target (**black up-pointing triangles ▲**).

Comparison of π^+ Results in Both Topologies and for Both Target Materials

The binned asymmetries from the exclusive and semi-inclusive topologies for both the NH_3 and ND_3 targets will be presented on the same graphs for a complete reference of the results for the π^+ DVMP process.

The binned beam-, target-and double-spin asymmetries are shown in figures 5.24, 5.25, and 5.26. The sine and cosine terms of the asymmetries require no luminosity corrections, and it is clear that they generally show good agreement. The constant terms which require luminosity corrections at least follow similar trends for each topology and each target material as would be expected if their differences are due to a normalisation factor.

Although the uncertainties are significantly larger for the analysis of the ND_3 target data, the results which require no corrections do seem to be rather consistent. This self consistency shows the success of sPlot method, in particular in being able to analyse the semi-inclusive topologies for the extraction of exclusive measurements, such as DVMP asymmetries.

All results show the $A_{UL}^{sin\phi}$ target-spin asymmetry term gradually increasing for large t (where the pion pole contribution no longer dominates). It is important to highlight that this trend was not observed for the π^0 channel.

Results for the free and quasi-free nucleon are broadly consistent and the semi-inclusive topology may be used to obtain them, which increases the statistical sample. This is the premise of the π^- channel analysis that follows in the next section.

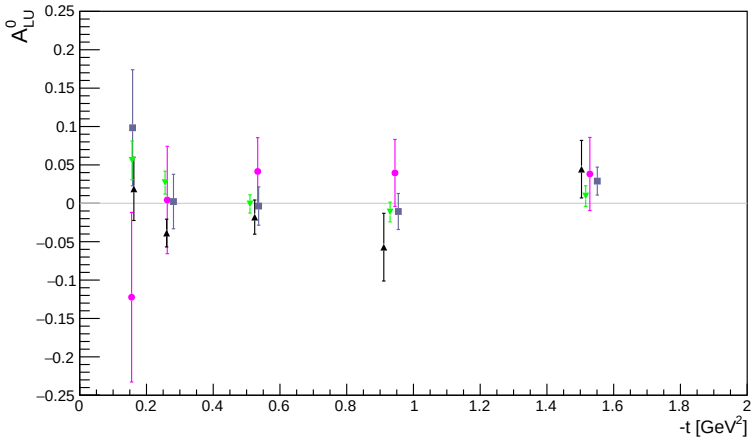

(a) A^0_{LU}

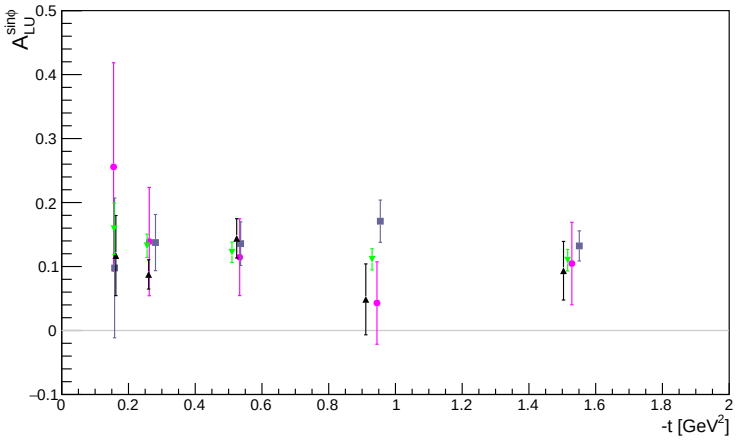

(b) $A^{sin\phi}_{LU}$

Figure 5.24: π^+ channel: all topologies. Beam-spin asymmetries binned in t. Shown for the data selected using the fits made to the pion missing mass using a bifurcated Gaussian for the exclusive NH_3 data (**blue-grey squares** ■), semi-inclusive NH_3 data (**green down-pointing triangles** ▼), exclusive ND_3 data (**magenta circles** ●), and semi-inclusive ND_3 data (**black up-pointing triangles** ▲).

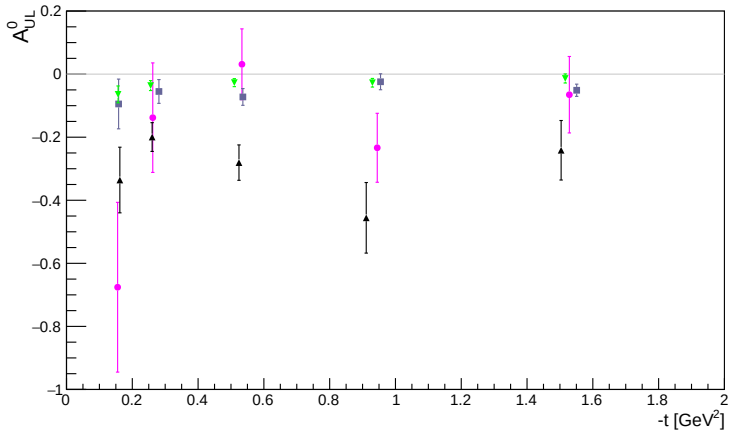

(a) A_{UL}^{0}

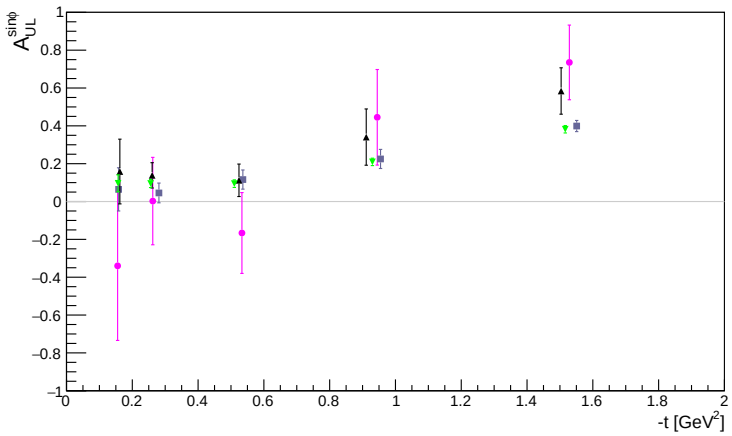

(b) $A_{UL}^{sin\phi}$

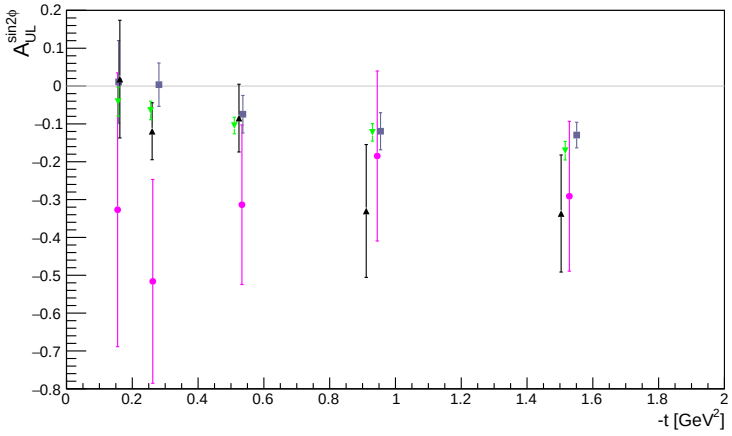

(c) $A_{UL}^{sin2\phi}$

Figure 5.25: π^+ channel: all topologies. Target-spin asymmetries binned in t. Shown for the data selected using the fits made to the pion missing mass using a bifurcated Gaussian for the exclusive NH_3 data (**blue-grey squares** ■), semi-inclusive NH_3 data (**green down-pointing triangles** ▼), exclusive ND_3 data (**magenta circles** ●), and semi-inclusive ND_3 data (**black up-pointing triangles** ▲).

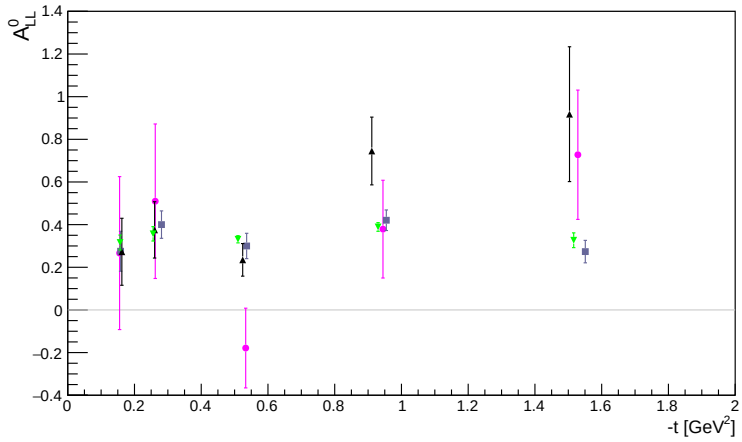

(a) A^0_{LL}

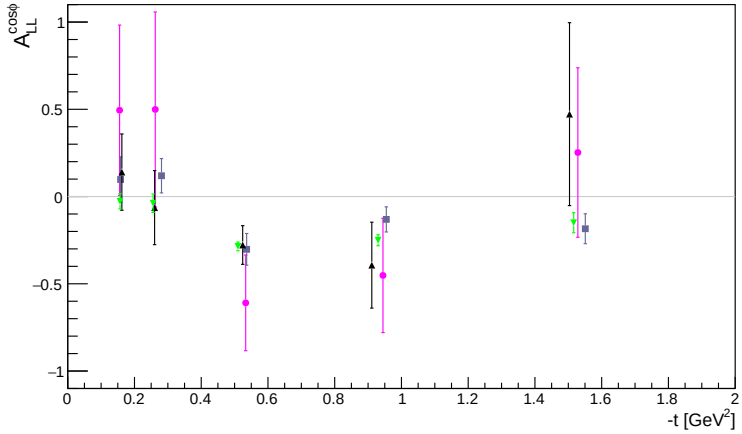

(b) $A^{cos\phi}_{LL}$

Figure 5.26: π^+ channel: all topologies. Double-spin asymmetries binned in t. Shown for the data selected using the fits made to the pion missing mass using a bifurcated Gaussian for the exclusive NH_3 data (**blue-grey squares** ■), semi-inclusive NH_3 data (**green down-pointing triangles** ▼), exclusive ND_3 data (**magenta circles** ●), and semi-inclusive ND_3 data (**black up-pointing triangles** ▲).

5.1.6 Results - π^- Channel

The spin asymmetry measurements presented are a first for this charged pion channel in this kinematic regime.

For the DVMP π^- channel the sPlot fits were performed on the pion missing mass and the spectator missing mass for the exclusive topology, and just the pion missing mass for the semi-inclusive topology. The fit to the spectator missing mass was carried out to further test the sPlot method's application to this low statistics channel with use of both the final state measured proton and π^- in CLAS which should provide a better description of the final state and remove the effect of Fermi momentum which is present in the pion missing mass distribution.

In particular, it was the low statistics of this channel that was problematic for the analysis of the exclusive topology and even the semi-inclusive topology. It was also the case that the statistics were low for the part C ^{12}C data and therefore the part B NH_3 data was instead used to model the background shape in the sPlot fits. This was a suitable choice for the sPlot method as it should better describe the background distribution and the statistics for this dataset were larger than those of the part C ND_3 signal dataset. Further details on this choice are given in a study presented in appendix B.

The sPlot fits and corresponding raw spin asymmetries will be compared for each of the three sPlot fits performed, and finally the asymmetry results binned in t will be presented for this channel.

Run Period C - ND_3 Target

Firstly, the exclusive topology was considered. The sPlot fits performed can be assessed for both the pion missing mass and spectator missing mass distributions, as shown in figures 5.27a and 5.27b respectively. The fit covered a very large range for the sPlot fit to the spectator missing mass and indicates a well suited choice of data modelling the background. With the peak being much more prominent for the spectator missing mass variable, the fitting procedure was easier than in the case of the pion missing mass. There is no smearing due to Fermi momentum in the spectator missing mass distribution, as is observed with both sides of the bifurcated Gaussian signal shape being narrower.

The yield of signal determined was 8300 +/- 200 for the pion missing mass fit, and 8500 +/- 200 for the spectator missing mass fit, and therefore should isolate the same sample of signal data. The corresponding raw asymmetries are shown below the sPlot fits in figure 5.27 and appear to be fairly similar but there seems to be a discrepancy in the double-spin asymmetry plots. Note, the same y-axis limits are used in both plots for each of the asymmetries.

Secondly, the semi-inclusive topology was considered. The sPlot fit was performed on the pion missing mass distribution, allowing for a direct comparison to the fit to this variable for the exclusive topology. These can be assessed for the exclusive and semi-inclusive topology in figures 5.28a and 5.28b respectively. The yield of signal increased from 8300 +/- 200 to

31800 +/- 500. The corresponding raw spin asymmetries are shown below the sPlot fits in figure 5.28 and appear to be fairly similar but there again seems to be a discrepancy in the double-spin asymmetry plots. Note, the same y-axis limits are used in both plots for each of the asymmetries.

Thirdly (and finally), the binned beam-, target- and double-spin asymmetries are shown in figures 5.29, 5.30, and 5.31. As for the π^+ channel, the pion pole contribution dominates the results in the region of $-t < 0.3$ GeV^2.

All fit terms can be compared as they are all from the same run period - part C ND_3. It would be more intuitive to use the result of the semi-inclusive topology as the main reference as the yield of signal was much higher for this, and therefore the errors are significantly smaller. The results seem to be in agreement, but there seems to be some discrepancy between the two fits for the exclusive topology, using data from the pion and the spectator missing masses, which is surprising as the signal sample isolated from the sPlot fits should be the same. The results presented for the beam-spin asymmetry term $A_{LU}^{sin\phi}$ seem to be non-zero and follow a trend consistent between all three methods of selecting the signal data - this seems to be a reliable result. The errors seem to be too large for this channel to assess if the terms are non-zero for the other parameters as a function of t. As the results seem to be centred around zero for the A_{LL}^0 term of the double-spin asymmetry, implementing beam and target luminosity corrections would confirm if this really is the case. Further discussion on the results obtained for the semi-inclusive topology for this channel are presented in section 5.1.6.

Within the magnitude of the uncertainties, there is, however, general agreement between the parameter values extracted in the three topologies for the π^- measurements.

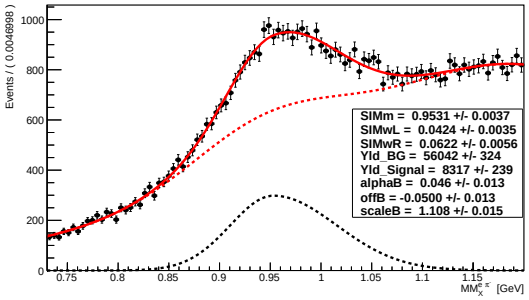

(a) Fit to the pion missing mass

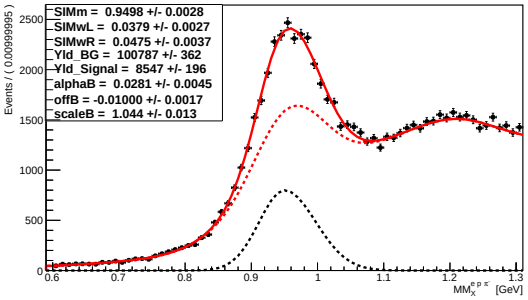

(b) Fit to the spectator missing mass

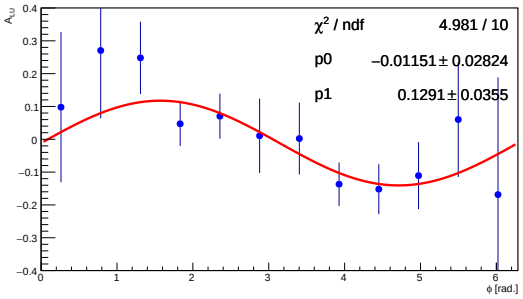

(c) Raw beam-spin asymmetry (A_{LU})

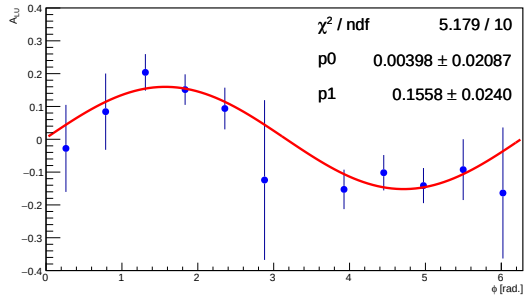

(d) Raw beam-spin asymmetry (A_{LU})

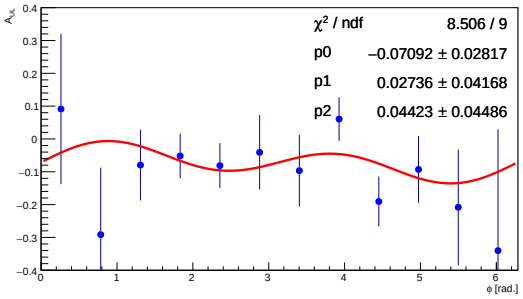

(e) Raw target-spin asymmetry (A_{UL})

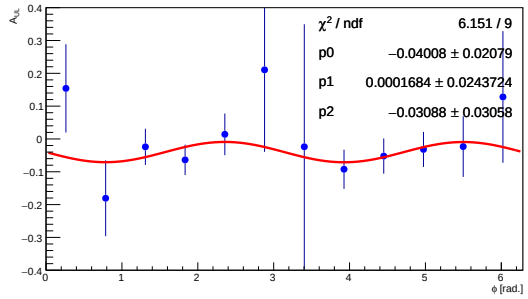

(f) Raw target-spin asymmetry (A_{UL})

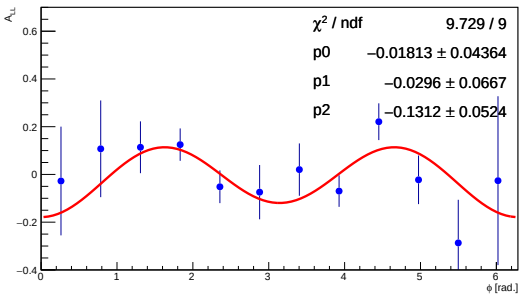

(g) Raw double-spin asymmetry (A_{LL})

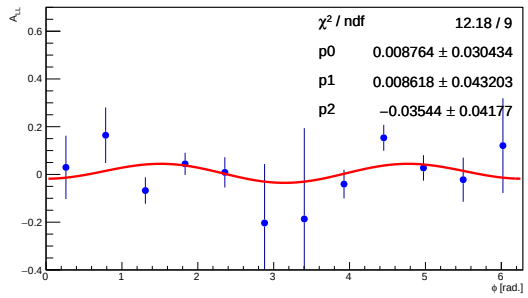

(h) Raw double-spin asymmetry (A_{LL})

Figure 5.27: π^- channel: exclusive topology, ND_3 target. sPlot fits made to the pion missing mass (left) and the spectator missing mass (right) using a bifurcated Gaussian as the signal shape. Corresponding "raw" spin asymmetries are shown below both fits (left and right) in three rows for the beam-, target- and double-spin asymmetries respectively.

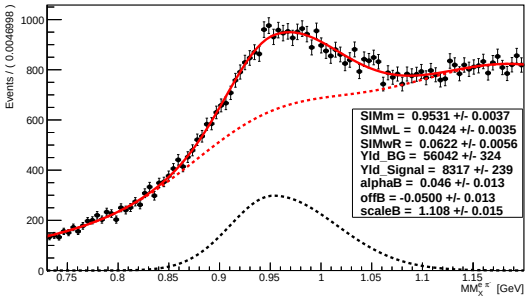

(a) Exclusive topology fit

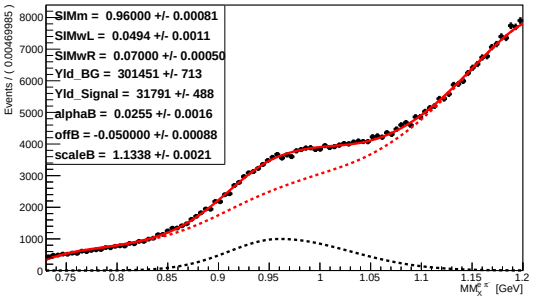

(b) Semi-Inclusive topology fit

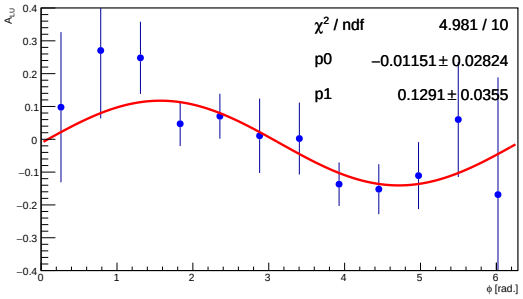

(c) Raw beam-spin asymmetry (A_{LU})

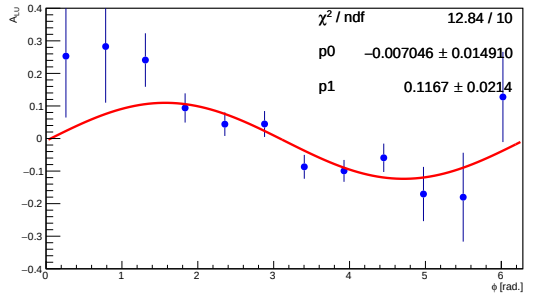

(d) Raw beam-spin asymmetry (A_{LU})

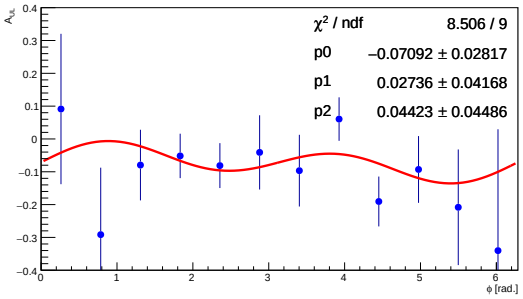

(e) Raw target-spin asymmetry (A_{UL})

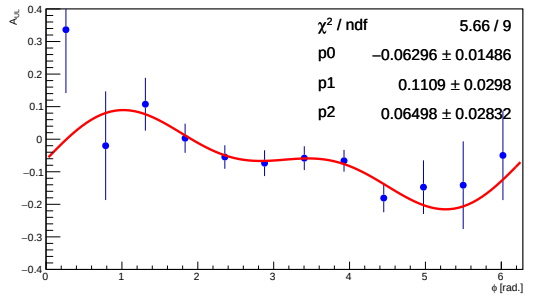

(f) Raw target-spin asymmetry (A_{UL})

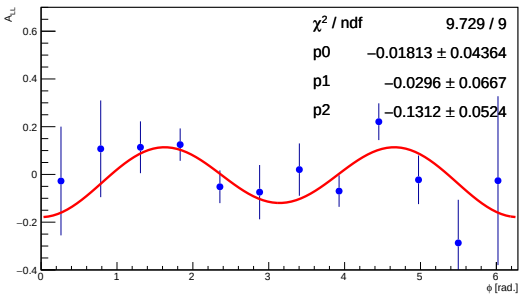

(g) Raw double-spin asymmetry (A_{LL})

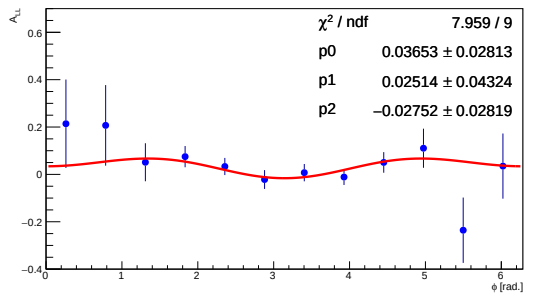

(h) Raw double-spin asymmetry (A_{LL})

Figure 5.28: π^- channel: exclusive topology (left) and semi-inclusive topology (right), ND_3 target. sPlot fits made to the pion missing mass using a bifurcated Gaussian as the signal shape. Corresponding "raw" spin asymmetries are shown below both fits (left and right) in three rows for the beam-, target- and double-spin asymmetries respectively.

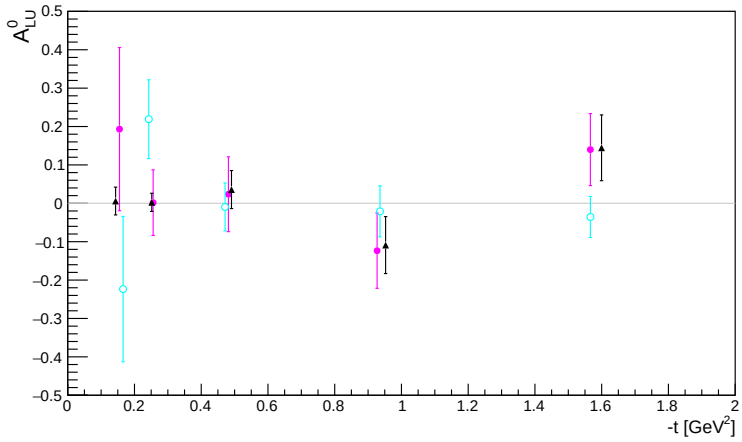

(a) A^0_{LU}

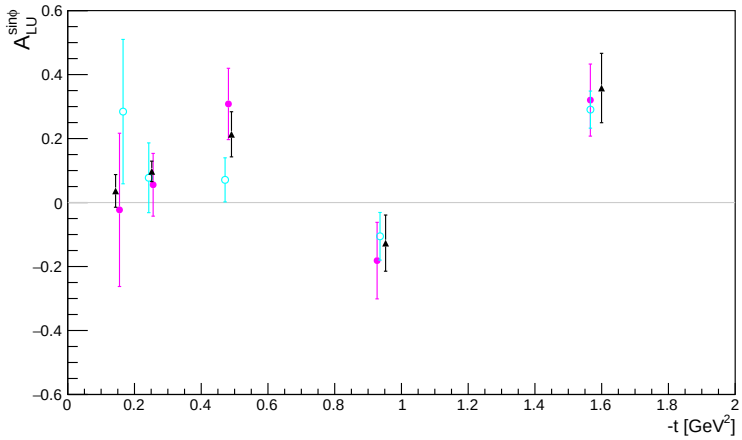

(b) $A^{sin\phi}_{LU}$

Figure 5.29: π^- channel: all topologies. Beam-spin asymmetries binned in t. Shown for the data selected using the fits made to the pion missing mass with a bifurcated Gaussian for the exclusive topology (**magenta circles ●**) and the semi-inclusive topology (**black up-pointing triangles ▲**), and for the data selected using the fit made to the spectator missing mass using a bifurcated Gaussian for the exclusive topology (**cyan open circles ○**).

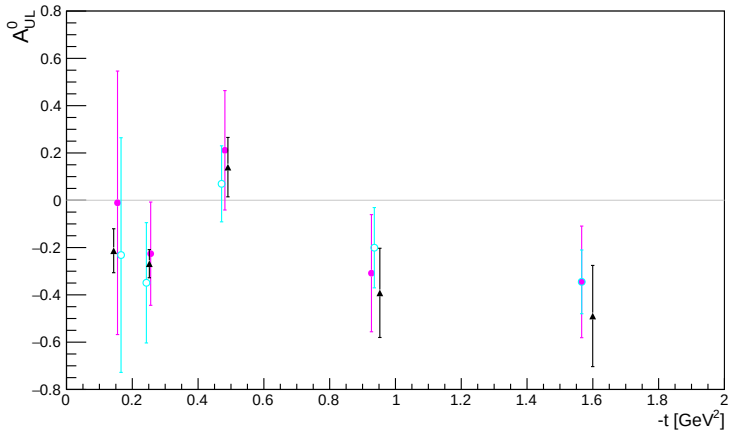

(a) A_{UL}^{0}

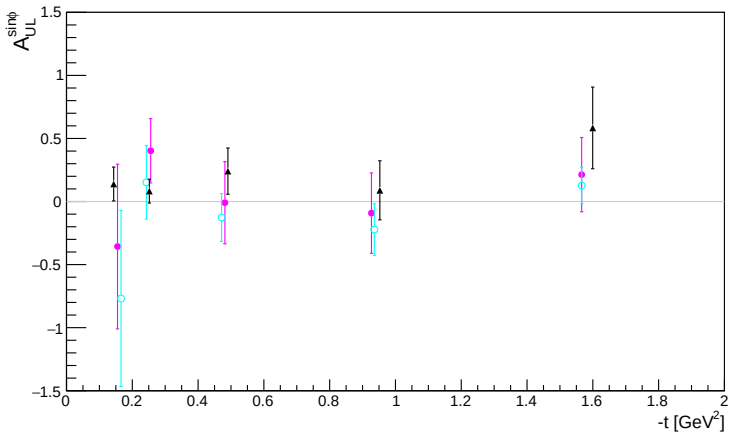

(b) $A_{UL}^{sin\phi}$

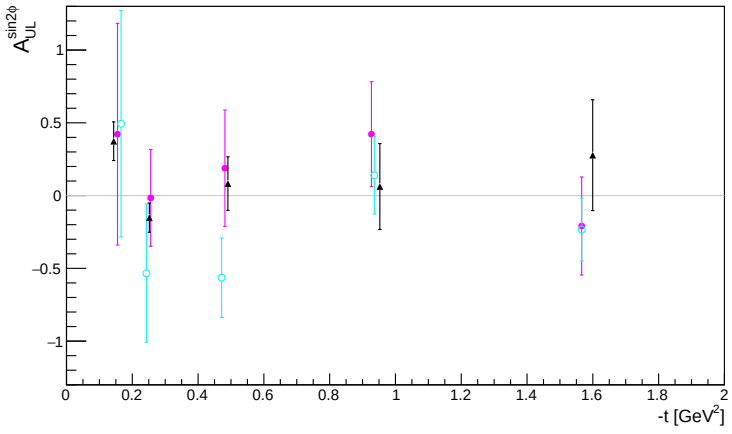

(c) $A_{UL}^{sin2\phi}$

Figure 5.30: π^- channel: all topologies. Target-spin asymmetries binned in t. Shown for the data selected using the fits made to the pion missing mass with a bifurcated Gaussian for the exclusive topology (**magenta circles ●**) and the semi-inclusive topology (**black up-pointing triangles ▲**), and for the data selected using the fit made to the spectator missing mass using a bifurcated Gaussian for the exclusive topology (**cyan open circles ○**).

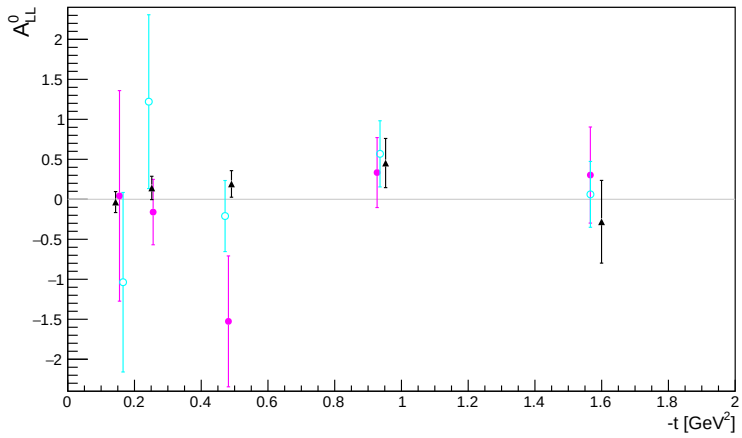

(a) A^0_{LL}

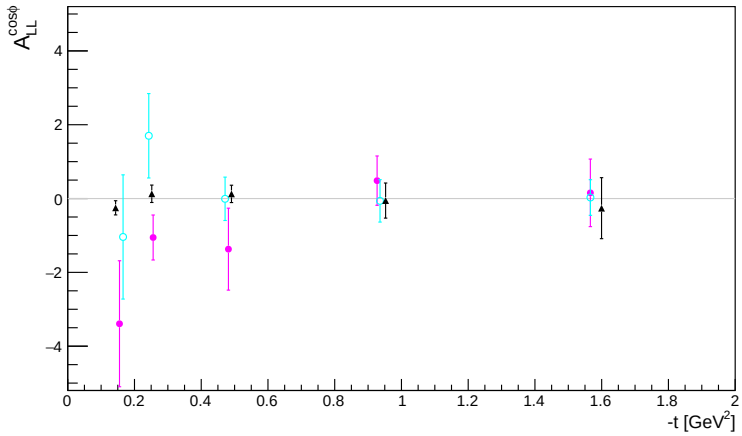

(b) $A^{cos\phi}_{LL}$

Figure 5.31: π^- channel: all topologies. Double-spin asymmetries binned in t. Shown for the data selected using the fits made to the pion missing mass with a bifurcated Gaussian for the exclusive topology (**magenta circles ●**) and the semi-inclusive topology (**black up-pointing triangles ▲**), and for the data selected using the fit made to the spectator missing mass using a bifurcated Gaussian for the exclusive topology (**cyan open circles ○**).

Semi-Inclusive π^- Results

As the highest statistics were obtained for the semi-inclusive topology (and therefore the errors are the smallest), it is best to view these results on their own. The binned beam-, target- and double-spin asymmetries are shown in figures 5.32, 5.33, and 5.34.

The results of the beam-spin A_{LU}^{0} term shown in figure 5.32a appear to show a flat trend, although an oscillation to a negative then positive result is observed in the fourth and fifth bin in t. The results of the beam-spin $A_{LU}^{sin\phi}$ term shown in figure 5.32b appear to show a gradual increase for the first three bins in t, before a significant oscillation to a negative value for the fourth bin, with the result for the fifth bin being significantly positive. Considering the magnitudes of the results, this trend is somewhat unique to this channel, although with errors taken into account the result for the fourth bin in t could also be classed as being negative for the π^+ channel when analysing the ND_3 target data. The result for the fifth bin in t is larger in magnitude than the measurements for both the π^0 and π^+ channels.

The graphs presented for the semi-inclusive topology help highlight that the beam-spin asymmetry magnitude is quite significant with a unique trait for this channel, and there may be a non-zero asymmetry for the target-spin asymmetry terms but the errors are too large to be really confident in this conclusion and discuss in detail.

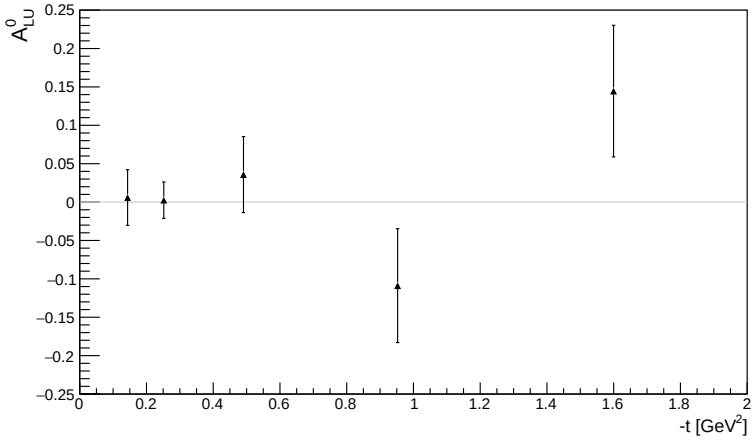

(a) A^0_{LU}

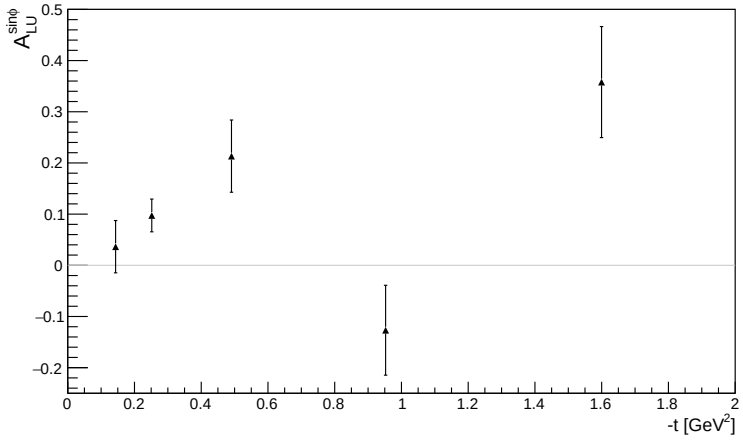

(b) $A^{sin\phi}_{LU}$

Figure 5.32: π^- channel: semi-inclusive topology. Beam-spin asymmetries binned in t. Shown for the data selected using the fit made to the pion missing mass with a bifurcated Gaussian.

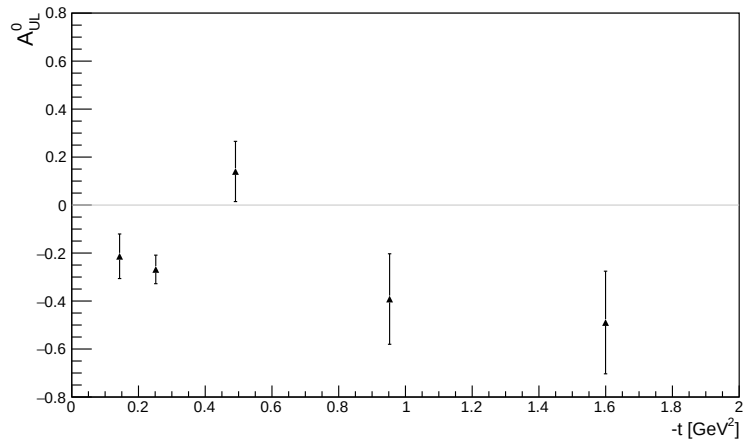

(a) A_{UL}^{0}

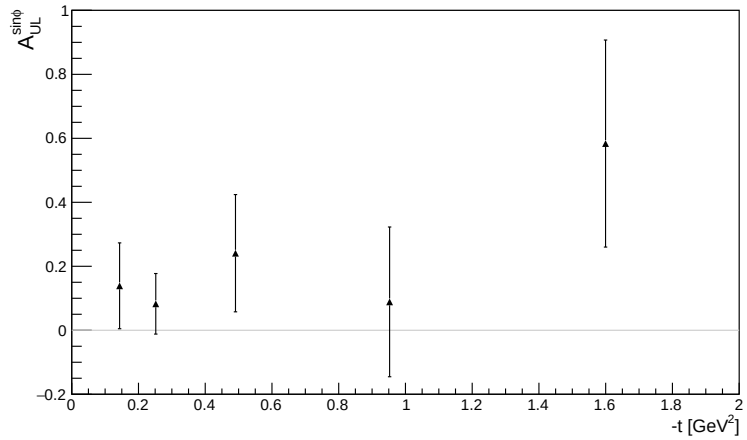

(b) $A_{UL}^{sin\phi}$

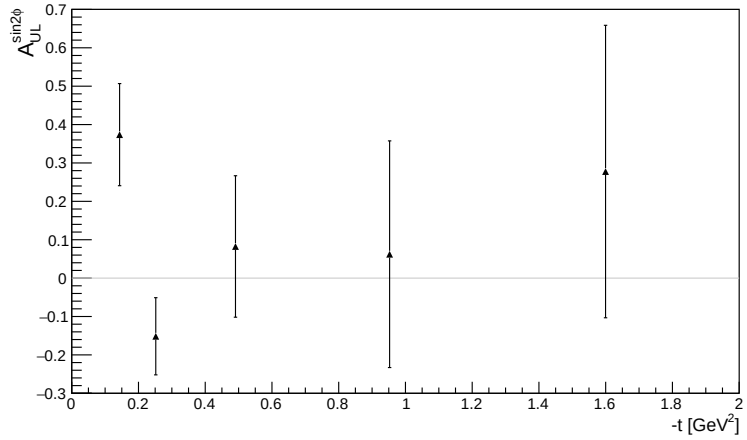

(c) $A_{UL}^{sin2\phi}$

Figure 5.33: π^- channel: semi-inclusive topology. Target-spin asymmetries binned in t. Shown for the data selected using the fit made to the pion missing mass using a bifurcated Gaussian.

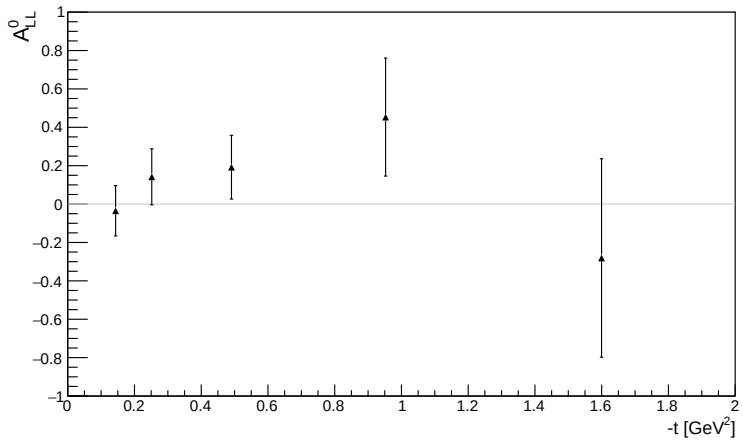

(a) A_{LL}^{0}

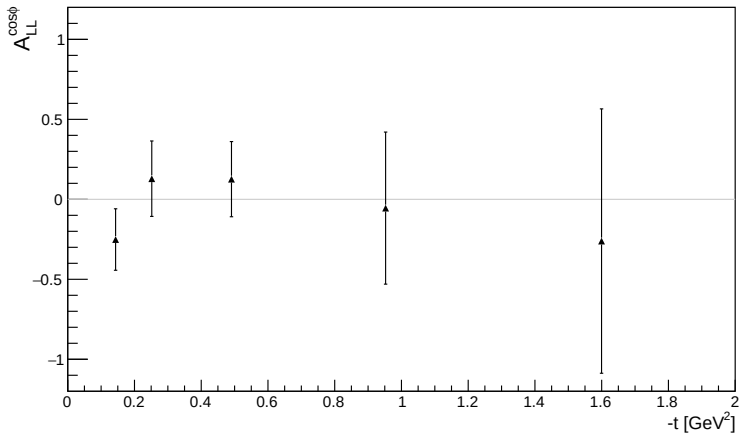

(b) $A_{LL}^{cos\phi}$

Figure 5.34: π^- channel: semi-inclusive topology. Double-spin asymmetries binned in t. Shown for the data selected using the fit made to the pion missing mass using a bifurcated Gaussian.

5.2 Systematic Uncertainties

Many sources of uncertainties can affect the extracted values for each of the three asymmetries analysed. The suspected main sources to contribute to the systematic uncertainties in the final results are discussed below.

Published results of target- and double-spin asymmetries for the π^0 and π^+ electroproduction channels across a large range of W in the EG1-DVCS experiment made suitable comments on key systematic uncertainties for the experiment [35]. The dominant source was stated as being that from the determination of the beam and target polarisations (P_B and P_T) which were used as scale normalisation factors in calculating the asymmetries. The error on the beam polarisation Møller measurement was $\sim 4\%$, and on the target polarisation was also $\sim 4\%$ for both the Part B NH_3 and Part C ND_3 targets [86]. The error on the measured value of P_BP_T through ep exclusive elastic scattering studies was found to be $\sim 1.1\%$ for the Part B NH_3 data [87]. Due to the average polarisation of the Part C ND_3 target being much smaller than that of the Part B NH_3 target, the systematic uncertainty on P_BP_T was of the order of 7% for the ND_3 target [72].

The sPlot technique was used in successfully isolating the signal source in each data analysis, and therefore unlike many cuts-based analyses, this meant that there were no uncertainties associated with exclusivity cuts and dilution factor (used to correct results for scattering reactions from unpolarised nucleons in the nitrogen element of the target material). Each sPlot fit was performed over a specified region of a discriminating variable and, as previously stated, can be considered as acting as a one dimensional cut on an exclusive variable. However, this fit (cut) range was sufficiently wide to allow the background data to be appropriately modelled to successfully isolate the signal source. The very strong agreement in the results obtained for the π^0 channel with and without the use of simulated data for the sPlot fit suggests that the systematic uncertainty in using a bifurcated Gaussian model shape is very small. The analysis was also performed with a standard Gaussian and Voigtian to provide some scope on the uncertainty introduced in the choice of signal shape, and was found to be negligible with reference to the bifurcated Gaussian chosen, as discussed in appendix C. This study obtained a good estimate of the systematic uncertainty as a fraction of statistical uncertainty as being ~ 0.11, and is quantified for the use of the sPlot technique for the removal of background sources. It is important to highlight that there was no correlation between the discriminating variable and the variable ϕ used in forming the asymmetries.

Some uncertainties are dependent on each reaction channel and topology. It should be highlighted that the statistical error appears to be larger than the systematic uncertainty for each analysis which can be seen from the agreement between the values obtained through different analysis methods and from different targets.

Chapter 6

Conclusions

The measurements of beam-, target-, and double-spin asymmetries have been presented for three single pion DVMP channels: π^0 and π^+ from a proton target, and π^- from the neutron target. The spin asymmetry measurements were presented for the charged pion channels for the first time in this kinematic regime. The results were obtained from the EG1-DVCS experimental run at JLab in 2009, making use of both a longitudinally polarised electron beam and target ($^{14}NH_3$ and $^{14}ND_3$). The inclusion of the inner calorimeter greatly improved the acceptance of events for the π^0 channel in comparison to CLAS experiments excluding this detector. The DVMP region criteria was set as being $Q^2 > 1$ GeV^2 and $W > 2$ GeV. Final event selection made use of a maximum likelihood fit-based background subtraction method - the sPlot technique. The data was binned in t, allowing for a meaningful interpretation with relation to Generalised Parton Distributions. The spin asymmetries were produced as functions of ϕ, and suitable fits were made to each to determine the main terms contributing to their form in relation to the theoretical description of the differential cross section of single pion electroproduction.

A thorough investigation was performed in the hopes of measuring asymmetries for the π^- channel which suffers from a lack of statistics, having firstly carried out analyses with a systematic approach on both the π^0 and π^+ channels. The analysis of each channel was performed in a consistent manner with the result presented such that they can be compared easily for the channels and topologies outlined. There was very strong agreement found in the comparison with the work of Smith for the asymmetry results of the π^0 channel. This provided confidence in the use of the sPlot method to conduct fit-based analyses, as opposed to a conventional cuts-based approach for final event selection. Tests were performed with the sPlot technique with and without simulated data to ascertain the best signal shape model PDFs to use for the π^+ and π^- channels. Further studies were performed with different target materials to provide a better understanding of the asymmetry results for numerous channels and topologies of single pion electroproduction via the DVMP mechanism. Testing on NH_3 and ND_3 targets allowed to check if there were any medium-modification effects or final state interactions which could affect the measurements, when the target nucleon is bound within a nucleus. The π^+ results are broadly consistent be-

tween these targets, implying such effects are not significant. The results presented for the π^+ channel are particularly important due to the high statistics and the clear trends in the results that are uniquely different to those of the π^0 channel, and therefore provides a strong reference point and motivation for future analyses on charged pion DVMP channels. There are clear non-zero results for the π^- channel for the beam-spin asymmetry, but the statistical uncertainties are too large to make conclusive statements about the target- and double-spin asymmetry terms. The beam-spin asymmetry measured for the π^- channel shows a unique trend to that of the π^+ channel, and is therefore a very significant result and stresses the importance to also further study this charged pion channel as there may also be important knowledge to be gained from future measurements of the target- and double-spin asymmetries. The results presented for the charged pion channels also motivate studies at higher t to investigate the extended trend progression of the spin asymmetries that were found to increase with t, and will therefore aid theoretical modelling. Beam and target luminosity corrections should be performed on the results to provide a complete set of the DVMP results, however, this is only required for the asymmetry terms in which the trends are meaningful with respect to GPDs. Experimentalists can use the results as reference point, and theorists can make detailed interpretations with respect to GPDs.

The measurement of the t dependence of the asymmetries gives information on the transverse position of the struck parton in the nucleon, and is fundamental to creating a three-dimensional picture of nucleons. The data-points presented can be used to constrain global fits for the extraction of GPDs. The results of the three asymmetries extracted are particularly useful in that they are from the same experimental data, thus provide data-points for very similar kinematics, which in turn provides much more stringent constraints for the fits used to extract GPD information. In particular, the pion channels analysed are particularly sensitive to the helicity dependent GPDs $\widetilde{H}$ and $\widetilde{E}$, with the π^- channel being uniquely sensitive to $\widetilde{E}$. With regards to QCD, use of a neutron target is an important route to understanding the orbital angular momentum of partons within the nucleon. Utilising GPD relations to Form Factors develops insight on the nucleon's charge radius as well as the nucleon spin fraction carried by quarks, for example.

The studies carried out linked the analysis of each channel together, providing confidence in both the means of measurement and the values extracted and presented as the final results. The results presented support the global effort in studying DVMP for the π^0 channel, as well as providing first measurements on the charged pion channels.

The unique analysis method used (sPlot technique) and set of results obtained will be beneficial as a reference point for future Hall B experiments at the upgraded JLab facility, known as the CLAS12 physics programme. There is great interest in nucleon imaging with respect to GPDs at a higher experimental reach in both Q^2 and W, with physics experiments commencing in 2018. There are opportunities to measure DVCS and DVMP with use of an 11 GeV polarised electron beam and longitudinally polarised targets [88] [89] [90], and is therefore a direct extension of work performed and presented in this thesis. There will be an opportunity for spin observables

to be measured for all pion channel variations including π^0 from a neutron target over a wide kinematic range, providing a much more comprehensive set of measurements. Experiments at the upgraded facility will significantly improve in both precision and kinematical coverage, and therefore JLab analyses will drastically improve GPD extraction in the very near future.

Appendix A

The CLAS12 Central Neutron Detector

Substantial time was allocated in the first half of the PhD programme to monitoring and calibration studies of the Central Neutron Detector (CND) prior to its installation in the next-generation CLAS physics program known as CLAS12. The CND was successfully installed in the Hall B experimental setup in 2017.

The CND's main purpose is to detect recoiling neutrons in Deeply Virtual Compton Scattering with use of a deuteron target in which the loosely bound neutron is the active particle in the reaction, i.e. $e\,d \rightarrow e'\,n\,\gamma\,(p)$. The CND's unique design takes the form of a barrel of plastic scintillators, with requirements to achieve good neutron timing and momentum resolutions of ~ 150 ps and within 10% respectively in the momentum and polar angle kinematic range of $0.2 < p < 1.2$ GeV and $40^\circ < \theta < 80^\circ$, as described in detail in the relevant literature [91]. The main background channel for DVCS on the neutron is the neutral pion channel of DVMP, i.e. $ed \rightarrow e'n\pi^0(p)$. A preliminary study on this channel was performed as part of the main analysis in this thesis using the EG1-DVCS data set, but there was not sufficient statistics for any meaningful analysis to be carried out. The CLAS12 physics program will provide an opportunity to successfully study this channel in detail, and therefore will extend the spin asymmetry measurements made for the other pion channels of DVMP analysed in this thesis. Use of the CND with a proton target will increase statistics for the fully exclusive topology of the π^+ channel, and use of the deuterium target provides an opportunity to increase statistics for the π^- channel which were rather limited for the EG1-DVCS experiment.

PhD work on the CND project included the development of software in line with the CLAS collaboration's requirements, and testing of calibration methods. This project covered data acquisition in extensive cosmic tests physically performed at JLab as well as involvement in simulated data generation. Due to the long timescale for detector development and installation in an experimental hall at JLab, a PhD programme cannot cover each stage of the process from beginning to end. The CND project offered a unique opportunity to gain and develop appropriate laboratory technical skills and a thorough understanding of the implementation of a detector system. Work involved, including calibration development, improved the scope of the main data

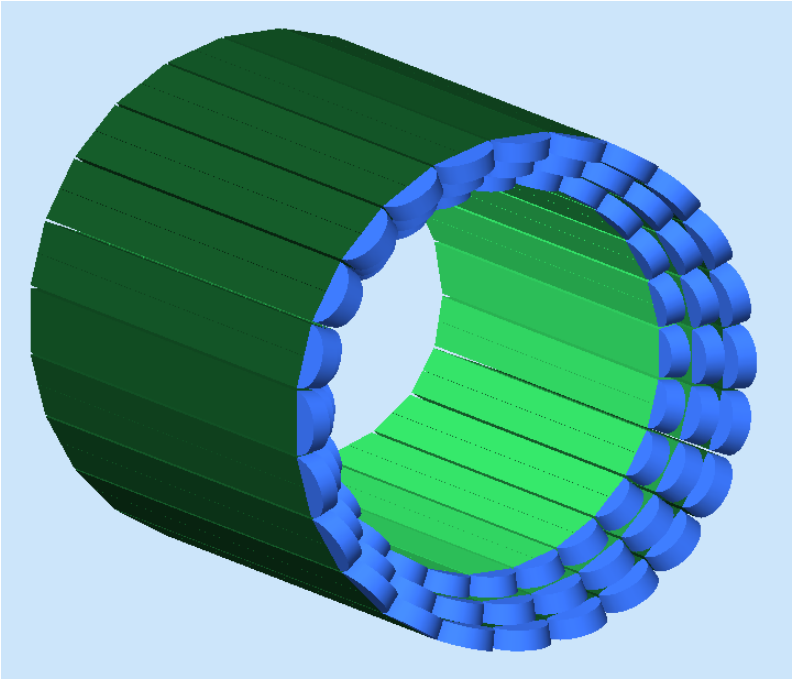

Figure A.1: The complete CND geometry built in the CLAS12 event simulation application, GEMC, showing the three-layer barrel design of scintillator paddles **(green)**, with each pair of scintillators coupled by a lightguide "u-turn" **(blue)** at the downstream end.

analysis project in the thesis presented which made use of calibration work performed by the EG1-DVCS run group.

The three main components of this project were:

- Creating the complete CND geometry for simulation work
- Carrying out cosmic tests at JLab in 2016 and developing monitoring software
- Developing calibration methods and software

The complete CND geometry was built in the CLAS12 event simulation application "Geant4 Monte-Carlo" (GEMC), and was key to extensive simulated data investigations which followed. This geometry is shown in figure A.1 and clearly illustrates the design of a three-layer barrel of scintillator paddles with each pair of scintillators coupled at the downstream end by a lightguide "u-turn". The CND makes use of an upstream readout system. There is a total of 24 paired scintillators, aligned for all layers, and therefore the CND is described as having 24 "sectors". This geometry was created in line with the design specifications including material sizes and offset, and therefore was an important step in generated simulated data that would successfully represent real experimental data.

Cosmic tests were performed at JLab in 2016 and utilised cosmic ray muons incident on the detector. The main goal of these tests were to determine the detector's timing resolution, required to be $\sim$ 150 ps as per the CND's design specification. These tests utilised the CLAS12 electronics equipment of high-resolution time-to-digital converters (TDCs) and flash analog-to-digital converters (fADCs). Six of the 24 sectors of the CND were tested due to time constraints, although this was an appropriate level of investigation. Each of these sectors were individually tested. An appropriate trigger was configured for the cosmic test experiment, in which the timing and charge information was measured for "good" events by the TDC and fADC respectively. This trigger required a muon to be measured in all three layers of the CND sector within a short time window. Experience was gained in the use of the electronics setup and signal readout, including operation of data acquisition software and hardware experience with high voltage units and signal splitters, as well as modules such as a constant fraction discriminator, mean timer, and coincidence unit. Monitoring software was developed as part of the cosmic test project, showing clear visualisations of important information in the data stream such as raw timing and charge information. After the acquisition of cosmic data, further processing of the data was investigated to correct timing offsets, remove poorly measured events and remove accidentals. Each coupled pair of scintillators were attached to lightguides with a corresponding PMT for each side of the pair, with each being referred to as a "counter". As outlined in detail in the relevant literature [91], the average time resolution (σ) for a coupled pair of counters could be determined for the cosmic test configuration used. Preliminary time resolution measurements were made for the six sectors during the time allocated to this project, with the results shown in figure A.2. The systematic uncertainty was previously estimated by the CND group as being $\sim$ 8%, based on extensive cosmic tests with studies of the time resolution. Four of the six sectors tested were found to meet the time resolution design specification criteria. Significant time during the cosmic tests project was spent studying the first data acquired with use of the final CLAS12 electronics (TDCs and fADCS), and included troubleshooting and implementing changes to improve on the trigger configuration. The results obtained highlighted the need for further investigations on the processing of data with regards to timing offsets and optimising the removal of poorly measured events, but were a good indication of the reality of achieving the required time resolution design specification of $\sim$ 150 ps, which was later successfully confirmed by the CND group.

The final component of the CND project was on the development of calibration methods and corresponding software's graphical user interface. A milestone in this work was the successful participation in the December 2016 CLAS12 Calibration Challenge organised by the Calibration Committee (CalCom) of Hall B. The purpose of this Challenge was to test the functionality of the calibration suite developed and the calibration procedures (including sequence and interdependencies of calibration steps). Smeared Monte Carlo simulated data was calibrated for the CND, and the exercise was useful in highlighting issues with regards to realistic particle

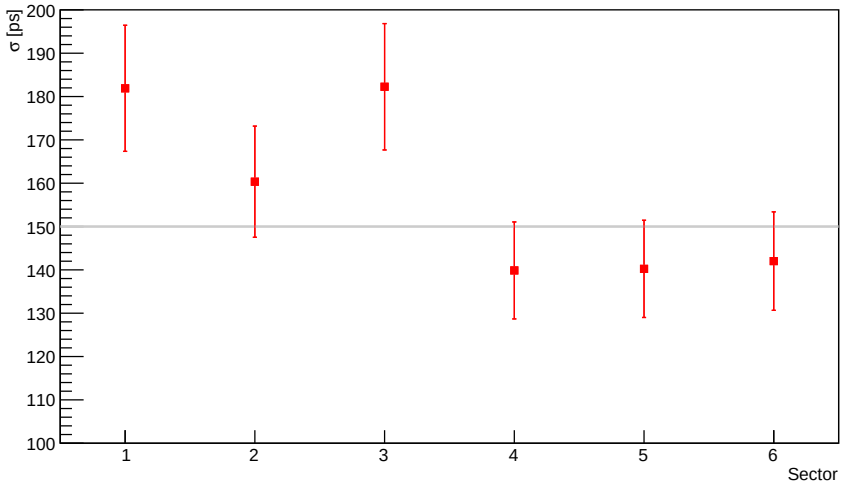

Figure A.2: Measurements of the time resolution (σ) for the six CND sectors used in the cosmic tests at JLab in 2016.

distributions and how to overcome these with suitable alterations to the calibration methods. Specific elements tested for the CND during the Challenge were:

- Counter status (checking for working TDC and fADC modules)
- Coupled-counter timing offsets
- Layer timing offsets
- Effective velocity

All the above elements were tested successfully with a good standard of results although they did highlight improvements, alternative calibration methods to develop, and systematic offset corrections required. The counter status was correctly identified for all counters, in which there were only two out of 144 classed as "dead" (no TDC and fADC information). Following the event, the internal CalCom Calibration Challenge Report was issued and stated that good agreement was found for the CND timing offsets and effective velocities at the level of $\leq$ 1.5%. Graphical comparisons of the original and extracted calibration constant values were generated by the CalCom team to report on the CND's success, and are displayed in figure A.3. The Calibration Challenge was critical in providing insight to finalise calibration methods and introduce additional required calibration methods (e.g. light attenuation). Further developments made use of additional simulated data and the real cosmic data acquired in 2016.

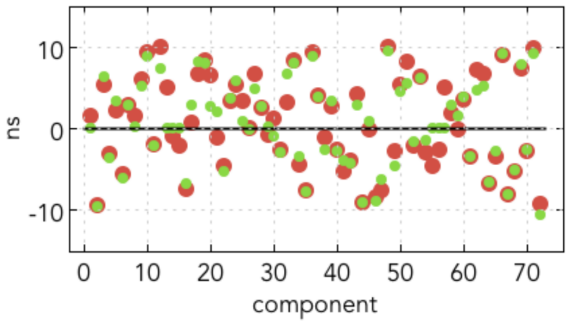

(a) Coupled-counter timing offsets

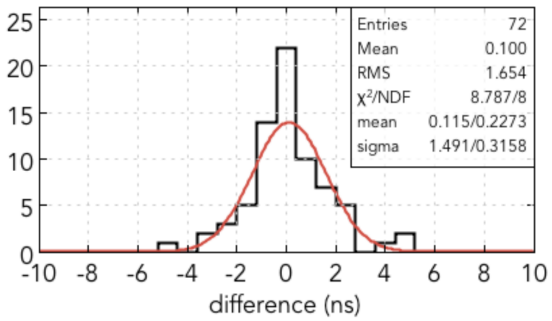

(b) Coupled-counter timing offsets discrepancy

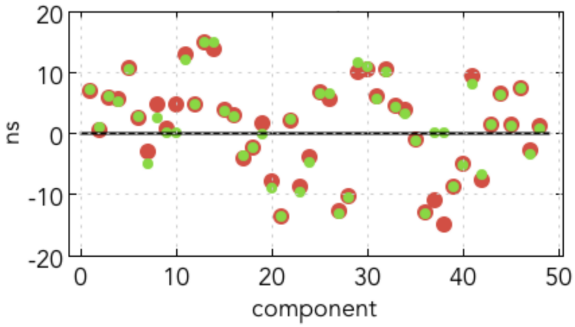

(c) Layer timing offsets

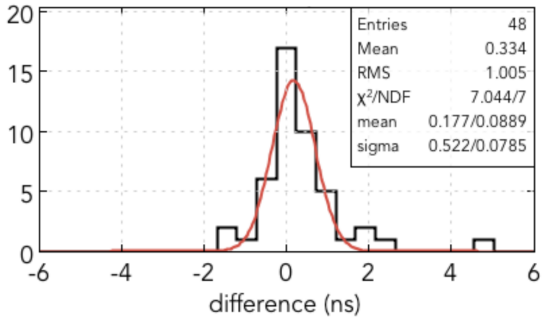

(d) Layer timing offsets discrepancy

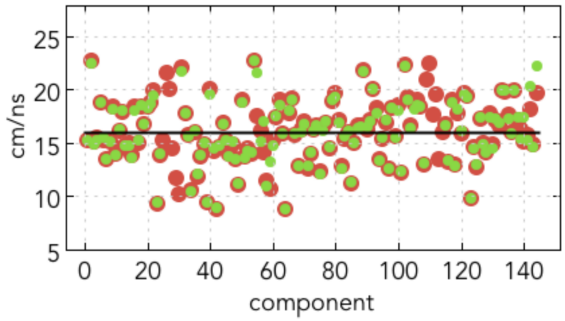

(e) Effective velocity

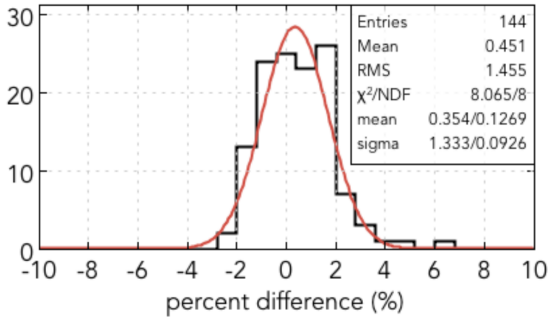

(f) Effective velocity discrepancy

Figure A.3: Results of the Calibration Challenge, graphs produced by the CalCom team. Graphs on the left show the comparison of the original **(red)** and extracted **(green)** calibration constant values for the coupled-counter timing offsets (top), layer timing offsets (middle) and effective velocity (bottom) as a function of the detector element. Lines in these graphs show the ideal values, although the original calibration constant values were purposefully not set to these to provide appropriate testing conditions. Graphs on the right show the discrepancy between the original and extracted calibration constant values, with a Gaussian fit to this data.

Appendix B

π^- Channel: Background Data Choice

A study was performed to check the suitability of the choice of the background data to use for the analysis of the π^- chanel. This was carried out to ensure there were no significant issues between the experimental run period B and C, and helps justify the use of part B NH_3 as the background data shape model for the π^- channel which uses the part C ND_3 data to obtain the signal.

The motivation to use the part B NH_3 dataset for the background model was that the statistics were much higher than for the part C ^{12}C data. The nitrogen element of the NH_3 should of course best describe the nitrogen element of the ND_3 target data, which essentially corresponds to background.

Having carried out the PID cuts for the exclusive topology of the π^- channel, a comparison of missing mass distributions was made between the carbon data for parts B and C, as shown in figure B.1. An appropriate scaling of the data was used to help match the luminosity for these data and the figure shows that the distributions are very similar for these datasets from the two different run periods, particularly in the region of the expected signal. This implies that the datasets are compatible.

As the statistics were higher for the part B ^{12}C data than that of the part C ^{12}C, the next comparison made was between the part B ^{12}C and part B NH_3, as shown in figure B.2. There should be no signal peak at the proton's invariant mass in the pion missing mass plot shown in figure B.2a, which is the case, and the two datasets are in agreement until approximately 1.05 GeV, which is where the multi-meson electroproduction peak becomes more prominent for the NH_3 data. There is also agreement in the spectator missing mass plot as shown in figure B.2b.

These findings indicate that it was suitable to use the part B NH_3 data as the background shape model for the π^- channel, as opposed to the part C ^{12}C data, as has been typically done in other analyses of the EG1-DVCS dataset.

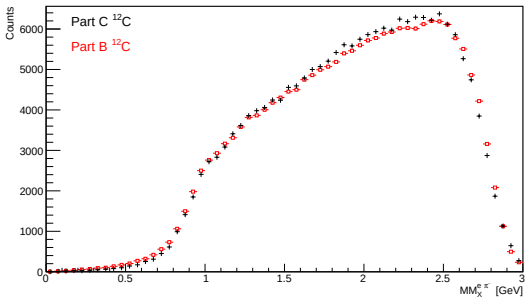

(a) Pion missing mass

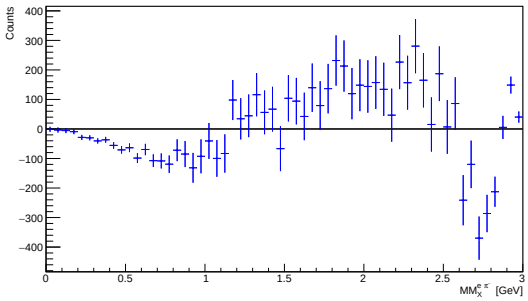

(b) Difference of pion missing mass distributions

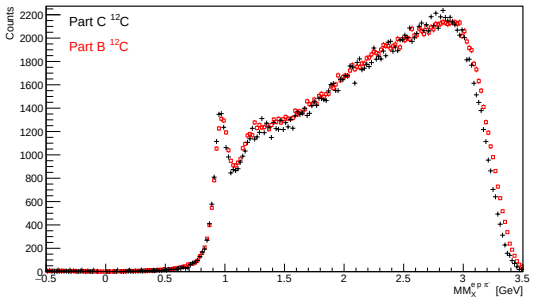

(c) Spectator proton missing mass

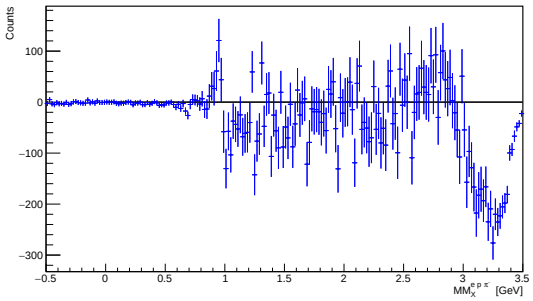

(d) Difference of spectator proton missing mass distributions

Figure B.1: Comparisons of ^{12}C data from part B and part C. Histograms on the left show part B ^{12}C data in **red** and part C ^{12}C data in **black**. Note, the histograms in (a) and (b) have been rebinned by 5 for visual purposes.

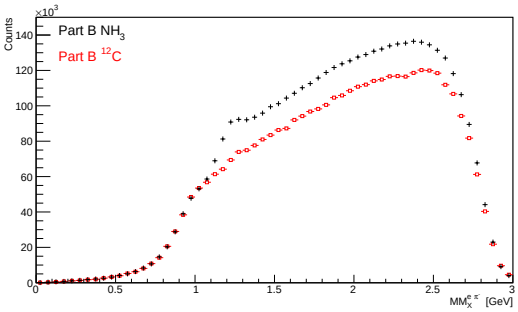

(a) Pion missing mass

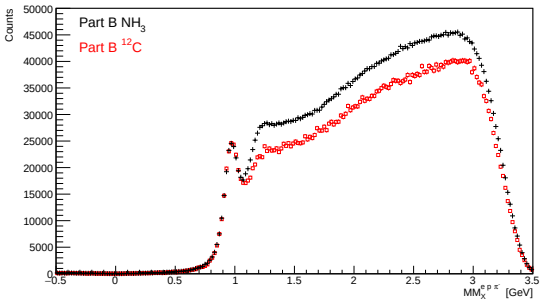

(b) Spectator proton missing mass

Figure B.2: Comparisons of part B NH_3 data **(black)** and part B ^{12}C data **(red)**. Note, the histogram in (a) has been rebinned by 5 for visual purposes.

Appendix C

Check of Signal Shape Model Choice

A study was performed to check the suitability of the final choice in using a bifurcated Gaussian to model the signal shape with the sPlot method. Such a choice of signal shape model was required to perform an analysis of the π^+ and π^- channels in which there was no simulated data (only available for the π^0 channel for the NH_3 target data). This therefore required an assessment of the signal shape models for the exclusive topology of the π^0 channel with use of the NH_3 target, as discussed in section 5.1.4. A good estimate was made on the systematic uncertainty in using the sPlot technique for the removal of background.

With regards to the simulated data model, the asymmetry results were compared for a bifurcated Gaussian (Gaussian with different widths on the left and right side), a standard Gaussian, and a Voigtian (convolution of Breit-Wigner and Gaussian).

The final binned asymmetries were compared for these signal shape models, but visually there is very little difference. This can be seen in the presented results of beam-, target-, and double-spin asymmetries in figures C.1, C.2 and C.3 respectively. There is very little difference between the results for the model shapes that do not make use of simulated data - and therefore the most appropriate choice was the bifurcated Gaussian, based on further checks with the simulated data.

To fully appreciate the differences observed, the uncertainty in the signal shape was quantified by the use of a pull distribution for each of the shape models. These distributions are error-weighted distributions of the measured value for one model shape around the mean values of the same parameter from all four model shapes. Pull distributions were produced for the two beam-, three target-, and two double-spin asymmetry parameters for each model shape, totalling 28 plots. The "pull" value for each plot was calculated for each of the 5 t bins (i), according to

$$pull = \frac{A_i - A_{mean}}{\sigma_i} \tag{C.1}$$

where A_i is the measured value for the model shape being assessed, σ_i is its error, and A_{mean} is the mean value of the same parameter from all four model shapes. The width of the distribution

essentially quantifies the systematic uncertainty as a fraction of the statistical uncertainty.

The statistics were low due to there only being 5 t bins for each pull distribution, therefore the combination of all pull distributions is shown in figure C.4 which has a total of 140 entries. The mean of the Gaussian fit to the histogram is -0.0052 which shows that there is no significant bias overall (no systematic shift), and the standard deviation (*Sigma*) essentially shows that overall the systematic uncertainty in the sPlot background removal technique accounts for approximately 11% of the statistical error. This study gives a good quantification of this systematic which had not been investigated before.

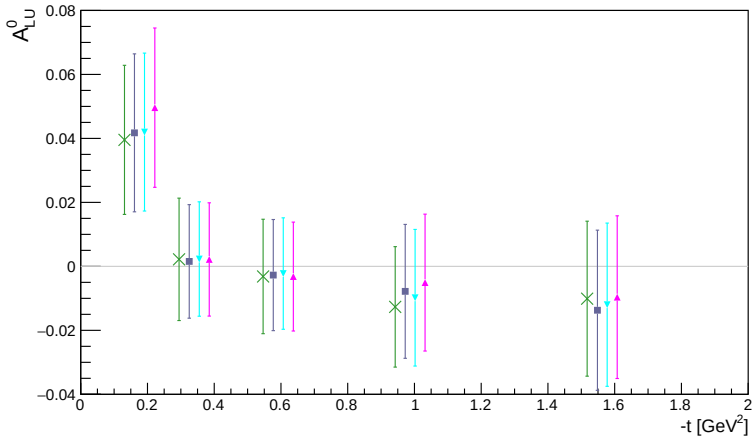

(a) A^0_{LU}

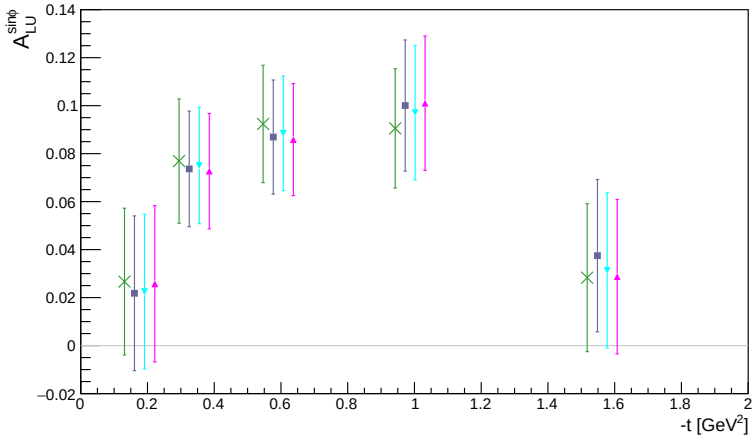

(b) $A^{sin\phi}_{LU}$

Figure C.1: π^0 channel: exclusive topology, NH_3 target. Beam-spin asymmetries binned in t. Shown for the data selected using the fits made to the proton missing mass squared using simulated data as the signal shape (**forest green multiplication signs** $\times$), bifurcated Gaussian (**blue-grey squares** ■), standard Gaussian (**cyan down-pointing triangles** ▼), and Voigtian (**magenta up-pointing triangles** ▲). All data points have been slightly offset in t.

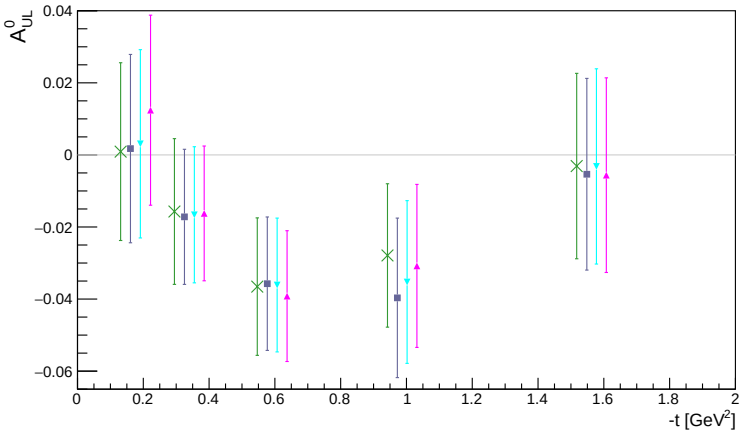

(a) A^0_{UL}

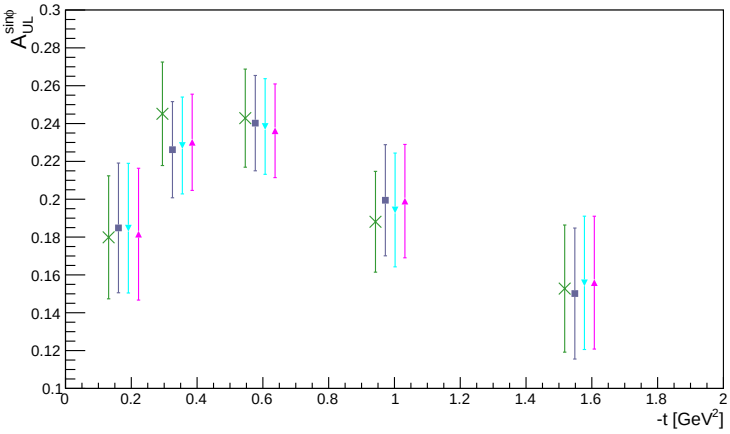

(b) $A^{sin\phi}_{UL}$

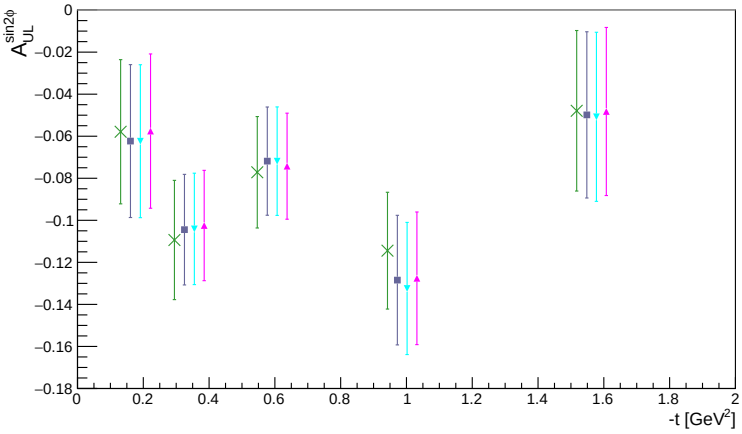

(c) $A^{sin2\phi}_{UL}$

Figure C.2: $\underline{\pi^0 \text{ channel:}}$ exclusive topology, NH_3 target. Target-spin asymmetries binned in t. Shown for the data selected using the fits made to the proton missing mass squared using simulated data as the signal shape (**forest green multiplication signs** $\times$), bifurcated Gaussian (**blue-grey squares** ■), standard Gaussian (**cyan down-pointing triangles** ▼), and Voigtian (**magenta up-pointing triangles** ▲). All data points have been slightly offset in t.

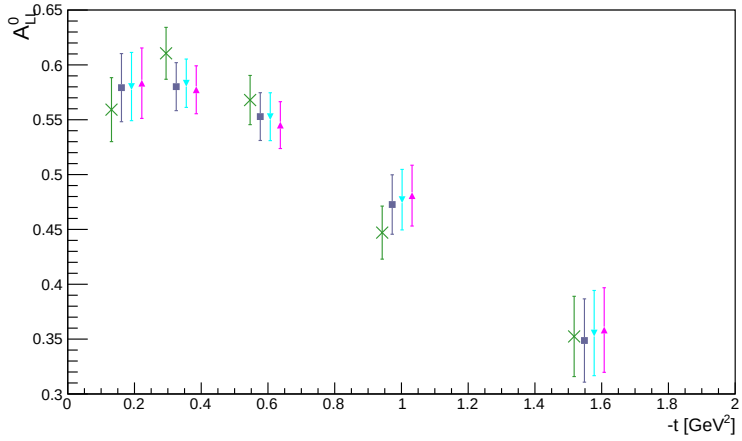

(a) A_{LL}^{0}

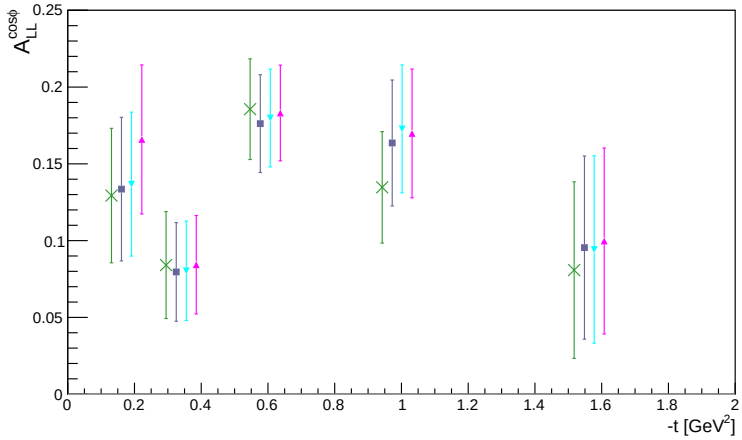

(b) $A_{LL}^{cos\phi}$

Figure C.3: π^0 channel: exclusive topology, NH_3 target. Double-spin asymmetries binned in t. Shown for the data selected using the fits made to the proton missing mass squared using simulated data as the signal shape (**forest green multiplication signs** $\times$), bifurcated Gaussian (**blue-grey squares** ■), standard Gaussian (**cyan down-pointing triangles** ▼), and Voigtian (**magenta up-pointing triangles** ▲). All data points have been slightly offset in t.

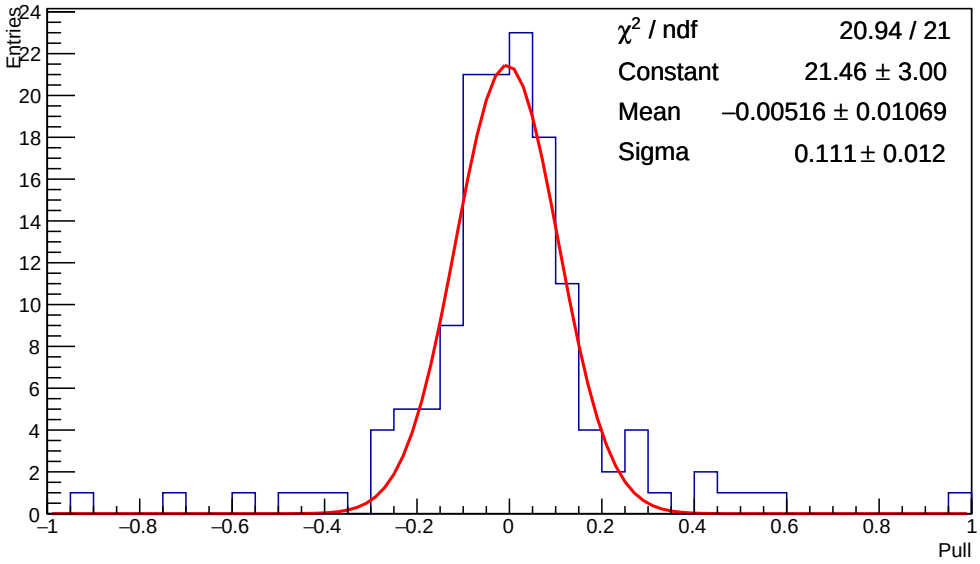

Figure C.4: Combination of all pull distributions for all four model shapes, representing the systematic uncertainty as a fraction of the statistical uncertainty. The histogram has been fit with a Gaussian.

Bibliography

[1] Dürr, S. et al. 2008. Ab-initio Determination of Light Hadron Masses. *Science.* **322**(5905), pp.1224-1227.

[2] Belitsky, A.V. and Radyushkin, A.V. 2005. Unraveling hadron structure with generalized parton distributions. *Physics Reports.* **418**(1), pp.1-387.

[3] Greiner, W., Schramm, S. and Stein, E. 2002. *Quantum Chromodynamics.* 2nd ed. Heidelberg: Springer-Verlag Berlin Heidelberg.

[4] Guidal, M. 2008. Generalized Parton Distributions and deep virtual Compton scattering. *Progress in Particle and Nuclear Physics.* **61**(1), pp.89-105.

[5] Smith, G.D. 2013. *Measurements of Spin Asymmetries for Deeply Virtual Compton Scattering off the Proton using the Extended Maximum Likelihood Method.* Ph.D. thesis, University of Glasgow.

[6] Kumericki, K., Liuti, S. and Moutarde, H. 2016. GPD phenomenology and DVCS fitting. *Eur. Phys. J. A.* **52**(6), 157.

[7] Diehl, M. 2003. Generalized parton distributions. *Physics Reports.* **388**(2), pp.41-277.

[8] Müller, D., Lautenschlager, T., Passek-Kumerički, K. and Schäfer, A. 2014. Towards a fitting procedure to deeply virtual meson production - the next-to-leading order case. *Nuclear Physics B.* **884**, pp.438-546.

[9] Collins, J.C., Frankfurt, L. and Strikman, M. 1997. Factorization for hard exclusive electroproduction of mesons in QCD. *Phys. Rev. D.* **56**(5), pp.2982-3006.

[10] Ahmed, Z. and Ye, Z. 2016. *E12-10-006B: Deep Exclusive π^- Production with transversely polarized He3 using SoLID* [PowerPoint presentation]. Presentation at the University of Regina, 15 July 2016, Saskatchewan.

[11] Kubarovsky, V. 2016. Deeply Virtual Pseudoscalar Meson Production at Jefferson Lab and Transversity GPDs. *Int. J. Mod. Phys. Conf. Ser.* **40**, 1660051.

[12] Goldstein, G.R., Liuti, S. and Gonzalez Hernandez, J.O. 2012. A flexible parameterization of GPDs, their role in DVCS, neutral meson leptoproduction. In: Steadman, S.G., Stephans, G.S.F. and Taylor, F.E. eds. *19th Particles and Nuclei International Conference (PANIC11), 24-29 July 2011, Massachusetts.* New York: AIP Publishing, **1441**, pp.141-145.

[13] Ji, X. 1998. Off-Forward Parton Distributions. *J. Phys. G: Nucl. Part. Phys.* **24**(7), pp.1181-1205.

[14] Mankiewicz, L., Piller, G. and Weigl, T. 1998. Hard leptoproduction of charged vector mesons. *Phys.Rev. D.* **59**, 017501.

[15] Lautenschlager, T. 2015. *Towards a Global Estimate for Generalized Parton Distributions.* Ph.D. thesis, University of Regensburg.

[16] Ji, X. 2004. Generalized parton distributions. *Annu. Rev. Nucl. Part. Sci.* **54**, pp.413-450.

[17] Cheoun, M.K. and Kim, K.S. 2007. The pseudo-scalar form factor of the nucleon, the sigma-like term, and the L_0^+ amplitude for charged pion electro-production near threshold. *Physics Letters B.* **645**, pp.422-426.

[18] Ji, X. 1997. Gauge-Invariant Decomposition of Nucleon Spin. *Phys. Rev. Lett.* **78**(4), pp.610-613.

[19] Burkardt, M. 2013. The Nucleon Spin Sum Rule. In: Fleming., B. ed. *11th Conference on the Intersections of Particle and Nuclear Physics: (CIPANP 2012), 29 May - 3 June 2012, Florida.* New York: AIP Publishing, **1560**, pp.495-499.

[20] Ji, X. 1997. Deeply virtual Compton scattering. *Phys. Rev. D.* **55**(11), 7114.

[21] Boffi, S. and Pasquini, B. 2007. Generalized parton distributions and the structure of the nucleon. *Riv.Nuovo Cim.* **30**, pp.387-448.

[22] Kim, A. 2013. *Single and Double Spin Asymmetries for Deeply Virtual Exclusive π^0 Production on Longitudinally Polarized Proton Target with CLAS.* Ph.D. thesis, Kyungpook National University.

[23] Goloskokov, S.V. and Kroll, P. 2010. An attempt to understand exclusive π^+ electroproduction. *Eur. Phys. J. C.* **65**(1), pp.137-151.

[24] Favart, L., Guidal, M., Horn, T. and Kroll, P. 2016. Deeply virtual meson production on the nucleon. *Eur. Phys. J. A.* **52**(6), 158.

[25] Bedlinskiy, I. et al. 2012. Measurement of Exclusive π^0 Electroproduction Structure Functions and their Relationship to Transverse Generalized Parton Distributions. *Phys. Rev. Lett.* **109**, 112001.

[26] Siddikov, M. and Schmidt, I. 2017. Generalized parton distributions from charged current meson production in ep experiments. *Phys. Rev. D.* **96**, 096006.

[27] Tiator, L., Workman, R. L., Wunderlich, Y. and Haberzettl, H. 2017. Amplitude reconstruction from complete electroproduction experiments and truncated partial-wave expansions. *Phys. Rev. C.* **96**, 025210.

[28] http://www.portal.kph.uni-mainz.de/MAID/; Drechsel, D., Hanstein, O., Kamalov, S.S. and Tiator, L. 1999. A unitary isobar model for pion photo- and electroproduction on the proton up to 1 GeV. *Nucl. Phys. A.* **645**, pp.145-174.

[29] Airapetian, A. et al. 2001. Measurement of the Beam-Spin Azimuthal Asymmetry Associated with Deeply-Virtual Compton Scattering. *Phys. Rev. Lett.* **87**, 182001.

[30] Stepanyan, S. et al. 2001. Observation of Exclusive Deeply Virtual Compton Scattering in Polarized Electron Beam Asymmetry Measurements. *Phys. Rev. Lett.* **87**, 182002.

[31] Mazouz, M. et al. 2007. Deeply Virtual Compton Scattering off the Neutron. *Phys. Rev. Lett.* **99**, 242501.

[32] Horn, T. et al. 2008. Scaling study of the pion electroproduction cross sections. *Phys. Rev. C.* **78**, 058201.

[33] De Masi, R. et al. 2008. Measurement of $ep \to ep\pi^0$ beam spin asymmetries above the resonance region. *Phys. Rev. C.* **77**, 042201.

[34] Kim, A. et al. 2017. Target and Double Spin Asymmetries of Deeply Virtual π^0 Production with a Longitudinally Polarized Proton Target and CLAS. *Phys. Lett. B.* **768**, pp.168-173.

[35] Bosted, P.E. 2017. Target and beam-target spin asymmetries in exclusive pion electroproduction for $Q^2 > 1$ GeV^2. I. $ep \to e\pi^+ n$. *Phys. Rev. C.* **95**, 035206.

[36] Bosted, P.E. et al. 2016. Target and Beam-Target Asymmetries in Exclusive π^+ and π^- Electroproduction with 1.6 to 5.7 GeV Electrons. *Phys. Rev. C.* **94**, 055201.

[37] Mecking, B.A. et al. 2003. The CEBAF large acceptance spectrometer (CLAS). *Nuclear Instruments and Methods in Physics Research Section A: Accelerators, Spectrometers, Detectors and Associated Equipment.* **503**(3), pp.513-553.

[38] Leemann, C.W., Douglas, D.R. and Krafft, G.A. 2001. The Continuous Electron Beam Accelerator Facility: CEBAF at the Jefferson Laboratory. *Annual Review of Nuclear and Particle Science.* **51**, pp.413-450.

[39] Kazimi, R. et al. 2004. CEBAF Injector Achieved World's Best Beam Quality for Three Simultaneous Beam with a Wide Range of Bunch Charges. *Proceedings of the 2004 European Particle Accelerator Conference.* pp.1512-1514.

[40] Reece, C.E. 2016. Continuous wave superconducting radio frequency electron linac for nuclear physics research. *Phys. Rev. Accel. Beams.* **19**, 124801.

[41] Grames, J.M. et al. 2010. Unique electron polarimeter analyzing power comparison and precision spin-based energy measurement. *Phys. Rev. ST Accel. Beams.* **13**, 069901.

[42] Raue, B.A. et al. 1998. *A double-arm Møller Polarimeter for Jefferson Lab's Hall B.* Division of Nuclear Physics 1998 Meeting Program, 28-31 October 1998, New Mexico.

[43] Beard, K.B. et al. 1995. Measurement of the polarization of a pulsed electron beam with a Møller polarimeter in the coincidence mode. *Nuclear Instruments and Methods in Physics Research Section A: Accelerators, Spectrometers, Detectors and Associated Equipment.* **361**, pp.46-52.

[44] Ursic, R. et al. 1997. 1 nA Beam Position Monitoring System. In: Comyn, M. Craddock, M.K., Reiser, M. and Thomson, J. eds. *The 1997 Particle Accelerator Conference, 12-16 May 1997, British Columbia.* New Jersey: IEEE, pp.2131-2133.

[45] Egberts, J. et al. 2009. Design of a beam halo monitor with a high dynamic range. In: *The XXIV International Linear Accelerator Conference (LINAC08), 29 September - 3 October 2008, British Columbia.* Geneva: JACoW, pp.570-572.

[46] Cuevas, C., Denard, J.C., Freyberger, A.P. and Sharabian, Y. 2001. Beam Charge Asymmetry Monitors for Low Intensity Continuous Electron Beam. *5th European Workshop on Diagnostics and Beam Instrumentation (DIPAC 2001), 13-15 May 2001, Grenoble.* Grenoble: ESRF, pp.91-93.

[47] Anghinolfi, M. et al. 2005. The CLAS Electromagnetic Calorimeter at Large Angles. *Nuclear Instruments and Methods in Physics Research Section A: Accelerators, Spectrometers, Detectors and Associated Equipment.* **537**(3), pp.562-570.

[48] O'Meara, J. et al. 1989. A Superconducting Toroidal Magnet for the CEBAF Large Acceptance Spectrometer. *IEEE Trans. Mag.* **25**(2), pp.1902-1905.

[49] Mestayer, M.D. et al. 2000. The CLAS drift chamber system. *Nuclear Instruments and Methods in Physics Research Section A: Accelerators, Spectrometers, Detectors and Associated Equipment.* **449**(1-2), pp.81-111.

[50] Gohn, W. et al. 2014. Beam-spin asymmetries from semi-inclusive pion electroproduction. *Phys. Rev. D.* **89**, 072011.

[51] Jefferson Laboratory. 2018. *CLAS - photo gallery.* [Online]. [Accessed 6 September 2018]. Available from: https://www.jlab.org/Hall-B/album/

[52] Adams, G. et al. 2001. The CLAS Cherenkov detector. *Nuclear Instruments and Methods in Physics Research Section A: Accelerators, Spectrometers, Detectors and Associated Equipment.* **465**(2-3), pp.414-427.

[53] Smith, E.S. et al. 1999. The time-of-flight system for CLAS. *Nuclear Instruments and Methods in Physics Research Section A: Accelerators, Spectrometers, Detectors and Associated Equipment.* **432**(2-3), pp.265-298.

[54] Amarian, M. et al. 2001. The CLAS forward electromagnetic calorimeter. *Nuclear Instruments and Methods in Physics Research Section A: Accelerators, Spectrometers, Detectors and Associated Equipment.* **460**(2-3), pp.239-265.

[55] Avakian, H. et al. 2006. PR06-003, Deeply Virtual Compton Scattering with CLAS at 6 GeV. *New Research Proposal, Jefferson Laboratory.*

[56] Jo, H.S. 2007. *Etude de la Diffusion Compton Profondément Virtuelle sur le Nucléon avec le Détecteur CLAS de Jefferson Lab: Mesure des Sections Efficaces polarisées et non polarisées.* Ph.D. thesis, University of Paris-Sud.

[57] Niyazov, R. and Stepanyan, S. 2005. CLAS-NOTE-2005-021, CLAS/DVCS Inner Calorimeter Calibration. *Technical report, Jefferson Laboratory.*

[58] Jefferson Laboratory. 2012. *FROST website.* [Online]. [Accessed 6 September 2018]. Available from: https://clasweb.jlab.org/rungroups/g9/wiki/

[59] Jefferson Laboratory. 2008. *CLAS HDice Target website.* [Online]. [Accessed 6 September 2018]. Available from: https://www.jlab.org/Hall-B/HDIce/

[60] Keith, C.D. et al. 2003. A polarized target for the CLAS detector. *Nuclear Instruments and Methods in Physics Research Section A: Accelerators, Spectrometers, Detectors and Associated Equipment.* **501**(2-3), pp.327-339.

[61] Doughty, D. et al. 2001. PR01-113, Deeply Virtual Compton Scattering with CLAS at 6 GeV. *New Research Proposal, Jefferson Laboratory.*

[62] Ball, J. et al. 2006. Progress Report 2004-2006, Superconducting solenoid for the CLAS DVCS experiment. *Technical report, The French Alternative Energies and Atomic Energy Commission.*

[63] Jefferson Laboratory. 2018. *CODA Documentation website.* [Online]. [Accessed 6 September 2018]. Available from: https://coda.jlab.org/

[64] Abbott, D. 2008. *Data Acquisition Systems for Experimental Nuclear Physics* [PowerPoint presentation]. Jefferson Laboratory. [Accessed: 6 September 2018]. Available from: https://www.jlab.org/div_dept/consortium/07Series/DAbbott.pdf

[65] Heyes, G. 2016. *Data Acquisition at JLab* [PowerPoint presentation]. JLab Summer Students Presentation 28 July 2016, Virginia.

[66] Avakian, H. et al. 2005. PR05-113, Semi-Inclusive Pion Production with a Longitudinally Polarized Target at 6 GeV. *New Research Proposal, Jefferson Laboratory.*

[67] Avakian, H. et al. 2005. PR05-114, Deeply Virtual Compton Scattering at 6 GeV with polarized target and polarized beam using the CLAS detector. *New Research Proposal, Jefferson Laboratory.*

[68] Jefferson Laboratory. 2012. *EG1-DVCS.* [Online]. [Accessed 6 September 2018]. Available from: https://clasweb.jlab.org/rungroups/eg1-dvcs/wiki/

[69] Jawalkar, S., Kvaltine, N., Bosted, P. and Prok, Y. 2010. EG1-DVCS Technical Note #017, Calculating length between the banjo windows and effective length of NH_3. *Technical report, Jefferson Laboratory.*

[70] Bosted, P. 2012. EG1-DVCS Technical Note #017, NH_3 contamination in ND_3 target. *Technical report, Jefferson Laboratory.*

[71] Rossi, P. 2009. *Eg1-DVCS report* [PowerPoint presentation]. JLab12 Third Collaboration Meeting, 19-20 October 2009, Rome.

[72] Bosted, P.E., Kvaltine, N. and Prok, Y. 2013. CLAS-NOTE-2013-010, Inclusive Polarized Structure Functions g_1^p and g_1^d from the eg1-DVCS experiment. *Technical report, Jefferson Laboratory.*

[73] Dodge, G. et al. 2003. PR03-012, The Structure of the Free Neutron Via Spectator Tagging. *New Research Proposal, Jefferson Laboratory.*

[74] Jawalkar, S. and Bosted, P. 2010. EG1-DVCS Technical Note #006, Ntuple 22 from Ntuple 10. *Technical report, Jefferson Laboratory.*

[75] Kim, A. 2012. EG1-DVCS Technical Note #22, Good File List from file rate study. *Technical report, Jefferson Laboratory.*

[76] Bosted, P. and Kim, A. 2010. EG1-DVCS Technical Note #002, Beam (x,y) and Target Center z from Raster ADCs. *Technical report, Jefferson Laboratory.*

[77] Prok, Y. 2010. EG1-DVCS Technical Note #009, Checking for beam scraping on target edges using raster ADCs. *Technical report, Jefferson Laboratory.*

[78] Bosted, P. 2011. EG1-DVCS Technical Note #004, Tracking from Drift Chambers to Target through Solenoid. *Technical report, Jefferson Laboratory.*

[79] Bosted, P. 2011. EG1-DVCS Technical Note #021, Photon Energy Corrections and Reduction of Backgrounds under π^0 Mass Peak. *Technical report, Jefferson Laboratory.*

[80] Bosted, P. 2011. EG1-DVCS Technical Note #013, Fiducial Cuts based on IC Shielding. *Technical report, Jefferson Laboratory.*

[81] Osipenko, M., Vlassov, A. and Taiuti, M. 2004. CLAS-NOTE-2004-020, Matching between the electron candidate track and the Cherenkov counter hit. *Technical report, Jefferson Laboratory.*

[82] Tanabashi, M. et al. (Particle Data Group). 2018. Review of Particle Physics. *Phys. Rev. D.* **98**, 030001.

[83] Agostinelli, S. et al. 2003. GEANT4 — a simulation toolkit. *Nuclear Instruments and Methods in Physics Research Section A: Accelerators, Spectrometers, Detectors and Associated Equipment.* **506**(3), pp.250-303.

[84] CERN. 2014. *RooFit.* [Online]. [Accessed 6 September 2018]. Available from: https://root.cern.ch/roofit

[85] Pivk, M. and Diberder, F.R.L. 2005. ${}_s\mathscr{P}lot$: A statistical tool to unfold data distributions. *Nuclear Instruments and Methods in Physics Research Section A: Accelerators, Spectrometers, Detectors and Associated Equipment.* **555**(1-2), pp.356-369.

[86] Bosted, P.E. 2014. CLAS-ANALYSIS, Spin Asymmetries in exclusive π^+, π^0, η and π^- electroproduction from the eg1-DVCS experiment. *Technical report, Jefferson Laboratory.*

[87] Biselli, A. et al. 2014. CLAS-ANALYSIS-2014-104, Measurements of single- and double-spin asymmetries for deeply virtual Compton scattering with a polarized electron beam and a longitudinally polarized proton target. *Technical report, Jefferson Laboratory.*

[88] Biselli, A. et al. 2006. E12-06-119. Deeply Virtual Compton Scattering with CLAS12 at 11 GeV. *New Research Proposal, Jefferson Laboratory.*

[89] Niccolai, S. et al. 2011. E12-11-003. Deeply Virtual Compton Scattering on the Neutron with CLAS12 at 11 GeV. *New Research Proposal, Jefferson Laboratory.*

[90] Niccolai, S. et al. 2016. E12-06-109A. Deeply virtual Compton scattering on the neutron with a longitudinally polarized deuteron target. *New Research Proposal, Jefferson Laboratory.*

[91] Niccolai, S. et al. 2018. The central neutron detector for CLAS12. *Nuclear Instruments and Methods in Physics Research Section A: Accelerators, Spectrometers, Detectors and Associated Equipment.* **904**, pp.81-92.